

Electrocaloric and barocaloric effects in organic materials



Zipeng Liu

Department of Materials Science & Metallurgy

Churchill College

University of Cambridge

This thesis is submitted for the degree of

Doctor of Philosophy

June 2022

Supervisor: Dr Xavier Moya

Declaration

This thesis is the result of my own work and includes nothing which is the outcome of work done in collaboration except as declared in the preface and specified in the text. It is not substantially the same as any work that has already been submitted before for any degree or other qualification except as declared in the preface and specified in the text. It does not exceed the prescribed word limit of 60,000 words for the Degree Committee. This report conforms to the University of Cambridge's guidelines on plagiarism. Where reference has been made to other research, this is acknowledged in the text and bibliography.

Abstract

Electrocaloric and barocaloric effects in organic materials

Zipeng Liu

Electrocaloric (EC) and barocaloric (BC) materials undergo reversible thermal changes in response to changes in applied electric field and pressure, respectively. These materials could potentially be exploited in novel solid-state cooling systems that may replace current vapour-compression systems, which are environmentally harmful, noisy, and relatively energy inefficient.

In this work, I studied EC effect and BC effects in multicaloric organic materials, which promise large caloric effects near room temperature. The dissertation is structured as follows.

Chapter 1 introduces the background for conventional refrigeration and traditional caloric materials. Chapter 2 then surveys the literature on EC materials and BC materials, as well as the literature on EC prototype devices.

Chapter 3 reviews the experimental and modelling methods used for this work. These include sample preparation methods, dielectric spectroscopy and ferroelectric polarisation measurements, calorimetry and infrared imaging, dilatometry and Landau models.

Chapter 4 describes the study of EC effects in two dabco-based organic salts, namely [Hdabco][BF₄] and [AH][ReO₄], where dabco is 1,4-diazabicyclo[2.2.2]octane and AH is a variant of dabco, 1-azabicyclo[2.2.1]heptanium. Experiments and modelling demonstrates that [Hdabco][BF₄] shows giant EC effects (isothermal entropy change $|\Delta S| = 15.5 \text{ J K}^{-1} \text{ kg}^{-1}$ for $|\Delta E| = 12 \text{ kV cm}^{-1}$) that are one order-of-magnitude larger than those observed in traditional EC oxides such as BaTiO₃ ($|\Delta S| = 2.1 \text{ J K}^{-1} \text{ kg}^{-1}$ for $|\Delta E| = 4 \text{ kV cm}^{-1}$). [AH][ReO₄] shows smaller EC effect of $|\Delta S| \sim 7.5 \text{ J K}^{-1} \text{ kg}^{-1}$ for $|\Delta E| = 11.2 \text{ kV cm}^{-1}$, but displays better mechanical integrity and operates closer to room temperature. It is concluded that dabco-based organic salts exhibit promising performance due to their large EC effects, non-toxicity and great tunability via chemical alterations. However, electrical leakage and breakdown remains an important challenge to be overcome for their use as EC working bodies.

Chapter 5 describes the study of BC effects in the aforementioned dabco-based organic salts. BC effects in these materials have the advantage to be driven using hydrostatic pressure instead

of electric field, thus avoiding issues related to electrical leakage and breakdown. Three compositions were selected for BC studies, namely [Hdabco][BF₄], [Hdabco][ClO₄] and [Hdabco][ReO₄]. Among these, [Hdabco][ClO₄] shows the largest reversible BC effects, $|\Delta S| = 73.2 \text{ J K}^{-1} \text{ kg}^{-1}$ for $|\Delta p| = 1200 \text{ bar}$, which compare well with those reported in state-of-the-art BC materials. Notably, BC effects in [Hdabco][BF₄] largely outperform EC effects in the same compound, thus demonstrating that pressure is a useful driving parameter for leaky organic ferroelectrics.

Chapter 6 describes BC studies in ureasil polymeric materials. These compounds show large changes in entropy when transforming from liquid to solid. By exploiting a gelation method, the liquid to solid phase transition in these compounds is transformed to a gel-to-solid phase transition, which is desirable for some caloric applications. By driving these transitions using pressure, very large BC effects of $|\Delta S| = 263 \text{ J K}^{-1} \text{ kg}^{-1}$ for $|\Delta p| = 1200 \text{ bar}$ are found, which are similar to those observed in commercial vapour-compression refrigerants, e.g. R134a. Moreover, the studied polymers have other advantages, in terms of being stretchable, non-toxic, inexpensive and have great tunability of transitions temperatures.

Finally, chapter 7 summarises the main results of this work and discusses interesting avenues for future work.

Acknowledgements

First and foremost, I am deeply grateful to my supervisor Dr Xavier Moya for his guidance and encouragement throughout my entire PhD studies. He provided me the freedom I needed to conduct independent research, and he has been very patient and supportive at every stage. I am also very grateful to Dr Gian Guzman-Verri for his supervision on Landau modelling and for his sharing of knowledge about ferroelectrics.

I thank Dr Bhaskaran Nair, Dr Enric Stern-Taulats, Dr Guillaume F. Nataf and (soon to be Dr) Melony Dilshad for sharing their knowledge and for their support in the laboratory.

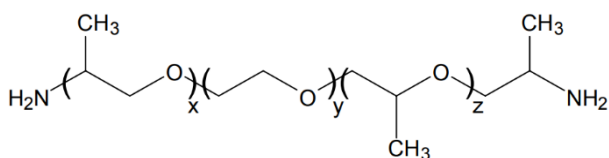
I thank Dr Jun Harada and his group at Hokkaido University (Japan) for providing samples of 1-azabicyclo[2.2.1]heptanium perrhenate. I thank Dr Dumitru Sirbu and Dr Pablo Docampo at Newcastle University for providing several organic ferroelectric crystals. I thank Dr Bolong Zhang and Prof. Rachel Evans at the Department for designing and synthesising the ureasil materials. I thank Kieran Richards at the Department for his assistance with conducting the polarized-light microscopy. I also thank Dr Qingshen Jing at the Department for assistance with technical issues in the lab.

Finally, I thank my parents for always supporting me, and I thank my girlfriend Qianyun Xu for all her unconditional support, which has calmed my anxiety and kept me going.

Abbreviations and Notation

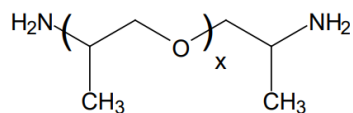
MC	Magnetocaloric
EC	Electrocaloric
mC	Mechanocaloric
eC	Elastocaloric
BC	Barocaloric
E	Electric field
P	Polarization
p	Pressure
S	Entropy
T_C	Phase transition temperature, subscript 'c' is 'critical'
T_s	Starting temperature
Q	Isothermal heat
c_p	Specific heat capacity
ΔS	Isothermal entropy change
ΔT	Adiabatic temperature change
BF4	1,4-diazabicyclo[2.2.2]octane tetrafluoroborate
AH	1-azabicyclo[2.2.1]heptanium perrhenate
ClO4	1,4-diazabicyclo[2.2.2]octane perchloric
ReO4	1,4-diazabicyclo[2.2.2]octane perrhenic
PEG	Poly(ethylene glycol)
PPG	Poly(propylene glycol)

ED



O,O'-Bis(2-aminopropyl) polypropylene glycol-block-polyethylene glycol-block-polypropylene glycol

D



Poly(propylene glycol) bis(2-aminopropyl ether)

Contents

Abstract	iii
1. Introduction	1
1.1 Conventional refrigeration	1
1.2 Caloric materials	6
2. Literature review	13
2.1 Survey of electrocaloric materials.....	13
2.2 Survey of barocaloric materials	24
2.3 Prototypes	28
3. Methodology	33
3.1 Sample preparation	33
3.2 Dielectric measurements	35
3.3 Ferroelectric measurements	38
3.4 Calorimetric measurements.....	42
3.5 Dilatometry	51
3.6 Infrared imaging.....	52
3.7 Evaluation methods for caloric effects.....	54
3.8 Landau theory for ferroelectrics.....	61
4. Electrocaloric effects in Dabco-based ferroelectric materials	66
4.1 Overview.....	66
4.2 Electrocaloric effects in 1,4-diazabicyclo[2.2.2]octane tetrafluoroborate	68
4.2.1. Experiments	68
4.2.2. Landau modelling	87
4.2.3. Summary	93
4.3 Electrocaloric effects in plastic crystals.....	94
4.3.1. Overview.....	94
4.3.2. Experiments	96
4.3.3. Landau modelling	113
4.4 Conclusions.....	117
5. Barocaloric effects in Dabco-based ferroelectric materials	120
5.1 Overview.....	120
5.2 Experiments	121
5.2.1 Material synthesis	121
5.2.2 X-ray diffraction	122

5.2.3	Calorimetry under zero pressure	125
5.2.4	Calorimetry under pressure	127
5.3	Evaluation of barocaloric effects	129
5.3.1	Construction of S - T curves.....	129
5.3.2	Isothermal entropy changes	136
5.3.3	Adiabatic temperature changes	138
5.3.4	Reversibility	140
5.4	Conclusions.....	142
6.	Barocaloric effects in ureasil materials	145
6.1	Overview.....	145
6.2	Precursor selection for designing ureasil materials.....	148
6.2.1	Chain-length selection.....	148
6.2.2	Molecular-shape tuning.....	153
6.3	Experiments on selected ureasil materials	157
6.3.1	Ureasil synthesis	157
6.3.2	Polarized optical microscopy	160
6.3.3	Specific heat capacity measurements.....	161
6.3.4	Dilatometry	162
6.3.5	Calorimetry under pressure	164
6.4	Evaluation of barocaloric effects	166
6.4.1	Construction of S - T curves.....	166
6.4.2	Isothermal entropy changes	171
6.4.3	Adiabatic temperature changes	174
6.4.4	Reversibility	175
6.4.5	Comparison with reported BC materials.....	176
6.5	Conclusions.....	178
7.	Conclusions and outlook.....	180
	References.....	184
	Appendices.....	195
1.	Interesting failed attempts and side projects	195
1.1	EC effects in metal-free perovskites	195
1.2	BC effects in metal-free perovskites.....	199
2.	Data processing script in Python 3.0.....	201
3.	Landau modelling script in Wolfram Mathematica	212

1. Introduction

1.1 Conventional refrigeration

History of refrigeration

Cooling is essential for perishable food, medicine, buildings and electronics. Current cooling technologies exploit large thermal changes that occur in fluids when driving liquid-gas phase transitions with pressure, using so-called vapour-compression cycles. The vapor compression system has been dominant since the early 19th century, and it continues almost unchallenged. The history of previous refrigerants is reviewed to understand the underlying principle of refrigeration (Fig.1-1). The concept of artificial refrigeration was invented by the Scottish scientist William Cullen, who demonstrated cooling effects by rapid evaporation of ether¹. This invention was credited to his previous studies on liquid-gas phase transitions in volatile fluids². Utilising thermal changes at phase transitions is the principle behind the first refrigeration systems, and it still remains today. In 1834, Jacob Perkins demonstrated a prototype generating continuous cooling by mechanical compression cycles of diethyl ether $C_2H_5OC_2H_5$ as cooling fluid, which can be easily obtained from the distillate of India rubber^{3,4}. This laid the foundation of the vapour-compression systems that are widespread nowadays.

In the following years, people investigated a range of natural occurring substances as first generation of commercial refrigerants. Materials such as ammonia NH_3 , diethyl ether $C_2H_5OC_2H_5$, carbon dioxide CO_2 , carbon tetrachloride CCl_4 , and sulphur dioxide SO_2 were explored but an ideal candidate was yet to be found considering issues of cost, compressibility, toxicity, flammability and explosivity^{2,4}.

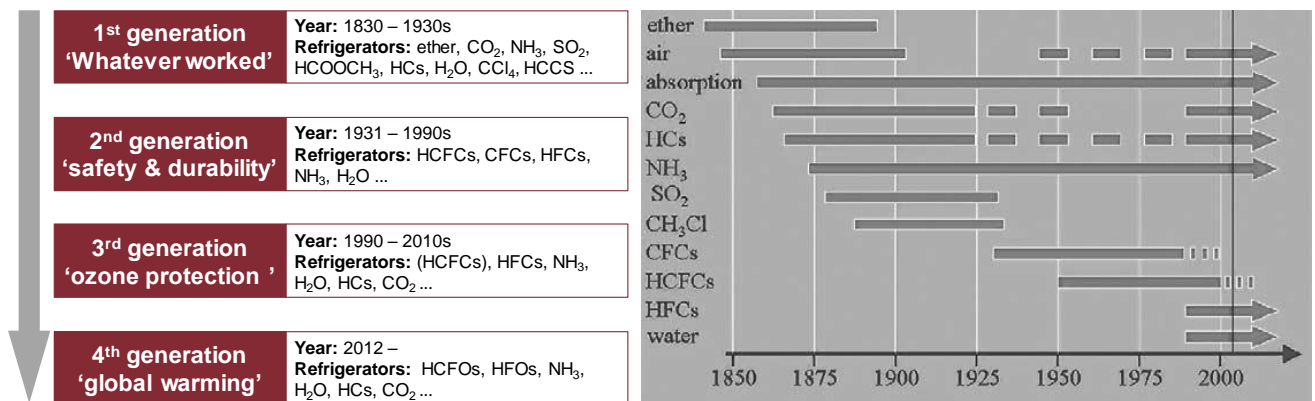


Figure 1-1. Timeline of refrigeration developments¹.

The discovery of the synthetic refrigerants chlorofluorocarbons by T. Midgley *et al.* in 1930⁵ introduced the second generation of refrigerants, as the problems of toxicity and flammability, which hindered the widespread domestic use, were addressed. This led to the mass production of these organic fluorides by General Motors and DuPont². Regarding the design strategy for refrigerants, people found that substitution of halogen for hydrogen in these organic compounds could bring the boiling point close to room temperature for the ease of compression; this is why e.g. carbon tetrachloride CCl₄ and 1,2-dichloroethene C₂H₂Cl₂ were studied. The drawbacks of those are flammability and toxicity when operated in the gas-liquid mixture because they are chemically active. To make them more inert, introducing fluorine atoms instead of chlorine atoms could be a solution. However, substitution of fluorine atoms was then believed to increase the boiling point and thus cause difficulty in liquefaction by compression near room temperature. Therefore, fluoro-based chemicals had not been tried. In reality, this is not the case, as for example, chloroform CHCl₃ boils at 61° C, and fluoro-trichloromethane CCl₃F boils at 24° C. This unexpected drop in boiling point is because of the elimination of the weak hydrogen bond by substituting the hydrogen atom⁶. However, no formal concept of hydrogen bonds existed until 1920 when it was described in the context of water by Latimer and Rodebush^{7,8}. Since then, the family of chlorofluorocarbons (CFCs) and hydrochlorofluorocarbons (HCFCs) dominated the industry significantly and facilitated the domestic use of fridges. In 1944, almost 70% of American households own refrigerators¹.

CFCs and HCFCs were later discovered to deplete the stratospheric ozone layer after being released into the air⁹, so demand for the third generation of refrigerants emerged. The environmental damage was so severe that on the Vienna Convention in 1985 and the Montreal

Protocol in 1987, countries decided to phase out CFCs by 2010. HCFCs which are low-ozone-depletion-potential substitutes were then set for transitional use¹⁰. Although policies were established, the reduction in the atmospheric concentration of CFCs is not a straightforward task. In 2018 Montzka *et al.*¹¹ shown an unexpected increase in global emissions of CFCs according to their observation and numerical analysis on sample gases in ambient air at several sites across the world. The reason is likely to be the unreported production and use of CFCs from eastern China¹².

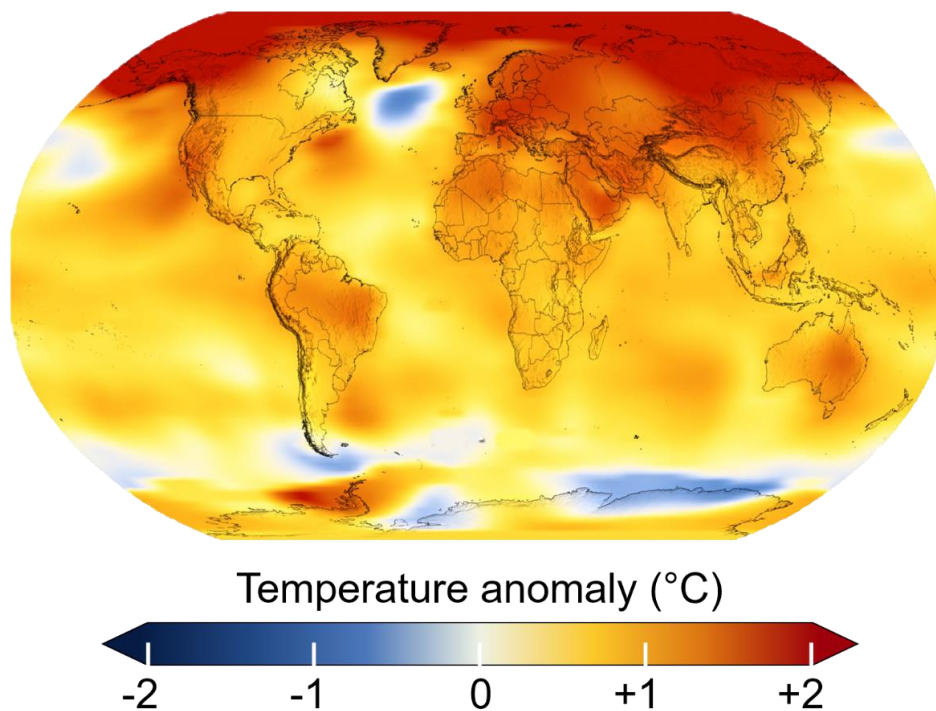


Figure 1-2. Changes of global temperature in the last 50 years, calculated as the difference between the average temperatures of 2014 – 2018 and that of 1951 – 1980. The image is taken from <https://svs.gsfc.nasa.gov/cgi-bin/details.cgi?aid=4626>.

The fourth generation of refrigerants focuses on the issue of global warming as those refrigerants contribute to the absorption and reflection of infrared emissions from the Earth¹³ and are referred as greenhouse gases. Partially as a consequence of historic use of CFCs and HCFCs, global temperature has increased up to 2°C in last 50 years (Fig.1-2). This rising temperature in the global scale has contributed to many environmental issues such as sea level rising¹⁴ and intense droughts that threaten wildlife¹⁵, crops¹⁶ and freshwater supplies¹⁷.

Another issue that results from the increasing demand in air-conditioning and refrigeration is high energy consumption (Fig.1-3). In the US and the UK, the electricity consumed by cooling applications accounts for 30% and 13% of the total amount, respectively. According to predictions from the University of Birmingham¹⁸, cooling applications are forecasted to consume 250% of their current consumption of energy by 2050 because 10.4 billion more cooling devices will be used. Moreover, conventional vapour-compression cooling systems suffer other limitations, such as the difficulty of scaling down, high noise levels and slow start-up times¹⁹. Therefore, the development of new cooling technologies is necessary to meet future needs of society.

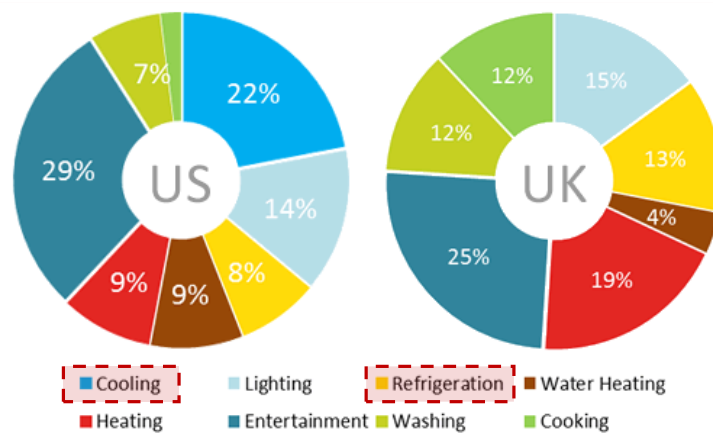


Figure 1-3. Household electricity consumption in the US and UK. Among those, sectors of cooling and refrigeration together account 30% in the US and 13% in the UK of the total amount. Data sources from EIA and DEFRA. <http://shrinkthatfootprint.com/how-do-we-use-electricity>.

Novel cooling techniques

To address those problems, a series of innovative cooling technologies have been investigated, such as thermoelectric refrigeration systems²⁰, absorption refrigeration systems²¹, enhanced radiative cooling technologies²², and solid-state cooling systems based on caloric materials²³. The working principle of thermoelectric systems is the Peltier effect, but thermoelectric coolers are limited by their very low energy efficiency²⁰. Absorption techniques²¹ rely on the evaporation and absorption of liquid refrigerants, but continuous operation is challenging because of the saturation of the refrigerant. Enhanced radiative technologies²² cover the object with certain films to increase the radiation and decrease the absorption of sunlight such that the object underneath would stay at a temperature lower than the ambient. This technology is

passive and promising for applications on buildings. Caloric materials, which form the basis of this report, are explained next.

1.2 Caloric materials

Caloric effects have the potential of overcoming the issues existing in the current cooling technologies mentioned above, and consequently their study is a fast-growing area in the international scientific community, as shown by the growing number of publications in Fig.1-4.

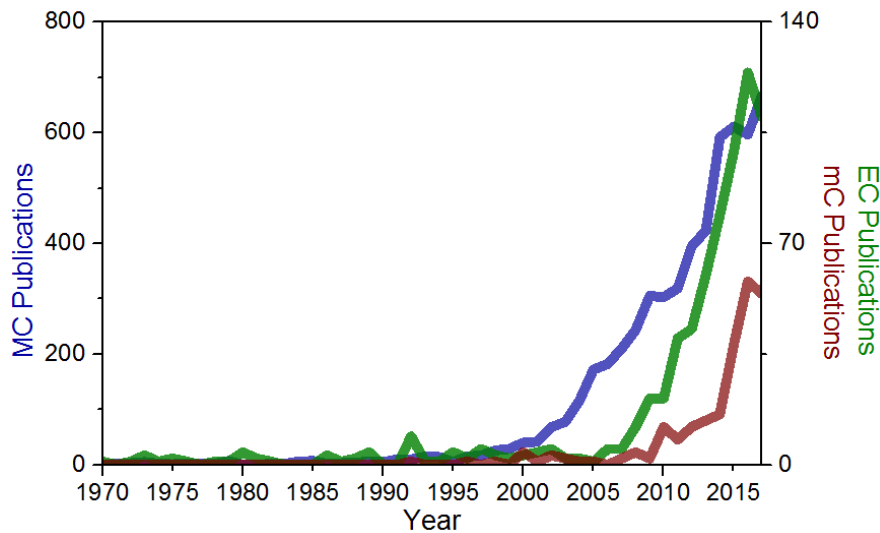


Figure 1-4. Caloric annual publications over the past five decades. Data is adopted from ref. ²³ and updated up to 2017. The left scale refers to magnetocaloric (MC) publications, the right scale to electrocaloric (EC) and mechanocaloric (mC) publications. These different types of caloric effects and materials are explained below.

Caloric materials are materials that undergo large thermal changes in response to changes in external fields such as electric field, magnetic field or mechanical stress. According to the nature of the driving field, caloric materials are classified²³ as electrocaloric (EC), magnetocaloric (MC), and mechanocaloric (mC). mC materials are further subdivided into two categories, elastocaloric (eC) materials where the driving field is uniaxial stress, and barocaloric (BC) materials where the driving field is hydrostatic pressure. If materials respond to more than one driving field, they are classified as multicaloric^{23,24}. Fig.1-5 compares the mechanism of MC, EC, eC and BC materials in response to the different categories of external fields, which can be exploited to absorb and release heat for cooling applications.

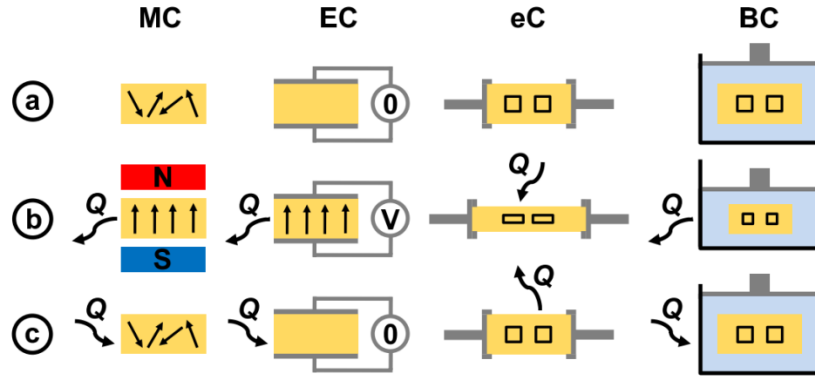


Figure 1-5. Schematic representation of different categories of caloric effects with different driving fields¹⁹. MC, EC, eC and mC refer to magnetocaloric, electrocaloric, elastocaloric and mechanocaloric, respectively. The notation Q represents heat. Arrows represent magnetic dipoles in MC materials and electric dipoles in EC materials. Black squares represent unit cells in eC and BC materials. The schematic shows caloric effects in isothermal conditions, during a three steps cycle: (a) initial, (b) under field application, (c) after field removal.

Thermodynamics of caloric materials

To characterize caloric effects, thermodynamic relations need to be laid down. Caloric effects rely on the interaction between material properties and external stimuli, e.g. in an EC material, these quantities are ferroelectric polarisation P and applied electric field E .

To understand the thermodynamics of caloric materials, let's consider their Gibbs free energy. As an example, the thermodynamic relations for EC materials are explained here. The relations in other caloric materials can be easily generalised by replacing the corresponding material properties and the external stimuli (e.g. replacing electrical polarisation P by specific volume V , and electric field E by hydrostatic pressure p).

For such a system, the differential change in Gibbs free energy G induced by a differential change in temperature T and electric field E is:

$$dG(T, E) = -SdT - PdE \quad (1.1)$$

where S is entropy. In this equation, temperature T can be interpreted as the external stimulus and entropy S as the corresponding generalised materials displacement.

The first partial derivatives are:

$$\left(\frac{\partial G}{\partial T}\right)_E = -S \quad (1.2)$$

$$\left(\frac{\partial G}{\partial E}\right)_T = -P \quad (1.3)$$

Next, by considering that the second derivative does not vary with the order of differentiation, we can write:

$$\frac{\partial^2 G}{\partial T \partial E} = \frac{\partial^2 G}{\partial E \partial T} \quad (1.4)^{23}$$

which yields one of the so-called Maxwell relations for EC materials:

$$\left(\frac{\partial S}{\partial E}\right)_T = \left(\frac{\partial P}{\partial T}\right)_E \quad (1.5)$$

The experimental insight behind this equation is that it is possible to calculate EC effects by measuring the polarization as a function of temperature and electric field, which is the so-called indirect method (details in Chapter 3). Rearranging and integrating Eq. (1.5) yields:

$$\Delta S = \int_{E_i}^{E_f} \left(\frac{\partial P}{\partial T}\right)_E dE \quad (1.6)^{23}$$

where E_i and E_f are the starting value and finishing value of the electric field applied, respectively. The relation above is valid for isothermal processes. For adiabatic processes, one could consider entropy as a function of T and E , and write after some algebra:

$$\Delta T = - \int_{E_i}^{E_f} \frac{T}{c} \left(\frac{\partial P}{\partial T}\right)_E dE \quad (1.7)^{23}$$

where c is the heat capacity of the sample, which is normally considered only under zero field and therefore assumed to be independent of electric field and temperature for the ease of calculation.

Those parameters can be related via:

$$Q = T\Delta S \approx -c\Delta T \quad (1.8)$$

where Q is the isothermal heat. Note that the last equality is only approximate when using a single value of c .

Cooling cycles based on caloric effects

Given the thermodynamic fundamentals, a heat pump based on caloric effects could be built. Fig.1-6 represents the working principle of an EC cycle based on a Brayton cycle, where electric field E is applied adiabatically. A similar BC cycle can also be built based on the same principle. In Fig.1-6, the left panel shows the thermodynamic cycle with the axes of temperature and entropy change at each individual step. The right panel represents how the EC material behaves throughout the cycle.

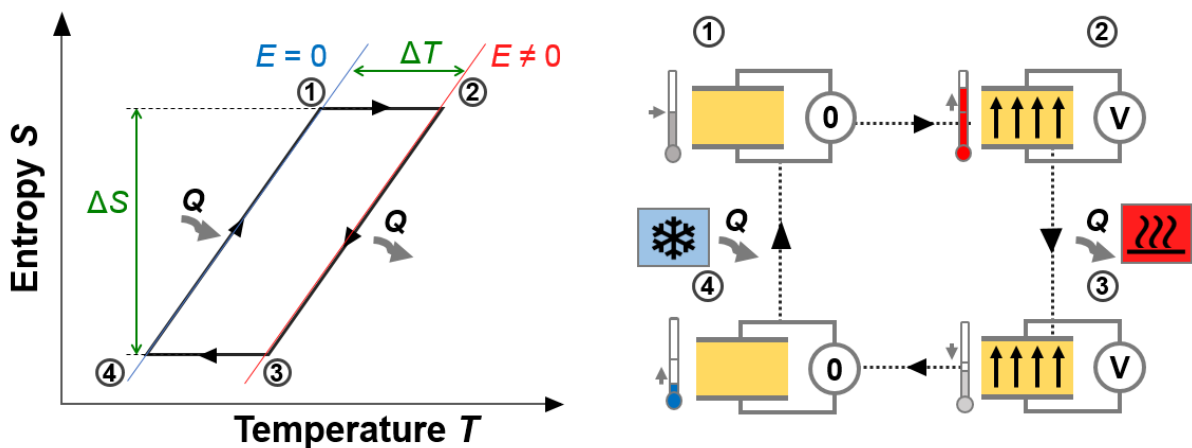


Figure 1-6. Left panel: A Brayton thermal cycle based on the EC effect. Parameters Q , ΔT and ΔS represent the isothermal heat, adiabatic temperature change, and isothermal entropy change, respectively. The blue and red lines describe how the entropy of the EC material responds to the temperature change under a fixed electric field, with the blue one standing for zero-field condition and the red one standing for non-zero-field condition. **Right panel:** the implementation of the Brayton cycle using EC materials. ‘V’ and ‘0’ in the circle represent the application and removal of electric field. The red block and blue block represent the hot sink and the cold load, respectively.

The cooling cycle is based on 4 steps (Fig.1-6 right): (1-2) The EC material undergoes adiabatic heating due to the applied electric field. At this stage, the material reaches its highest temperature, but S remains constant. The temperature change generated provides the driving force for the heat rejection in the next step. (2-3) Heat rejection step: the hot EC material releases heat to the hot sink under constant electric field. Both S and T decrease in this step. (3-4) The EC material experiences adiabatic cooling as the electric field is removed. At this stage the material reaches its lowest temperature but S remains constant. The reduced temperature drives the heat absorption in the next step. (4-1) Heat absorption step: the cold EC material

absorbs heat from the cold load. Both S and T increase in this step. These four steps constitute a complete cooling cycle.

Based on the thermal cycle, the key parameters below are normally used to quantitatively characterise caloric effects and materials:

- ΔS , isothermal entropy change, and Q isothermal heat. They determine the maximum cooling load during a single thermodynamic cycle.
- ΔT , adiabatic temperature change. ΔT drives heat flow, as it determines the maximum temperature increase and decrease that the material can generate per thermodynamic cycle.

Below, I will briefly describe the history and some important materials in the modern development of MC and eC materials research. EC and BC effects are explained separately in the next section, as they represent the focus of this thesis.

MC materials

In 1917, Weiss and Piccard reported MC effects for the first time in nickel Ni near its Curie temperature (T_C). In 1933, Giauque and MacDougall²⁵ used MC effects in paramagnetic salts of $\text{Gd}_2(\text{SO}_4)_3 \cdot 8\text{H}_2\text{O}$ to reach temperatures below 1 K. This novel cryogenic technique for approaching absolute zero later led Giauque to the Noble Prize in Chemistry in 1949. A few years later, this technique was improved by research groups in the US²⁶ and the UK²⁷ in order to achieve continuous cooling. In 1976, MC effects were exploited for the first time in a room-temperature cooling prototype by G. Brown²⁸ at NASA (The National Aeronautics and Space Administration) using gadolinium Gd. This was a seminal paper that started research on caloric materials for room-temperature solid-state cooling applications²⁹⁻³¹. According to B. Yu *et al.*³², since the first machine of G. Brown²⁸, 41 working prototypes had been built by 2010 and 39 of them adopted the idea of using Gd-related materials.

In the last two decades, giant MC effects that outperform those observed in Gd have been observed in a number of magnetic compounds. In 1997, V. Pecharsky *et al.*³³ discovered giant MC effects in $\text{Gd}_5\text{Si}_2\text{Ge}_2$ alloys, and reported an improved MC effect of $|\Delta T| \sim 15$ K under an applied magnetic field of 5 T, at ~ 280 K. More recently, $\text{MnCoGeB}_{0.02}$ compounds have been studied by N. Trung *et al.*³⁴ with an estimated MC effect of $|\Delta T| \sim 24$ K at 277 K under an applied magnetic field of 5 T. Those reported MC effects are relatively large in comparison to

other caloric effects (discussed later), but the driving fields of 5 T are very expensive to generate. In general, MC effects were mainly investigated in a range of magnetic metallic alloys. However, despite these large magnitudes, the large-scale applications of MC materials are still hindered by the requirement of precious earth metals as well as large and expensive permanent magnets.

eC materials

In the early 19th century, the blind natural philosopher John Gough in England first discovered eC effects in natural rubber. He found that rubber becomes warmer after being stretched and then becomes colder after releasing the stress. In 1859, Joule³⁵ reported small eC effects in a number of metals and woods. More recently, giant eC effects have been observed in several metallic alloys that include shape-memory alloys based on Cu³⁶⁻³⁸, Fe^{39,40} and Ni-Ti⁴¹⁻⁴³. Amongst these materials, Ni-Ti alloys reported by E. Pieczyska *et al.*⁴² show the best performance, with an eC effect of $|\Delta T|$ as large as 36 K at room temperature under uniaxial stress of 200 MPa. Apart from shape-memory alloys, natural rubber has been reported as a new candidate for large eC effects⁴⁴⁻⁴⁷. Unlike shape-memory alloys, natural rubber could be driven by a stress that is smaller than 10 MPa to achieve an eC effect of $|\Delta T|$ of 10 K⁴⁵. This feature of being easy-to-drive indicates the potential for household cooling applications. The challenge is to achieve efficient heat transfer, as natural rubber has much lower thermal conductivity than shape-memory alloys.

2. Literature review

2.1 Survey of electrocaloric materials

EC effect occurs in all materials which are electrically polarisable but is larger near ferroelectric phase transitions²³. The earlier Maxwell relation (Eq. 1.6) suggests that large EC effects could also exist in a dielectric material system possessing large polarization changes under field variations. Ferroelectric materials exhibit this feature near their ferroelectric-paraelectric transition temperature and were selected to investigate EC effects.

EC effects were firstly investigated as the electrical analogue of MC effects. This led to the first observation of EC effects by former Soviet Union scientists Kobeko and Kurtschatov⁴⁸, when they were studying the dielectric and ferroelectric properties of Rochelle salt ($\text{NaKC}_4\text{H}_4\text{O}_6 \cdot 4\text{H}_2\text{O}$). Following this discovery, no EC reports were published during World War II (1939 – 1945) because scientific research shifted towards military purposes in Japan and the USA. Kurtschatov, the co-discoverer of EC effects, had gradually changed over to research into nuclear physics since 1932⁴⁹, and was later appointed as the director of the Soviet atomic weapons project⁵⁰.

Hydrogen-bonded ferroelectrics

Academic interest in EC effects resumed after World War II, and studies were done in hydrogen-bonded ferroelectrics and perovskite oxides. In 1950, a hydrogen-bonded ferroelectric material, potassium dihydrogen phosphate (KDP)⁵¹ was reported to show EC effects of $|\Delta T| \sim 1$ K in response to $|\Delta E| = 10$ kV cm⁻¹ at ~ 123 K. Strukov⁵² later reported EC effects in triglycine family crystal, TGS $[(\text{NH}_2\text{CH}_2\text{COOH})_3 \cdot \text{H}_2\text{SO}_4]$ and TGSe $[(\text{NH}_2\text{CH}_2\text{COOH})_3 \cdot \text{H}_2\text{SeO}_4]$ with $|\Delta T| \sim 0.1$ K under $|\Delta E| = 1.7$ kV cm⁻¹ near ~ 323 K.

The family of KDP and TGS materials is a typical example of hydrogen-bonded ferroelectric materials in which proton movements on hydrogen bonds trigger the ferroelectric ordering of the lattice⁵³. In KDP, the collective site-to-site transfer of protons in the O–H···O bonds switches the spontaneous polarization. Due to the lower bonding strength in comparison to covalent bonds and ionic bonds, hydrogen-bonded ferroelectrics only require small $|\Delta E|$ to

drive large EC effects. However, the proton transfer may lead to Joule heat which could diminish the cooling effect.

Oxide perovskite ferroelectrics

A perovskite material is that with formula ABO_3 , where A and B are two cations (the ionic radius of A being larger than the ionic radius of B) and O stands for oxygen anions, as shown in Fig.2-1. In the high-symmetry cubic phase, the cation B coordinates with six oxygen anions, forming an octahedron, and cation A fills the space between octahedron units⁵⁴.

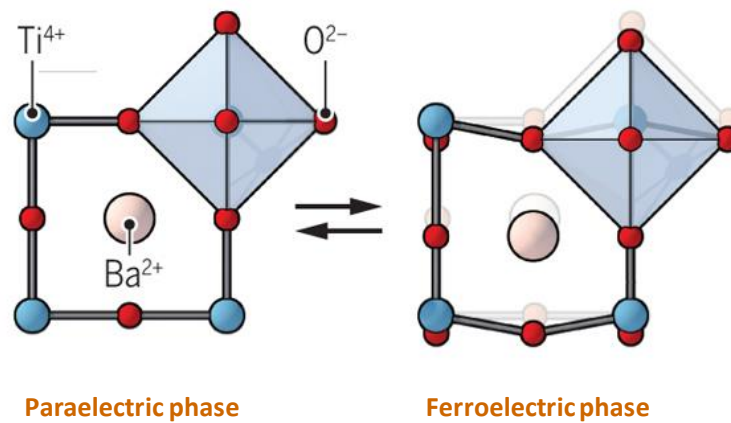


Figure 2-1. The change in the crystal structure at the ferroelectric-paraelectric phase transition, using $BaTiO_3$ as example. In the tetragonal phase, $BaTiO_3$ can develop a spontaneous polarization because the Ti^{4+} is off the charge centre. The figure is adapted from ref⁵⁵.

Many oxide perovskites have been investigated for EC effects ranging from $BaTiO_3$ -based, $PbTiO_3$ -based, $SrTiO_3$ -based single crystals, in the form of single crystals, ceramics, and solid solutions. Sixteen years after the discovery of ferroelectricity in $BaTiO_3$ ⁵⁶, its EC effects were reported in 1962⁵⁷ and were recently re-visited by X. Moya *et al*⁵⁸. Two years later, Kikuchi and Sawaguchi⁵⁹ reported EC effect in a $SrTiO_3$ single crystal with a temperature change of $|\Delta T| = 0.3$ K at 11 K under $|\Delta E| = 7$ kV cm^{-1} . After that, many lead-based perovskites were studied. Thacher⁶⁰ investigated a range of doped PZT^[1] compositions with EC effects of $|\Delta T| = 1$ K. In 1981, Tuttle and Payne⁶¹ reported EC effects of $|\Delta T| = 2.5$ K for $|\Delta E| = 30$ kV cm^{-1} in

^[1] **Doped PZT:** $Pb(Zr,Ti,Sn)O_3$

PZST^[2] near ~ 318 K. In the 1990s, Shebanovs *et al.*⁶²⁻⁶⁵ published a series of papers on PST^[3] and its solid solutions with many different cations doping and achieved EC effects $|\Delta T| = 0.6 \sim 1.5$ K in response to $|\Delta E| = 25$ kV cm⁻¹. The chemical doping led to many relaxor ferroelectrics, which display transitions that are broad in temperature due to the chemical disorder²³. Relaxor ferroelectrics tend to perform over wide ranges of temperature but usually at the cost of smaller entropy changes. A few years later, a series of papers⁶⁶⁻⁶⁸ were published reporting EC effects in PMN-PT^[4] ceramics, with the largest EC effects of $|\Delta T| \sim 2.7$ K for $|\Delta E| = 90$ kV cm⁻¹. For oxides, modification in microstructure⁶⁹ or chemical composition⁷⁰⁻⁷³ was attempted for tuning phase transitions.

One major limitation of EC effects is the breakdown field of the material. The most effective way to increase the breakdown field is to work with thin films. For example, PMN-PT bulk ceramics can support $|\Delta E| = 90$ kV cm⁻¹ to generate $|\Delta T| \sim 2.7$ K⁶⁸, whereas PMN-PT thin films withstand $|\Delta E| = 747$ kV cm⁻¹ and are predicted to show $|\Delta T| = 31$ K⁷⁴. To assemble films for higher cooling power, Lawless and Clark⁷⁵ in 1987 first designed a multi-layer capacitor (MLC) of (Cd_{0.83}Pb_{0.17})₂Nb₂O₇ for EC measurements. The geometry of 45 μ m layer-thickness allowed high electric fields up to 200 kV cm⁻¹. This work inspired many researches^{65,76-79} to improving EC effects by fabricating MLCs. The largest EC effects were reported in PZT^[5] thin films⁸⁰ showing $|\Delta T| \sim 12$ K for $|\Delta E| = 776$ kV cm⁻¹.

The major issue in EC oxide perovskites is their small thermal changes, in the order of a few kelvins (Table 2-1), which seriously limit their practical application. This is because the small ionic displacements associated with the ferroelectric phase transitions correspond to small entropy changes. Therefore, it is worth exploring EC effects in materials associated with larger entropy changes during phase transitions.

^[2] **PZST**: Pb(Zr_{0.455}Sn_{0.455}Ti_{0.09})O₃

^[3] **PST**: Pb(Sc_{*x*}Ta_{1-*x*})O₃

^[4] **PMN-PT**: (1-*x*)[Pb(Mg_{1/3}Nb_{2/3})O₃]-*x*[PbTiO₃]

^[5] **PZT**: Pb(Zr_{0.95}Ti_{0.05})O₃

Table 2-1 . EC properties of different inorganic materials. ‘/’ denotes not reported. The units are shown as following: T (K), $|\Delta S|$ ($\text{J K}^{-1} \text{kg}^{-1}$); $|\Delta T|$ (K), $|\Delta E|$ (kV cm^{-1}), $|\Delta S|/|\Delta E|$ ($10^{-2} \text{J cm K}^{-1} \text{kg}^{-1} \text{kV}^{-1}$) and $|\Delta T|/|\Delta E|$ ($10^{-2} \text{K cm kV}^{-1}$).

Inorganic material	T	$ \Delta S $	$ \Delta T $	$ \Delta E $	$ \Delta S / \Delta E $	$ \Delta T / \Delta E $	Ref.
KH_2PO_4 (single crystal)	123	3.5	1	10	35.0	0.1	[⁵¹]
TGS(single crystal)	323	/	0.1	1.7	/	5.9	[⁵²]
BaTiO_3 (ceramic)	391	2.1	0.4	7.5	28.0	5.3	[⁵⁷]
BaTiO_3 (single crystal)	402	2.1	0.9	12	17.5	7.5	[⁵⁸]
SrTiO_3 (single crystal)	11	/	0.3	7	/	4.3	[⁵⁹]
PZT(ceramic)	318	/	1	30	/	3.3	[⁶⁰]
PZST(ceramic)	430	/	2.5	30	/	8.3	[⁶¹]
PST(ceramic)	293	/	2.3	50	/	4.6	[⁶²]
0.87PMN-0.13PT (ceramic)	343	0.6	0.6	24	2.5	2.5	[⁶⁷]
0.75PMN-0.25PT (ceramic)	383	1	1.0	25	4.0	4.0	[⁶⁶]
0.70PMN-0.30PT (ceramic)	429	2.3	2.7	90	2.6	3.0	[⁶⁸]
PMN ^[6] (ceramic)	340	/	2.5	90	/	2.8	[⁶⁸]
PZT(film)	499	8	12	776	1.0	1.5	[⁸⁰]

^[6]PMN: $\text{Pb}(\text{Mg}_{1/3}\text{Nb}_{2/3})\text{O}_3$

Polymer ferroelectrics

One underlying reason for the small EC effects in oxide perovskites is that the small ionic displacements in these ferroelectric phase transitions may only correspond to small entropy changes. Also, polymer structures of long semi-crystalline chains act as a buffer to stop crack propagation and prevent breakdown so polymers can withstand large electric field strengths. Therefore, the ordering-disordering transitions of dipoles in ferroelectric polymers were investigated. In 2008, Neese *et al*⁸¹. first reported large EC effects in poly(vinylidene fluoride-trifluoroethylene) [P(VDF-TrFE)] (55/45 mol%) copolymer with $|\Delta T| \sim 12.5$ K under $|\Delta E| = 2090$ kV cm⁻¹ at 353 K. In this order-disorder type phase transition, the polymer chains undergo conformational changes (Fig.2-2). In the ferroelectric phase, polymer chains adopt all-trans (TTTT) conformation so that all the fluorine atoms are on the same side of the chain, forming dipoles perpendicular to the chain direction. Above T_C , polymer chains adopt a mixture of trans and gauche forms, forming a non-polar paraelectric phase.

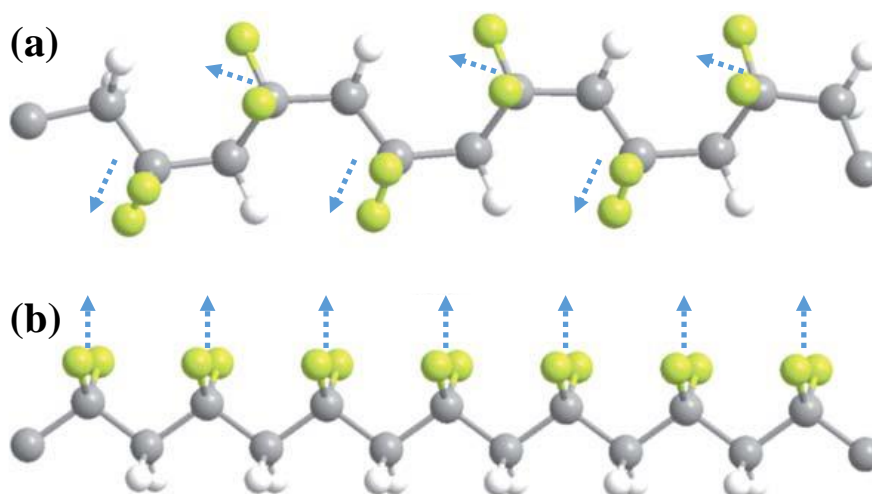


Figure 2-2. Schematic illustration of two phases of PVDF polymer chains (a) paraelectric phase with trans and gauche conformations and (b) ferroelectric phase with all-trans conformations. The blue arrows correspond to dipole directions in each unit. The yellow, grey and white balls are fluorine, carbon and hydrogen atoms, respectively. The figure was adopted from ref⁸².

Additionally, with defect modification such as high energy irradiation or copolymerizing with a third bulky monomer⁸³, the normal ferroelectric polymers can be converted into relaxor ferroelectrics, in which the phase transitions can avoid hysteresis and become wider near room temperature to benefit practical refrigerators. However, this tailoring would be at the expense of lowering the total $|\Delta S|$ and $|\Delta T|$.

A few polymers based on P(VDF-TrFE) were studied (Table. 2-2), including P(VDF-TrFE) with slightly different monomer ratios^{84,85} and P(VDF-TrFE-CFE)⁸⁶. The highest EC effect was for P(VDF-TrFE) (65/35 mol%) copolymers, with $|\Delta T| = 28$ K under $|\Delta E| = 1800$ kV cm⁻¹ at 323 K⁸⁵. However, it should be noted that all of those values of ΔT are indirectly calculated so direct calorimetry or thermometry measurements are required to verify the results.

Overall, polymer ferroelectrics show large EC effects due to order-disorder phase transitions. The issue, however, is that EC effects in polymer ferroelectrics are driven using very large high electric fields, and that display large energy losses due to hysteresis. The EC strength $|\Delta T|/|\Delta E|$ is not as high as those in oxide ferroelectric. Therefore, materials with higher EC strength are desired.

Table 2-2. EC properties of different ferroelectric polymers. The units are shown as following: T (K), $|\Delta S|$ (J K⁻¹ kg⁻¹); $|\Delta T|$ (K), $|\Delta E|$ (kV cm⁻¹), $|\Delta S|/|\Delta E|$ (10⁻² J cm K⁻¹ kg⁻¹ kV⁻¹) and $|\Delta T|/|\Delta E|$ (10⁻² K cm kV⁻¹).

Polymer material	T	$ \Delta S $	$ \Delta T $	$ \Delta E $	$ \Delta S / \Delta E $	$ \Delta T / \Delta E $	Ref.
P(VDF-TrFE) 55/45 mol %	353	60	12.5	2090	2.9	0.6	[⁸¹]
P(VDF-TrFE-CFE) 69.7/30.3/6 mol %	313	/	12	1000	/	1.2	[⁸⁶]
P(VDF-TrFE) 55/45 mol %	340	70	12	1200	5.8	1.0	[⁸⁴]
P(VDF-TrFE) 65/35 mol%	323	130	28	1800	7.2	2.0	[⁵⁸]

Composite materials

On the one hand, polymers show significant potential due to their high breakdown strength, easy processability, lightweight, and low cost⁸⁷. On the other hand, oxide ferroelectrics tend to have larger EC strength and the EC effects can be driven under relatively low electric fields. For instance, PZT thin films⁸⁰ (~ 350 nm thick) require an electric field of 776 kV cm⁻¹ to generate a $|\Delta T|$ of 12 K, while an electric field as high as 2090 kV cm⁻¹ is required for P(VDF-TrFE) films⁸¹ (~ 0.4 – 2 μ m) to produce similar changes in temperature.

To combine the properties of ferroelectric polymers and oxides, the attention was focused on a range of composites which consists of P(VDF-TrFE-CFE) matrices and inorganic inclusions

that include PMN-PT⁸⁸, BST⁸⁹, BST nanowires⁹⁰ and BZT⁹¹(Table. 2-3). As can be seen, the EC strengths $|\Delta T|/|\Delta E|$ of composites are higher than those of the oxide inclusions, rather than an average number between those of the polymer and oxides. This enhancement was investigated using phase field simulations, which indicate that oxide/polymer interfaces would promote the polarization and thus improve the EC effects⁹¹. The experimental results proved that the crystallinity of the polymer increases, and the crystal sizes decrease after introducing the interfaces. This means that the polarization of the polymer matrix is improved and is in accordance with the simulations⁹⁰. However, it should be noted that all the values of $|\Delta T|$ above were derived from indirect measurements.

Extending the interfacial enhancement to other composite structures, Zhang *et al.*⁹² in 2019 suggested to confine P(VDF-TrFE-CFE) nanowires into anodic aluminium oxide membranes (Fig.2-3), in which the EC performance at relatively low field is improved, with $|\Delta T| = 2.5$ K under $|\Delta E| = 500$ kV cm⁻¹ at room temperature. In the meantime, the aluminium oxide membrane forms channels for heat transfer because its thermal conductivity is around 30 times higher than that of the polymer filaments. This new design facilitates application of ferroelectric polymers.

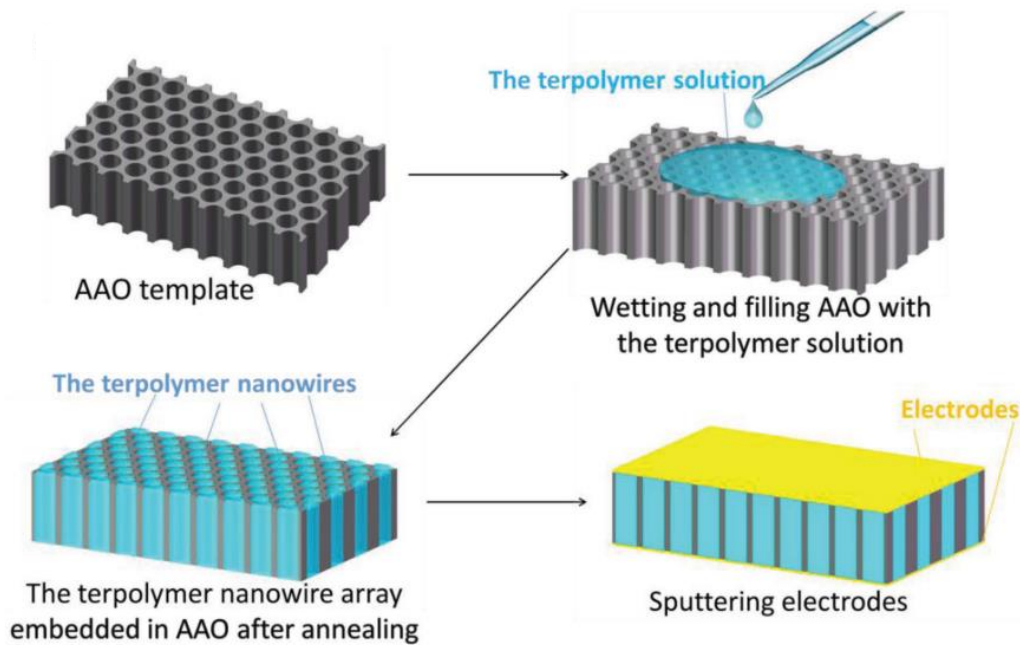


Figure 2-3. Schematic of the fabrication process of the polymer nanowire array within the anodic aluminium oxide(AAO) template.

Table 2-3. EC properties of composite materials in comparison of a individual polymer and individual oxides. The units are shown as following: T (K), $|\Delta S|$ ($\text{J K}^{-1} \text{kg}^{-1}$); $|\Delta T|$ (K), $|\Delta E|$ (kV cm^{-1}), $|\Delta S|/|\Delta E|$ ($10^{-2} \text{J cm K}^{-1} \text{kg}^{-1} \text{kV}^{-1}$) and $|\Delta T|/|\Delta E|$ ($10^{-2} \text{K cm kV}^{-1}$).

Composite material	T	$ \Delta S $	$ \Delta T $	$ \Delta E $	$ \Delta S / \Delta E $	$ \Delta T / \Delta E $	Ref.
0.75PMN-0.25PT(ceramic)	383	1	1	25	4.0	4	[66]
0.70PMN-0.30PT(ceramic)	429	2.3	2.7	90	2.6	3	[68]
BST ^[7] (ceramic)	303	1.3	0.83	40	3.3	2.1	[73]
BZT ^[8] (ceramic)	410	/	1.2	30	/	4	[93]
P(VDF-TrFE)	353	60	12	2090	2.9	0.6	[81]
P(VDF-TrFE-CFE)	328	65	12.5	3070	2.1	0.4	[81]
P(VDF-TrFE-CFE)/PMN-PT	303	150	25	1800	8.3	1.7	[88]
P(VDF-TrFE-CFE)/BST	300	210	50.5	2500	8.4	2	[89]
P(VDF-TrFE-CFE)/BST(nanowires)	296	150	32	1500	10.0	3.2	[90]
P(VDF-TrFE-CFE)/BZT(nanowires)	298	190	42	2000	9.5	2.1	[91]
P(VDF-TrFE-CFE) (nanowires confined in aluminum oxide membranes)	298	/	2.5	500	/	0.5	[92]

^[7]**BST:** $\text{Ba}_{0.65}\text{Sr}_{0.35}\text{TiO}_3$

^[8]**BZT:** $\text{Ba}(\text{Zr}_{0.2}\text{Ti}_{0.8})\text{O}_3$

Molecular ferroelectric materials

Molecular ferroelectric materials have been in rapid development in recent years. Till now, no clear definition for molecular ferroelectric materials has been proposed. In this work, molecular ferroelectric materials are regarded as ferroelectric materials consisting of positively/negatively charged organic molecules. They are studied due to the advantages of being lightweight, inexpensive, environmentally friendly and do not need high-temperature processing⁹⁴. Molecular ferroelectric materials are also very promising for EC effects as they tend to show much larger ΔS than the traditional oxides. However, there are very few papers that are directly concerned with the EC effect of molecular ferroelectric materials because they are relatively new.

The first discovery of molecular ferroelectric materials was [Hdabco][BF₄] and [Hdabco][ClO₄] (dabco = 1,4-diazabicyclo[2.2.2]octane) by Szafranski *et al.* in 1998⁹⁵. Then in 2002⁹⁶, they reported a similar molecular ferroelectric material [Hdabco][ReO₄]. For the design principle, ferroelectric materials exhibit spontaneously generated electric polarization, which can be reversed by an external electric field⁹⁴. The design principle⁹⁴ is firstly to create dipolar molecules, which is achieved by introducing N to organic molecules. Then, enable the rotation of the dipolar molecules within the lattice such that they can be aligned by the external electric field. Following this strategy, a few globular organic molecules with N substitutions were used such as dabco, 1-azabicyclo[2.2.2]octane, imidazolium, tetramethylammonium and etc. After the spark of Szafranski *et al.* Jun Harada's group in Japan and Rengen Xiong's group in China have developed many molecular ferroelectric materials.

In 2016 and 2019, Jun Harada *et al.* have developed four materials^{97,98} which consist of molecular cations of 1-Azabicyclo[2.2.1]heptanium and quinuclidinium as well as tetrahedral anions of [ReO₄]⁻ and [IO₄]⁻. Among those materials, 1-Azabicyclo[2.2.1]heptanium perrhenate was studied for its EC effects in collaboration with Jun Harada, see Chapter 4.

Ren-gen Xiong has predicted a number of molecular ferroelectric materials⁹⁴. In 2018, Rengen Xiong's group found a family of metal-free organic ferroelectric perovskites⁹⁹, which have spontaneous polarization $P_s \sim 21 \mu\text{C cm}^{-2}$. This is the highest P_s ever reported in organic molecular ferroelectric materials. The value of P_s also decreases sharply when crossing the sharp first-order phase transition, indicating giant EC effects. Wang, Jian-Jun, *et al.*¹⁰⁰ predicts $|\Delta S| = 36 \text{ J K}^{-1} \text{ kg}^{-1}$ under $|\Delta E| = 20 \text{ kV cm}^{-1}$. This material has been attempted by us, but the EC

effects were not successfully measured, see Appendix. The molecular ferroelectric materials with reported EC effects are listed in Table 2-4, including $(\text{C}_5\text{H}_{14}\text{N})_2\text{CsPb}_2\text{Br}_7$ ($[(\text{C}_5\text{H}_{14}\text{N})_2]^+ = \text{isopentylammonium})^{101}$ and ImClO_4 ($\text{Im}^+ = \text{imidazolium})^{102}$.

Table 2-4. EC properties of molecular ferroelectric materials. The units are shown as following: T (K), $|\Delta S|$ ($\text{J K}^{-1} \text{kg}^{-1}$); $|\Delta T|$ (K), $|\Delta E|$ (kV cm^{-1}), $|\Delta S|/|\Delta E|$ ($10^{-2} \text{J cm K}^{-1} \text{kg}^{-1} \text{kV}^{-1}$) and $|\Delta T|/|\Delta E|$ ($10^{-2} \text{K cm kV}^{-1}$).

Molecular ferroelectric material	T	$ \Delta S $	$ \Delta T $	$ \Delta E $	$ \Delta S / \Delta E $	$ \Delta T / \Delta E $	Ref.
$(\text{C}_5\text{H}_{14}\text{N})_2\text{CsPb}_2\text{Br}_7$	345	4.1	2	13	31.5	15.4	[¹⁰¹]
ImClO_4	373	5.4	1.26	15	36.0	8.4	[¹⁰²]
$[\text{MDABCO}](\text{NH}_4\text{I}_3)$	448	36	16	20	180.0	80.0	[¹⁰⁰]

At present, cooling technologies based on EC effects cannot yet compete with conventional vapour-compression systems in terms of cooling power. The commonly used haloalkane refrigerant R134-a shows $|\Delta S| \sim 520 \text{ J K}^{-1} \text{kg}^{-1}$ under $|\Delta p| = 10 \text{ bar}$ at 310 K^{103} (p is pressure) while most of the oxide materials have $|\Delta S| < 10 \text{ J K}^{-1} \text{kg}^{-1}$, e.g. BaTiO_3 single crystal has a $|\Delta S| \sim 2.3 \text{ J K}^{-1} \text{kg}^{-1}$ under $|\Delta E| = 4 \text{ kV cm}^{-1}$ at 398 K^{58} . In essence, the entropy change is a measure of the molecular disorder so the gas-liquid system has much larger entropy changes than the solid-state one. Therefore, EC effects in solid materials could be explored for some niche applications e.g. chip-size cooler⁸⁰. Yet larger EC effects are required for practical applications.

Important parameters for improving EC effects

As stated above, EC is parameterised by isothermal heat Q , isothermal entropy change ΔS , and adiabatic temperature change ΔT . To find the best material, several physical parameters can be screened:

- The thermally driven entropy change $|\Delta S_0|$ at the phase transition. This gives an indication of the maximum entropy that can be obtained when driving the transition with an electric field. However, a high zero-field entropy change does not necessarily mean a large EC effect because the transition may not be drivable by an electric field or because the entropy change of the transition can decrease quickly with an applied electric field.

- Ferroelectric polarisation loops. As seen in Eq. 1.9, strongly temperature-dependent polarisation values will lead to large entropy changes (via $\left| \frac{\partial P}{\partial T} \right|$). Therefore, we look for materials with large polarization and first-order phase transition.
- Maximum change in applied field $E_f - E_i$. As stated above, a high breakdown field allows applying a larger electric field, which increases the EC response¹⁰⁴.

2.2 Survey of barocaloric materials

In 1998, the Nobel-Prize recipient K. A. Müller¹⁰⁵ first reported BC effects near phase transitions in the polycrystalline nickelate $\text{Pr}_{0.66}\text{La}_{0.34}\text{NiO}_3$. Following this discovery, there was not much research into BC materials for decades, possibly because BC cooling is diminished by elastic heating during mechanical compression in many materials. However, in the last decade, giant BC effects have been reported in a number of metallic alloys^{106–109}, ferroelectric materials^{110–113}, and superionic conductors¹¹⁴.

Metallic alloys

As a spark in the research of giant BC effects in metallic alloys, Ni–Mn–In magnetic shape-memory alloys reported by Mañosa *et al.*¹⁰⁶ in 2010 show BC effects of $|\Delta S| \sim 24 \text{ J K}^{-1} \text{ kg}^{-1}$ and $|\Delta T| \sim 4.5 \text{ K}$ at room temperature, for changes in pressure of 2.5 kbar. Shape memory alloys undergo a structural transition where the latent heat of the transition is associated with the lattice distortion. This led to BC effects. After that, some other metallic compounds were investigated.

Table 2-5. BC properties of selected metallic compounds. The units are shown as following: T (K), $|\Delta S|$ ($\text{J K}^{-1} \text{ kg}^{-1}$); $|\Delta T|$ (K), $|\Delta E|$ (kV cm^{-1}), $|\Delta S|/|\Delta E|$ ($10^{-2} \text{ J cm K}^{-1} \text{ kg}^{-1} \text{ kV}^{-1}$) and $|\Delta T|/|\Delta E|$ ($10^{-2} \text{ K cm kV}^{-1}$).

Metallic materials	T	$ \Delta S $	$ \Delta T $	$ \Delta E $	$ \Delta S / \Delta E $	$ \Delta T / \Delta E $	Ref.
$\text{Ni}_{49.26}\text{Mn}_{36.08}\text{In}_{14.66}$	293	24	4.5	2600	9.2	1.7	[⁸¹]
$\text{LaFe}_{11.35}\text{Co}_{0.47}\text{Si}_{1.2}$	237	9	2.2	2000	4.5	1.1	[⁸⁶]
$\text{Gd}_5\text{Si}_2\text{Ge}_2$	270	11	1.1	2000	5.5	0.6	[⁸⁴]
$\text{Fe}_{49}\text{Rh}_{51}$	308	13	8.1	2500	5.2	3.2	[⁸⁵]
Mn_3GaN	285	22	4.5	1400	15.7	3.2	[¹¹⁵]
$(\text{MnNiSi})_{0.62}(\text{FeCoGe})_{0.38}$	330	70	16	2700	25.9	5.9	[¹¹⁶]

Inorganic ferroelectric materials

Among the ferroelectric BC materials, ammonium sulphate $[(\text{NH}_4)_2\text{SO}_4]$ ¹¹³ showed larger BC effects than those reported in ferroelectric perovskites such as BaTiO_3 and PbTiO_3 , with a thermal change of ~ 8 K and the largest value of $|\Delta S| \sim 60 \text{ J K}^{-1} \text{ kg}^{-1}$ in response to the driving pressure of 1 kbar. This relatively large BC effects originate from the order–disorder phase transition in $(\text{NH}_4)_2\text{SO}_4$. Electric breakdown is an issue for driving cooling effects using electric fields. This can be avoided in BC effects. Therefore, there is no need to fabricate multilayer devices to exploit giant effects in films.

Superionic conductors

Superionic conductors are materials that have very high ionic conductivity in the solid state at temperatures substantially lower than the fusion points. They are intensively studied for solid-state batteries due to their high ionic conductivity¹¹⁷. Notably, changes in the ionic conductivity are normally associated with large changes in the crystal structure and volume so they are considered for BC cooling applications.

The superionic conductor AgI reported by Aznar *et al.*¹¹⁴ exhibits the giant BC effect of $|\Delta T| \sim 18$ K for changes in pressure of 2.5 kbar. However, other similar superionic compounds like CaF_2 ¹¹⁸, PbF_2 ¹¹⁸ and Li_3N ¹¹⁹ are studied only via theoretical modelling without experimental demonstrations. Also, many of those materials have a phase transition well above room temperature¹¹⁸. This makes the BC cooling applications more challenging.

Table 2-6. BC properties of selected superionic conductors. All data except AgI are from theoretical modelling. The units are shown as following: T (K), $|\Delta S|$ ($\text{J K}^{-1} \text{kg}^{-1}$); $|\Delta T|$ (K), $|\Delta E|$ (kV cm^{-1}), $|\Delta S|/|\Delta E|$ ($10^{-2} \text{J cm K}^{-1} \text{kg}^{-1} \text{kV}^{-1}$) and $|\Delta T|/|\Delta E|$ ($10^{-2} \text{K cm kV}^{-1}$).

Superionic conductors	T	$ \Delta S $	$ \Delta T $	$ \Delta E $	$ \Delta S / \Delta E $	$ \Delta T / \Delta E $	Ref.
AgI	390	60	18	2500	24.0	7.2	[¹¹⁴]
CaF ₂	1350	200	163	50000	4.0	3.3	[¹¹⁸]
PbF ₂	600	60	22	6000	10.0	3.7	[¹¹⁸]
LiIO ₃	1000	16	9	10000	1.6	0.9	[¹²⁰]
Li ₃ N	300	20	2	58000	0.3	0.0	[¹¹⁹]

Plastic crystals

Notably, in 2019 Lloveras *et al.*¹²¹ reported a colossal BC effects at 320 K in plastic crystals of neopentylglycol $(\text{CH}_3)_2\text{C}(\text{CH}_2\text{OH})_2$ (NPG), with $|\Delta T| \sim 30$ K and $|\Delta S| \sim 510 \text{ J K}^{-1} \text{kg}^{-1}$ driven by a pressure change of 5.7 kbar. NPG displays such large BC effects that outperform any type of caloric materials observed. The performance of NPG is also comparable with the commercial refrigerant fluid R134a¹⁰³, which displays $|\Delta S| = 520 \text{ J K}^{-1} \text{kg}^{-1}$ at ~ 310 K in a pressure of 10 bar.

Plastic crystals consist of nearly spherical molecules whose centres of mass remain localized in a crystal lattice. Due to the nearly spherical shape, plastic crystal molecules can freely rotate around their mass centres with little steric hindrance. Therefore, plastic crystals can be highly orientationally disordered at the high-temperature phase and fully ordered at the low-temperature phase. Similarly, Zhang Kun, *et al.*¹⁶⁸ in 2022 reported another plastic crystal system, carboranes $(\text{C}_2\text{B}_{10}\text{H}_{12})$, which forms a globular shape by ten boron atoms and two carbon atoms. The maximum reversible entropy change in this system is $|\Delta S| = 97 \text{ J kg}^{-1} \text{K}^{-1}$ responding to $|\Delta p| = 300$ bar. The discovery of plastic crystals is promising for safe environmentally friendly cooling.

Polymers

Polymer molecules are composed of a sequence of repeating units. These repeating units can adapt to different configurations such as folded chain segments and randomly intertwined coils. This configurational change in polymers is associated with large entropy changes and can be reversely responsive to pressure. Therefore, polymers are interested in BC effects.

There are very few papers about BC effects on polymers in recent years. Polyurethane(PU), PVDF-TrFE-CTFE, vulcanized natural rubber and nitrile natural rubber were reported for BC effects, as shown in Table 2-7. Among those, PVDF-TrFE-CTFE has exhibited the largest BC effects with $|\Delta S| = 120 \text{ J kg}^{-1} \text{ K}^{-1}$ under $|\Delta p| = 2000 \text{ bar}$ at $\sim 368 \text{ K}$.

Table 2-7. BC properties of selected polymers. The units are shown as following: T (K), $|\Delta S|$ ($\text{J K}^{-1} \text{ kg}^{-1}$); $|\Delta T|$ (K), $|\Delta E|$ (kV cm^{-1}), $|\Delta S|/|\Delta E|$ ($10^{-2} \text{ J cm K}^{-1} \text{ kg}^{-1} \text{ kV}^{-1}$) and $|\Delta T|/|\Delta E|$ ($10^{-2} \text{ K cm kV}^{-1}$).

Polymer material	T	$ \Delta S $	$ \Delta T $	$ \Delta E $	$ \Delta S / \Delta E $	$ \Delta T / \Delta E $	Ref.
Polyurethane(PU)	333	95.6	13	2180	43.9	6.0	[¹²²]
PVDF-TrFE-CTFE	368	120	18.6	2000	60.0	9.3	[¹²³]
Vulcanized natural rubber	293	21	10	434	48.4	23.0	[¹²⁴]
Nitrile butadiene rubber	323	59	16.4	3900	15.1	4.2	[¹²⁵]

Important parameters for improving BC effects

- The thermally driven entropy change $|\Delta S_0|$ at the phase transition. This gives an indication of the maximum entropy that can be obtained when driving the transition with an electric field.
- Volume change $\left| \frac{\partial V}{\partial T} \right|$. Materials with large thermal expansion coefficient and large volume change across the phase transition will lead to large entropy changes. However, literature data about thermal expansion in solid materials are not easy to find.

2.3 Prototypes

This section, the reported prototypes based on EC cooling are reviewed. BC prototypes are more similar to the traditional vapour-compression system, so they are rarely reported. In 1991, the first household-size EC prototype was built in the Moscow Power Engineering Institute¹²⁶. This prototype could achieve a cooling power up to $\sim 0.1 \text{ W g}^{-1}$ driven by the EC effects of $1 - 5 \text{ K}$ under $|\Delta E| = 90 \text{ kV cm}^{-1}$, between $170 - 300 \text{ K}$. The working body consisted of two sets of $\text{PbSc}_{0.5}\text{Ta}_{0.5}\text{O}_3$ plates of $20 \times 10 \times 0.3 \text{ mm}$ with the gaps filled by the heat-transfer fluid. This paper also indicated that the future development of EC refrigerators should be via (1) optimized heat transfer e.g. heat-transfer agents and cyclic parameters, and (2) better working materials e.g. larger adiabatic temperature changes and a wider temperature range for operation.

In 2009 and 2010, two simulation papers^{127,128} studied prototype design parameters. In both cases, the heat transfer was designed to be on cyclical mechanical motion instead of flowing fluid, as shown in Fig.2-4. The heat is moved by the cyclical actuation of the EC work elements towards the hot sink and cold load. Following this proposed design, commercially made doped BaTiO_3 MLCs^{129,130}, $[\text{Pb}(\text{Mg}_{0.33}\text{Nb}_{0.66})\text{O}_3]_{0.9}[\text{PbTiO}_3]_{0.1}$ (PMN-10PT) ceramic plates¹³¹ and P(VDF-TrFE-CFE) thin films¹³² were used as the EC working body in three experimental implementations. The highest cooling power was 2.8 W g^{-1} , shown by the prototype based on P(VDF-TrFE-CFE) thin films¹³², but this number depends on the normalisation criteria (in this case mass is used and the low density of polymers is beneficial).

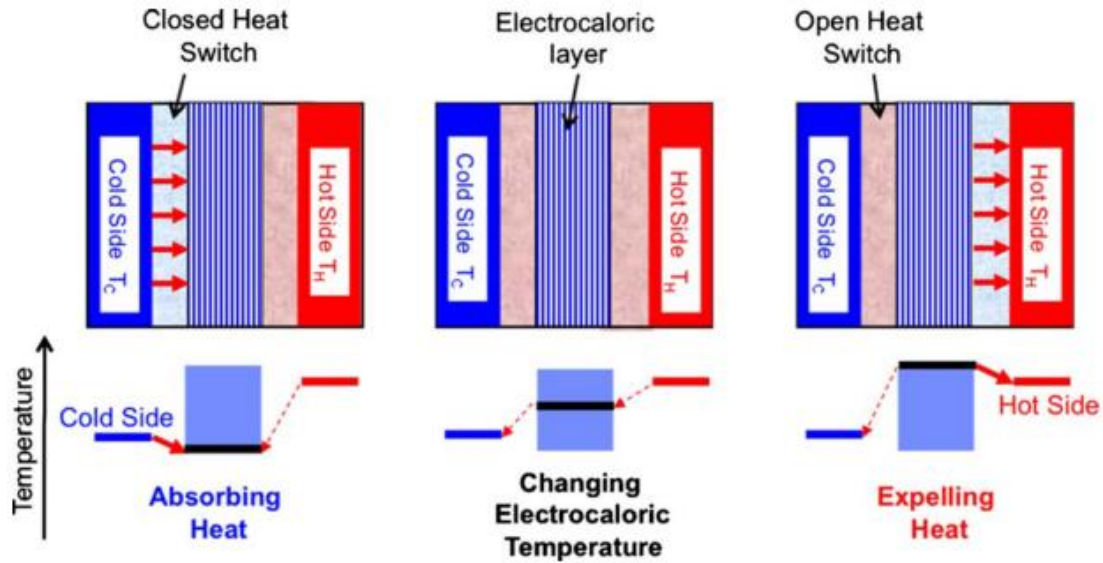


Figure 2-4 Schematic of an EC prototype design based on the cyclic motion heat-transfer working principle¹²⁷. The top panels indicate the operation of transferring heat from cold load to hot sink. The striped block in the middle, the blue block and the red block represent the EC working body, the cold load and the hot sink, respectively. The bottom panels show the temperature of the EC working body and how it drives the heat flow between the cold load and the hot sink. The solid arrows show the preferred direction of heat flow and the dashed arrows show unwanted direction.

One challenge to make small size refrigerators is that the EC material must cyclically make thermal contact between the heat source and heat sink, causing limitations for portability. Bradeško *et al.*¹³³ in 2016 proposed a numerical design in which the PMN-PT ceramics couple both EC effects and electromechanical properties due to the piezoelectricity. With a cantilever structure, also called bimorph actuators, the PMN-PT plates can generate cooling effects under electric field and at the same time bend to make contact with the cold load and the hot sink (Fig.2-5). This concept allows the heat transfer within the device without external mechanical motions as previously used. However, the stiffness and fatigue of ceramic EC materials might cause difficulties for practical applications.

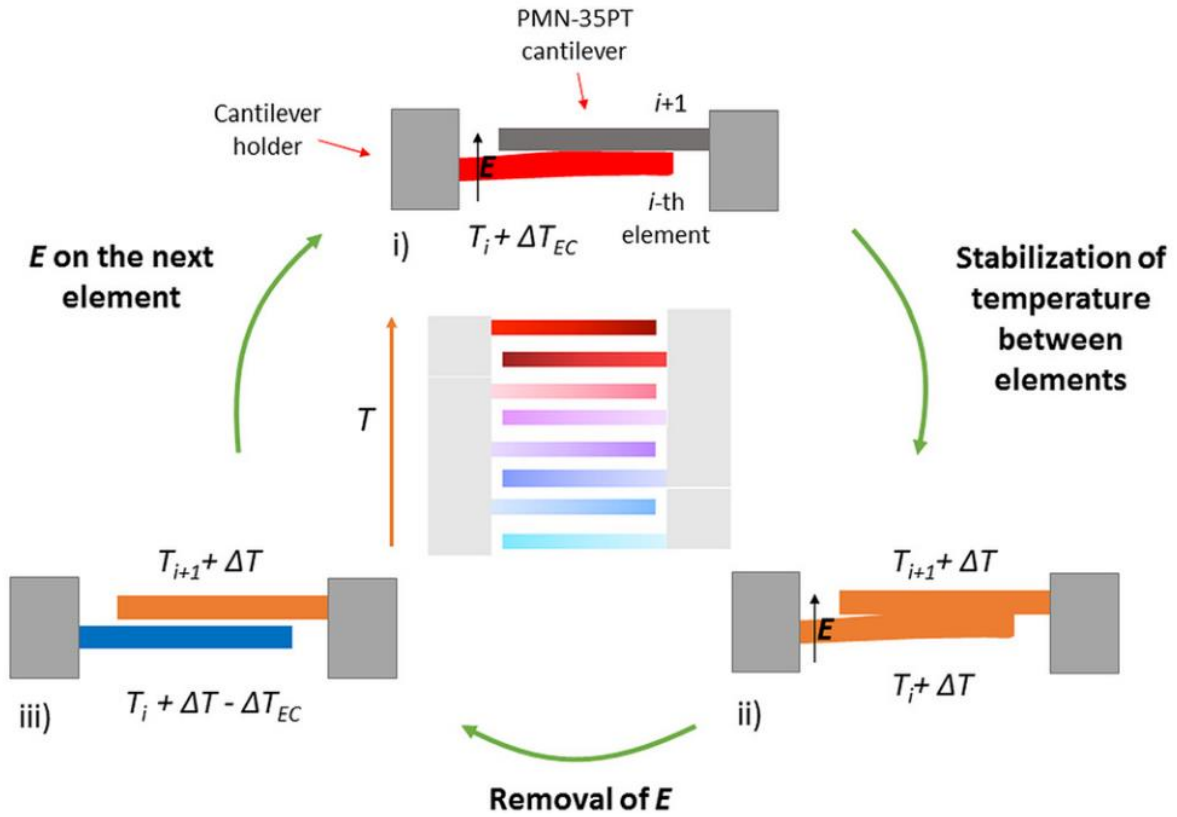


Figure 2-5. Schematic of the refrigeration cycle based cantilever elements showing both an EC and electromechanical response. The cycle operates in three steps: (i) application of the electric field E to the PMN-PT cantilever causing the temperature increase from T_i to $(T_i + \Delta T_{EC})$. T_i and ΔT_{EC} correspond to the initial temperature and the temperature change due to EC effects, respectively. The cantilever element also bends to the neighbour element; (ii) the heat is transferred from i -th cantilever to the neighbouring $(i + 1)$ one, reaching $(T_i + \Delta T)$; (iii) removal of E causing the temperature decreases to $(T_i + \Delta T - \Delta T_{EC})$.

Similar to the above electromechanical EC material, Ma *et al.*¹³² developed a moving EC materials based on P(VDF-TrFE-CFE) films but using reversible electrostatic forces to drive the motion (Fig.2-6). The electrostatic forces are generated when applying voltage to the EC polymer laminates and the insulating layers simultaneously. With different charges, the flexible polymer films are attracted to insulating layer and contact with the cold load or the hot sink. Owing to the polymer's light weight and low bending stiffness, the EC laminates could be shuttled rapidly between the upper cold load and the lower hot sink in less than 30 ms and with energy consumption of ~ 0.02 W. This electrostatic actuation is compact, noiseless, and avoids substantial frictional forces that might cause material damage and energy consumption. As shown experimentally, a smartphone battery could be cooled by 8°C in 5 s on the surface under $|\Delta E| = 667 \text{ kV cm}^{-1}$, but this cooling power is likely due to intermittent conduction between the hot battery and the cold sink, instead of due to electrocaloric cooling. In comparison to the pre-mentioned PMN-PT cantilever system, the P(VDF-TrFE-CFE) system tend to be cheaper

and easier to manufacture, thus suggesting higher potential for applications on electronic devices.

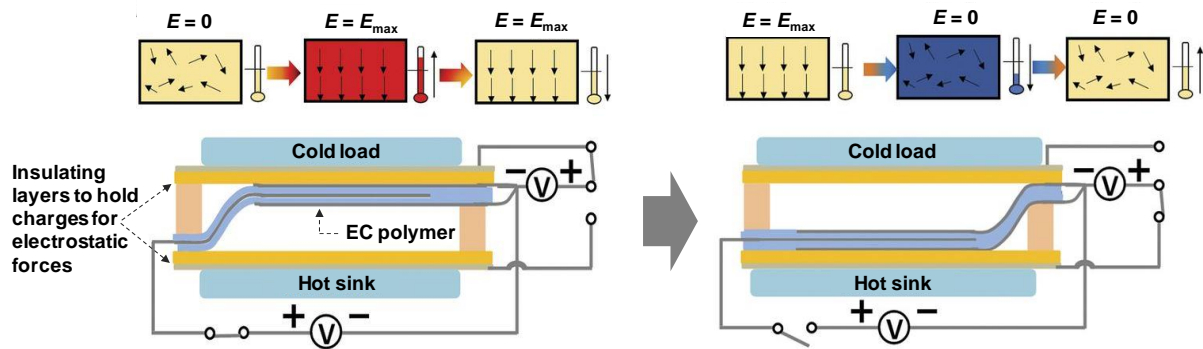


Figure 2-6. Working principle of the P(VDF-TrFE-CFE) system to transfer heat from the heat source to heat sink by electrostatic actuation¹³². In the left panel, the electric field E generates EC heating in the polymer laminates and bend up the flexible laminates to absorb heat from the cold load. The changes in temperature and E are illustrated in the 3 boxes on the top left. In the right panel, the polymer laminates undergo EC cooling and bend down to the hot sink for dumping heat. The cyclic motion is achieved by electrostatic forces between the EC polymer and the insulating tape covering the cold load and hot sink (yellow blocks in the figure).

Compared with well-established MC prototypes, EC counterparts offer a number of advantages: (i) it is easier and cheaper to generate large electric fields than large magnetic fields (large magnetic fields require pre-cooled superconductors or expensive permanent magnets). This indicates promising applications in small-size scales; (ii) EC materials tend to be cheaper than MC materials, as MC materials normally contain expensive rare-earth elements. However, EC effects tend to be smaller than MC effects, as the maximum EC response is limited by the maximum electric field that EC materials can sustain before electrical breakdown occurs.

3. Methodology

This chapter describes several experimental and theoretical methodologies, which were used for the present work in this thesis. Each section explains the general working principle of each method and describes the experimental implementation. In section 3.7, I explained how those experimental methods are used for evaluating caloric effects.

3.1 Sample preparation

Crystals of organic ferroelectric materials were synthesised for EC and BC studies. In principle, crystallization happens when the concentration of a compound in a solvent is higher than its solubility. A common way is to slowly cool down a saturated solution as the solubility normally decreases with temperature. An alternative way is to increase the concentration by evaporating the solvent. In practice, the first method can be faster but requires precise control of the temperature. In this thesis, both techniques were attempted but the second method has been found more effective due to its simplicity.

Slow evaporation method for crystallization

Precursor materials are mixed and dissolved in the solvent at the stoichiometric ratio. The mixed aqueous solution is placed in a glass jar covered by a piece of Parafilm with slits, which let the water evaporate at room temperature. After around one to two weeks, the desired crystals precipitated out.

For EC materials, the water evaporation is designed to be slow to yield single crystals and avoid defects during the crystal precipitation. Defects degrade the EC performance as they lead to unwanted Joule heat when the electric field is applied. In addition, single crystals generally have higher polarization and thus possibly larger EC effects.

A few key points were found for the crystal growth. Firstly, the container needs to be properly cleaned and the solution needs to be filtered to remove impurities. Secondly, the evaporation rate greatly affects the crystal size. In practice, different numbers of slits on the parafilm were

attempted to identify the best crystals. Thirdly, the air/mechanical disturbance should be avoided during the crystallization.

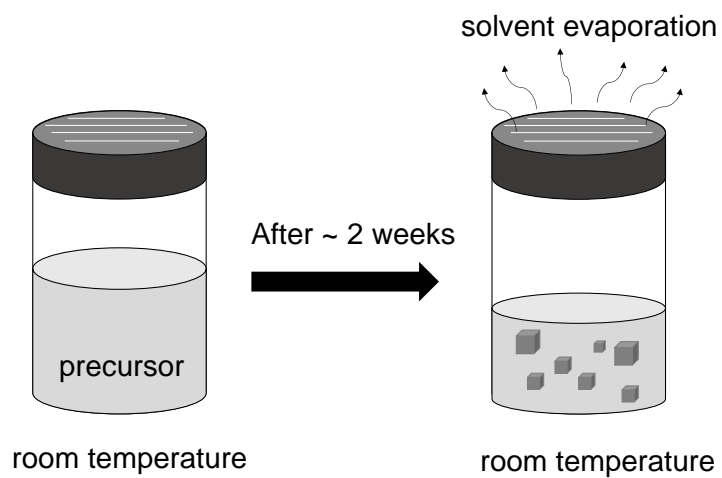


Figure 3-1 Crystal growth process via the slow evaporation method.

3.2 Dielectric measurements

The electrical properties of dielectric materials are usually described in terms of their dielectric constant. For EC studies, dielectric measurements could provide information such as T_C , and help to construct theoretical models (discussed in section 3.8). The fundamentals of this type of measurement are explained here. All dielectric measurements in this thesis were performed using an Agilent 4294A impedance analyser.

Dielectric constant ε is a complex frequency-dependent parameter with real part ε' and imaginary part ε'' . The real part ε' is associated with stored energy, whilst the imaginary part ε'' is associated with energy loss.

$$\varepsilon = \varepsilon' + j\varepsilon'' \quad (3.1)$$

The dielectric constant is measured using an impedance analyser, which generates an AC (alternating current) voltage source $U = U_0 \exp(j\omega t)$ where U_0 is the magnitude of the AC voltage, ω is frequency and t is time. The samples I studied are modelled as non-ideal capacitors, through an equivalent circuit¹³⁴ consisting of a capacitor C_P in parallel with a resistance R , as shown in Fig. 3-2.

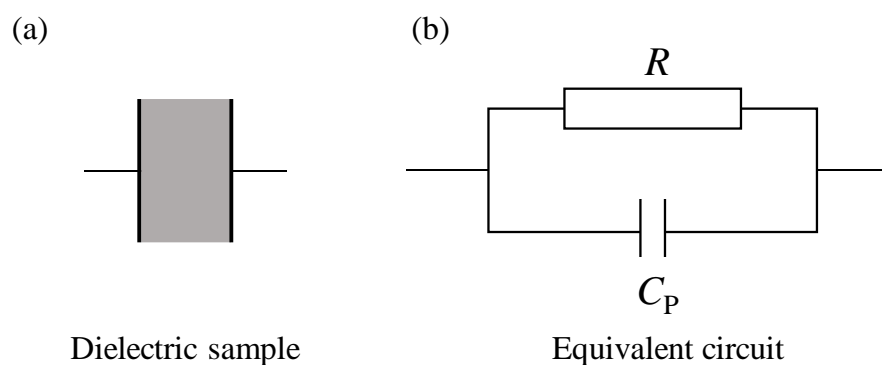


Figure 3-2. (a) a parallel capacitor sample. (b) the equivalent circuit assumed during experimental measurements.

Then the impedance Z of this equivalent circuit can be written as

$$\frac{1}{Z} = \frac{1}{R} + j\omega C_P \quad (3.2)$$

After rearrangement, Z can be expressed as

$$Z = \left(\frac{R}{1 + \omega^2 R^2 C_P^2} \right) + j \left(- \frac{\omega R^2 C_P}{1 + \omega^2 R^2 C_P^2} \right) \quad (3.3)$$

Knowing the voltage U and current I , the values of R and C_P can be obtained through $Z = U/I$.

For a capacitor, the real part of dielectric constant ϵ' can be calculated with C_P .

$$\epsilon' = \epsilon_0 \epsilon_r = \frac{C_P d}{A} \quad (3.4)$$

where ϵ_0 is the vacuum permittivity ϵ_r is relative permittivity which is an intrinsic property of each material, d is the thickness of the capacitor and A is its area.

The lossy part of a dielectric material results from the phase difference δ between the voltage U and the current I . This can be described as the ratio of the imaginary part Z' and the real part Z'' of impedance, which is expressed in term of C_P and R shown in Eq. 3.3. This leads to the imaginary part of the dielectric constant ϵ'' .

$$\tan \delta = \frac{Z''}{Z'} = \frac{\epsilon''}{\epsilon'} \quad (3.5)$$

For classic ferroelectric e.g. PbTiO_3 ⁵⁴, the temperature-dependency of dielectric constant ϵ is usually in the shape shown in Fig.3-3. A peak arises when the ferroelectric phase transition happens. The temperature-dependency of the relative dielectric constant is described by Curie-Weiss Law⁵⁴ as follow:

$$\epsilon' - 1 = \frac{W}{T - T_C} \quad (3.6)^{54}$$

where W is the material-specific Curie constant, T is temperature and T_C is Curie temperature. This equation holds only for temperatures above the phase transition. This plot is also used to construct Landau models, which are described in section 3.8.

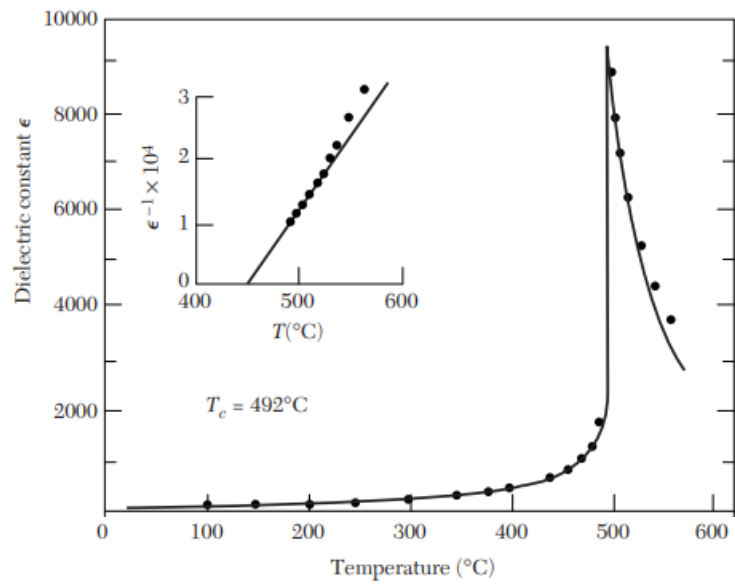


Figure 3-3. The dielectric constant of PbTiO_3 as a function of temperature⁵⁴. The inset is a linear fitting of $1/\epsilon$ as function of temperature T based on Eq.3.6.

3.3 Ferroelectric measurements

Standard method

In principle, Radiant tester measures charge-voltage characteristics of capacitors, which are then geometrically normalized to yield the polarization-field relation $P(E)$, where $\Delta P = \Delta Q/A = \frac{1}{A} \int_{t=0}^{t=\Delta t} Idt$, where Δt is the time duration of the applied voltage, A is the electrode area of the parallel capacitor, ΔQ is the amount of charge through the sample during Δt and ΔP is the measured change in polarization. In words, the polarization change ΔP is calculated through the integration of current density over a given time frame Δt , which corresponds to a measurement frequency $f = 1/\Delta t$.

The ferroelectric polarization is measured using the Precision Premier II, from Radiant Technologies combined with an external amplifier, Trek type 609E-6 to extend the voltage range from 200 V to 4000 V. Here, $P(E)$ is measured in a continuous temperature sweeping to yield the temperature and electric-field dependent polarisation $P(T, E)$, which is the core of an indirect method for evaluating caloric effects, as described in section 3.7. In practice, the temperature is controlled by the Lakeshore Cryotronics PID controller and a resistance heater.

Modified method

A common problem of measuring ferroelectric polarization is leakage, which means that the sample is not a perfect insulator but has a conduction current. In theory, the measured polarization of a lossy ferroelectric consists of three contributions: (1) dielectric current, (2) ferroelectric switching current and (3) leakage current¹³⁵. Therefore, an equivalent circuit with a capacitor, a non-linear switching and a resistance in parallel was constructed. This is shown in Fig.3-4. In our measurement, the modified driving voltage profile aimed to subtract the leakage from measured polarization.

$$P_{\text{total}} = P_{\text{switching}} + P_{\text{dielectric}} + P_{\text{leakage}} \quad (3.7)^{54}$$

$$P_{\text{dielectric}} = \epsilon_0 \epsilon_r E \quad (3.8)^{54}$$

$$P_{\text{leakage}} = \Delta Q/A = 1/R \int U(t) dt \quad (3.9)^{54}$$

The measured $P(E)$ loop can break down into the contributions from the resistance (leakage) and the non-leaky ferroelectric, which can be further broken down into the parts from ferroelectric switching and intrinsic linear dielectric. The plots are illustrated in Fig. 3-4 top. Fig. 3-4 bottom shows the corresponding equivalent circuit, which consists of a capacitor, a non-linear switching and a resistance in parallel.

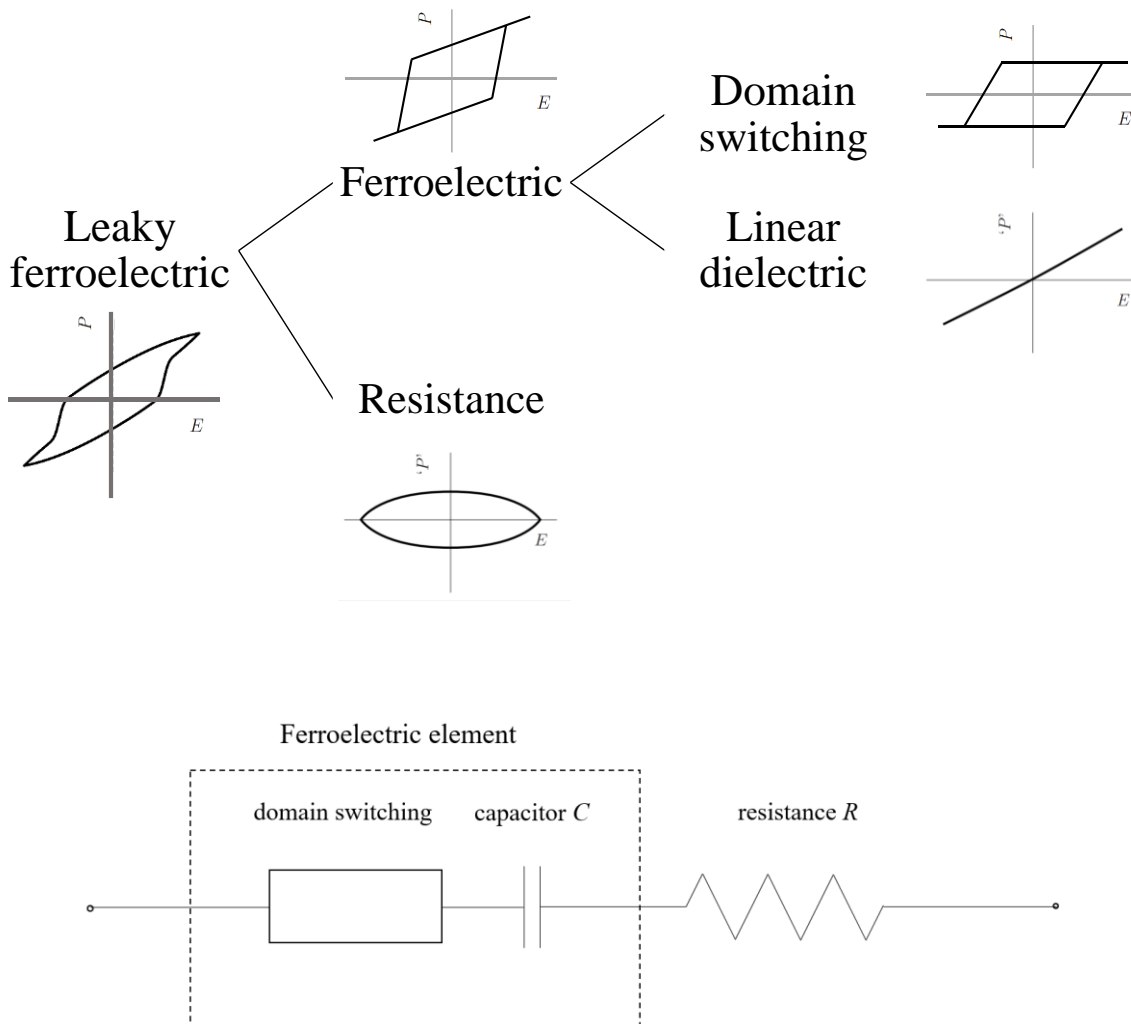


Figure 3-4. Top: illustrations of the decomposition of $P(E)$ loop measured from a leaky ferroelectric. **Bottom:** The corresponding equivalent circuit.

The traditional driving voltage profile measures those three sources simultaneously. To decompose the measured polarization, a modified driving voltage profile was applied, which contains double waves in both positive and negative directions. The first wave measures three contributions while the following wave measures only the (2) linear dielectric response and (3) the leakage, without (1) polarization switching because the domains are already aligned by the first wave. By subtracting the peak value of P on the first wave from that of the second wave, the polarization resulted from conduction can be derived because it is the only part that increases with the integration of time. According to the modelled equivalent circuit, the leakage is from a resistance R in series (Figure 3-5 bottom). Therefore, the relation between the resistance value and the associated extra polarization ΔP is given by $\Delta P = \Delta Q/A = (\int U dt)/(A R)$. A demonstration in Fig 3-5d shows the measured $P(E)$ loops before and after the subtraction of leakage. Fig 3-5e is the polarization from the subtracted leakage, corresponding to a resistance of $2.2 \times 10^8 \Omega$. The data was measured from a 1,4-diazabicyclo[2.2.2]octane tetrafluoroborate crystal sample.

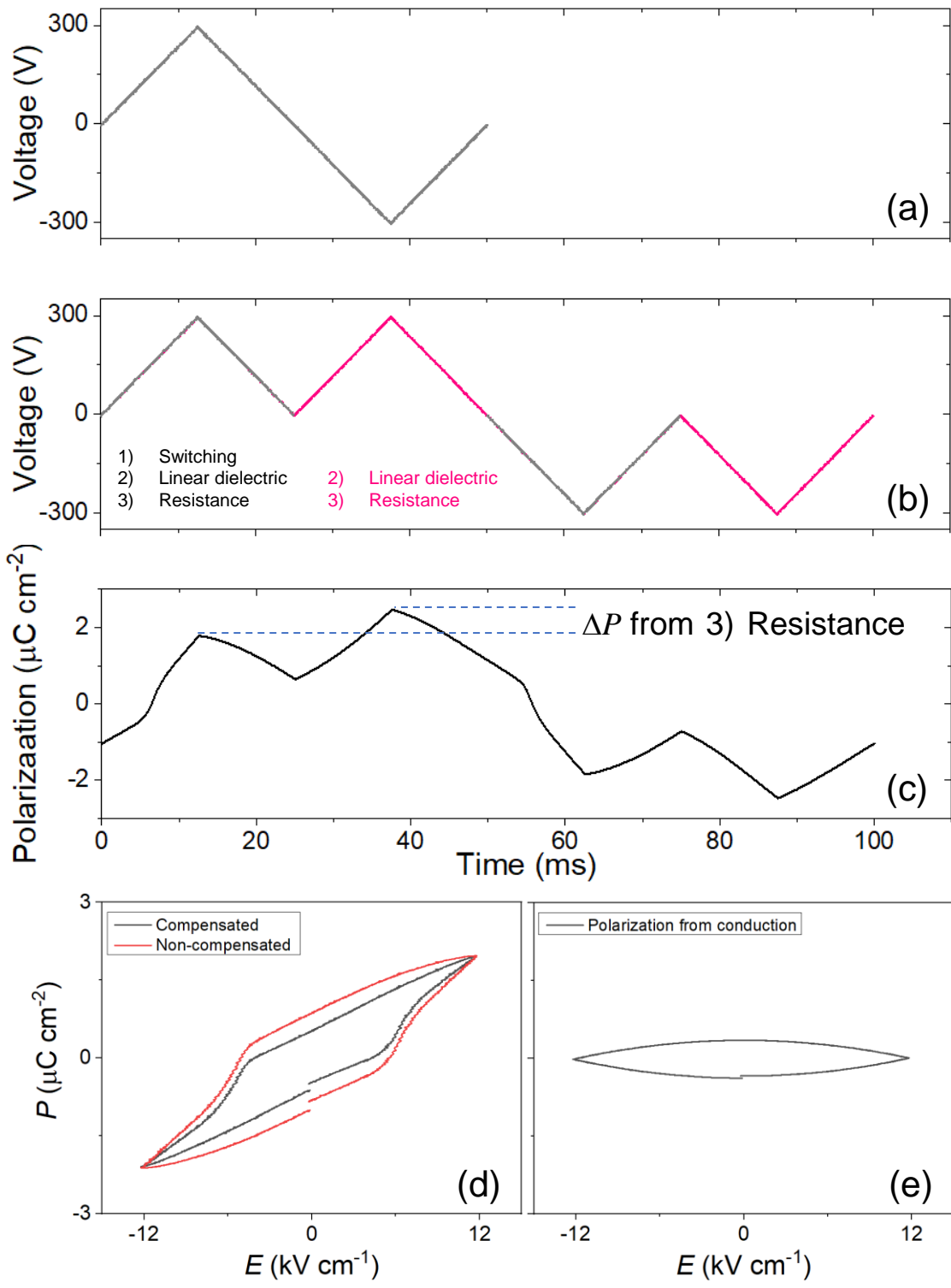


Figure 3-5. (a) the standard waveform of the driving voltage. (b) the modified version of the voltage wave, which aims to separate different sources of polarization, namely the (1) ferroelectric switching, (2) the linear dielectric and (3) the leakage. (c) the total measured polarization P as a function of time. The difference in P between the first and second peaks is from the leakage only. The value of ΔP is used to calculate the resistance value associated with leakage. (d) demonstrates the leakage subtraction. (e) is the leakage subtracted from (d).

3.4 Calorimetric measurements

As stated in Section 1.2, the isothermal entropy change ΔS and isothermal heat Q are typically used for characterizations of EC effects. Calorimetry is used to experimentally measure Q and then derive ΔS .

In this thesis, three instruments were used, including

- a differential scanning calorimeter (DSC) Q2000 from TA Instruments that operates at zero field
- a homemade DSC that operates under variable electric fields
- a Setaram Instrumentation μ DSC7 EVO microcalorimeter equipped with a 260D Teledyne Isco Syringe Pumps with nitrogen gas as a pressure-transmitting media. This instrument operates under variable hydrostatic pressures

Using those experimental setups, values of thermally driven, electrically driven and pressure-driven heat Q and entropy change ΔS can be obtained to characterise phase transitions and the electrocaloric/barocaloric responses.

The following paragraphs explain the DSC instrumentations in terms of (i) working principle, (ii) experimental set-ups and (iii) data processing.

Working principle

The working principle of the homemade DSC is described here and it also applies to the other two commercial instruments. DSC relies on symmetry considerations where two measuring sensors¹³⁶ – one for a reference and one for the sample under study – are approximately in the same physical conditions during the measurement. It is used to monitor heat flows, associated with phase transitions, as a function of temperature (or applied fields). The following paragraphs explain the origin of measured heat flows in the homemade calorimeter step by step.

A simplified sketch of the DSC is shown in Fig.3-6. The heat flow between two points is in a linear relation to the temperature difference between those points. This is also known as thermal Ohm's law. Secondly, the system is assumed under thermal equilibrium during the entire

measurement process, which requires a sufficiently slow heating or cooling rate. Hereby, the balance between the reference and the copper block leads to

$$\frac{T_0 - T_R}{R_R} = C_R \frac{dT_R}{dt} \quad (3.10)$$

where T_0 and T_R are the temperatures of the copper block and the reference, respectively. C_R is the heat capacity of the reference, in this case a piece of copper. R_R is the thermal resistance between the reference and the copper block. t is time.

Eq. (3.10) means that a heat flow, generated from the copper block (T_0) towards the reference (T_R) when heating the calorimetry is written as $\frac{T_0 - T_R}{R_R}$. This heat flow is absorbed by the metal reference, and amounts to $C_R \frac{dT_R}{dt}$.

The thermal balance between the sample and the copper block can be described similarly but with the additional contribution of the latent heat during the phase transitions.

$$\frac{T_0 - T_s}{R_s} = C_s \frac{dT_s}{dt} + \frac{dQ_0}{dt} \quad (3.11)$$

Where T_s and C_s are the temperatures and the heat capacity of the sample, respectively. R_s is the thermal resistance between the reference and the copper. Q_0 corresponds to the latent heat of the sample during phase transitions.

For simplicity, R is regarded as the same value for the reference and the sample. This is a fair assumption because thermal resistance is mainly from the Peltier sensor between the sample/reference and the copper block.

$$R_R = R_s = R \quad (3.12)$$

Subtracting Eq.3.10 from Eq.3.11 yields

$$\Delta T(t) = T_s(t) - T_R(t) = R \left(C_R \frac{dT_s}{dt} - C_s \frac{dT_R}{dt} + \frac{dQ_0}{dt} \right) \quad (3.13)$$

The system is assumed to be under thermal equilibrium during the entire measurement process, and so

$$\frac{dT_R}{dt} \sim \frac{dT_S}{dt} \sim \frac{dT_0}{dt} \quad (3.14)$$

The Eq. (3.14) can be further simplified as

$$\Delta T(t) = T_S(t) - T_R(t) = [(C_R - C_S) \frac{dT_0}{dt} + \frac{dQ_0}{dt}] \quad (3.15)$$

Using Peltier sensors, the temperature difference can be converted into a voltage signal V and recorded by a multimeter.

$$V(t) = B \Delta T(t) \quad (3.16)$$

where B is the Seebeck coefficient.

Overall, the DSC measures the temperature difference between the sample and an inert metal reference, which is then converted to heat flow associated with the phase transitions after suitable calibration of the sensors.

Experimental setups

The schematic of the homemade DSC and the photo are shown in Fig.3-6 and Fig.3-7, respectively. The whole body of the setup is enclosed using a copper lid, which minimizes air convection inside and keeps the system in isothermal conditions. There is a Pt-100 sensor, embedded inside the copper block to monitor the temperature (T_0). Two Peltier sensors are placed symmetrically under the reference (a copper piece) and the sample for detecting heat flow signals. All output signals are fed into multimeters (Keithley 2110) through GPIB-usb cables (National Instrument) for data acquisition. A sourcemeter (Keithley 2410) is used to apply electric fields to the sample through two copper wires, which are very thin to minimize thermal losses. The entire setup is placed in a thermal bath (Lauda ECO Heating Circulators), which has a chamber filled with silicon oil to uniformly control the temperature from -50 °C to 150 °C.

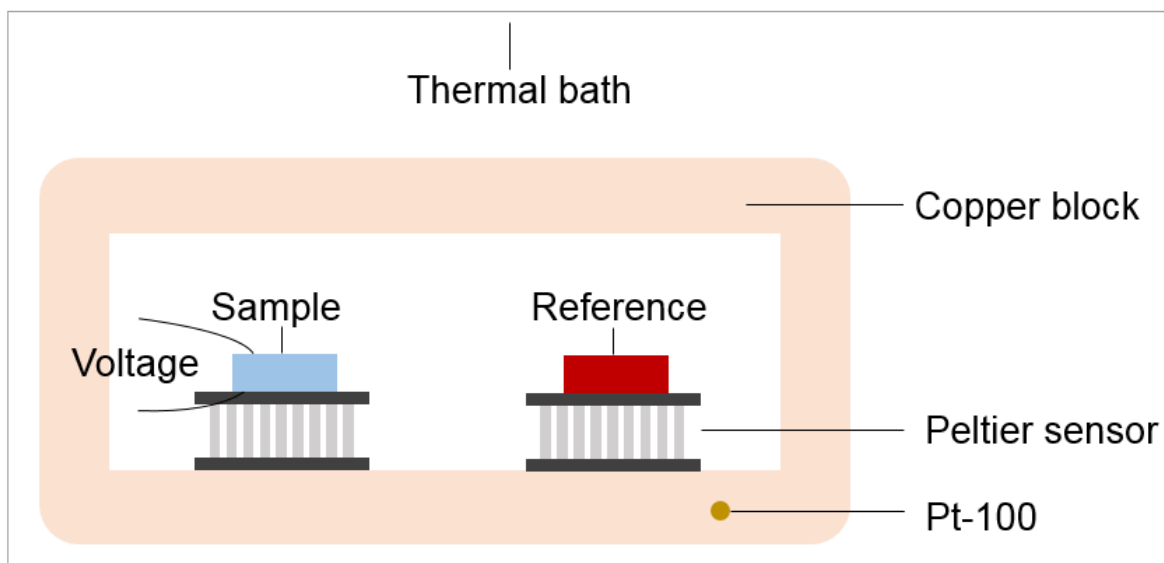


Figure 3-6. Schematic of the homemade DSC setup. The Pt 100 sensor embedded in the copper block is used to record the temperature of the whole setup. The Peltier sensors are designed to capture the heat flow signals. The copper block is to ensure the homogeneous temperature distribution. The voltage source for calorimetry under electric field is a Keithley 2410 sourcemetre. The thermal bath is used to change the temperature slowly for the setup.

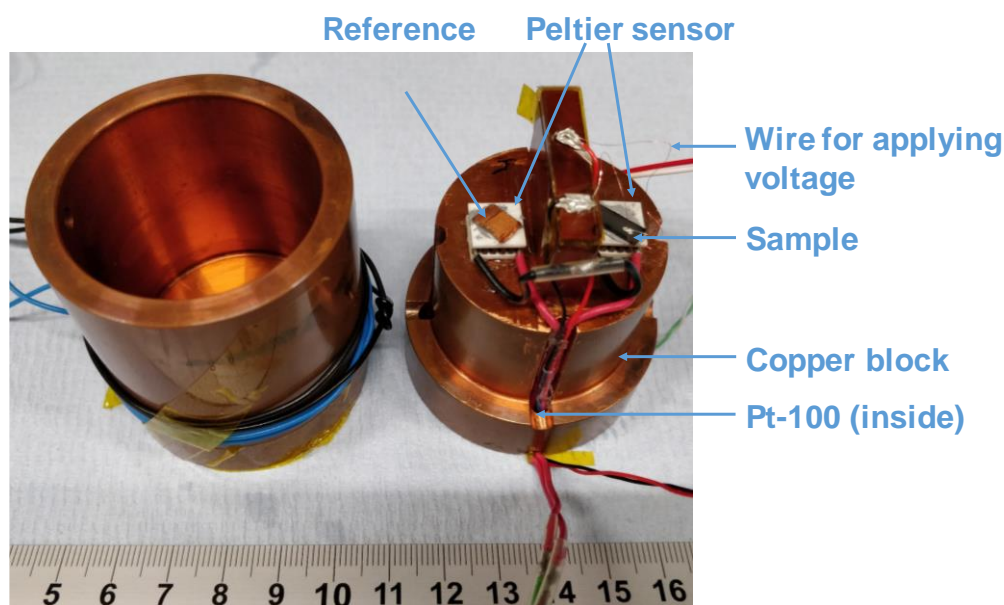


Figure 3-7. Photo of the homemade DSC setup. The main functional elements are explained in the schematic in Fig. 3-6.

Data processing

From calorimetry measurement, Q and S can be obtained. The raw data acquired is dQ/dt , as shown in Fig.3-8 the heat flow of the sample releasing or absorbing heat as a function of time t . The integration of dQ/dt over t yields the heat Q during the phase transition (when transitions are driven thermally this heat is known as latent heat Q_0).

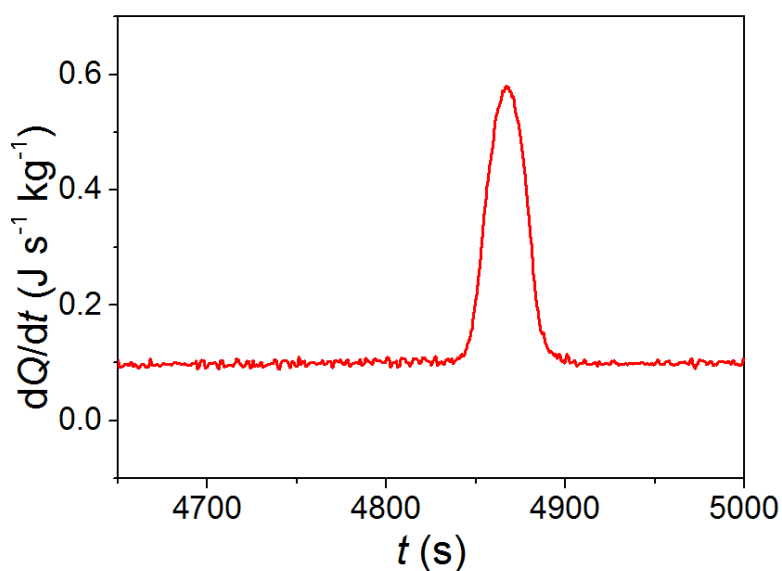


Figure 3-8. Raw data dQ/dt as a function of t , recorded using the homemade DSC. Data taken using a 1,4-diazabicyclo[2.2.2]octane perrhenate sample.

For an easy comparison of measurements at different cooling and heating rates, dQ/dT is normally calculated:

$$\frac{dQ}{dT} = \left(\frac{dQ}{dt}\right) \left(\frac{dT}{dt}\right)^{-1} \quad (3.17)$$

where dQ/dt is heat flow and dT/dt is heating/cooling rate, which is ideally constant during the calorimetric measurements. The plot is shown in Fig.3-9.

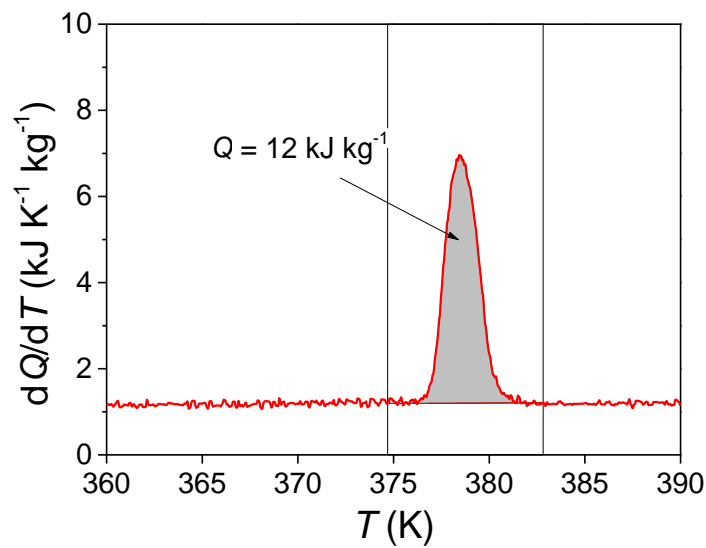


Figure 3-9. The plot of heat flows dQ/dT as a function of T . The area under the curve is the latent heat Q_0 . Data taken using a 1,4-diazabicyclo[2.2.2]octane perchrenate sample.

According to Eq. (1.8), the entropy change ΔS as a function of T of phase transitions can be obtained from the integral of $(dQ/dT)/T$, shown in the grey area in Fig. 3-10. In Fig. 3-11, the value of ΔS is plotted as a function of T . The saturation value of $\Delta S(T)$ corresponds to ΔS for the full transition.

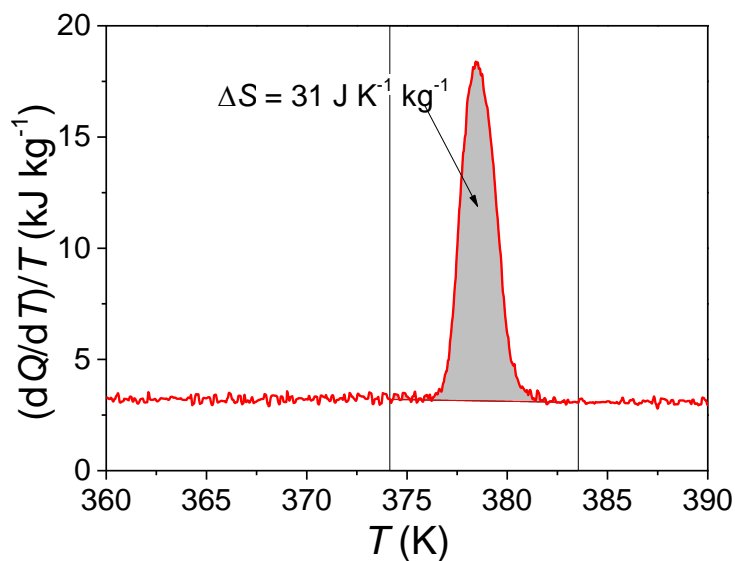


Figure 3-10. The plot of heat flows $(dQ/dT)/T$ as a function of T . This is to calculate the value of entropy change ΔS for the phase transition. Data taken using a 1,4-diazabicyclo[2.2.2]octane perchrenate sample.

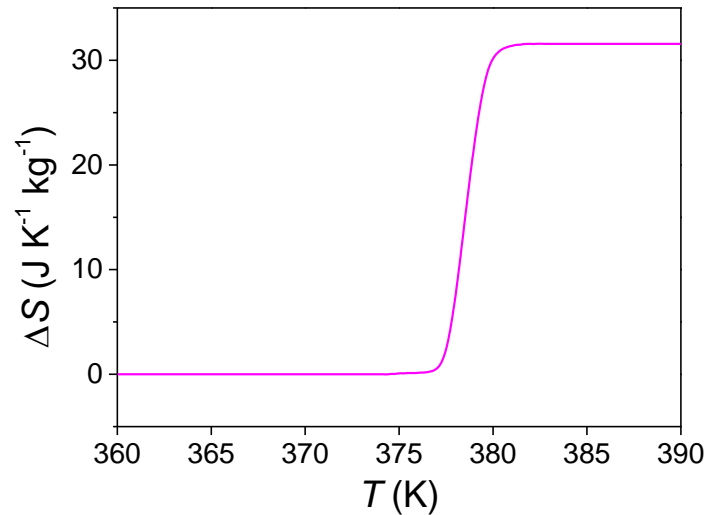


Figure 3-11. The plot of $\Delta S(T)$. Data taken using a 1,4-diazabicyclo[2.2.2]octane perrhenate sample.

Specific heat capacity measurement

The experimental measurement of specific heat capacity c_p is adopted from M. J. O'Neil. The specific heat capacity is the amount of heat required to change temperature of 1 kg of material by 1 K. During the temperature sweeping in DSC, c_p links the heat flow and the temperature change of the sample as $(dQ/dt) = c_p (dT/dt)$. This suggests that c_p is actually the mass-normalized heat flow (dQ/dT) .

However, this measured c_p needs to calibration because there is always unwanted signal from the instrument. The calibration is done by comparing the sample with a well-known reference sample. Experimentally, three DSC measurements can be performed at the same heating/cooling rate, in the same temperature range, in the following sequences: (1) an empty pan, (2) the sample to study and (3) a standard reference of sapphire (α -aluminium oxide / α - Al_2O_3). Subtraction step (1) data from step (2) is to subtract the signal from the instrument, mainly from the metallic sample container. Step (3) measures the well-known sapphire as the reference.

Pressure-dependent calorimetry

In this thesis, a pressure-dependent calorimetry was used in the quasi-direct method (explained in Section 3.7) to evaluate the BC effects. The schematic of the setup is shown in Fig.3-12. The whole setup consists of three parts: (1) the nitrogen gas cylinder; (2) the 260D Teledyne Isco Syringe Pumps and (3) the Setaram Instrumentation μ DSC7 EVO calorimetry. The nitrogen gas cylinder is the source of nitrogen gas as a pressure-transmitting media. The pressure coming directly from the cylinder is up to 100 bar. Then the syringe pump boosts the pressure up to 1200 bar by pressing the piston. Through the stainless steel tubes, the boosted pressure is transmitted to the sample cell and reference cell for calorimetry measurements. Inside the stainless steel tube near the calorimetry, one pressure sensor was installed to monitor the pressure inside the calorimetry cells. The working principle of this calorimetry is the same as the ones mentioned above so is not repeated here.

The following points summarize some key details that help to perform valid experimental measurements.

- Firstly, isobaric conditions are required during the quasi-direct measurements where the sample is subjected to temperature sweeps under the different pressures. The applied pressure was increased from 0, 100, 200, 300, 400 up to 1200 bar for each sweep cycle, with an interval of 100 bar. The first cycle of 0 applied pressure was repeated 3 times to test the reproducibility of measurements and stability of the instrument. From our measurements, no obvious differences were observed from the repetitions so the cycles at higher pressures were not repeated to save time. It might be worth to test the reproducibility of high-pressure measurements in the future. At the end of each sweep, the syringe pump takes 1.2 min to increase the pressure by 100 bar for the subsequent sweep. At the pressure change stage, a time gap of 10 min is programmed, which is much longer than 1.2 min, for the pressure to stabilize. Therefore, one can ensure that the measurements were performed under isobaric conditions.
- Secondly, as the same reference cell is used for different samples, it would be good to keep the amount of heat from samples around the same. This means the mass of the samples should vary according to its heat capacity. The values of sample mass were recorded in Section 5.2.4 and Section 6.3.5. Ideally, more samples of ReO_4 should have been added for better reference comparison.

- Thirdly, a key assumption is the isotropic pressure condition. For BC measurements, all samples are ground into powders and then subjected to hydrostatic pressure. In practice, the impact from uneven distribution of pressure and crystal orientations is assumed to be negligible.

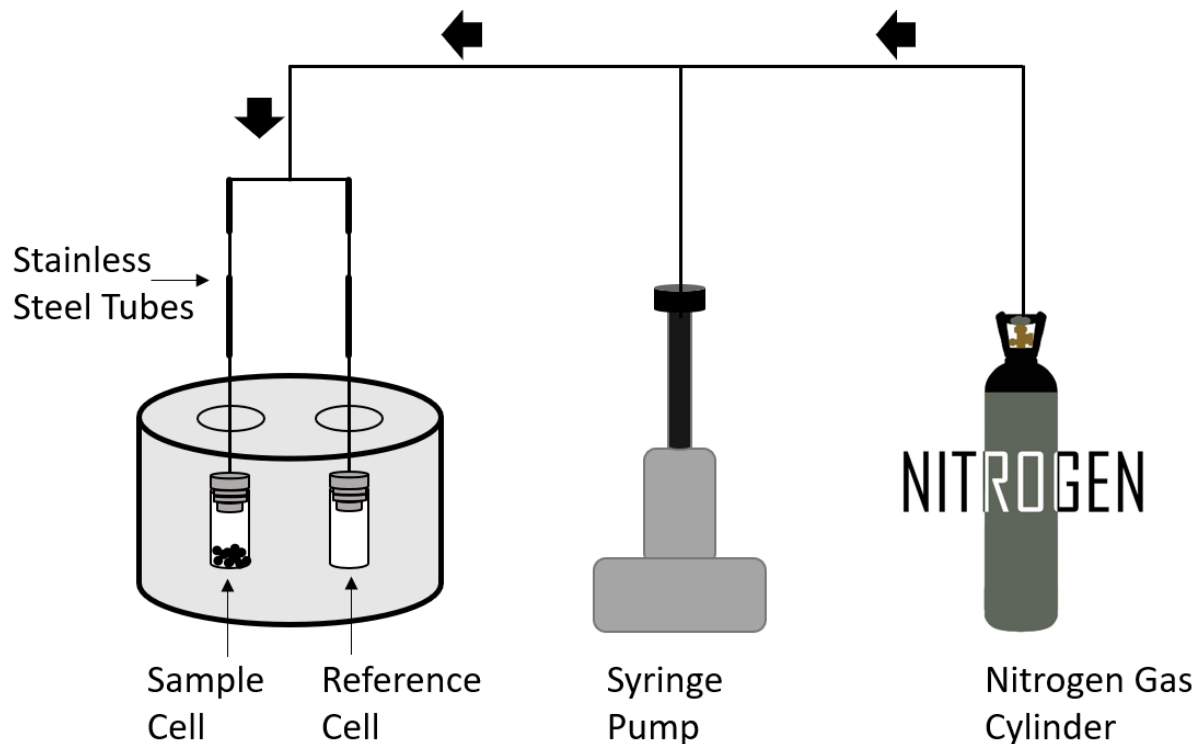


Figure 3-12. Schematic of the pressure-dependent calorimetry. This shows how the pressure is generated from a nitrogen gas cylinder, then boosted up to 1200 bar by a syringe pump and finally transmitted to sample powders inside the calorimetry. The black arrows represent the direction of nitrogen flow i.e. the pressure-transmitting media. The stainless steel tubes are deliberately selected for high-pressure measurements.

3.5 Dilatometry

A dilatometry measures the dimension changes of a sample material caused by temperature sweeping. More specifically, the dilatometer records the length changes that occur during the heat treatment of a sample. Length changes can be used to determine the volume change. The volume change ΔV is assumed as $\frac{(L_i + \Delta L)^3}{L_i^3} - 1$, where L_i is the initial length and ΔL is the change in length. Then the specific volume as a function of temperature $V_{sp}(T)$ can be obtained in combination with the density of the sample at a temperature within the measurement range.

Experimentally, a push-piston type TMA Q400 dilatometer from TA Instruments is used for results in Chapter 6. Normally, a cube of the sample with edge ~ 3.5 mm is subjected to length measurement upon heating and cooling at the rate of 5 K min^{-1} .

3.6 Infrared imaging

A FLIR SC 7500 infrared (IR) camera was used for the adiabatic temperature change ΔT results in Chapter 4. IR camera is commonly used for investigating caloric effects because it has a few advantages. Firstly, the IR camera records temperature without contacting the sample, so it does not cause heat leaks due to contact. This is an advantage in comparison to contact thermometry such as thermocouple sensors. Secondly, the IR camera is capable of capturing temperature changes in a very short time scale, ~ 0.02 s or a frame rate of 50Hz. The fast frame rate is particularly important for direct measurement of adiabatic temperature change ΔT , as discussed in Chapter 3.7. Thirdly, the IR camera provides a spatial resolution of the temperature information, which can be useful to investigate the heat flow in devices¹³⁷ and the heat transfer with environment¹³⁸.

To capture the temperature change driven by electric field, it is essential to avoid heat leaks. An experimental setup in Fig.3-13 was used, in which a cardboard box covers the sample and the IR camera to prevent heat exchange with the environment. In addition, the sample is placed on the heating stage with black tape at two ends, which keeps the sample in a nearly ‘floating’ state to avoid heat leaks during the measurements of the adiabatic temperature change.

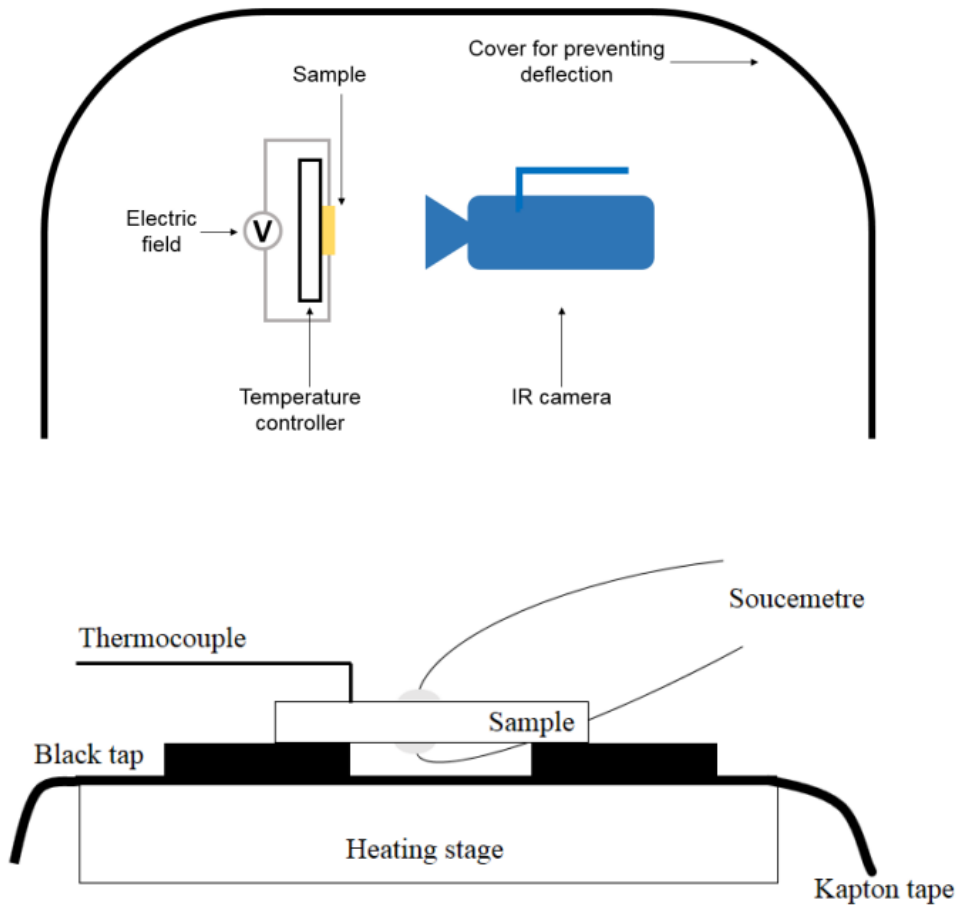


Figure 3-13. **Top:** experimental configuration for direct measurements. **Bottom:** the zoom-in of the sample configuration. The electric field is applied using two copper wires. The K-type thermometer is attached to the surface to record ΔT . The sample is in a nearly 'floating' state to avoid contact and heat leaks.

3.7 Evaluation methods for caloric effects

Three methods to characterise the EC and BC effects were used in this thesis, namely indirect, direct, and quasi-direct methods. The theory and experimental implementation are explained in detail later in this section. At the beginning, a summary of pros and cons of each method is presented so one can select the best measurement strategy in different situations.

Indirect method

- Pros: Indirect method measures the temperature and field dependencies of the corresponding order parameter, which is polarization P and volume V in EC and BC effects, respectively. This is easy for experimental implements in EC measurements. In addition, unlike quasi-direct and direct methods where usually only a few $|\Delta E|$ are selected for measurements, indirect methods can collect dense datasets easily. This allows one to see the continuous curve of $|\Delta S|$ or $|\Delta T|$ as a function of $|\Delta E|$ instead of a few discrete points.
- Cons: Particular attention must be paid to the use of the indirect method in EC measurements. A single-valued function of polarization needs to be carefully selected (details in Fig. 3-14). For deriving the $|\Delta T|$ driven by electric fields, one should be cautious that the heat capacity is electric field dependent. This could cause large errors especially when the T_C is shifted little (details in Section 4.3.2). In BC measurements, the indirect methods are very challenging. The temperature and pressure dependences of volume requires a bespoke dilatometry or a bespoke X-ray diffraction instrument to operate at variable pressures. These instruments are rare in labs.

Direct method

- Pros: Direct methods measure thermal response driven by fields so they provide the closest scenario with the practical applications i.e. generating cooling effect when fields are applied.
- Cons: The experimental design is challenging because no absolutely perfect isothermal or adiabatic conditions can be achieved in practice (details in Fig. 3-15 and Fig. 3-16). For adiabatic measurements, one usually encounters the heat leaking problem, which is significant for thin film samples due to their small thermal mass. In addition, adiabatic measurement requires very fast application of fields, which is challenging for pressure-

generating instruments and can be dangerous in the lab. For isothermal measurements, heat exchanges can be an issue when the sample has low thermal conductivity. The uneven temperature distribution in the sample can cause errors. In the data processing stage, Joule heating is always an issue for EC materials(details in Chapter 4).

Quasi-direct method

- Pros: Quasi-direct method is frequently used in BC measurements as the indirect and direct methods are both experimentally challenging for BC measurements.
- Cons: Quasi-direct method relies on the heat flow measurement using calorimetry, especially near the phase transition(details in Section 3.4). This is normally only sufficiently sensitive for first-order transitions, which have a latent heat. However, many relaxor ferroelectrics are not applicable.

Indirect method

The indirect method yields ΔS from the thermodynamic analysis using the Maxwell relation²³, which was explained in Chapter 1.2. In EC effects, using $(\partial S/\partial E)_T = (\partial P/\partial T)_E$ derived from the Gibbs free energy, $\Delta S(T, E) = \int (\partial P/\partial T)_E dE$ can be obtained. Similarly in BC effects, $(\partial S/\partial E)_T = (\partial P/\partial T)_E$ yields $\Delta S(T, p) = \int (\partial V/\partial T)_p dp$. The derivation of ΔS relies on the temperature and field dependences of the corresponding order parameter, which is polarization P and volume V in EC and BC effects, respectively.

Experimentally, the indirect method in EC effects is performed as successive measurements of $P(E)$ loops at different T . To get a single-value function of $P(E)$, the field-removal branches obtained ($0 \leq E \leq E_{\max}$) is selected for further processing. In this step, data interpolation is applied to align P at different T for a fixed E . This yields a $P(T, E)$ matrix. $\Delta S(T, E)$ can be obtained by differentiation of $P(T)$ and then integration along E . Data smooth could be necessary before differentiation to remove artificial spikes. The process is explained in Fig.3-14. Alternatively, one can also measure $P(T)$ at different E via the pyroelectric measurements. However, sweeping the temperature in practice could be time-consuming.

In BC effects, the indirect method is commonly implemented by measuring the thermal expansion at different pressures, i.e., $V(T)$ at different p . This can be measured by dilatometry at different pressures¹²¹ or temperature-dependent X-ray diffractions at different pressures^{113,121}.

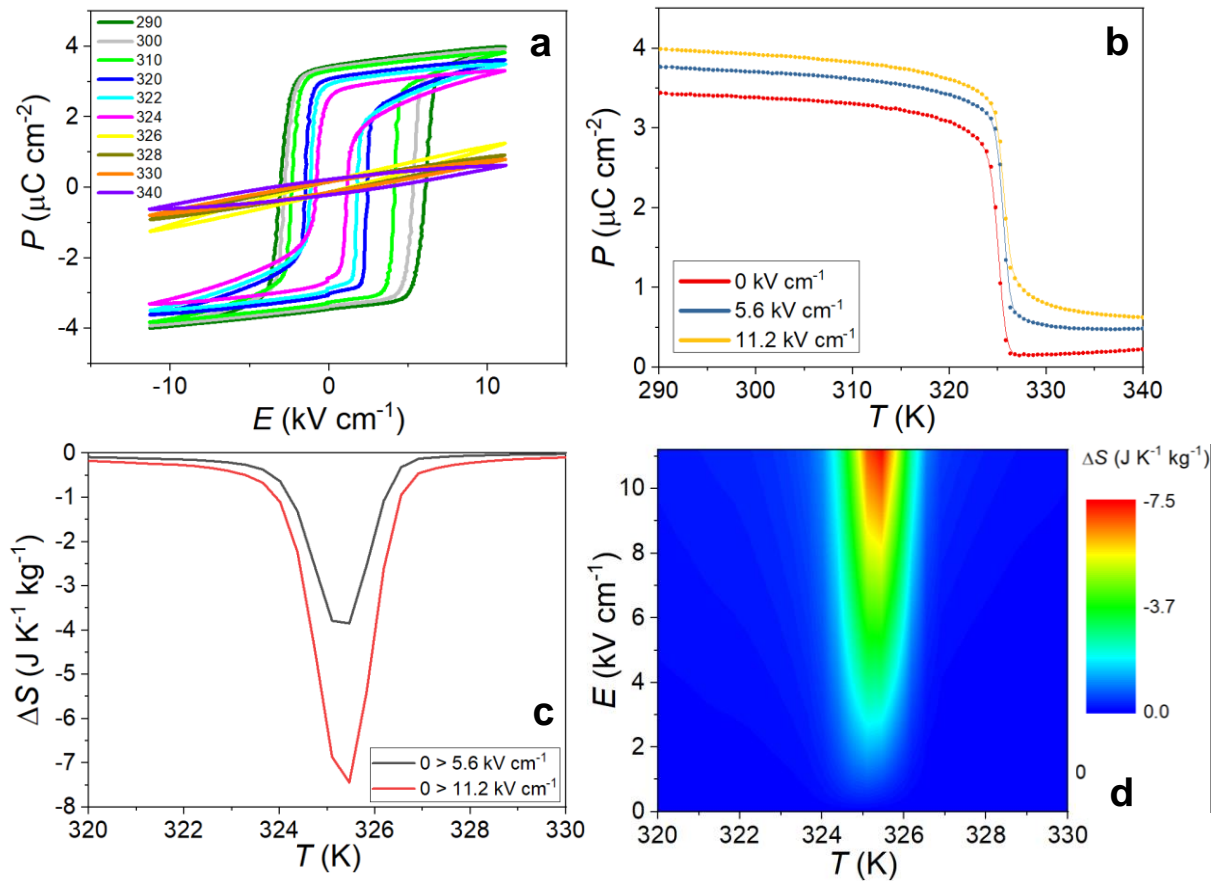


Figure 3-14. The process of indirect methods. (a) The lines in colour represent the $P(E)$ loops measured at different E (b) Selected $P(T)$ derived from the $P(E)$ loops by extracting P at different T when E is fixed. The lines are smoothed for the subsequent derivation and integration. (c) The absolute value of isothermal entropy change $|\Delta S|$ as a function of T at different E . The calculation is performed via $\Delta S(T, E) = \int (\partial P / \partial T)_E dE$. (d) The contour plot of $|\Delta S|(T, E)$ with the colour bar showing the magnitude of $|\Delta S|$.

Direct method

The direct method directly evaluates the thermal response ΔT and ΔS upon applying electric field or pressure. Let's discuss the EC effects first. To measure the adiabatic temperature change ΔT , the sample temperature should be monitored from the application and the removal of the electric field. In the ideal adiabatic condition, the sample has no heat exchange with its environment (Fig.3-15a). However, in practice, the experiments are carried out under near-adiabatic conditions (Fig. 3-15b), where EC cooling happens in a shorter timescale than the time scale over which the heat is permitted to flow towards the environment. Then the peak value of temperature change can be regarded as an adiabatic ΔT . Experimentally, ΔT is usually measured by a thermocouple or an IR camera¹³⁹.

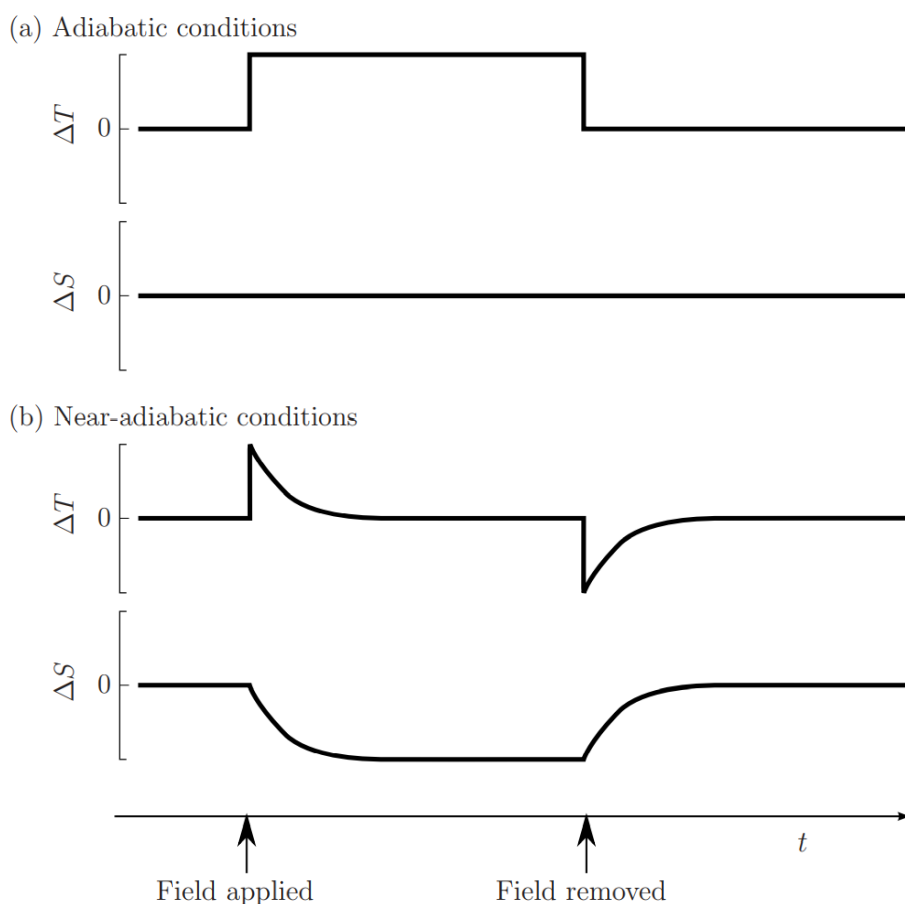


Figure 3-15. Schematic of the experimental approach to measure adiabatic temperature changes. The figure compares the evolution of $\Delta T(t)$ (where t is time) for an EC cycle in the adiabatic **(a)** and near-adiabatic **(b)** conditions. The bottom panel shows when the electric field change ΔE is applied, and subsequently removed. This figure is reproduced from the Ph.D. thesis of S. Crossley¹⁴⁰.

Direct measurement of isothermal ΔS is achieved by measuring isothermal heat Q via $Q = T\Delta S$ because entropy cannot be directly measured. Experimentally, direct isothermal heat-flow (Fig.3-16b) dQ/dt measurements are performed when the electric field is applied gradually and sufficiently slowly (Fig.3-16c) such that the sample temperature stays constant (Fig.3-15a).

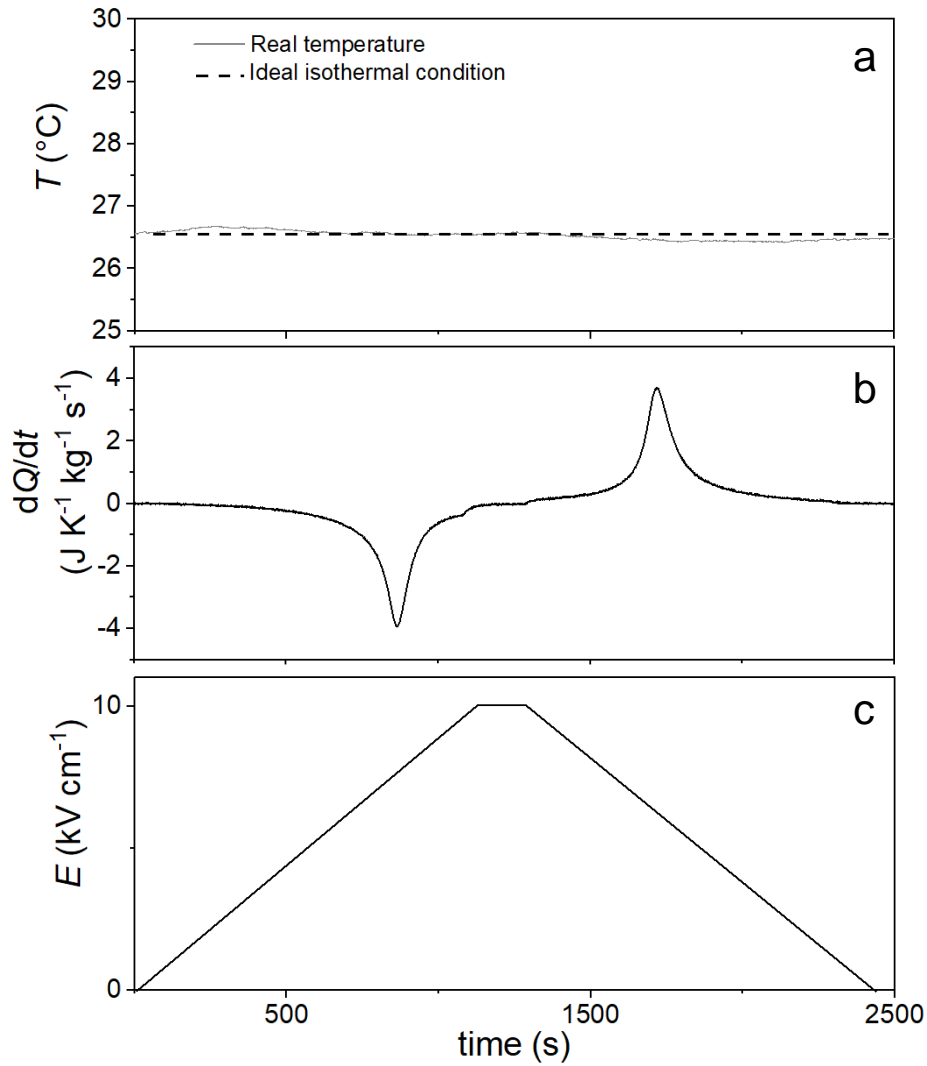


Figure 3-16. The direct measurement of ΔS via isothermal Q from the dQ/dt integration. **(a)** the temperature of the sample monitored as a function of time. Ideally, T should stay constant. In practice, variation may be tolerated. **(b)**, the heat flow dQ/dt as a function of time. The integration of the peak yields isothermal Q and thus the isothermal ΔS . **(c)**, the electric field profile. The electric field is gradually applied and removed so the sample temperature does not change. The results were measured from a $\text{PbSc}_{0.5}\text{Ta}_{0.5}\text{O}_3$ ceramic.

In the context of BC effects, direct measurement of ΔT and ΔS follows the same principle as EC effects. However, the experimental setup for BC is more challenging. Firstly, the adiabatic condition requires a very fast application and removal of pressure p , which could be dangerous in laboratory. Secondly, recording ΔT using an IR camera requires a infra-red transparent chamber, which is also strong enough to withstand high pressure. Recording ΔT using a thermal couple is also very challenging because the thermal couple usually breaks at high pressure. Overall, the most common approach for BC effects is the direct measurement of ΔS using calorimetry while applying and removing pressure.

Quasi-direct method

The quasi-direct method relies on $\Delta S(T, 0 \rightarrow E) = S'(T, E) - S'(T, 0)$ for EC effects or $\Delta S(T, 0 \rightarrow p) = S'(T, p) - S'(T, 0)$. This method is used for both EC and BC effects in Chapter 4, Chapter 5 and Chapter 6. Quasi-direct method is also frequent in magnetocaloric¹⁴¹ and other barocaloric¹²¹ studies. Experimentally, this involves heat flow measurements under the isofield conditions. The reason this method is called ‘quasi-direct’ is that it directly evaluate the thermal response ΔS not the order parameter but using a subtraction approach. In contrast, the direct method measures ΔS or ΔS directly driven by the field E or p . An example of quasi-direct measurements for EC effects in 1,4-diazabicyclo[2.2.2]octane perhenate is shown in Fig.3-17.

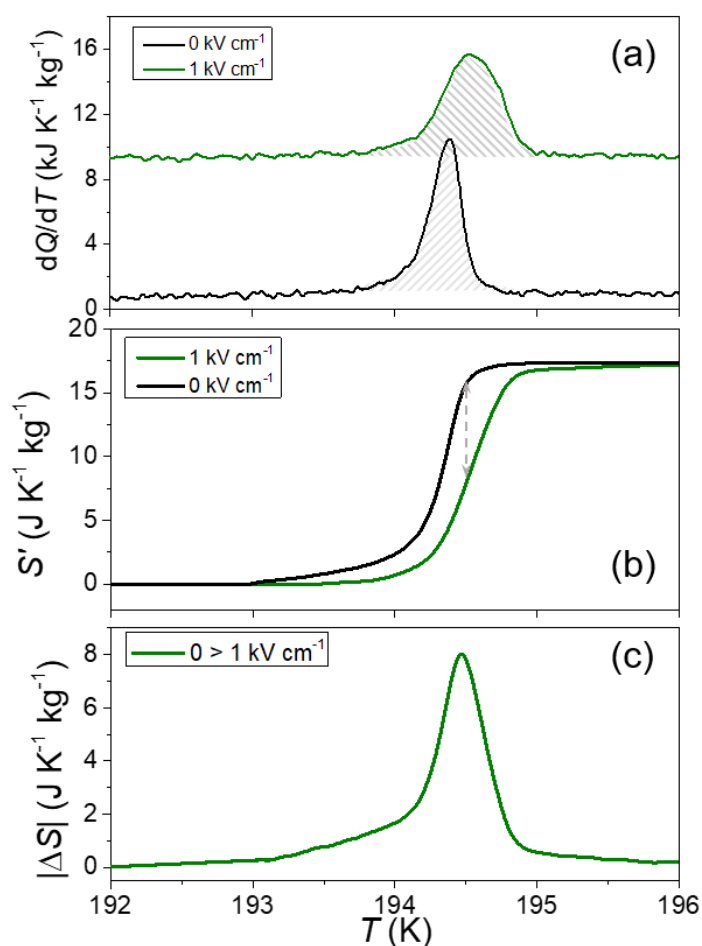


Figure 3-17. The process of quasi-direct measurements for EC effects based on calorimetric measurements. **(a)** plot of dQ/dT as a function of T , under zero-field and under $E = 1 \text{ kV cm}^{-1}$, yielding the entropy changes $S'(T, E=1 \text{ kV cm}^{-1})$ and $S'(T, E=0)$. **(b)** subtraction of entropy yields $S'(T, E=1 \text{ kV cm}^{-1}) - S'(T, E=0) = \Delta S(T, 0 \rightarrow E)$ **(c)** isothermal entropy change $|\Delta S|$ for $0 \rightarrow E$ deduced from step (b). Data taken from a 1,4-diazabicyclo[2.2.2]octane perhenate sample.

3.8 Landau theory for ferroelectrics

In the present work, I describe the models based on Landau-Devonshire (LD) theory¹⁴² that I built to predict EC effects. Computations were performed using Wolfram Mathematica version 11.3 and the codes are attached in the Appendix. The Landau theory of phase transitions was first applied to the field of superconducting materials, and then extended to ferroelectrics by Devonshire¹⁴³.

In this work of the LD models, the materials are assumed in bulk form with uniform spatial polarization and no surface boundaries. In essence, LD theory mathematically expresses the free energy landscape of a system $F(E, P)$ using its order parameter, which is polarization P in the case of ferroelectrics. Assuming the P is sufficiently small, which is valid near phase transitions, then the free energy F can be expressed using a Taylor expansion.

$$F = F_0 + \frac{1}{2} a(T-T_0) P^2 + \frac{1}{4} b P^4 + \frac{1}{6} c P^6 - E P \quad (3.18)$$

Where a , b , and c are material-specific Landau coefficients, T_0 is a temperature near or equal to two-phase equilibrium temperature T_C . Materials that show $a = a_0(T - T_0)$ satisfy the Curie-Weiss law, where T_0 is a temperature near or equal to T_C . Parameter c is always positive to ensure divergence of F towards at large $|P|$. Negative values of b correspond to first-order phase transitions, and positive values of b correspond to second-order phase transitions. The energy plot and order parameter plot are compared in Fig.3-18 for first-order and second-order phase transitions. All coefficients are derived from experimental data. The power series are truncated at the 6th term for the ease of calculation. Odd-power terms in P do not appear for symmetry reasons.

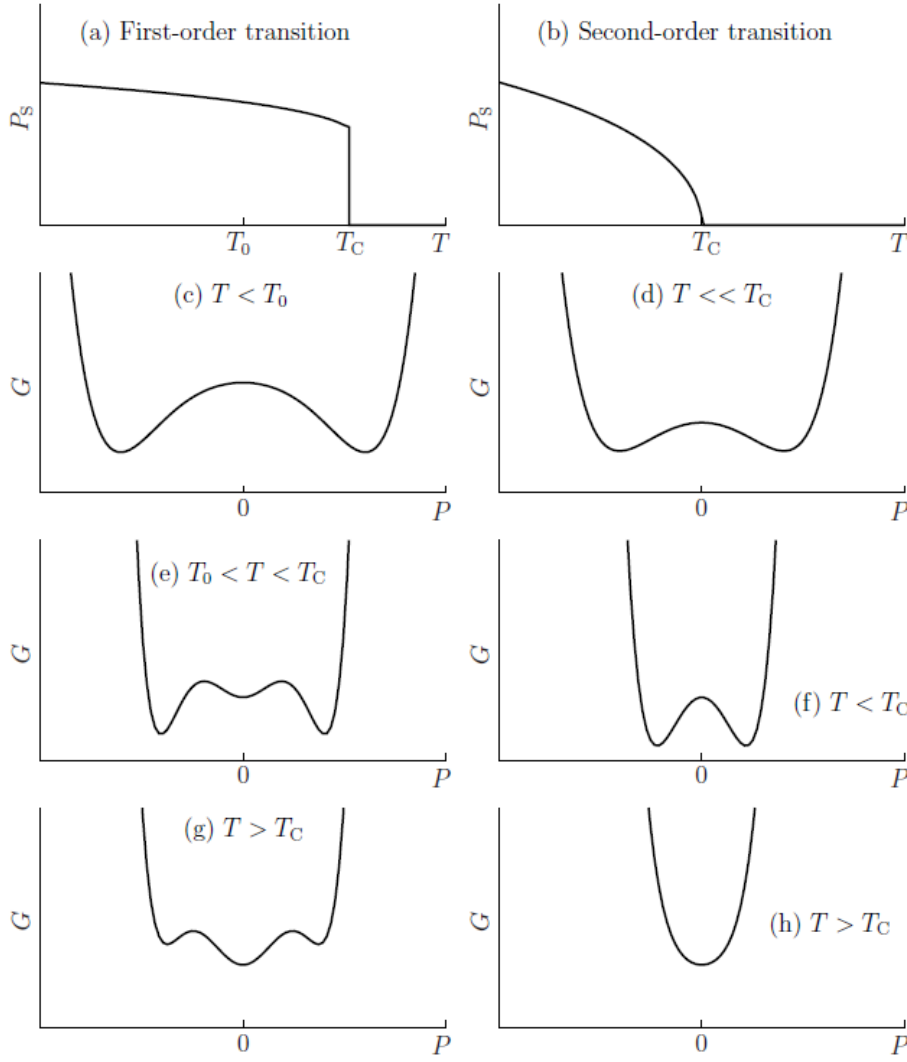


Figure 3-18. (a)(b) The plot of spontaneous polarization P_s as a function of temperature T for first-order and second-order phase transitions, respectively. (c)(e)(g) The evolution of G against order parameter P at different T for first-order transitions. Similarly (d)(f)(h) correspond to second-order transitions. This figure is adopted from a PhD thesis¹⁴⁰.

Model construction

In the model above, four coefficients, namely a , b , c and T_0 are to be derived. The order parameter P is zero above the critical temperature, indicating that the system is disordered in the high-symmetry phase. P is finite below the critical temperature, indicating that the system is ordered in a low-symmetry phase. Therefore, F can be expressed as below:

$$F = \begin{cases} F_0 & T > T_C \\ F_0 + \frac{1}{2} a(T-T_0) P^2 + \frac{1}{4} b P^4 + \frac{1}{6} c P^6 - E P & T < T_C \end{cases} \quad (3.19)$$

At the phase transition temperature T_C , the ferroelectric phase and paraelectric phase have the same free energy, $\Delta F = 0$ at T_C . This leads to $\Delta F = \frac{1}{2} a(T-T_0) P^2 + \frac{1}{4} b P^4 + \frac{1}{6} c P^6 = 0$ at T_C and $E = 0$.

At a given temperature, the equilibrium configuration of the system is determined by finding the minima of F , via $\partial F/\partial P = 0$.

$$\partial F/\partial P = a(T-T_0) P + b P^3 + c P^5 - E \quad (3.20)$$

This yield $P(T, E)$.

Then setting $E = 0$ to find the equilibrium configuration, polarization P here is actually spontaneous polarization P_s . The analytical solution of P_s is derived as

$$\begin{aligned} P_s &= 0 & T > T^* \\ P_s &= 0, \pm \sqrt{\frac{-b + \sqrt{b^2 - 4ac(T-T_0)}}{2c}} & T^* > T > T_0 \\ P_s &= \pm \sqrt{\frac{-b + \sqrt{b^2 - 4ac(T-T_0)}}{2c}} & T < T_0 \end{aligned} \quad (3.21)$$

Where T_0 was the coefficient obtained from the model fitting, T^* is the superheating temperature, beyond which P_s turns to zero.

Entropy can be calculated as $S = \partial F/\partial T$. The entropy change $\Delta S_0 = \frac{1}{2} aP$, where P is the spontaneous polarization P_s of the ferroelectric phase at T_C when $E = 0$.

$$\partial F/\partial T = S = \begin{cases} S_0 & T > T_C \\ S_0 - \frac{1}{2} a P^2 & T < T_C \end{cases} \quad (3.22)$$

LD models also predict material properties such as dielectric constant and specific heat capacity. When E is finite, $\partial P/\partial E$ yields the susceptibility χ , which can be experimentally measured from the dielectric constant as described in Section 3.2. Susceptibility $\varepsilon_0 \chi = \partial P/\partial E$ in combination with Eq. 3.20 yields:

$$\begin{aligned}\varepsilon' = \chi + 1 &= 1 + \frac{1}{\varepsilon_0 a (T - T_0)} & T > T_C \\ \varepsilon' = \chi + 1 &= 1 + \frac{1}{\varepsilon_0 [a(T - T_0) + 3bP^2 + 5cP^4]} & T < T_C\end{aligned}\quad (3.23)$$

At the paraelectric phase, there is a linear relation between coefficient a and dielectric constant ε' . This can be used to determine coefficient a from dielectric measurements.

We now calculate the specific heat capacity $c_p = T(\partial S/\partial T)$

$$c_p = \begin{cases} c_p^0 & T > T_C \\ c_p^0 + \frac{a^2 T}{\sqrt{b^2 - 4ac(T - T_0)}} & T < T_C \end{cases} \quad (3.24)$$

where $c_p^0 = T(\partial S^0/\partial T)$ is a reference heat capacity in the high-temperature phase.

Based the equations above, multiple equations can be built using the experimental data as input to yield model coefficients. Sometimes LD models will be expanded to 8th order for better fitting for materials in which the free energy surface requires more terms to fit. Then the functions may not have analytical solutions, but the principle should still hold.

The main advantage of LD modelling is that it provides a prediction of EC effects using data that are easy to find in the literature, or measured in the lab, e.g. dielectric measurements and polarization against temperature, $P(T)$. This helps identify candidate materials for large EC effects before performing time-consuming EC measurements. This is especially useful when studying organic ferroelectric materials, which tend to be leaky and therefore tend to fail under long EC experiments. However, LD models are only valid when several assumptions are satisfied. Firstly, the temperature should be close to T_C . Secondly, the material should be homogenous, i.e. an ideal monodomain crystal. For thin films^{144,145} and ceramics¹⁴⁶, modified free energy considering the effects of strain, surface and size was proposed. Thirdly, the coefficients b and c are assumed to be independent of T and E in the present work, which may not be true practically. In this case, modifications have been proposed for the temperature-dependency into b and c ^{147,148}. Lastly, LD models are not capable of revealing any microscopic mechanism so experimental investigations are still necessary for mechanistic insight.

4. Electrocaloric effects in Dabco-based ferroelectric materials

4.1 Overview

Motivation

Solid-state refrigeration based on caloric effects has been intensively studied as the eco-friendly and effective alternative to the traditional vapour-compression systems. Electrocaloric (EC) effects are particularly interesting in the field of chip-scale cooling applications¹⁴⁹ because of the easy employment of electric fields in electronics.

In the past, EC effects were mainly investigated in inorganic oxides e.g. BaTiO₃⁵⁸ and PZT⁶¹ but they tend to show small entropy changes. To increase the EC effects, thin films were fabricated to withstand a higher electric field. However, the resulting EC strength is low. For higher cooling performance, the organic polymers e.g. P(VDF-TrFE-CFE)⁸¹ with order-disorder phase transition were attempted for EC cooling. Still, the limitation is that P(VDF-TrFE-CFE) only generates considerable entropy change when under huge electric fields, $|\Delta E| = 2090 \text{ kV cm}^{-1}$. Recently, composite materials that consist of polymers and oxides were developed to combine the advantages of those individual components. However, the EC strength still falls behind the new molecular ferroelectric materials, causing difficulties for practical applications.

Here we present organic ferroelectric materials with high EC strength, [Hdabco][BF₄] (dabco = 1,4-diazabicyclo[2.2.2]octane, BF₄ = tetrafluoroborate) and [AH][ReO₄] (AH = 1-azabicyclo[2.2.1]heptanium, ReO₄ = perrhenate). For convenience, [Hdabco][BF₄] is referred as BF₄ while [AH][ReO₄] is referred as AH. They tend to show relatively large $|\Delta S|$ using small $|\Delta E|$. The resulting EC strength $|\Delta S|/|\Delta E|$ of BF₄ is five times higher than BaTiO₃, forty-five times higher than P(VDF-TrFE-CFE) and ten times higher than P(VDF-TrFE-CFE)/PMN-PT composite. Among the molecular ferroelectric materials, materials presented in this work show the highest EC strength. This comparison does not include the computational results of [MDABCO](NH₄I₃) as this material may not show reversible phase transitions, and the failed attempts on experimentally measuring EC effects of [MDABCO](NH₄I₃) are in Appendix.

Apart from high EC strength, molecular ferroelectric materials add advantages of easy and environment-friendly processing, light weight, and low fabrication temperature. Notably, [AH][ReO₄] exhibits mechanical flexibility and can be processed into bulk polycrystalline forms with desired geometry. All the above properties make molecular ferroelectric materials more useful for industrial applications.

The main challenge in studying those materials was the electrical and mechanical breakdown. In fact, multiple compositions such as [Hdabco][ClO₄]⁹⁵ and [Hdabco][ReO₄]⁹⁶ were attempted for EC measurements. Dozens of crystals in multiple batches were fabricated. However, very few crystals were found sufficiently insulating for studying EC effects. Selected crystals were then subject to polishing for the standard geometry, i.e. parallel capacitors. Many samples failed in this stage because they were mechanically brittle. Pressed powder pellets were also found to be highly conductive. Eventually, only one BF₄ crystal and some AH pellets from our Japanese collaborators survived for the full EC characterizations.

Table 4-1. EC properties of selected ferroelectric materials. The units are shown as following: T (K), $|\Delta S|$ (J K⁻¹ kg⁻¹); $|\Delta T|$ (K), $|\Delta E|$ (kV cm⁻¹), $|\Delta S|/|\Delta E|$ (10⁻² J cm K⁻¹ kg⁻¹ kV⁻¹) and $|\Delta T|/|\Delta E|$ (10⁻² K cm kV⁻¹).

Molecular ferroelectric material	T	$ \Delta S $	$ \Delta T $	$ \Delta E $	$ \Delta S / \Delta E $	$ \Delta T / \Delta E $	Ref.
Oxide							
BaTiO ₃ (single crystal)	402	2.1	0.9	12	17.5	7.5	[⁵⁸]
0.70PMN-0.30PT(ceramic)	429	2.3	2.7	90	2.6	3	[⁶⁸]
BST ^[9] (ceramic)	303	1.3	0.83	40	3.3	2.1	[⁷³]
BZT ^[10] (ceramic)	410	/	1.2	30	/	4	[⁹³]
Polymer							
P(VDF-TrFE)	353	60	12	2090	2.9	0.6	[⁸¹]
P(VDF-TrFE-CFE)	328	65	12.5	3070	2.1	0.4	[⁸¹]
Composites							
P(VDF-TrFE-CFE)/PMN-PT	303	150	25	1800	8.3	1.7	[⁸⁸]
P(VDF-TrFE-CFE)/BST	300	210	50.5	2500	8.4	2	[⁸⁹]
Molecular ferroelectric							
(C ₅ H ₁₄ N) ₂ CsPb ₂ Br ₇	345	4.1	2	13	31.5	15.4	[¹⁰¹]
ImClO ₄	373	5.4	1.26	15	36.0	8.4	[¹⁰²]
[MDABCO](NH ₄ I ₃)	448	36	16	20	180.0	80.0	[¹⁰⁰]
This work							
BF ₄	376	11.5	0.48	12	97.46	0.49	/
AH	325	7.5	1	11.2	66.96	1.49	/

^[9]BST: Ba_{0.65}Sr_{0.35}TiO₃

^[10]BZT: Ba(Zr_{0.2}Ti_{0.8})O₃

4.2 Electrocaloric effects in 1,4-diazabicyclo[2.2.2]octane tetrafluoroborate

4.2.1. Experiments

Material synthesis

Growth of [Hdabco][BF₄] crystals was performed by me via the slow-evaporation method as discussed in the Methodology Chapter. The precursor materials 1,4-diazabicyclo[2.2.2]octane (Dabco) and tetrafluoroboric acid solution (HBF₄, 48 wt. % in H₂O) were purchased from Sigma-Aldrich. Water was obtained from a Millipore Simpak 2 water purification system. All materials were used as received.

The HBF₄ (2 ml, 15.3 mmol) and Dabco (1.71 g, 15.3 mmol) were mixed in water (8 ml) at a 1:1 mole ratio. The mixed aqueous solution is placed in a glass jar covered by a piece of Parafilm with slits, which let the water evaporate at room temperature. The water evaporation is designed to be slow to yield single crystals and avoid defects during the crystal precipitation. Defects degrade the EC performance as they lead to unwanted Joule heat when the electric field is applied. In addition, single crystals generally have higher polarization and thus possibly larger EC effects. As shown in Fig. 4-1, multiple colourless rod-like or plate-like crystals are obtained. Among those, single crystals can be selected for further study.

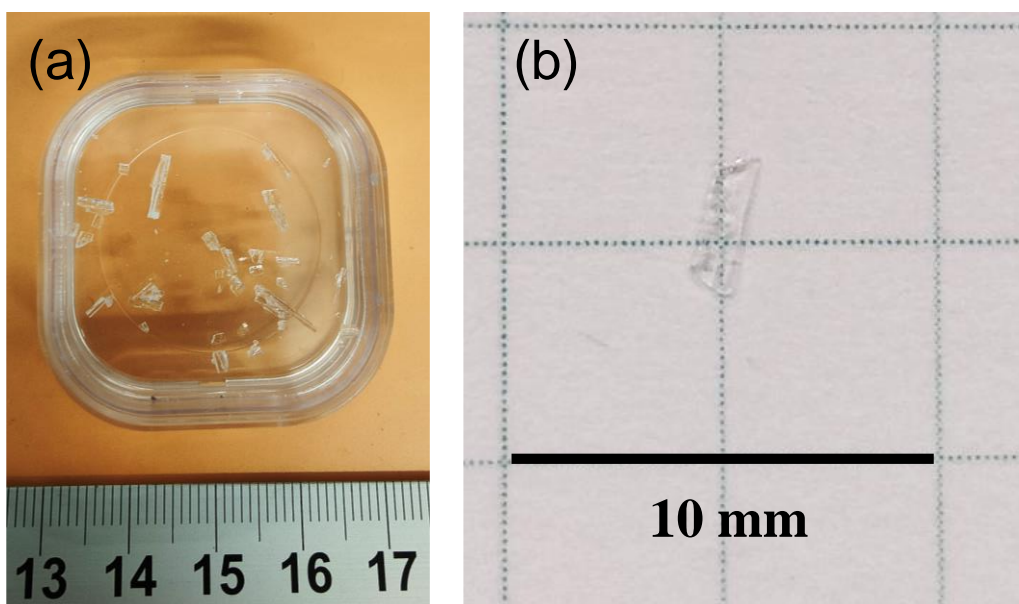


Figure 4-1. (a) The transparent crystals of [Hdabco][BF₄] grown from the aqueous solution. (b) the selected crystal for further EC measurements.

However, preparing defect-free single crystals is extremely challenging. Impurities and voids can easily form during the evaporation process. These can degrade the EC performance as discussed later. Ideally, a mirror-like smooth surface can be observed for a good single crystal. As shown in Fig. 4-2, our crystals are not in optimal quality. To fabricate large and defect-free single crystals, more advanced techniques^{150–153} for controlling the crystal nucleation and growth process can be attempted in the future.

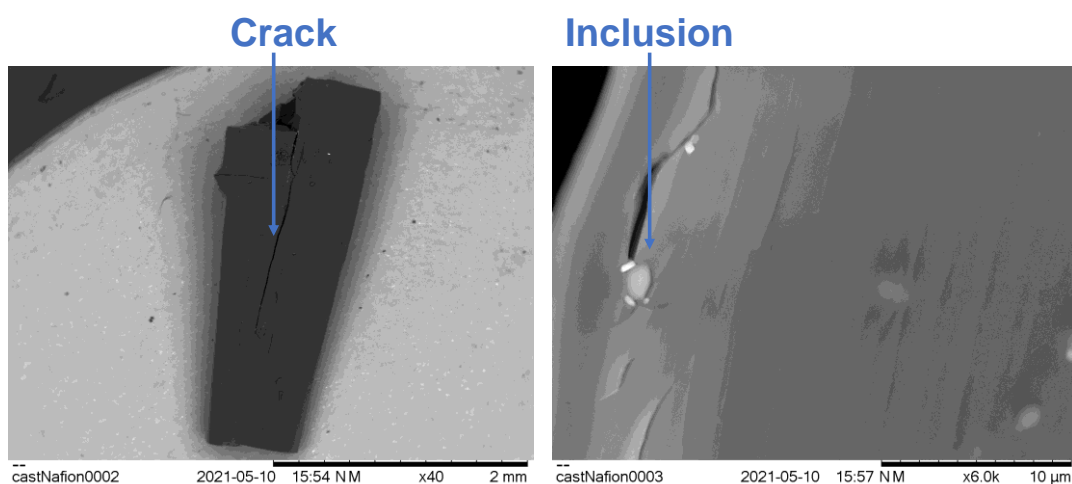


Figure 4-2. SEM pictures on BF₄ crystals show the defects of crack and inclusion.

X-ray Diffraction

To confirm the correct chemical composition, BF₄ crystals are ground into powders and measured with X-ray diffraction. The measured diffraction pattern shown in Fig. 4-3, is compared with that from the database. Good matches in the diffraction peaks indicate the correct chemical composition and no secondary crystalline phases.

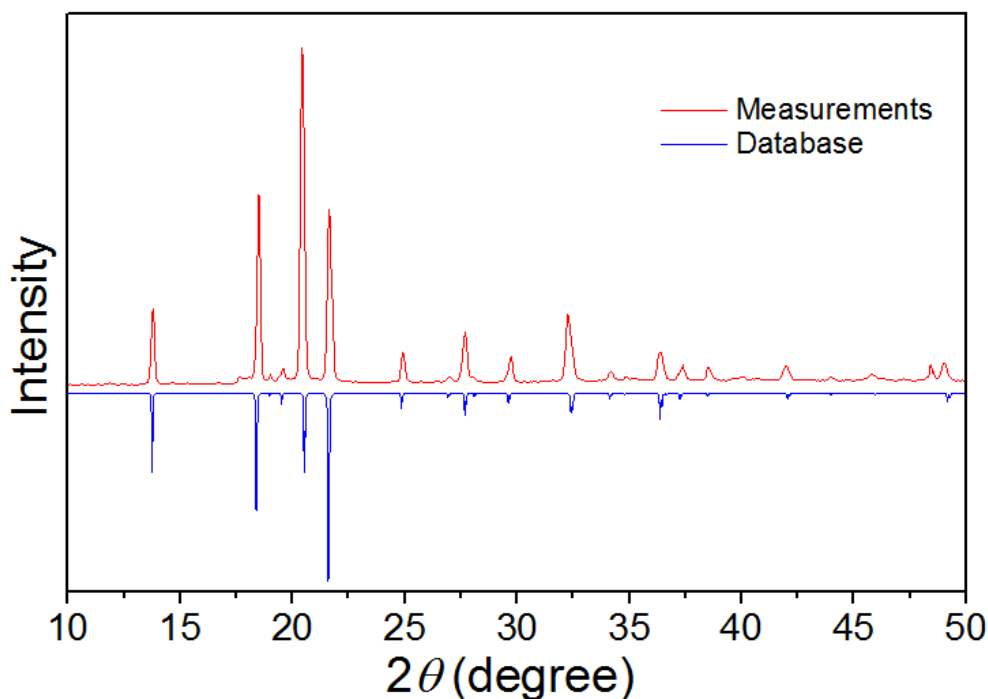


Figure 4-3. Comparison of the simulated XRD pattern from database and the experimentally measured one of the [Hdabco][BF₄] powder sample at room temperature.

Based on the temperature-dependent X-ray diffraction data from literature⁹⁵, BF₄ exhibits orthorhombic structure below $T_C = 377$ K and tetragonal structure above T_C . This is shown in Table 4-2. As shown in Fig. 4-4 right, all [Dabco]⁺ cations are displaced along [010] of the orthorhombic unit cell by δ with respect to the [ClO₄]⁻ anions. The spontaneous polarization in BF₄ arises from that.

Table 4-2. Summary of properties of BF₄ for different phases. The information was taken from ref⁹⁵.

Temperature	290 K – 377 K	> 377 K
Ferroelectricity	Ferroelectric	Paraelectric
Crystal structure	Orthorhombic	Tetragonal

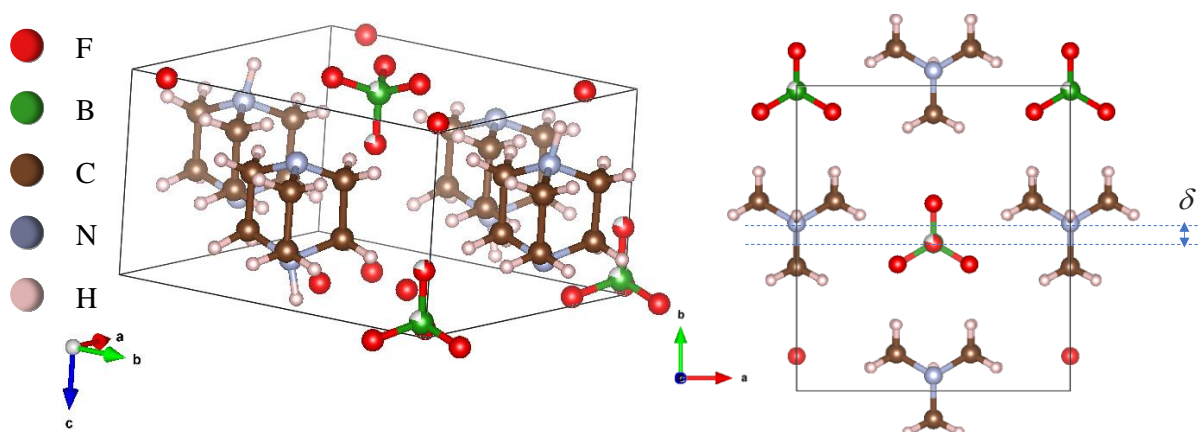


Figure 4-4. **Left:** The atomic structure of the [Hdabco][BF₄] crystals at room temperature simulated from the diffraction pattern. **Right:** All [Dabco]⁺ cations are displaced along [010] by δ with respect to the [BF₄]⁻ anions.

Calorimetry measurements under zero field

The differential scanning calorimetry (DSC) Q2000 from TA Instruments was used to perform heat flow measurements on BF₄ crystals of mass ~ 12.364 mg at ± 5 K min⁻¹. BF₄ undergoes a reversible phase transition at 375 K on cooling and 380 K on heating, with a hysteresis of ~ 5 K as shown in Fig. 4-5. The latent heat is $|Q_0| \sim 21$ J g⁻¹ and the zero-field entropy change $|\Delta S_0|$ is ~ 58 J K⁻¹ kg⁻¹ (Fig.4-5 bottom panel). Those observations are in good agreement with the data of Katrusiak, A. and Szafranski, M⁹⁵, with corresponding $|Q_0| \sim 22$ J g⁻¹ and $|\Delta S_0| \sim 58$ J K⁻¹ kg⁻¹. The value of $|\Delta S_0|$ is one order of magnitude higher than most traditional ferroelectric oxides such as BaTiO₃ and PbTiO₃. This indicates much larger EC effects in BF₄.

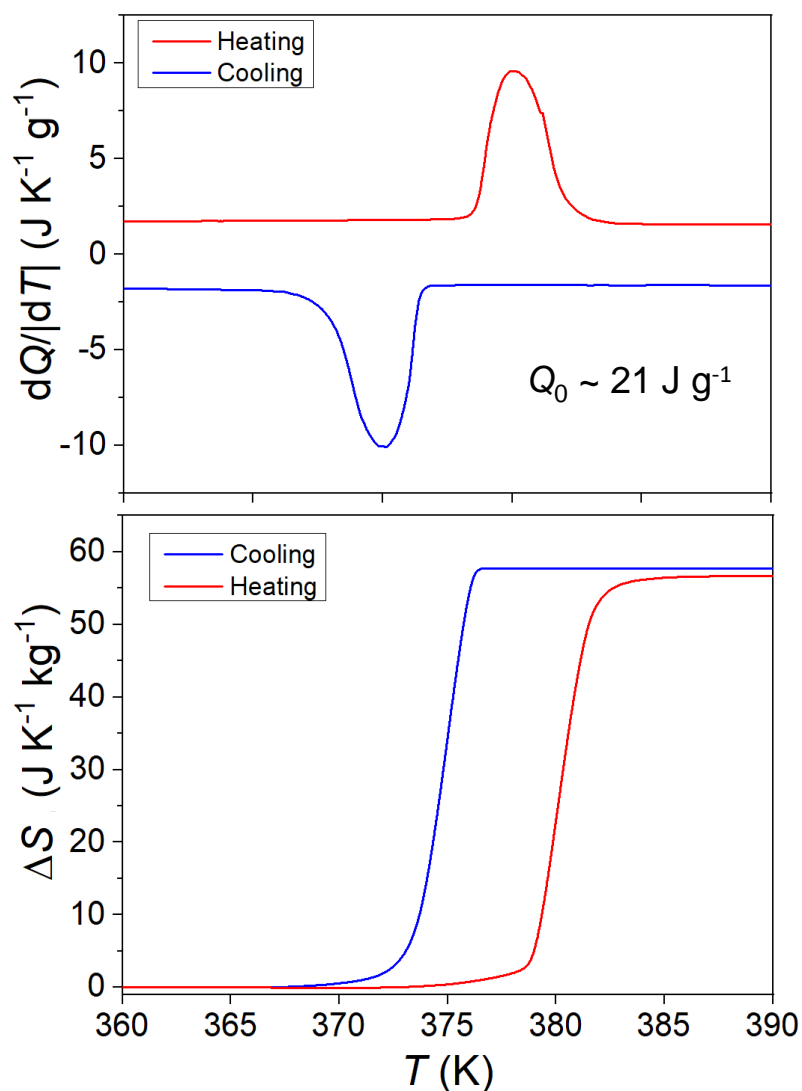


Figure 4-5. Top: Heat flow measurements for BF₄ crystals. $dQ/dT > 0$ means endothermic. **Bottom:** The values ΔS with respect to 360 K, which is derived from the integration of $(dQ/dT)/T$ over T .

Specific heat capacity measurements

The procedure of experimental measurements of $c_p(T)$ is described in Methodology. The specific heat capacity $c_p(T)$ under zero-field is displayed in Fig. 4-6. At the phase transition, c_p increases sharply and the peak value of $c_p = 9.1 \text{ J K}^{-1} \text{ g}^{-1}$ at 380 K. In the following section of calculating EC effects of [Hdabco][BF₄], $c_p(T)$ is used to determine the adiabatic temperature change ΔT via $-c_p \Delta T \approx T_C \Delta S = Q_0$.

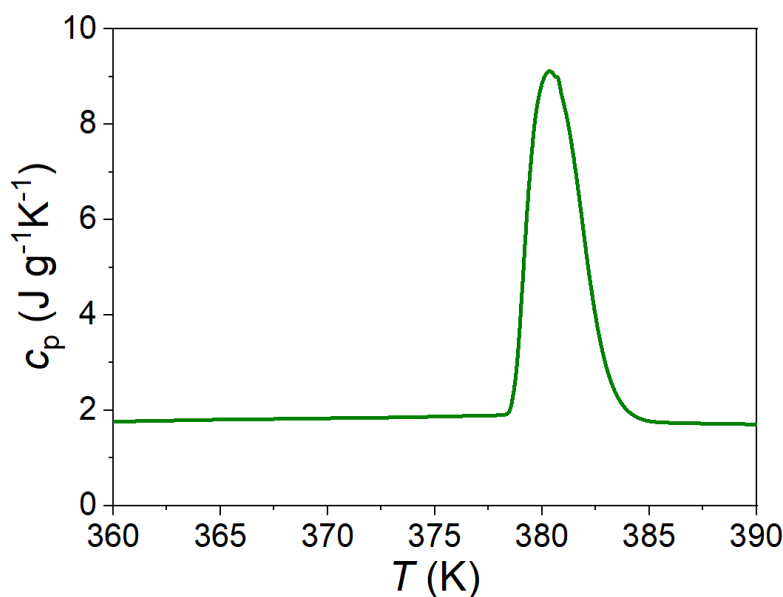


Figure 4-6. Specific heat capacity c_p of [Hdabco][BF₄] measured from calorimetry on heating.

Dielectric measurements

Dielectric measurements were performed in the frequency range $10^3 \text{ Hz} - 10^6 \text{ Hz}$ with an applied AC-voltage of 500 mV. The temperature dependence of the dielectric constant ϵ' was studied between 300 K and 430 K with heating and cooling rates of 1 K min^{-1} , yielding 1119 values with a temperature interval of $\sim 0.12 \text{ K}$.

To make disk-shape parallel capacitors for dielectric measurements, a crystal $\sim 250 \mu\text{m}$ thick and 2.42 mm^2 area was selected for measurements. Gold $\sim 40 \text{ nm}$ thick was sputtered on both sides of the crystal as electrodes. The sample configuration is shown in Fig. 4-7. According to the literature⁹⁵, single crystal [Hdabco][BF₄] exhibits plate shape with shortest dimension along [010] and longest along [001]. Therefore, the electrodes are applied such that the electric field is along [010] direction, which is the polarization orientation shown in the atomic structure in Fig. 4-4.

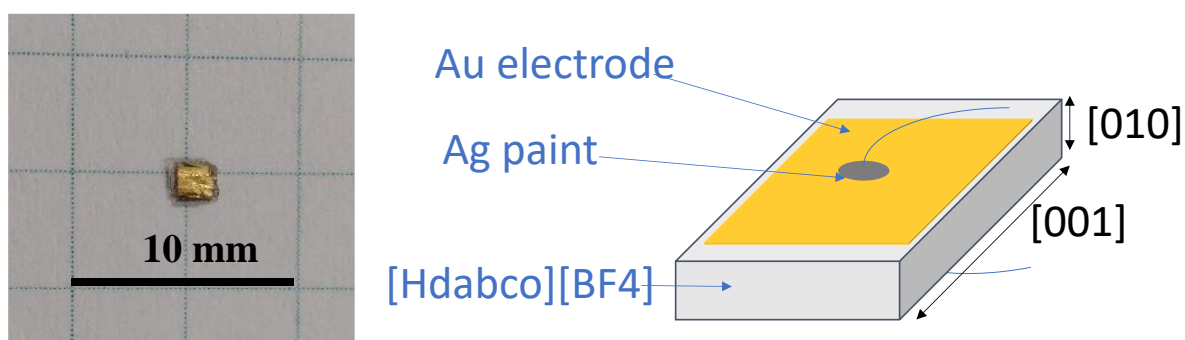


Figure 4-7. **Left:** the sample fabricated as a parallel capacitor, with gold sputter on both sides. Two sides of electrodes are not in contact to avoid conduction. **Right:** the schematic showing the sample configuration. According to the literature, single crystal $[\text{Hdabco}][\text{BF}_4]$ exhibits plate shape with shortest dimension along $[010]$ and longest along $[001]$ ⁹⁵.

The dielectric constant ϵ' and loss tangent $\tan(\delta)$ as a function of temperature at various frequencies for the $[010]$ -oriented BF_4 single crystal are shown in Fig. 4-8. In the spectrum of dielectric constant ϵ' , a sharp change was observed at 378 K for the ferroelectric-paraelectric phase transition, which is in good agreement with the transition detected from calorimetry (at 379 K, shown in Fig 4-5). The value of ϵ' at the lower-temperature phase shows little frequency-dependence while at the higher-temperature phase, the value of ϵ' changes with frequency. To compare with literature data, the value of $\epsilon' \sim 25$ at the lower-temperature phase was higher than the corresponding value of ~ 10 from Katrusiak, A. and Szafranski, M⁹⁵. At the higher temperature phase, the value of $\epsilon' \sim 55$ at 10^6 Hz is much closer to the corresponding value ~ 42 ¹⁵⁴ at 10^7 Hz. The discrepancy is likely due to the extra capacitance picked from the measurement circuit. The noise level (~ 2 pF) is very close to the capacitance from the sample at the lower-temperature phase. That explains why the discrepancy decreases at the higher-temperature phase where the capacitance signal is much higher. Ideally, a more significant signal-to-noise ratio can be obtained by using a thinner and bigger sample in shape like a piece of paper. However, no such crystal was obtained. Dielectric losses are ~ 0.01 below the transition, rising to ~ 0.3 above T_C .

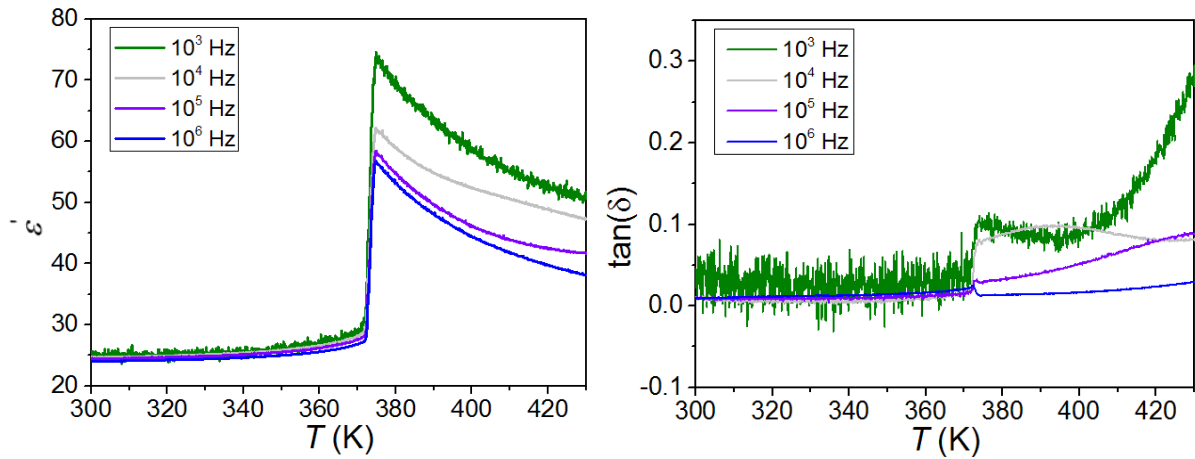


Figure 4-8. Left: Dielectric constant $\epsilon'(T)$ at different frequencies on heating at the rate of 1 K min^{-1} . Right: loss tangent $\tan(\delta)$ as function of T .

For normal ferroelectrics, the Curie–Weiss law can fit the dielectric constant at a temperature higher than the Curie temperature. The Curie-Weiss constant above T_C was $\sim 5484 \text{ K}$, based on the linear fitting of $[1/(\epsilon' - 1)]$ against T (Figure 4-9) where the slope is $1/C$. The value Curie-Weiss constant is used as an input parameter for the Landau modelling discussed later.

$$\epsilon' - 1 = \frac{C}{T - T_C} \quad (3.1)^{54}$$

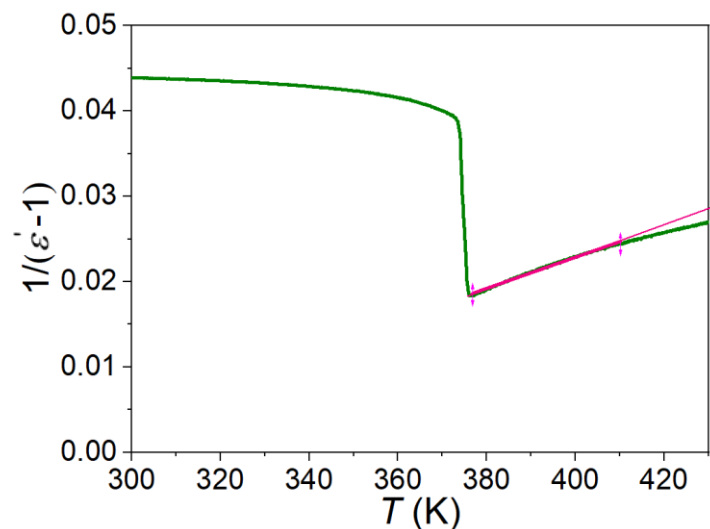


Figure 4-9. Reciprocal of dielectric susceptibility as a function of temperature. The red line is the linear fitting.

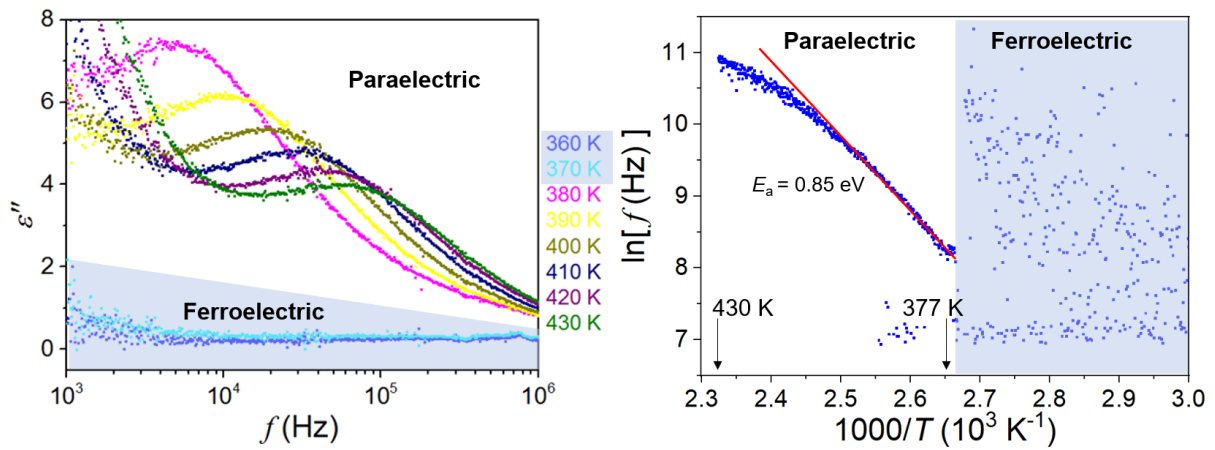


Figure 4-10. Left: the imaginary part of dielectric constant ϵ'' as function of frequency at different temperatures. Right: plots of $\ln f_0$ versus $1000/T$ for fitting the activation energy of the associated relaxation mechanism.

The imaginary part of the dielectric constant clearly exhibited distinct anomalies at frequencies ranging from 10^3 to 10^5 Hz. The relaxation frequency anomaly followed the Arrhenius equation $f = f_0 \exp(E_a/k_B T)$, where f_0 represents the characteristic macroscopic relaxation frequency and the relaxation time $\tau_0 = 1/f_0$, E_a is the activation energy or potential barrier required for dielectric relaxation, and k_B is the Boltzmann's constant. The relaxation peaks shown in Fig. 4-10 are shifted to higher frequencies on heating.

The value of E_a can be a characteristic of a certain relaxation mechanism. By checking literature, the reorientation of Dabco+ in the $[\text{Co}(\text{HPO}_3)_2][\text{H}_2\text{Dabco}]^{155}$ material has been observed with $E_a = 0.82 \text{ eV}$, which is close to our fitting result of 0.85 eV . This indicates Dabco+ can rotate at the paraelectric phase. No such relaxation was observed in the ferroelectric phase, suggesting Dabco+ is stationary at the ferroelectric phase.

Notably, one innovation here is that a dense $\epsilon''(T, f)$ dataset with 0.12 K temperature interval was subjected to the Arrhenius fitting. In some publications^{156,157}, fitting was performed with a few data points with 10-20 K temperature intervals. Our measurements include more datasets for fitting and thus are less prone to fitting errors. The Python 3.0 script for handling multiple $\epsilon''(T, f)$ files and finding relaxation peaks are included in Appendix. The 3D plot of dense $\epsilon''(T, f)$ and $\epsilon''(T, f)$ datasets are displayed in Fig.4-11.

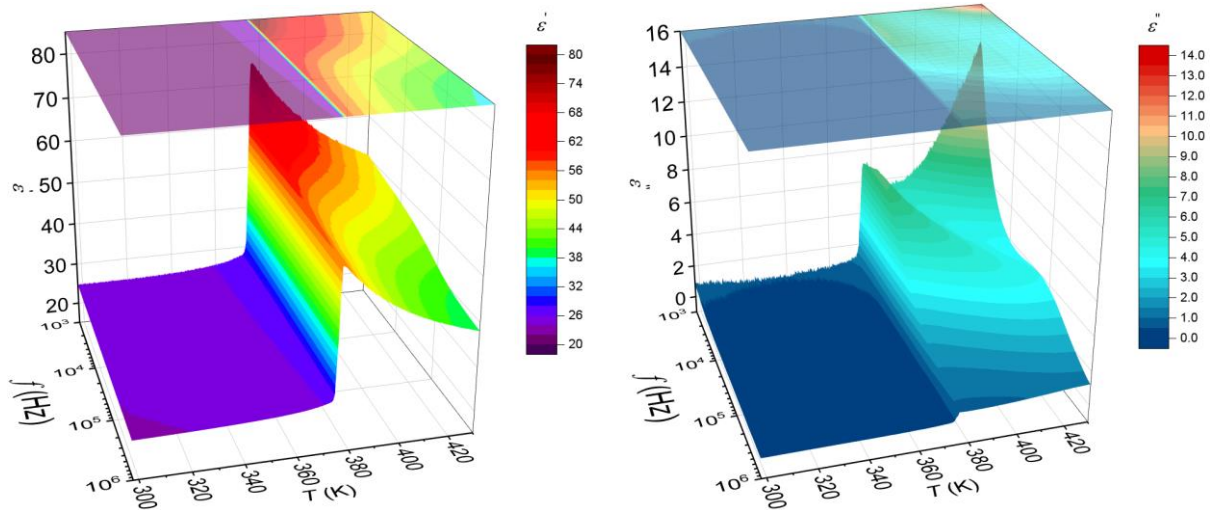


Figure 4-11. The $\epsilon'(T, f)$ and $\epsilon''(T, f)$ datasets. This plot gives dense data points of how dielectric constant changes with temperature and frequency. The phase transition at ~ 380 K is distinctive in both plots. $\epsilon'(T, f)$ was used for the fitting in Fig.4-10.

Ferroelectric polarization measurements

Fig. 4-12 shows the $P(E)$ at different temperatures measured from the crystal $\sim 250 \mu\text{m}$ thick and 2.42 mm^2 . The duration of the applied triangular voltage wave is 50 ms, corresponding to a frequency of 20 Hz. Fig. 4-12 shows the characteristic $P(E)$ loops before and after the ferroelectric-paraelectric phase transition. The fatty round shape $P(E)$ loops at paraelectric phase (377 K and 378 K) indicate a combination of conduction and dielectric behaviours. Due to conduction, the distorted P may cause inaccuracy in EC isothermal entropy change via $\Delta S(T, E) = \int (\partial P / \partial T)_E dE$.

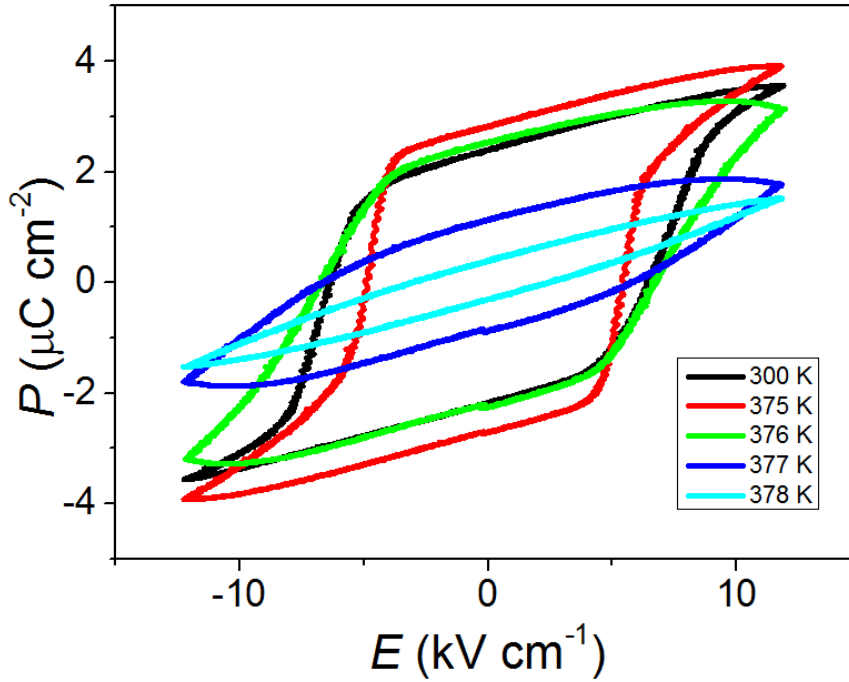


Figure 4-12. $P(E)$ loops measured at electric field magnitude of 12 kV cm^{-1} . The change in the shape of indicates the phase transition from the ferroelectric phase to paraelectric phase.

Ferroelectric polarization $P(E)$ was measured every 0.94 K at 106 values of increasing temperature T , with a heating rate of 2 K min^{-1} . Field-removal branches obtained ($0 \leq E \leq 12 \text{ kV cm}^{-1}$) were used to plot $P(T, E)$ phase diagram (Fig. 4-13). The red colour represents the ferroelectric phase, while the blue colour represents the paraelectric phase. Notably, the phase boundary does not shift with the applied electric field. This indicates that a larger electric field is required for driving the phase transition.

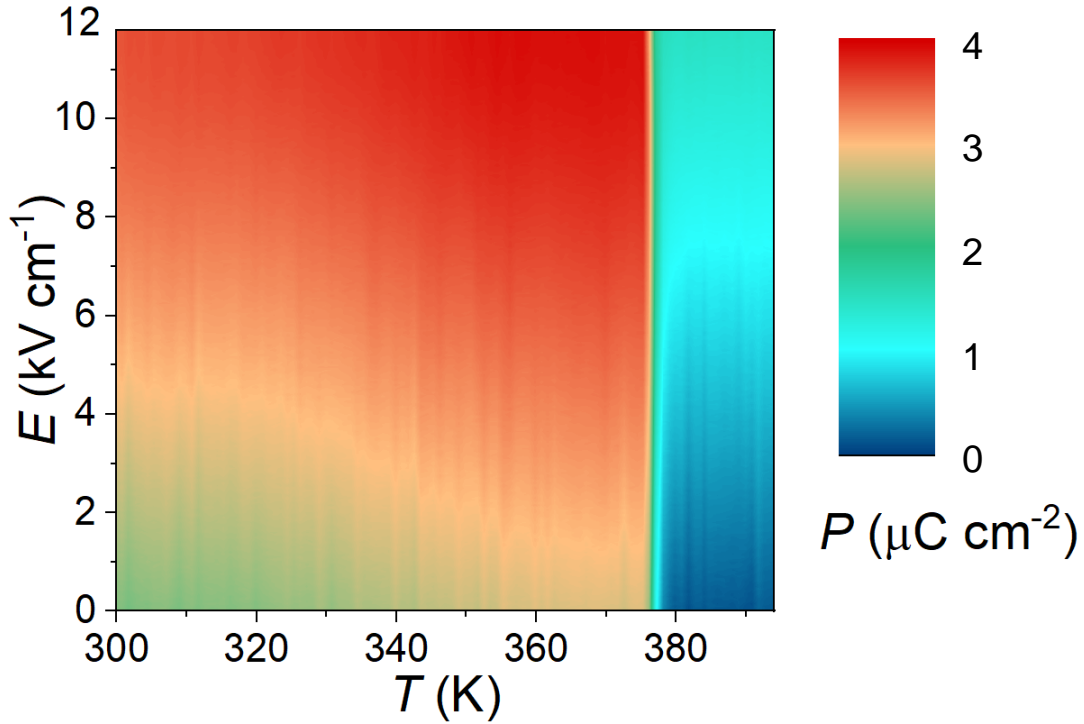


Figure 4-13. $P(E,T)$ obtained from upper ($E>0$) branches of approximately 106 $P(E)$ loops, some of which are shown in Fig.4-12.

Electrocaloric effects from standard indirect method

EC effects were evaluated using the well-known indirect method. The dense $P(T, E)$ data (Fig.4-13) were used to evaluate the isothermal entropy change $\Delta S(T, E) = \int (\partial P / \partial T)_E dE$ (Fig. 4-14 right) for field application ($0 \rightarrow E$) at temperature T , using the Maxwell relation $(\partial S / \partial E)_T = (\partial P / \partial T)_E$. The largest field used in the indirect measurements ($E = 12 \text{ kV cm}^{-1}$) yields a maximum entropy change of $\Delta S \sim -11.5 \text{ J K}^{-1} \text{ kg}^{-1}$ near 376 K, while the corresponding adiabatic temperature change is $\Delta T \sim 0.48 \text{ K}$ via $\Delta T \approx -T\Delta S / c_p$ using the specific heat capacity as a function of temperature $c_p(T)$, which is assumed unchanged under electric field. Density ρ of 1.496 g cm^{-3} was taken from Katrusiak, A¹⁵⁸. The plots of $\Delta S(T, E)$ and $\Delta T(T_s, E)$ are displayed in Fig. 4-15.

Following the method above, the $\Delta S \sim -11.5 \text{ J K}^{-1} \text{ kg}^{-1}$ in responding to $\Delta E = 12 \text{ kV cm}^{-1}$ is only $\sim 20\%$ of the ΔS_0 for the full phase transition measured from DSC at zero electric field. This indicates a higher electric field is required to fully transform from the paraelectric phase to the ferroelectric phase, or vice versa.

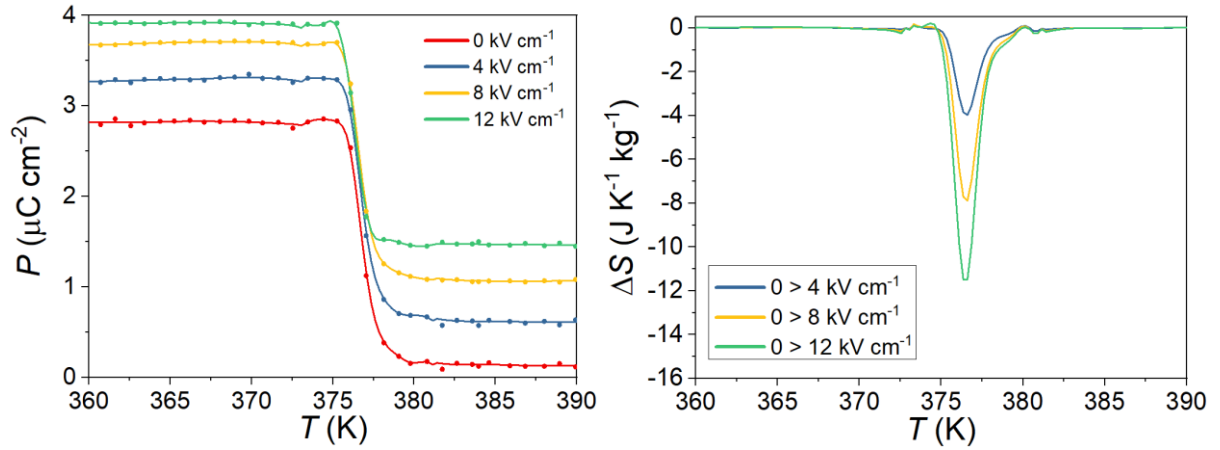


Figure 4-14. Left: Selected $P(T)$ derived from the $P(E)$ loops by extracting P at different T when E is fixed at 0, 4, 8 and 12 kV cm^{-1} respectively. The dots are raw data while the lines are smoothed fitting for the subsequent derivation and integration. Right: the resulting ΔS derived from the left panel.

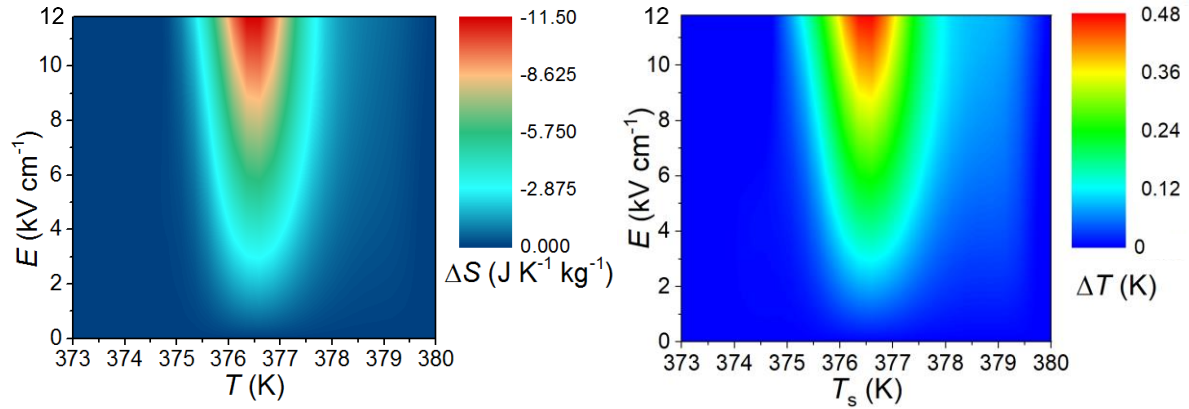


Figure 4-15. The contour plots of isothermal entropy change $\Delta S(E, T)$ and adiabatic $\Delta T(E, T_s)$ due to the application of field E . the slice of $\Delta S(E, T)$ is shown in Fig. 4-14.

The remaining question is the minimum ΔE required to achieve the full phase transformation. To estimate the electric field necessary for achieving full transition $\Delta S_0 = 58 \text{ J K}^{-1} \text{ kg}^{-1}$, the ΔS_{max} from $\int (\partial P / \partial T)_E dE$ is plotted as a function of ΔE . The data is derived from the contour plot of $\Delta S(T, E)$ in Fig. 4-16. Extrapolation indicates that $\Delta E \sim 60 \text{ kV cm}^{-1}$ will lead $|\Delta S| \sim 58 \text{ J K}^{-1} \text{ kg}^{-1}$. This is still two orders of magnitudes lower than the ΔE used in P(VDF-TrFE-CFE), suggesting that BF4 is a promising EC material.

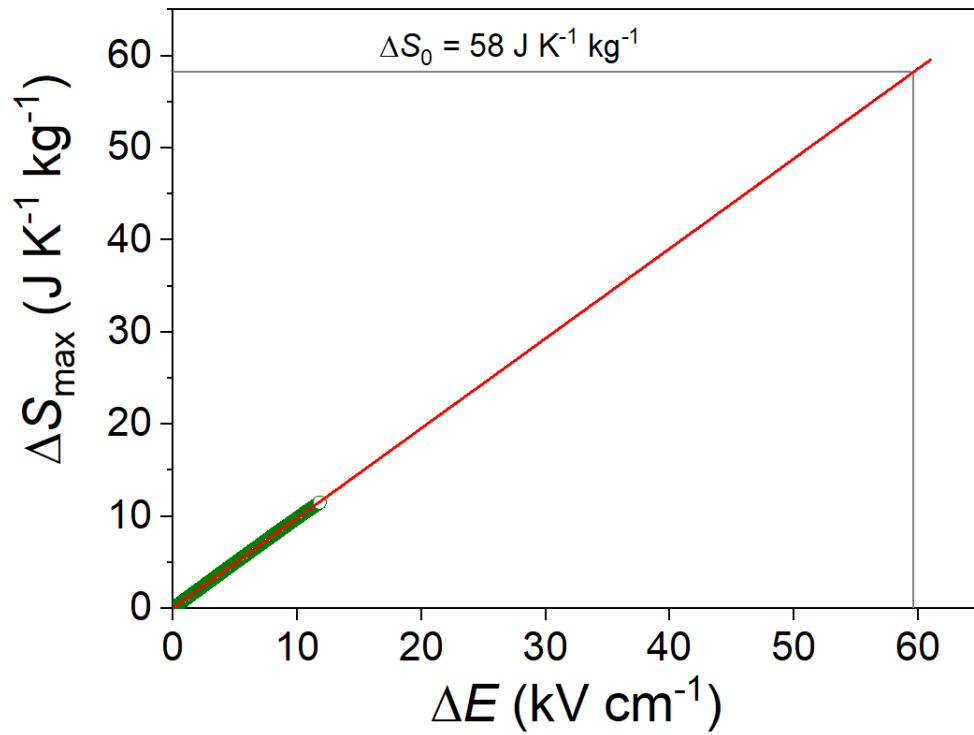


Figure 4-16. linear extrapolation of required ΔE for achieving $\Delta S_0 = 58 \text{ J K}^{-1} \text{ kg}^{-1}$. This assumes that ΔS_{\max} increases linearly with ΔE . The green dots are the data point selected from Fig. 4-15 left. The red line is the linear fitting.

Electrocaloric effects from modified indirect method

Modified ferroelectric measurements which are described in Chapter 3 were performed to subtract leakage. Extending the data processing to all $P(E)$ loops at different temperatures, both the corrected loops (black) and the raw loops (red) are shown in Fig. 4-17. The corrected loops appear slim. Especially at the paraelectric phase above 378 K, a linear dielectric shape is observed.

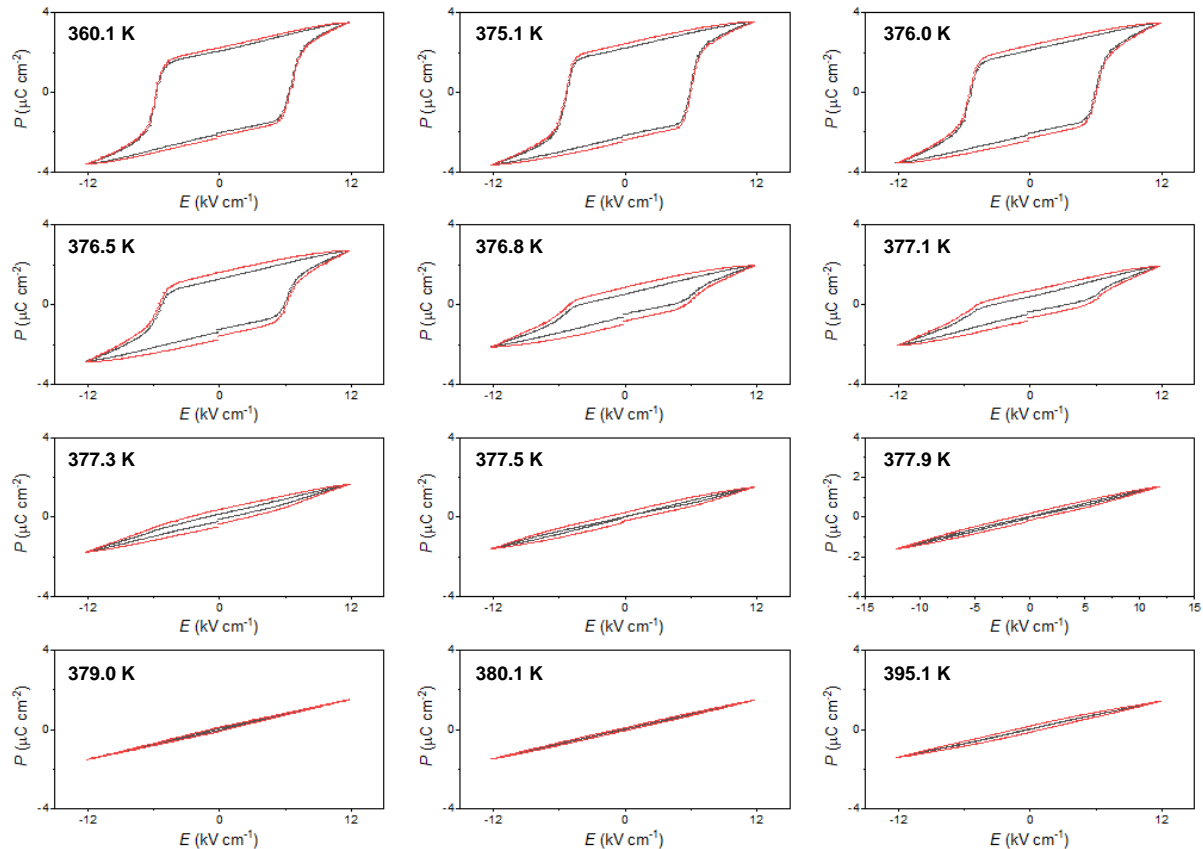


Figure 4-17. $P(E)$ loops at 20 Hz for BF4 at multiple temperatures across $T_C = 376$ K. Loops before (red) and after (black) leakage subtraction are shown.

To extract the resistance value of the leakage. The ΔP between the first peak maximum and the second one is plotted as function of temperature in Fig. 4-18 left. Accordingly, the resistivity is derived in Fig. 4-18 right. The resistivity is $\sim 5 \times 10^6 \Omega \text{ m}$ and peaks to $\sim 13 \times 10^6 \Omega \text{ m}$ at the phase transition.

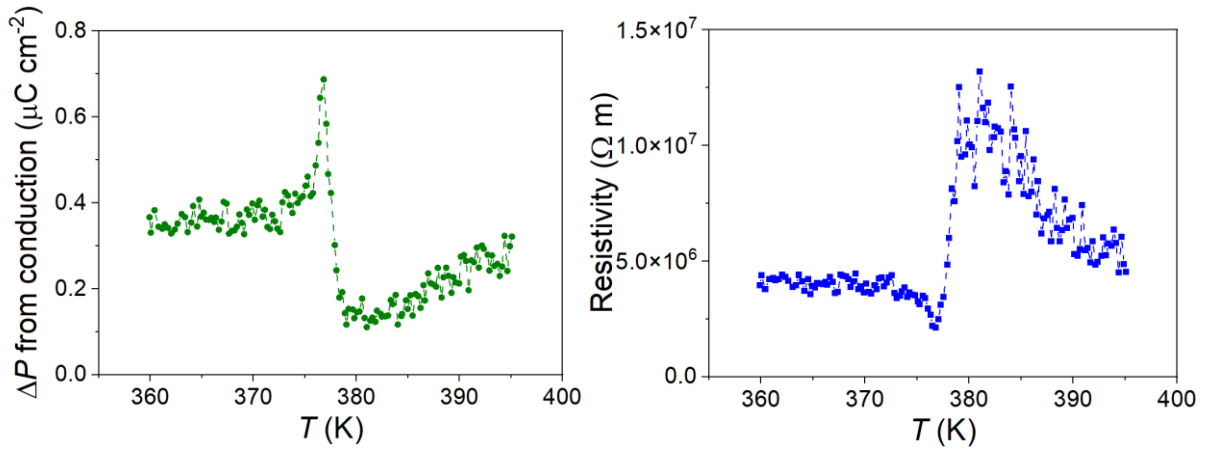


Figure 4-18. Left: The value of ΔP from leakage as function of temperature. The method of calculating ΔP in each $P(E)$ loop is explained in Fig.3-5(c). Right: The equivalent resistivity extracted from $P(E)$ loops.

The $P(E, T)$ phase diagram before and after the leakage subtraction is constructed in Fig. 4-19. Ferroelectric polarization $P(E)$ was measured every 0.25 K at 121 values during heating from 360 K to 395 K, with a heating rate of 0.8 K min^{-1} . Notably, the value of polarization decreased after the leakage subtraction, especially at the paraelectric phase. This is shown by the shade of blue colour in the non-compensated phase diagram is lighter than that of the compensated counterpart.

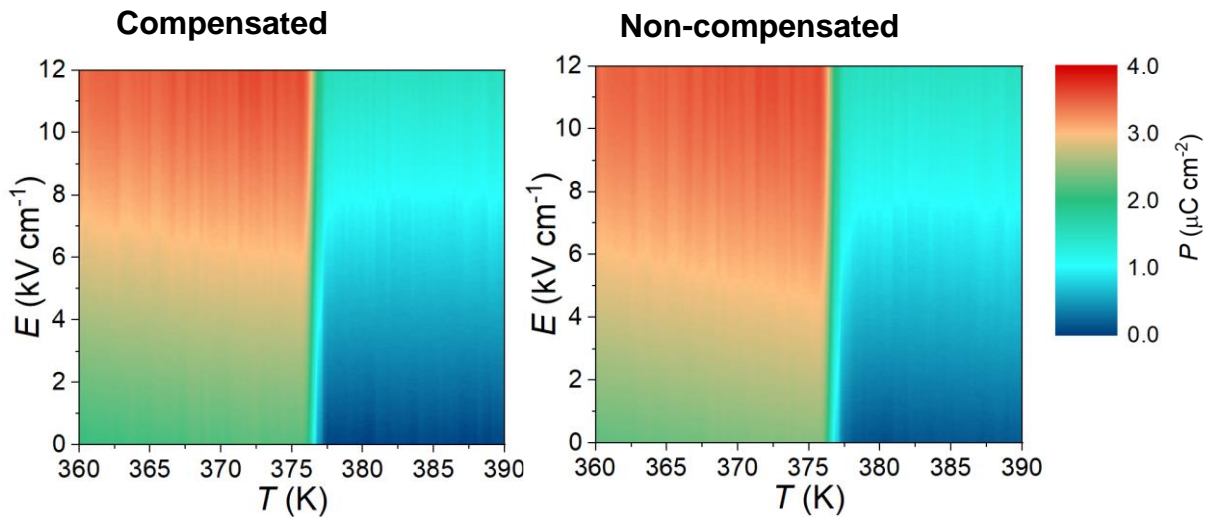


Figure 4-19. $P(E, T)$ obtained from the field-removal ($E > 0$) branch of approximately 121 $P(E)$ loops, some of which are shown in Fig. 4-17 for comparing the $P(T)$ before and after the leakage subtraction.

To take a closer look at the leakage compensation. The leakage current correction is only big at the lower electric fields. At the highest field $E = 12 \text{ kV cm}^{-1}$, the values of P are the same before and after the correct, as shown in Fig. 4-20.

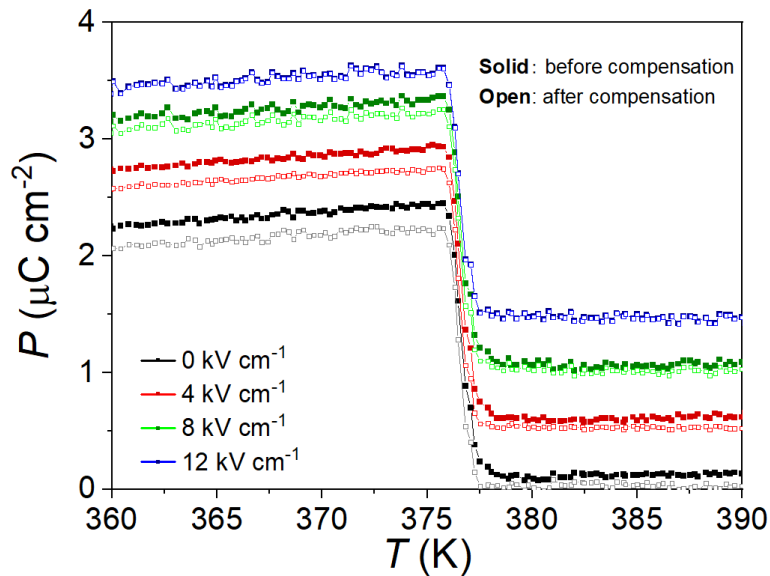


Figure 4-20. $P(T)$ at different E before and after the leakage subtraction.

To investigate the impact of leakage current on the EC ΔS , the $P(T)$ from non-compensated data was also evaluated. Using the data shown in Fig. 4-20, the results $\Delta S(T, E)$ are compared in Fig. 4-21. The top panel shows that ΔS before and after the leakage corrections are similar. This is because ΔS is mainly decided by the slope of P changing with T , i.e. dP/dT . Although the leakage subtraction corrects the absolute values of P , the values of dP/dT tend to be similar. The comparison in contour plots is also shown in Fig. 4-21.

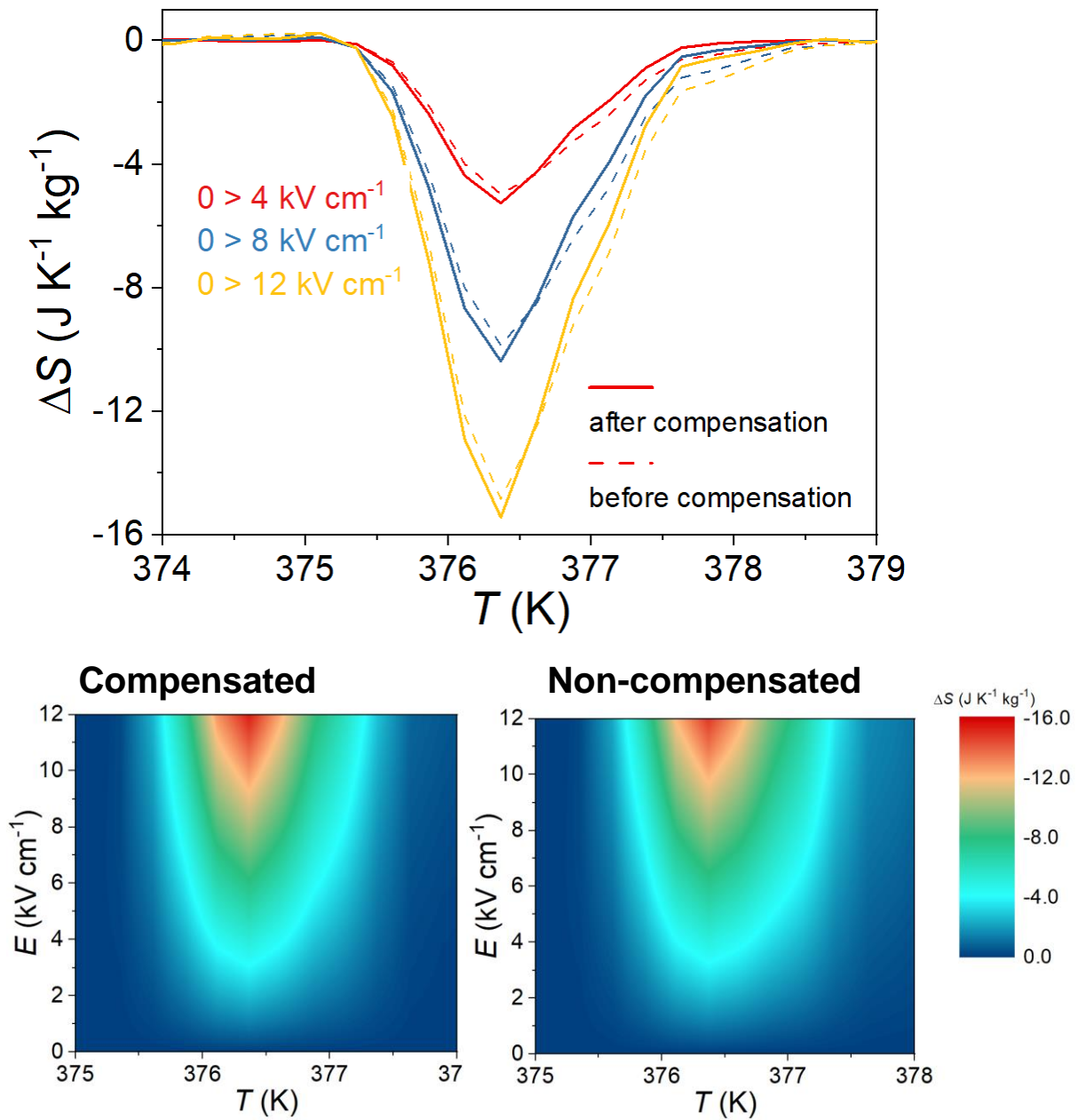


Figure 4-21. Top: Comparison of selected $\Delta S(T)$ before and after leakage compensation. The values of ΔS are derived from $P(T)$ loops shown in Fig. 4-20. **Bottom:** The contour plots of isothermal entropy change $\Delta S(E, T)$ before and after leakage compensation. The values are very similar. The slice of $\Delta S(E, T)$ is shown in the top panel.

Figure 4-22 compares $\Delta S(T)$ the maximum field change of 12 kV cm^{-1} derived from three approaches — one via the ‘standard’ indirect method and two via the ‘modified’ method. The ‘standard’ method gives a more smoothed peak of ΔS and a slightly smaller magnitude of $\Delta S(T)$. The difference is likely due to the different data densities, namely 0.94 K intervals for ‘standard’ method and 0.25 K interval for ‘modified’ method. This would cause a difference in the subsequent differentiation and integration. The most critical takeaway point here is that EC ΔS is mainly decided by dP/dT rather than the absolute value of P .

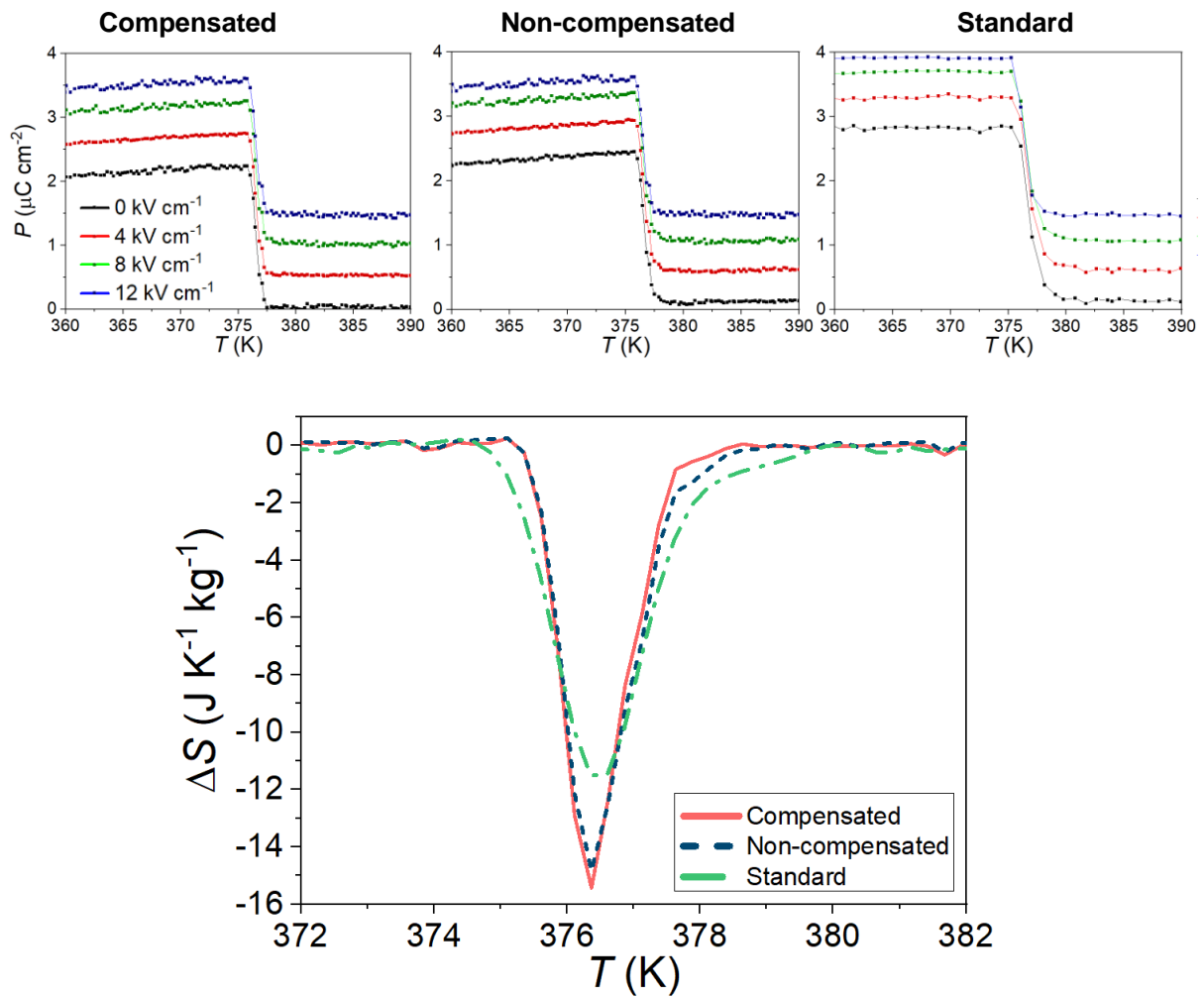


Figure 4-22. Top: $P(T)$ datasets that were used for deriving ΔS in three methods. **Bottom:** Comparison of resulting $\Delta S(T)$ in three methods due to the application of $E = 12 \text{ kV cm}^{-1}$ near the phase transition.

4.2.2. Landau modelling

Due to the practical issue of sample breakdown, models based on Landau-Devonshire (LD) theory were constructed to predict the EC effects of BF₄ at higher electric fields. This will show the potential achievable by an insulating sample. B. Nair, *et al.*¹³⁹ have shown that highly insulating PbSc_{0.5}Ta_{0.5}O₃ which are commercially manufactured can undertake a very high electric field up to $\Delta E = 290 \text{ kV cm}^{-1}$ to achieve large EC effects.

In this work of the LD models, the materials are assumed in bulk form with uniform spatial polarization and no surface boundaries. In essence, LD theory mathematically expresses the free energy landscape of a system $F(E, P)$ using its order parameter, which is polarization P in the case of ferroelectrics. Assuming the P is sufficiently small, which is valid near phase transitions, then the free energy F can be expressed using a Taylor expansion.

$$F = F_0 + \frac{1}{2} a(T-T_0) P^2 + \frac{1}{4} b P^4 + \frac{1}{6} c P^6 - E P \quad (4.1)$$

Where a , b , c and T_0 are Landau coefficients derived from experimental data.

Model construction

In the model above, four coefficients, namely a , b , c and T_0 are to be derived. At the phase transition temperature T_C , the ferroelectric phase and paraelectric phase have the same free energy, $\Delta F = 0$ at T_C . Based on the DSC measurement on heating and cooling, T_C is identified as 375 K. Therefore, these yields $\Delta F = \frac{1}{2} a(T-T_0) P^2 + \frac{1}{4} b P^4 + \frac{1}{6} c P^6 - E P = 0$ at $T_C = 375 \text{ K}$ and $E = 0$.

At a given temperature, the equilibrium configuration of the system is determined by finding the minima of F , via $\partial F/\partial P = 0$ to yield $P(T, E)$.

$$\partial F/\partial P = a(T-T_0) P + b P^3 + c P^5 - E \quad (4.2)$$

Then setting $E = 0$. Plugging two data points in (P_s, T) , $P_s = 3.0 \text{ } \mu\text{C cm}^{-2}$ at $T = 371 \text{ K}$, and $P_s = 2.8 \text{ } \mu\text{C cm}^{-2}$ at $T = 375 \text{ K}$ yielded two equations.

Entropy can be calculated as $S = \partial F/\partial T$. The entropy change $\Delta S_0 = \frac{1}{2} aP$, where P is the spontaneous polarization P_s of the ferroelectric phase at T_C when $E = 0$, if E plugging $P_s =$

$2.8 \mu\text{C cm}^{-2}$, $\Delta S_0 = 58 \text{ J K}^{-1} \text{ kg}^{-1}$ and density of 1.496 g cm^{-3} yields the fourth equation. Overall, four equations for fitting the Landau coefficient are as follows:

- $\Delta F = 0$ at $T_C = 375 \text{ K}$ and $E = 0$
- $\partial F/\partial P = 0$ at $T_C = 375 \text{ K}$ and $P_s = 2.8 \mu\text{C cm}^{-2}$
- $\partial F/\partial P = 0$ at $T_C = 371 \text{ K}$ and $P_s = 3.0 \mu\text{C cm}^{-2}$
- $\Delta S_0 = \frac{1}{2} a P_s$ at $P_s = 2.8 \mu\text{C cm}^{-2}$, $\Delta S_0 = 58 \text{ J K}^{-1} \text{ kg}^{-1}$

The model parameters are obtained as below, and the free energy curve simulated using those coefficients is displayed in Fig. 4-23.

Table 4-3. Landau coefficients derived for BF4.

<i>a</i>	$2.13 \times 10^8 \text{ C}^{-2} \text{ m}^{-2} \text{ N K}^{-1}$
<i>b</i>	$-1.45 \times 10^{13} \text{ C}^{-4} \text{ m}^6 \text{ N}$
<i>c</i>	$1.36 \times 10^{16} \text{ C}^{-6} \text{ m}^{10} \text{ N}$
<i>T</i>₀	361 K

Notably, coefficient *a* is usually fitted from the data of dielectric constant because *a* is temperature-dependent and in the form of $a(T) = a'(T - T_0)$, where T_0 is near or equals T_C . This coefficient can be deduced from the plot of $(1/\chi)$ against T , where χ is susceptibility and equals to $(\epsilon' - 1)$. However, the value of T_0 from this approach is $\sim 280 \text{ K}$ which deviates a lot from the $T_C = 375 \text{ K}$, so this fitting was not applied in our model. The possible reason is the inaccuracy in ϵ' measurements. As explained previously, a sample with big electrode area and smaller thickness can improve the accuracy.

In addition, all the P_s values are assumed to be the value of P at $E = 0$. Considering the typical square shape of the $P(E)$ loops, this assumption is reasonable.

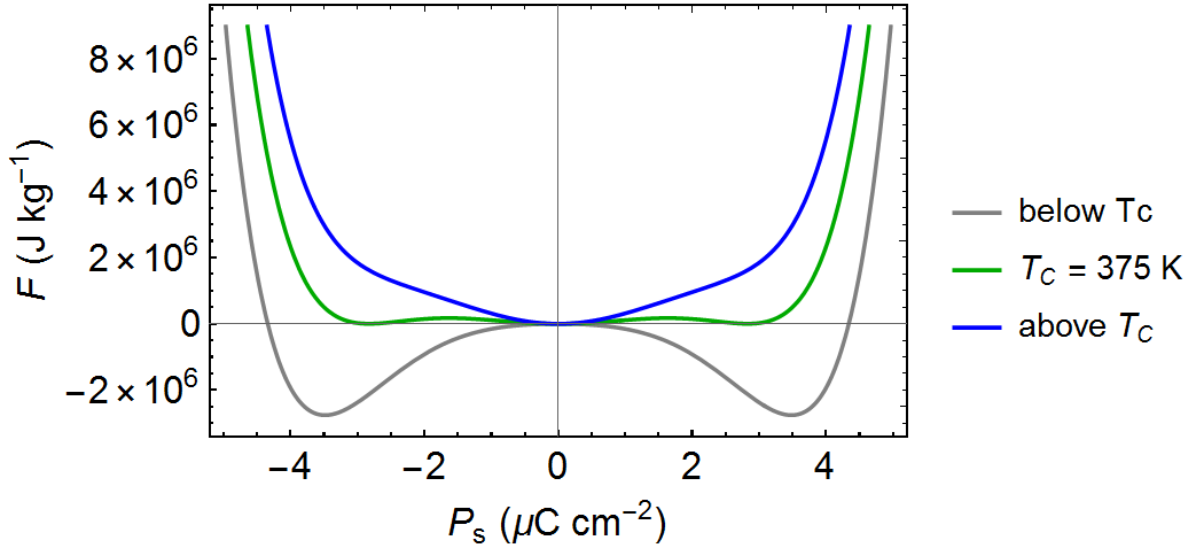


Figure 4-23. The Landau free energy $F(P, T)$ simulated for BF₄ using a model for first-order ferroelectric phase transition. Above T_C , the local minimum corresponds to $P = 0$. At T_C , the local minimum has three values, 0, $-P_S$ and $+P_S$. Below T_C , local minimum has $-P_S$ and $+P_S$.

Model results

As shown in Eq. 4.5, isothermal entropy change driven by E is the difference of S between two phases, which can be expressed as $\Delta S = \frac{1}{2} aP$. With the completed model, P as a function of T and E can be calculated (Fig. 4-24b). The model predicts that P instantly decreases to nearly zero during the phase transition. Then the magnitude of ΔP gives the corresponding ΔS , which is the EC effects.

However, the model results do not match well with our experiments results where P does not decrease instantly. The decrease of P spreads ~ 2 -3 K temperature range. In words, the experimentally observed $P(T)$ is more diffused. This also explains why the LD model overestimates the $|\Delta S| \sim 45 \text{ J K}^{-1}\text{kg}^{-1}$ driven by $|\Delta E| = 12 \text{ kV cm}^{-1}$.

For a better model fitting, it is essential to obtain experimental results in which the transition temperature shows a distinguishable shift under electric fields. In the work of B. Nair, *et al.*¹³⁹, $\sim 100 \text{ K}$ of shift in T_C was experimentally achieved. Their LD model yielded a close match with the experimental results.

According to Clausius–Clapeyron equation $dT = - (dE \Delta P) / \Delta S_0$, a larger dT/dE value can be achieved by a larger E , which can be tried in the future on new samples. The main challenge is the material breakdown. Therefore, more insulating BF₄ samples are desirable. Alternatively,

other materials with larger ΔP or smaller ΔS_0 would also be easier for EC measurements and LD modelling. This also motivated us to study the EC effects in $[\text{AH}][\text{ReO}_4]$ in the next section.

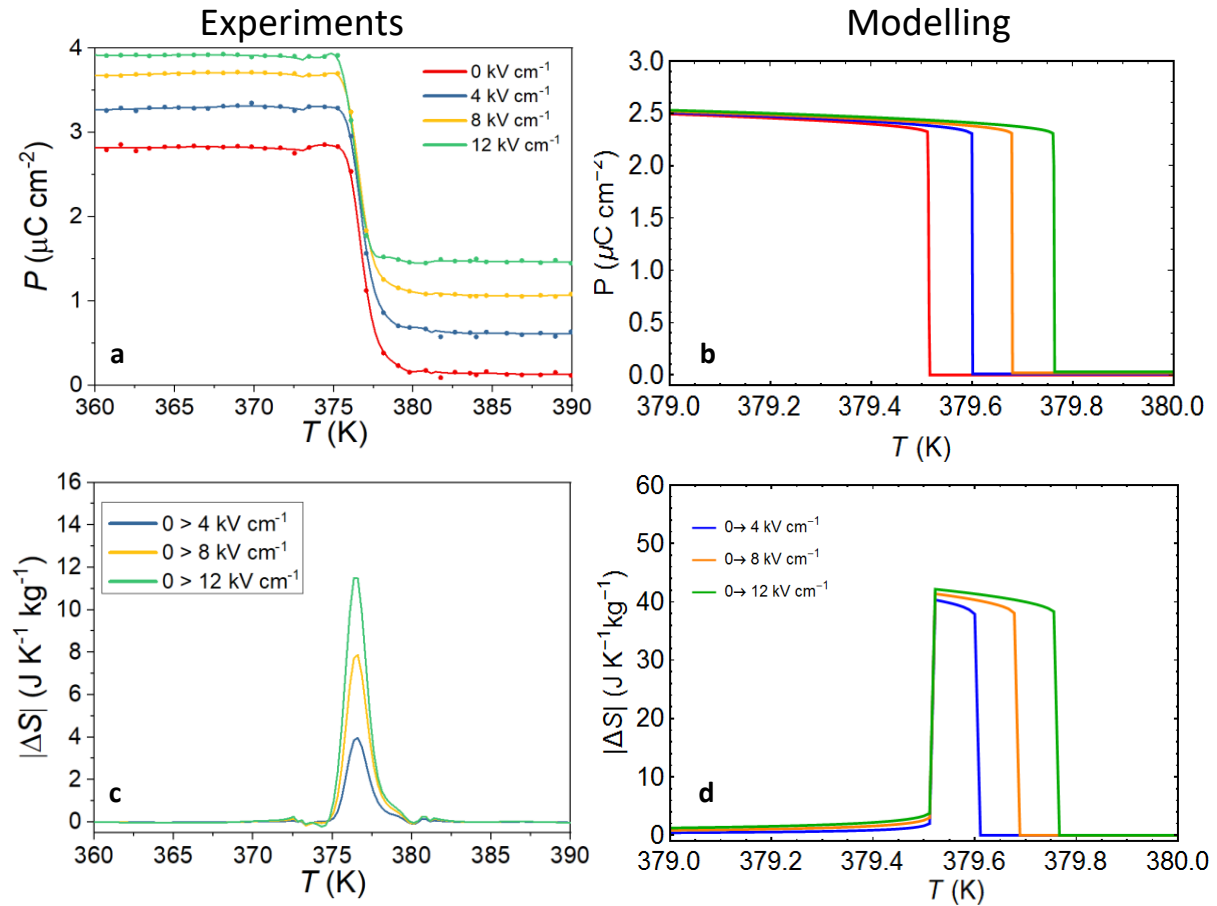


Figure 4-24. Comparison of results from experiments(left) and Landau modelling(right). **(a)(b):** $P(T)$ under electric fields. **(c)(d):** $\Delta S(T)$ driven by electric fields.

In Fig. 3-25, there is a good agreement between the model results and experimental results in dielectric constant and specific heat capacity.

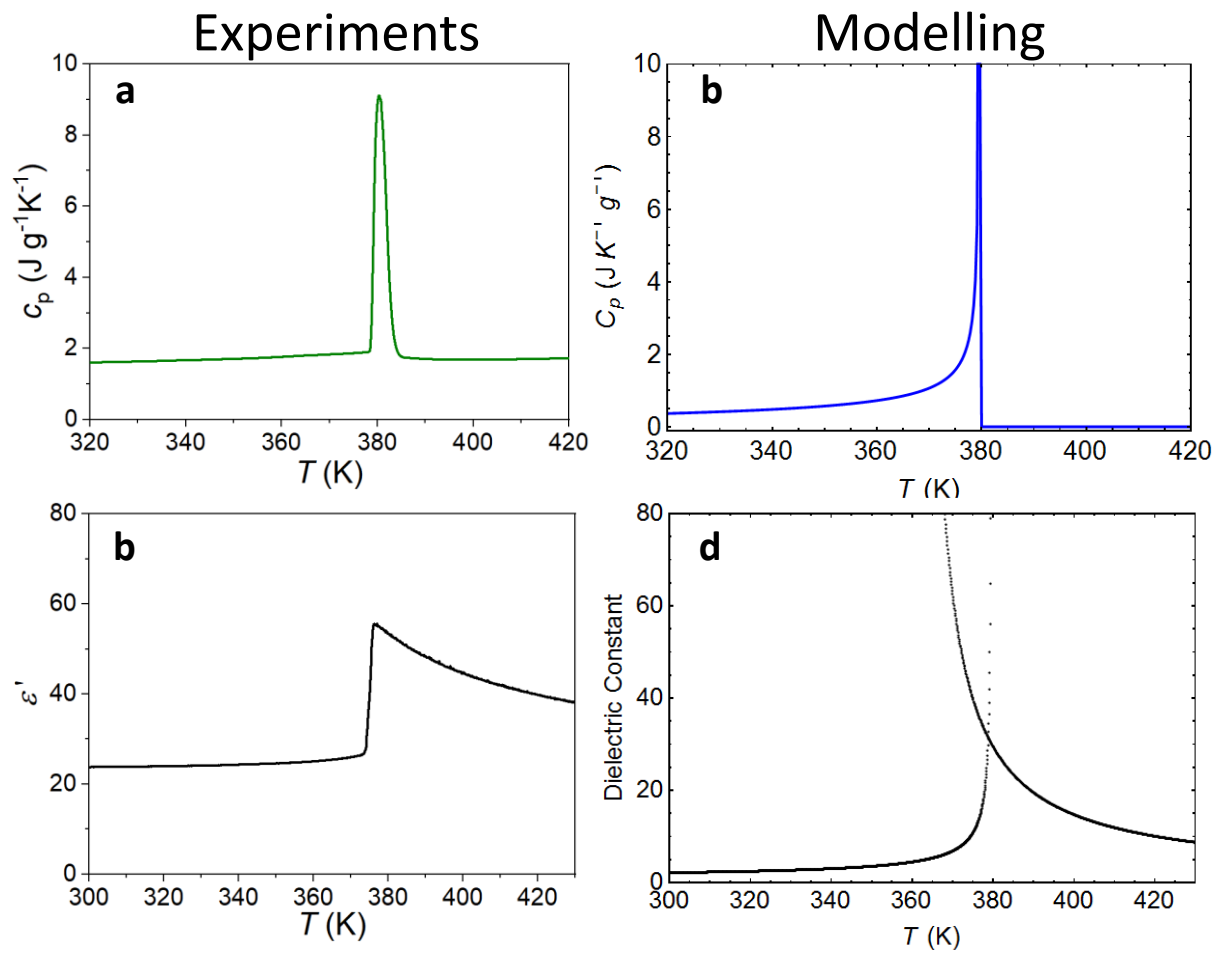


Figure 4-25. Comparison of results from experiments (left) and Landau modelling (right). **(a)(b):** heat capacity $c_p(T)$ under zero fields. **(c)(d):** Dielectric constant as function of T .

To predict the EC effects in BF4 at a very high electric field. The critical point is calculated as (394 K, 663.6 kV cm⁻¹) by following:

$$\frac{(\partial F)}{\partial P} = \frac{\partial^2 F}{\partial P^2} = \frac{\partial^3 F}{\partial P^3} \quad (4.3)$$

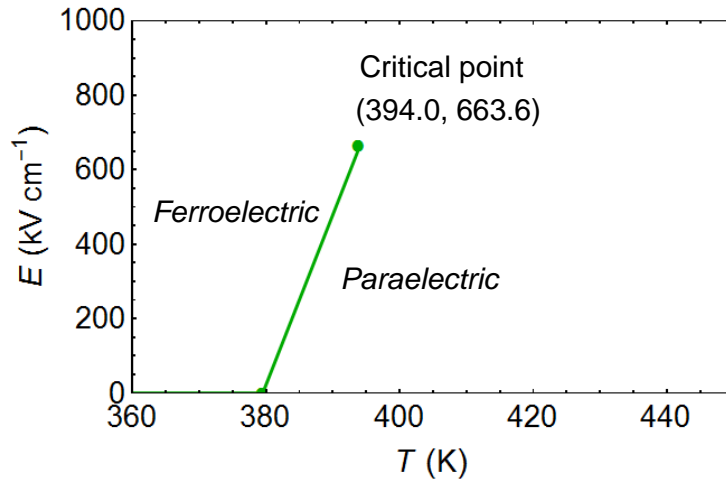


Figure 4-26. Calculated E - T phase diagram for BF4.

The value of dT/dE is 0.022 cm kV⁻¹. This is in an order-of-magnitude agreement with the Clausius–Clapeyron value of $dT/dE = -\Delta P/\Delta S_0 \sim 0.028$ cm kV⁻¹. Then the EC effects at critical electric field E_C and up to $2E_C$ are predicted. This gives $\Delta S_0 \sim 80$ 45 J K⁻¹kg⁻¹ for around 40 K of operating temperature range.

However, it is difficult to justify the prediction at E_C because no close experiments were observed. Also, the shifting in phase transition temperature was not experimentally observed either. This prediction is regarded as preliminary and needs to be further verified.

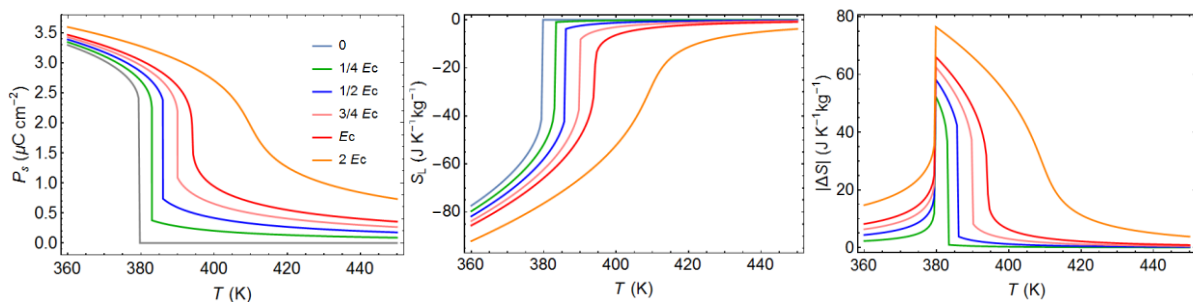


Figure 4-27. The model results of $P(T, E)$, $S_L(T, E)$ and $|\Delta S(T, E)|$ at high fields up to $2E_C$, where $E_C = 663.6$ kVcm⁻¹.

4.2.3. Summary

In this work, the crystals of BF₄ were synthesized via the slow-evaporation method. The EC effects in BF₄ were evaluated using both the ‘standard’ and ‘modified’ versions of indirect methods. The ΔS are higher than the traditional inorganic EC materials, showing the potential of BF₄. The ΔS can be even higher if a larger electric field could be applied. Based on our estimation, $|\Delta E| \sim 60 \text{ kV cm}^{-1}$ can drive the full transition with $\Delta S \sim 58 \text{ J K}^{-1} \text{ kg}^{-1}$. However, due to sample breakdown, higher electric measurements were not implemented. Therefore, a Landau model was contrasted using the measured experimental results and to predict the EC effects at higher fields. According to our model, BF₄ material can reach the critical point at 394 K with $|\Delta E| \sim 663.57 \text{ kV cm}^{-1}$, which accesses a wide range of operating temperatures.

The ‘modified’ version of indirect method quantified the impact of leakage to the polarization and the $|\Delta S|$ driven by electric field. The conclusion is that leakage only affects the ΔS values at low fields while has nearly no impact on $|\Delta S|$ values near E_{max} . This is because EC effects are mainly determined by dP/dT , while leakage mainly changes the absolute value of P .

4.3 Electrocaloric effects in plastic crystals

4.3.1. Overview

In the last section, BF₄ has shown great potential for EC effects. With the same structure, other compositions of Dabco-based materials were also discovered similar ferroelectric properties^{95,96,159,160}, indicating good EC effect as well. Nevertheless, this structure has two issues for practical cooling applications. Firstly, the crystals are brittle and mechanical breakdown happens frequently. Secondly, the phase transition is around 100 °C, which is not optimal for room-temperature applications.

Our collaborators Jun Harada *et al.* at the Department of the Department of Chemistry, Hokkaido University, Japan, have done chemical alterations to the Dabco-based materials to fabricate [AH][ReO₄]⁹⁷ (AH = 1-azabicyclo[2.2.1]heptanium, ReO₄ = perrhenate). Here, [AH][ReO₄] is referred as AH for convenience. The structural difference between AH and BF₄, shown in Fig. 4-28 is that the organic molecular cation has one carbon less. Also, the inorganic anion is different. Plasticity is mainly credited to the globular molecular cation [AH]⁺, which can undergo rotational motions during mechanical deformation⁹⁸.

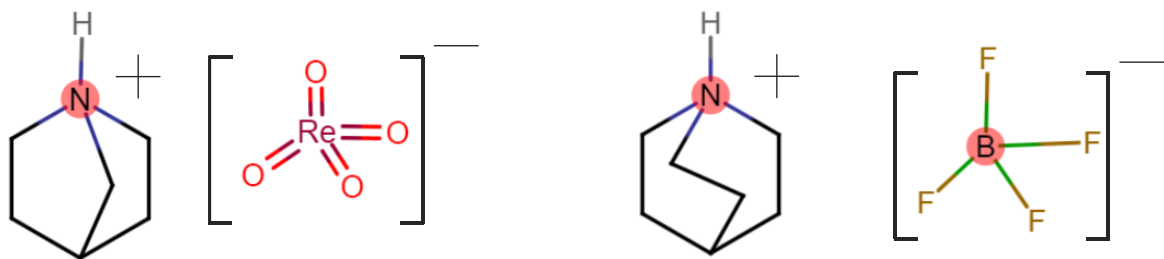


Figure 4-28. The chemical structure of [AH][ReO₄] (left) and [Hdabco][BF₄] (right).

Due to its plasticity, AH can be processed into bulk polycrystalline forms with desired geometry, such as pellets and free-standing films, shown in Fig.4-29. This greatly avoids mechanical breaking issues which frequently happened in BF₄ and makes the materials more approaching to industrial applications. Moreover, AH has a ferroelectric-paraelectric phase transition at ~ 325 K, closer to room temperature.

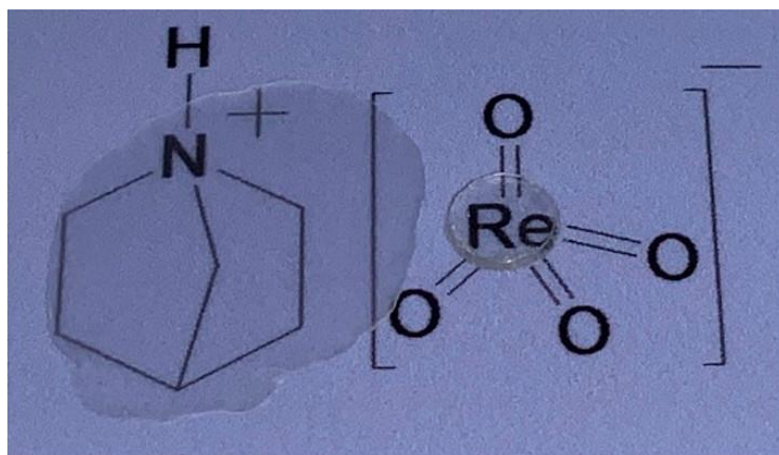


Figure 4-29. Photo of a transparent polycrystalline film and a pellet of AH. Left: a large film (thickness: 80 μm ; width: ~ 1 cm). Right: a small pellet (thickness: 380 μm ; diameter: 3 mm). This figure is taken from ref⁹⁷.

4.3.2. Experiments

Materials synthesis

The materials synthesis was performed by our collaborator Jun Harada *et al.* at Department of Chemistry, Hokkaido University, Japan. All the experiments conducted in this materials were done by the author and Lingfang Xu, who was visiting our group from Faculty of Physics and Electronic Science, Hubei University, China. The precursor materials 1-azabicyclo[2.2.1]-heptane (Tokyo Chemical Industry) and perrhenic acid (SigmaAldrich) at a 1:1 mole ratio were mixed in aqueous ethanol. The synthesis of 1-Azabicyclo[2.2.1]heptanium perrhenate (AH) is similar to BF₄ via slow-evaporation. White precipitated powders of AH were obtained from the neutralization reaction between the amine and the acid. Those powders were recrystallized by dissolving in the solution on heating and subsequent precipitation by cooling to room temperature. After that, the obtained microcrystalline powders of AH were filtered and dried under reduced pressure.

As crystals of AH exhibit plastic deformation, bulk polycrystalline pellets were fabricated by applying uniaxial stress to powders at high temperatures. For the electric measurements, carbon paste was applied to both faces of the samples to form electrodes, as shown in Fig. 4-30.



Figure 4-30. The transparent AH pellet with carbon paste on the surface as electrodes. This electrode sample was then subjected to electric measurements.

Calorimetry measurements under zero field

The heat flow dQ/dT measurements were performed on an AH pellet ~ 7.073 mg at ± 10 K min^{-1} . The results in Fig. 4-31 show that AH undergoes a reversible phase transition at 323 K on cooling and 321 K on heating, with a hysteresis of ~ 2 K. The latent heat $|Q_0|$ is ~ 5.7 J K^{-1} kg^{-1} . The entropy change under zero electric field is $|\Delta S_0| \sim 17.8$ J K^{-1} kg^{-1} (Fig. 4-31 bottom).

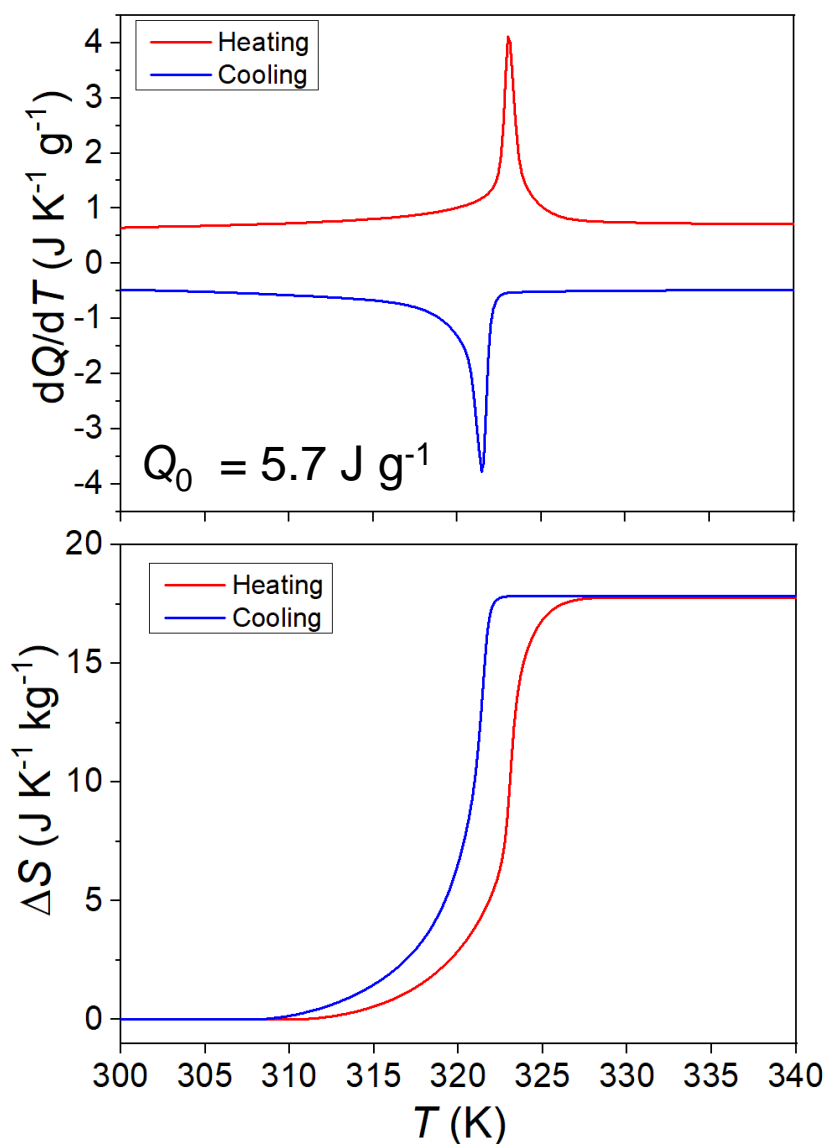


Figure 4-31. Top: Heat flow measurements for AH pellet at 10 K min^{-1} . $dQ/dT > 0$ means endothermic. The integration of dQ/dT yields values of Q_0 . **Bottom:** ΔS_0 can be derived from the integration of $(dQ/dT)/T$.

Characterisation of the specific heat capacity $c_p(T)$ under zero-filed is displayed in Fig. 4-32. This is the total c_p including the contribution from the latent heat at the phase transition. At the phase transition, c_p increases sharply and the peak value of $c_p = 4.7 \text{ J K}^{-1} \text{ g}^{-1}$ at 326 K. In the following section of calculating EC effects, $c_p(T)$ is used in two approaches to determine the adiabatic temperature change ΔT . The first approach is via $-c_p \Delta T \approx T \Delta S = Q$. The second one is based on the entropy integration associated with $c_p(T)$. This will be discussed in later sections.

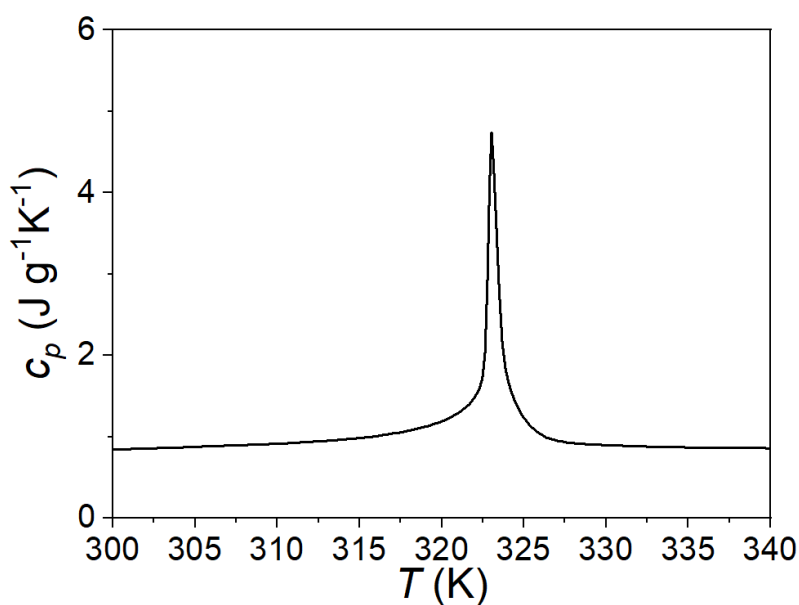


Figure 4-32 Specific heat capacity c_p of $[\text{AH}][\text{ReO}_4]$ measured from calorimetry on heating.

Dielectric measurements

Fig. 3-50 shows the dielectric constant for AH polycrystalline pellet in the frequency range 10^3 Hz - 10^6 Hz with an applied AC-voltage of 1 V on heating at 1 K min^{-1} , yielding every 0.15 K at 480 values of increasing temperature. The ferroelectric-paraelectric transition was observed as a sharp peak in ϵ' at ~ 320 K. The Curie-Weiss constant above T_C was ~ 1445 K, which is lower than the corresponding value of 4300 K in Jun Harada *et al.*⁹⁷.

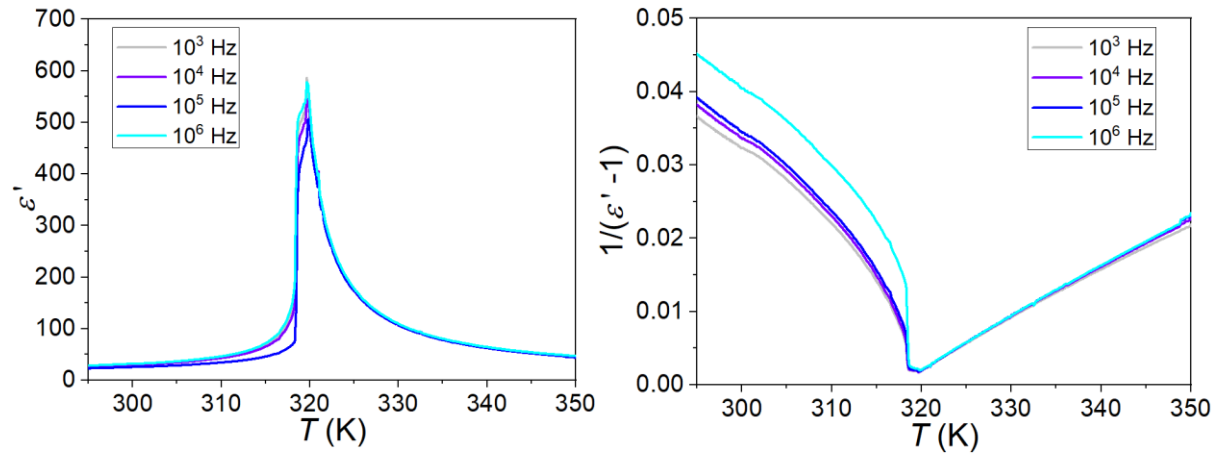


Figure 4-33. Left: Dielectric constant ϵ' (T) at different frequencies on heating at the rate of 1 K min^{-1} . Right: Reciprocal of dielectric susceptibility as a function of temperature.

EC effects via the indirect method

Ferroelectric polarization measurements at different temperatures were performed in polycrystalline Pellet 1 and Pellet 2. Pellet 1 is $\sim 491 \mu\text{m}$ thick and has an electrode area $\sim 15.54 \text{ mm}^2$ covered by carbon paste. The standard triangular voltage wave was applied, with the electric field amplitude of 11.2 kV cm^{-1} and duration $\sim 100 \text{ ms}$ corresponding to a frequency of 10 Hz . Pellet 2 is $\sim 404 \mu\text{m}$ thick and has an electrode area $\sim 15.53 \text{ mm}^2$ covered by carbon paste. The standard triangular voltage wave was applied, with the electric field amplitude of 11.2 kV cm^{-1} and duration $\sim 100 \text{ ms}$ corresponding to frequency of 10 Hz . Ferroelectric polarization $P(E)$ was measured every 0.45 K , with a 0.85 K min^{-1} heating rate.

Fig. 4-34 shows the characteristic $P(E)$ loops before and after the ferroelectric-paraelectric phase transition. At the ferroelectric phases, clear $P(E)$ loops are in square shape with distinct ferroelectric switching while $P(E)$ loops at paraelectric phase are linear loops, accompanied decreased polarization. The right panel shows the magnitude of polarization as a function of temperature. The sharp decrease of P at 325 K indicates a first-order phase transition where the order parameter P changes discontinuously at T_C .

In Pellet 1, the transition temperature is shifted $\sim 1.0 \text{ K}$ towards higher temperatures under $E \sim 12 \text{ kV cm}^{-1}$, corresponding to $dT/dE = 0.083 \text{ cm kV}^{-1}$. This is in an order-of-magnitude agreement with the Clausius–Clapeyron value of $dT/dE = -\Delta P/\Delta S_0 \sim 0.062 \text{ cm kV}^{-1}$ (where $\Delta S_0 = 17.8 \text{ J K}^{-1} \text{ kg}^{-1}$ [Fig. 4-31] and $\Delta P \sim 2.7 \mu\text{C cm}^{-2}$ [Fig. 4-34b at $E = 0 \text{ kV cm}^{-1}$]).

In Pellet 2, the transition temperature is shifted $\sim 1.4 \text{ K}$, with $dT/dE = 0.117 \text{ cm kV}^{-1}$. This is higher than the corresponding Clausius–Clapeyron value of $dT/dE = -\Delta P/\Delta S_0 \sim 0.057 \text{ cm kV}^{-1}$ (where $\Delta S_0 = 17.8 \text{ J K}^{-1} \text{ kg}^{-1}$ [Fig. 4-31] and $\Delta P \sim 2.5 \mu\text{C cm}^{-2}$ [Fig. 4-34e at $E = 0 \text{ kV cm}^{-1}$]). However, the shift in transition temperature is very small and slightly vary with the data extraction. These results of dT/dE are regarded as preliminary.

Field-removal branches obtained ($0 \leq E \leq 11.2 \text{ kV cm}^{-1}$) were used to plot $P(T, E)$ phase diagrams (Fig. 4-34c and Fig. 4-34f). The red colour represents the ferroelectric phase while the blue colour represents the paraelectric phase. The dotted lines in (c)(f) show phase boundary derived from the Clausius–Clapeyron with T_C at zero field $\sim 325 \text{ K}$ and the corresponding dT/dE .

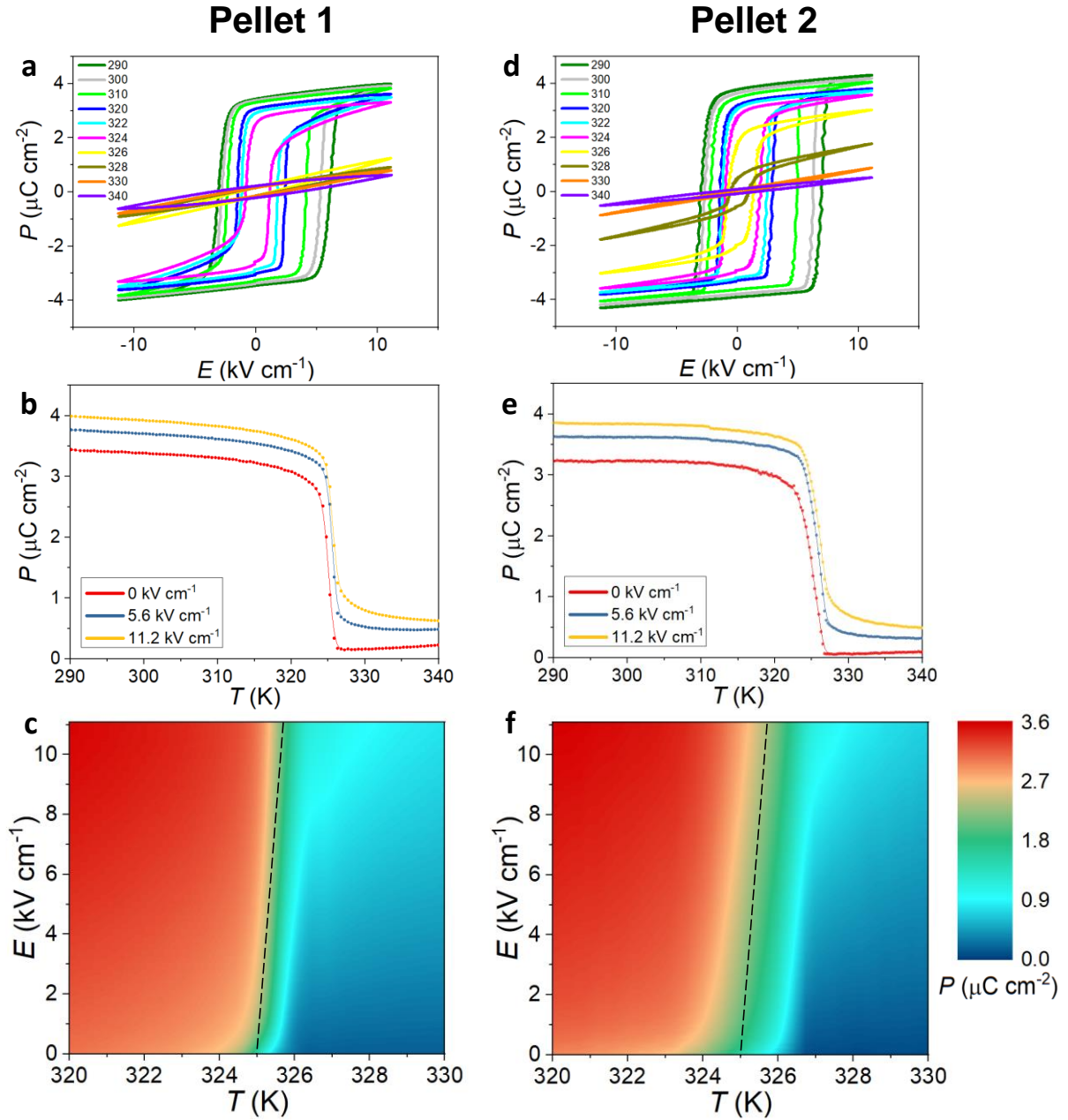


Figure 4-34. (a) (d): $P(E)$ loops measured at an electric field magnitude of 11.2 kV cm^{-1} . The change in the shape indicates the phase transition from the ferroelectric phase to the paraelectric phase. (b)(e) Selected $P(E,T)$ obtained from the field-removal ($E>0$) branch of approximately: (c)(f): The T - E phase diagram. The black dotted lines are phase boundary derived by Clausius–Clapeyron with $T_C = 325 \text{ K}$ as well as $dT/dE = -\Delta P/\rho\Delta S_0 \sim 0.062 \text{ cm kV}^{-1}$ (pellet 1) and 0.057 cm kV^{-1} (pellet 2).

Similar to the data analysis in the last section of BF4, EC effects in AH were evaluated using the indirect method. The dense $P(T, E)$ data (Fig. 4-34) were used to evaluate the isothermal entropy change $\Delta S(T, E) = \int (\partial P / \partial T)_E dE$ (Fig. 4-35) for field application ($0 \rightarrow E$) at temperature T . The largest field used in the indirect measurements ($E = 11.2 \text{ kV cm}^{-1}$) yields a maximum entropy change of $\Delta S \sim -7.5 \text{ J K}^{-1} \text{ kg}^{-1}$ for Pellet 1 and $\Delta S \sim -5.0 \text{ J K}^{-1} \text{ kg}^{-1}$ for Pellet 2. Assuming ΔS_{max} increases linearly with ΔE , the entropy of full transition of $|\Delta S| \sim 17.8 \text{ J K}^{-1} \text{ kg}^{-1}$, $|\Delta E| \sim 26.6 \text{ kV cm}^{-1}$ and 39.9 kV cm^{-1} are required.

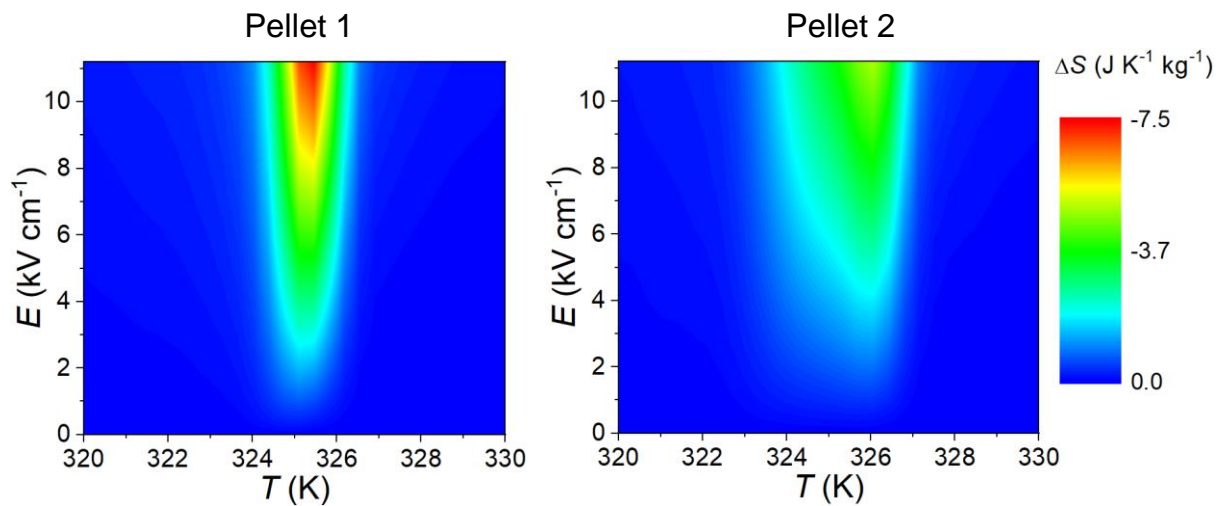


Figure 4-35. The contour plots of isothermal entropy change $\Delta S(E, T)$ due to the application of field E .

Adiabatic temperature change ΔT is also evaluated as an important parameter for EC effects via the indirect method. The values ΔT are also compared with corresponding values from the direct method in later sections. ΔT is derived in two approaches.

The first approach is via $\Delta T \approx -T\Delta S/c_p$, using the ΔS data derived above. Ideally, c_p should be measured under electric field. However, due to experimental complexity, the c_p is assumed to be unchanged with electric field here. The data in Fig. 4-35 is used to derive ΔT . Fig. 4-36 bottom shows the obtained ΔT from the selected ΔS (Fig. 4-36 top). Pellet 1 shows maximum $\Delta T \sim 1 \text{ K}$ while Pellet 2 shows $\sim 0.8 \text{ K}$.

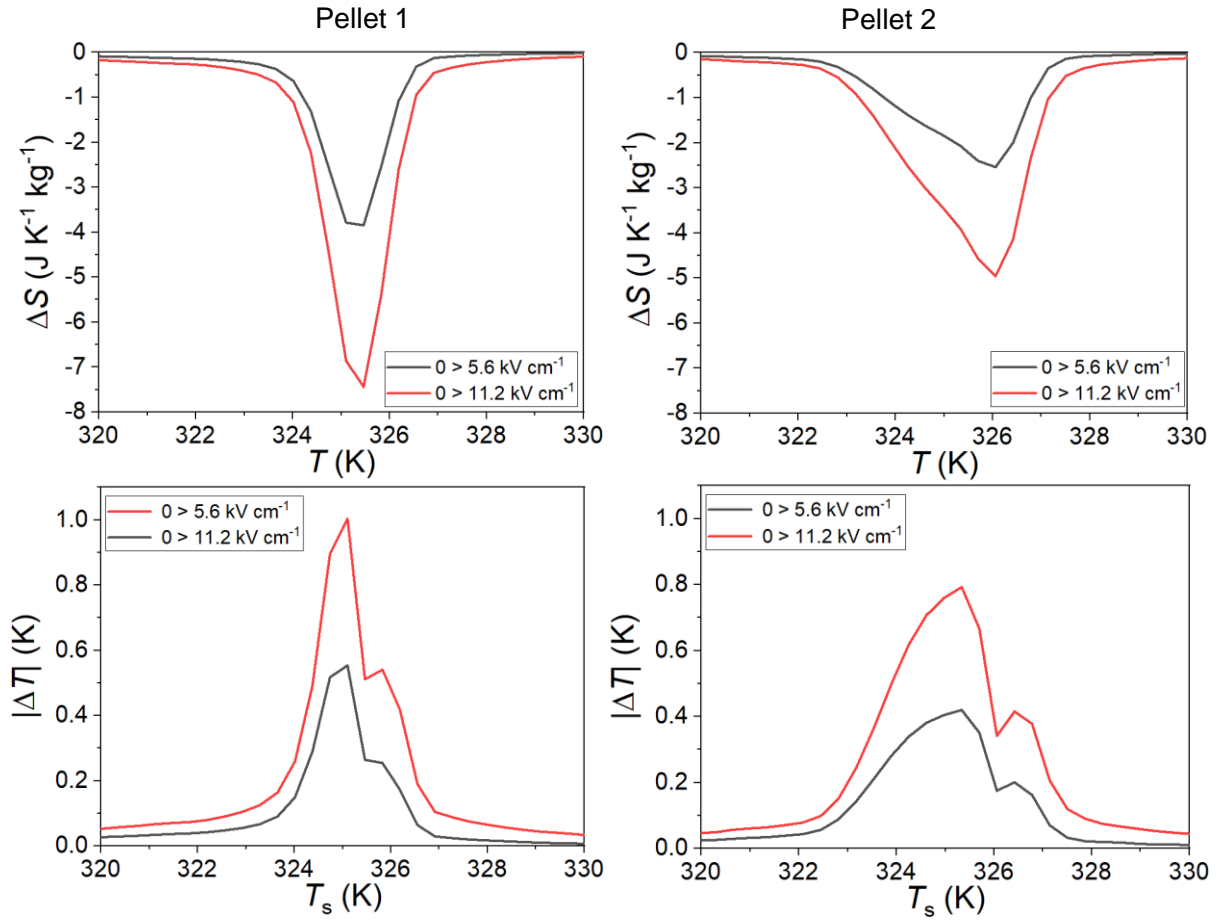


Figure 4-36. Top: $\Delta S(E, T)$ selected from Fig. 4-35 to calculate ΔT . **Bottom:** the resulting ΔT derived via $\Delta T \approx -T\Delta S/c_p$. Here, ΔS and ΔS are the changes when the material is subjected to an electric field application from 0 to 5.6/11.2 kV cm^{-1} .

The second approach to derive ΔT is based on the S - T curves at different electric fields. Firstly, the S - T curve at zero-field is constructed via the integration of $c_p(T)/T$ as a function of T . The dataset of $c_p(T)$ in Fig. 4-32 is used. This shows how the entropy of the material changes without electric field. Then combining the ΔS driven by electric field (data taken from Fig. 4-35) yields the S - T shifted by electric fields. Notably, the $c_p(T)$ and ΔS driven by electric field were measured using two different instruments so there is a difference in temperature recording. To compensate for that difference, T in $c_p(T)$ is added by 1.6 K for Pellet 1 and by 2.5 K for Pellet 2.

The adiabatic temperature change can be obtained via $\Delta T(E, T) = T'(E, S) - T'(0, S)$. By following adiabatic trajectories in $S(T, E)$ (Fig. 4-37 top), we established both the adiabatic temperature change $\Delta T(T_s, \Delta E)$ on applying the electric field at starting temperature T_s , shown in Fig. 4-37 bottom. As a result, Pellet 1 shows maximum $\Delta T \sim 0.80$ K while Pellet 2 shows ~ 0.73 K.

In our results, the second approach gives slightly lower values of ΔT . This difference will be a lot larger when the shift of phase transition is larger. This can be seen in the next chapter of barocaloric effects where the shift in T_C is larger.

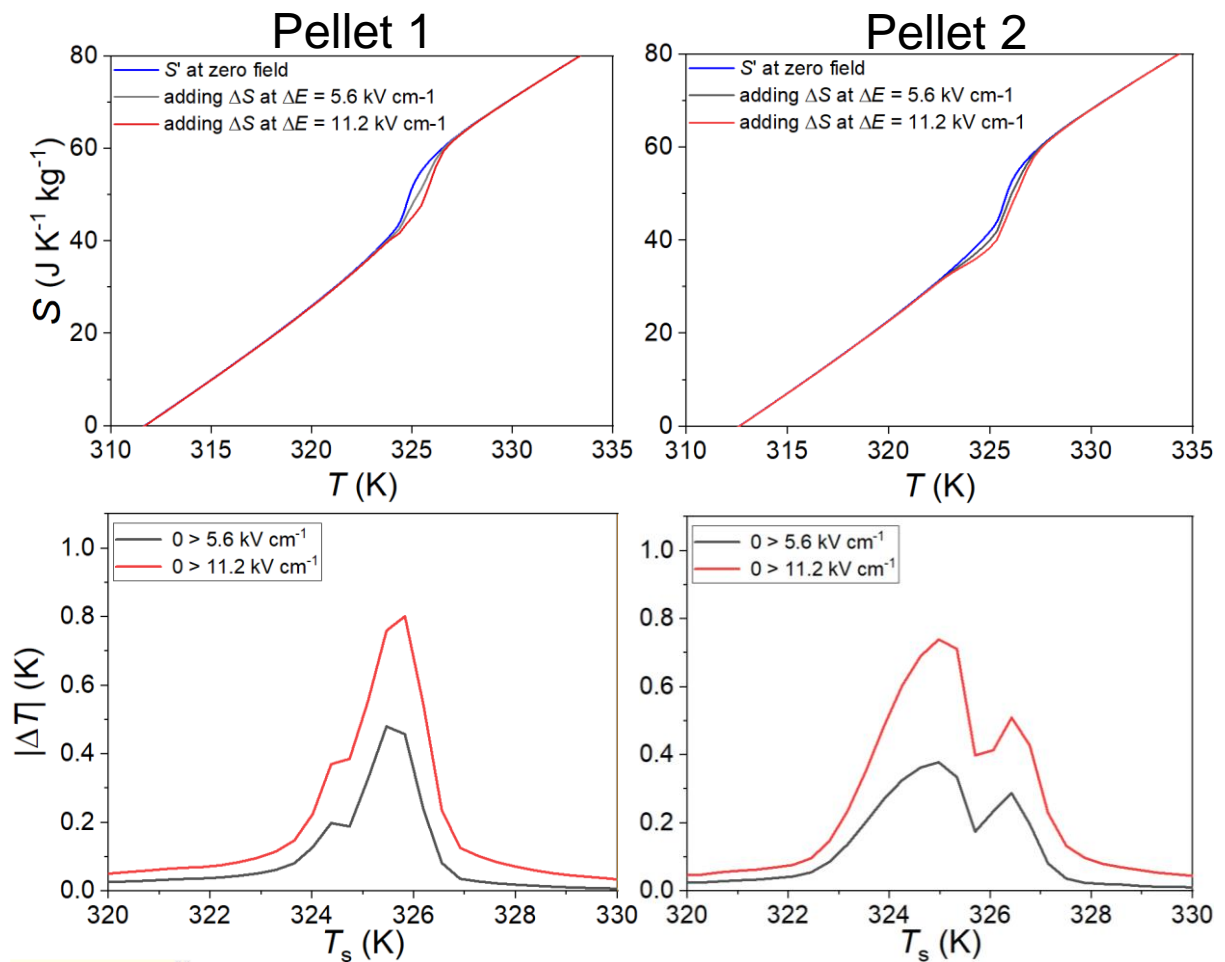


Figure 4-37. Top: a combination of S - T curve at zero-field and $\Delta S(E, T)$ to derive the S - T at electric fields. **Bottom:** the resulting ΔT By following adiabatic trajectories in $S(T, E)$. Here, ΔS and ΔS are the changes when the material is subjected to an electric field application from 0 to 5.6/11.2 kV cm^{-1} .

EC effects via the quasi-direct method

The measurements of calorimetry under electric fields are commonly used for the quasi-direct method for evaluating Caloric effects. Since the electric field stabilizes the ferroelectric phase, so the phase transition will be shifted towards higher temperature by an electric field. Therefore, the electrically driven entropy change can be obtained by $S'(T, E) - S'(T, 0)$.

Calorimetric measurements of heat flow under $E = 0$ and 5.6 kV cm^{-1} were performed with an in-house DSC described below. The temperature control was achieved by immersing the copper chamber in a thermal bath with a heating or cooling rate of 0.75 K min^{-1} .

Notably, a data correction, shown in Fig. 4-38 is applied here to subtract the Joule heat such the heat flow from phase transition can be analysed. In principle, the DSC aims to measure the heating power associated with the phase transition. However, the presence of leakage also generates heat, which is noise and may diminish the desired signal. Therefore, the subtraction of leakage current was performed. The voltage and current from the sourcemeter was recorded, so the heating power can be calculated as voltage multiplies current. After the subtraction of the power corresponding to Joule heating, the corrected heat flow dQ/dT can be obtained.

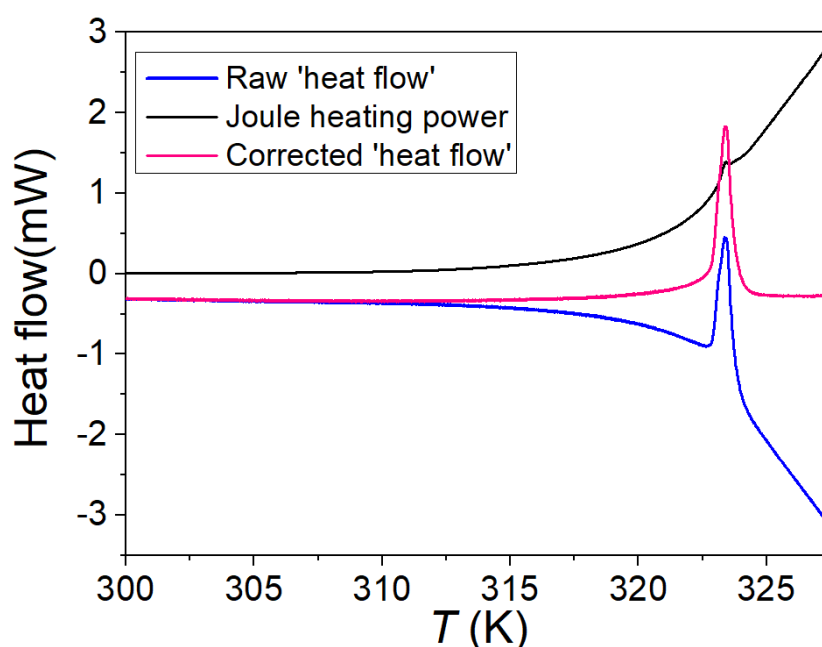


Figure 4-38. Illustration of the data correction for the heat flow dQ/dT measurements for Pellet 1 under $E = 5.6 \text{ kV cm}^{-1}$. The raw data (blue) contains unwanted Joule heating. The power of Joule heat (black) can be calculated as the voltage times current through the voltage source - Keithley 2410. The subtraction of Joule heating yields the heat dQ/dT without the contamination of Joule heating (red).

The calculation of ΔS via the quasi-direct method is illustrated in Fig. 4-39. By holding Pellet 1 at first 0 kV cm^{-1} and then 5.6 kV cm^{-1} at a heat rate of 0.75 K min^{-1} , measurements of heat flow dQ/dT on heating are integrated to yield $S'(T)$ at 0 and 5.6 kV cm^{-1} . The difference $|\Delta S(T, 5.6 \text{ kV cm}^{-1}) - \Delta S(T, 0 \text{ kV cm}^{-1})|$ peaks at $\sim 3.8 \text{ J K}^{-1} \text{ kg}^{-1}$.

The shift of the phase transition temperature T_C is identified by the peaks of dQ/dT . At zero field, $T_C = 323.21 \text{ K}$ while at $E = 5.6 \text{ kV cm}^{-1}$, $T_C = 323.40 \text{ K}$, so the $\Delta T_C \sim 0.2 \text{ K}$. Using Clausius–Clapeyron value of $dT/dE = 0.062 \text{ cm kV}^{-1}$, $E = 5.6 \text{ kV cm}^{-1}$ is expected to shift T_C 0.35 K . This is in an order-of-magnitude agreement with our observed value of 0.2 K .

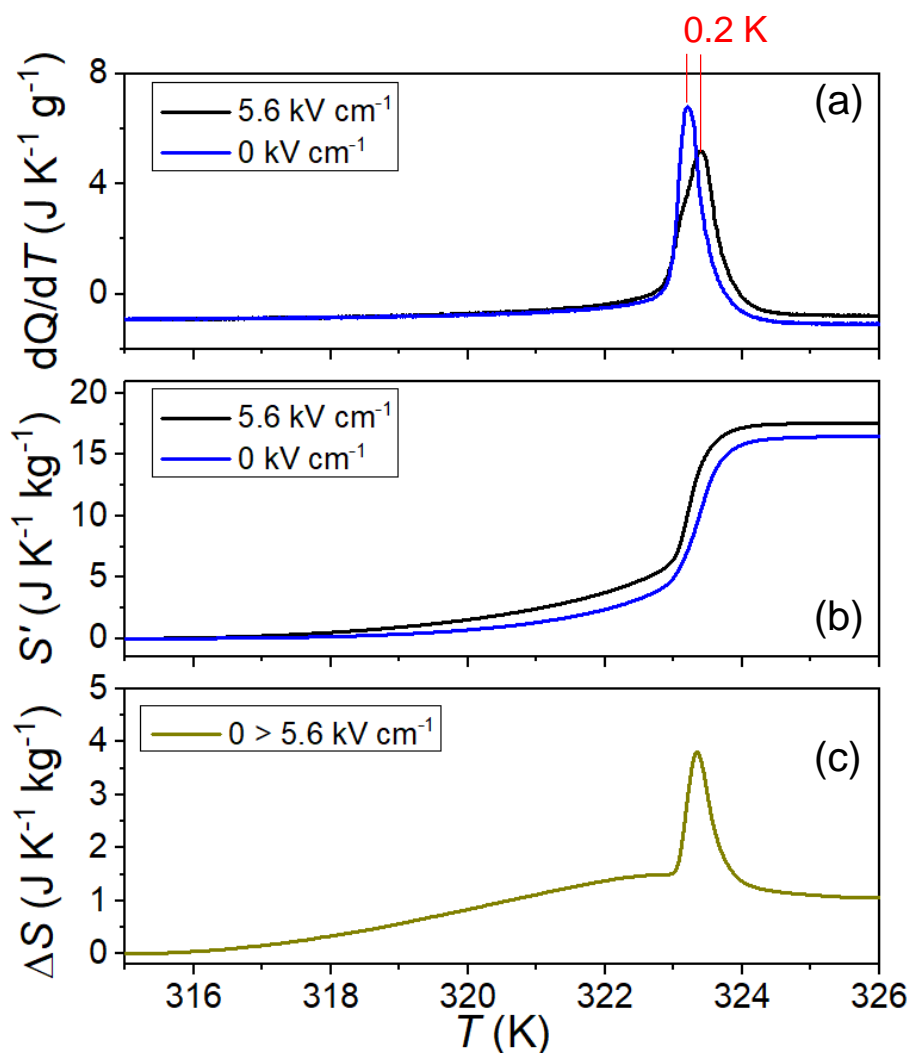


Figure 4-39. (a) the heat flow dQ/dT measured under $E = 0$ (black) and 5.6 kV cm^{-1} (blue). The blue line is corrected to subtract Joule heating as explained in Fig. 4-38. (b) the $S'(T)$ via integration of $(dQ/dT)/T$. (c) the isothermal entropy change driven by electric field, derived from $\Delta S(T) = |\Delta S(T, 5.6 \text{ kV cm}^{-1}) - \Delta S(T, 0 \text{ kV cm}^{-1})|$.

EC effects via the direct method

Direct measurements of EC effects were carried out using both the non-contact and contact approaches. Non-contact measurements were performed using a FLIR SC 7500 Infrared (IR) camera with a 50 Hz frame rate, while contact measurements were conducted using a K-type thermocouple attached on the sample surface.

The measurements of temperature via the IR camera vary with the surface. As shown in Fig. 4-40. The temperature reading in Box 2 is larger than that in Box 1. This might be due to the difference in reflectivity or the real local temperature. A cleaner surface needs to be provided for a more accurate temperature reading.

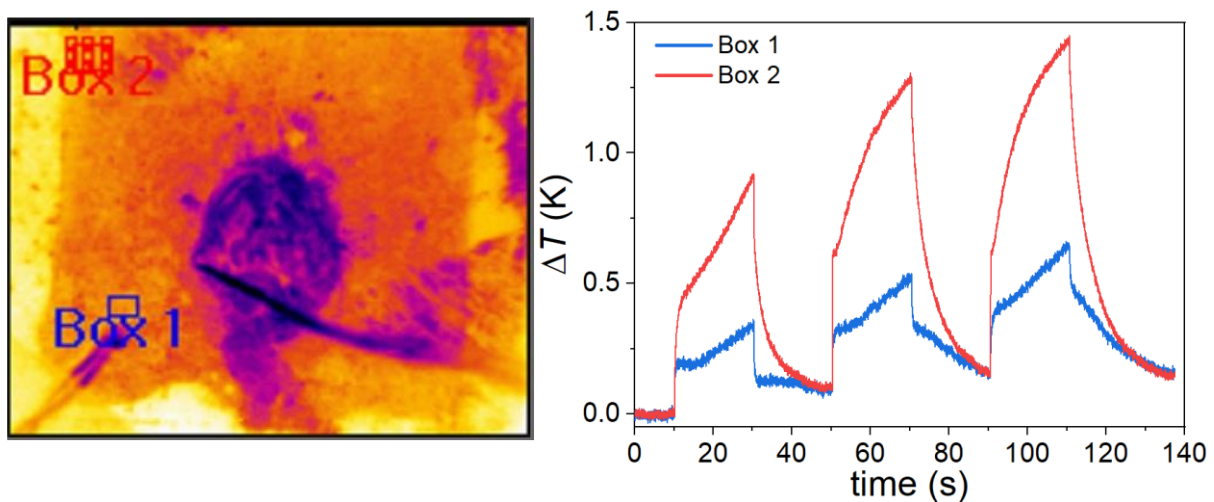


Figure 4-40. **Left:** the image of Pellet 1 in the IR camera. Box 1 and Box 2 sample areas for reading the temperature of the sample. **Right:** the temperature change in Box 1 and Box 2 when applying and removing $\Delta E = 11.2 \text{ kV cm}^{-1}$.

The adiabatic temperature change ΔT in Pellet 1 recorded by the IR camera is displayed in Fig. 4-41. In an EC material without unwanted Joule heating, one should expect ΔT as an instantaneous temperature change when there is an application or removal of E . Then followed by a slow decay when holding E constant, which is the heat exchange process with the environment after the temperature gradient ΔT is generated.

Here in our measurements, the instantaneous temperature change can be observed, and it should correspond to the ΔT due application or removal of the $E = 11.2 \text{ kV cm}^{-1}$. The biggest ΔT was observed as $\sim 0.5 \text{ K}$ when applying $E = 11.2 \text{ kV cm}^{-1}$ at $T_s = 323.0 \text{ K}$. For removing the field, the biggest value is $\sim 0.3 \text{ K}$ at $T_s = 322.6 \text{ K}$. However, instead of decaying over time as

described in Fig. 3-14, the temperature keeps increasing. This is due to the Joule heat dissipating when the electric field is held constant to the sample. This explains why the temperature changes more when E is applied (Joule heating plus heat exchange with the environment) than E is removed (only heat exchange with the environment). In an insulating sample, the gradient of temperature change should be the same when E is held constant or removed.

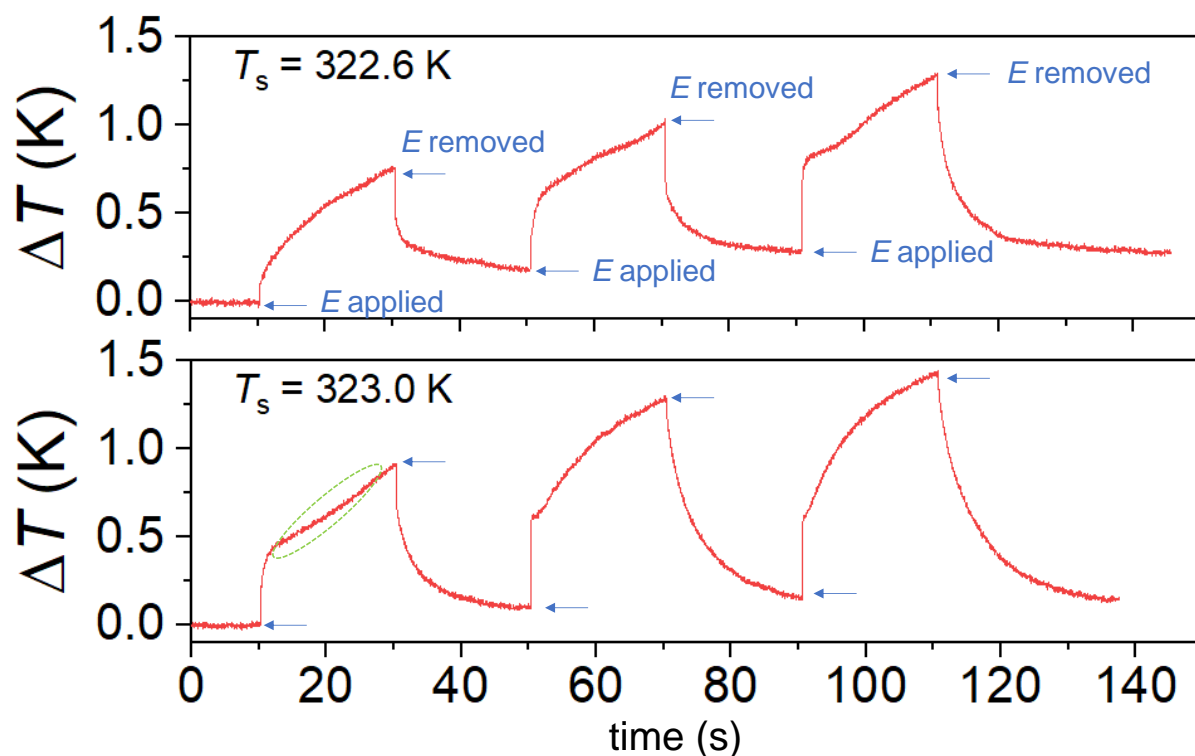


Figure 4-41. Adiabatic ΔT in Pellet 1 recorded by the IR camera at starting temperature $T_s = 322.6$ K and 323.0 K under $|\Delta E| = 11.2$ kVcm⁻¹. The arrows represent the application and removal of the electric fields. The green dotted circle marks the heat dissipation from Joule heating.

The same direct measurements were also performed in Pellet 2. It also shows the spatial variance of the temperature reading. The values of ΔT recorded by the IR camera and thermocouple are compared in Fig. 4-42. The magnitudes of ΔT from the two recording are similar and the response times to the electric field are very similar. The noise level of the IR camera is higher than that of the thermocouple. The IR camera shows a noise level of ~ 0.04 K while the thermocouple shows a noise level ~ 0.01 K. A possible explanation is the different rate of data acquisition. The IR camera records with the frame rate of 50 Hz while the thermocouple has only 4.5 Hz, so the data is ‘smoothed’ by the thermocouple.

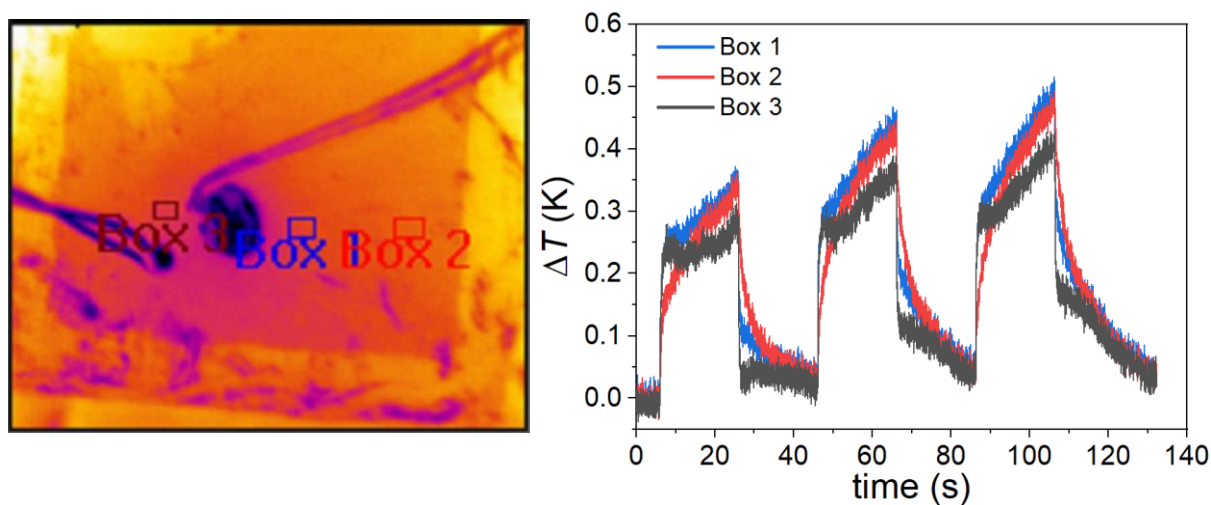


Figure 4-42. Left: the image of Pellet 2 in the IR camera. Box 1 and Box 2 sample areas for reading the temperature of the sample. Right: the temperature change in Box 1 and Box 2 when applying and removing $|\Delta E| = 11.2 \text{ kV cm}^{-1}$.

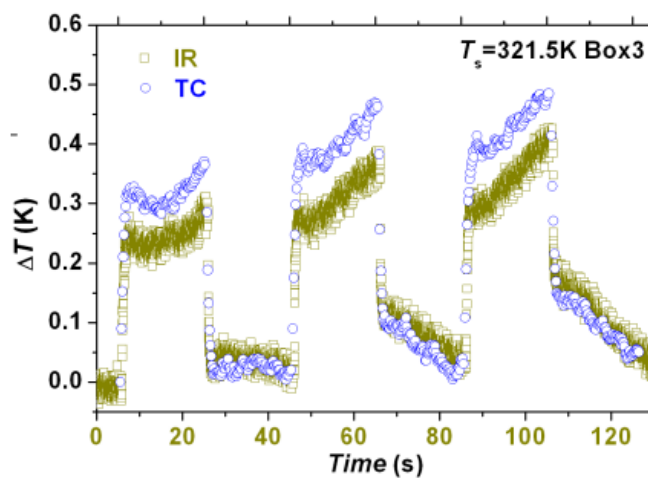


Figure 4-43. Comparison of values for ΔT recorded by the thermocouple (TC) and the IR camera (IR) for Pellet 2 at 321.5 K under $|\Delta E| = 11.2 \text{ kV cm}^{-1}$.

Fig. 4-44 shows the adiabatic ΔT in Pellet 2 recorded by the IR camera while fields were successively applied and removed at $|\Delta E| = 5.6 \text{ kV cm}^{-1}$ and 11.2 kV cm^{-1} . However, data for $|\Delta E| = 5.6 \text{ kV cm}^{-1}$ were only observed with Joule heating with distinguishable adiabatic change. Similar to Pellet 1, Pellet 2 was also observed to dissipate Joule heat when applying the electric field. This caused difficulties and inaccuracy in the measurement of adiabatic temperature changes. The ΔT over T_s is plotted and compared with the value derived from the indirect measurements in Fig. 4-45.

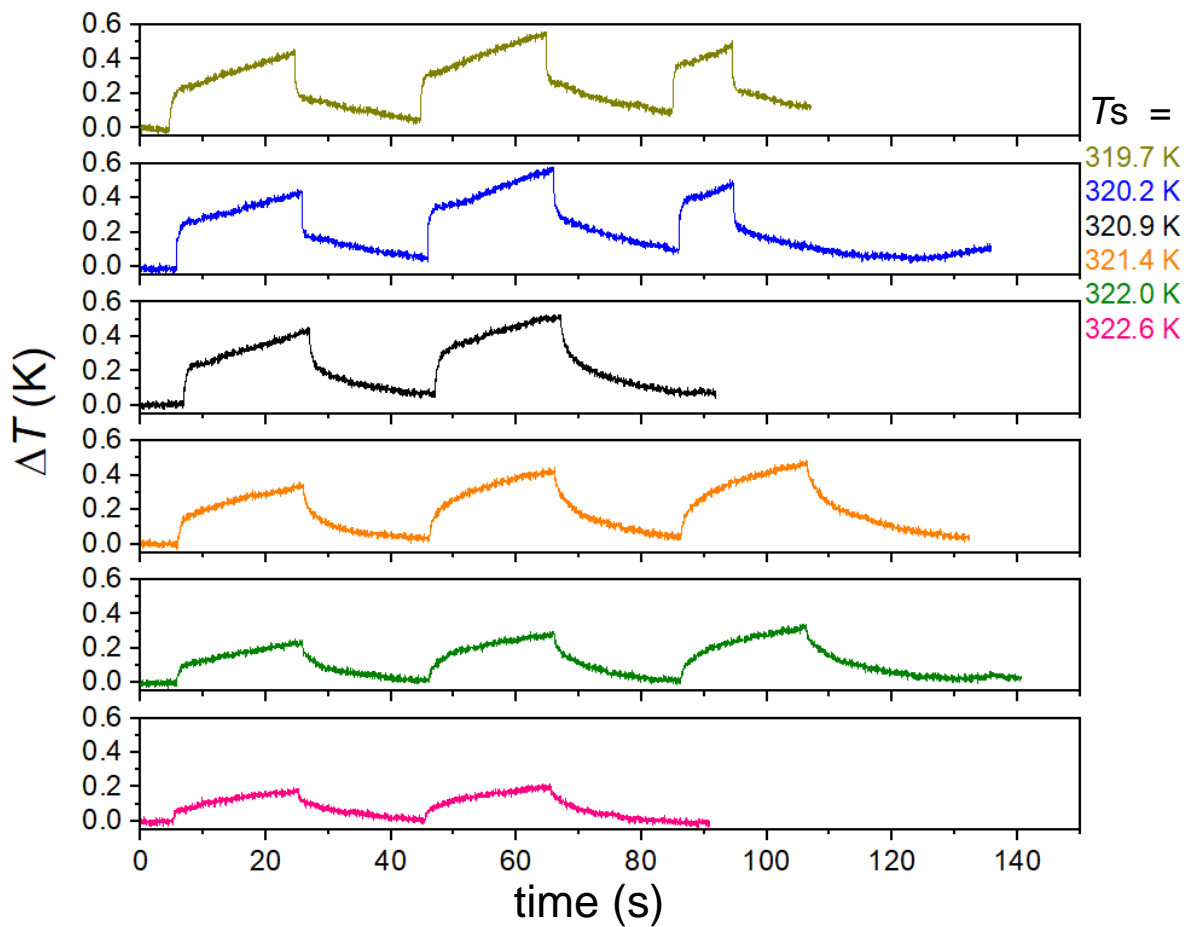


Figure 4-44. Adiabatic ΔT for Pellet 2 at different starting temperatures T_s , when the sample is subjected to $|\Delta E| = 11.2 \text{ kV cm}^{-1}$. Data recordings are all for Box 2.

Comparison of results from different methods

In Fig. 4-45 left, the ΔS in Pellet 1 from the indirect method and from the quasi-direct method are compared. The magnitudes of $|\Delta S/|$ are in a good agreement, with the $|\Delta S_{\max}| \sim 3.8 \text{ J K}^{-1} \text{ kg}^{-1}$ at $|\Delta E/| = 5.6 \text{ kV cm}^{-1}$ from the indirect method (data selected from Fig. 4-37) and the corresponding value of $|\Delta S_{\max}| \sim 3.8 \text{ J K}^{-1} \text{ kg}^{-1}$ from the quasi-direct measurement. Considering the dataset was measured in two different instruments, $\sim 2 \text{ K}$ difference in the peak position is understandable, marked in the different scale colours (black and dark green).

In Fig. 4-45 right, the $|\Delta T/|$ in Pellet 2 from the indirect method and from the direct method are compared. The magnitudes of $|\Delta T/|$ from the direct measurements are lower than the corresponding values from the indirect measurements. The results from the direct measurements are regarded as preliminary due to the uncertainty resulted from Joule heating, which is out of control during measurements.

Owing to the uncertainty, an error bar is plotted for the data of direct measurements, as shown in Fig. 4-45 right. The blue and red dots are the average values of multiple cycles of application and removal of $|\Delta E/|$ as shown above in Fig.4-44. As explained previously, each data point of $|\Delta T/|$ was recorded as the instantaneous temperature change shown when there is an application or removal of $|\Delta E/|$. The upper and lower bounds of the error bar represent the highest and lowest observed values, respectively. This error bar should give an indication of how the value of $|\Delta T/|$ varies during repeated cycles. Ideally, more cycles are needed to improve the confidence of the data reading and to do some statistical analysis.

Even though an error bar is added, the joule heat still exists and significantly affects the direct measurements which involve holding a large electric field for 20 seconds. Therefore, a more insulating sample will be required for better comparison. Alternatively, a creditable approach to subtract Joule heating from $|\Delta T/|$ reading can also generate better datasets for comparison.

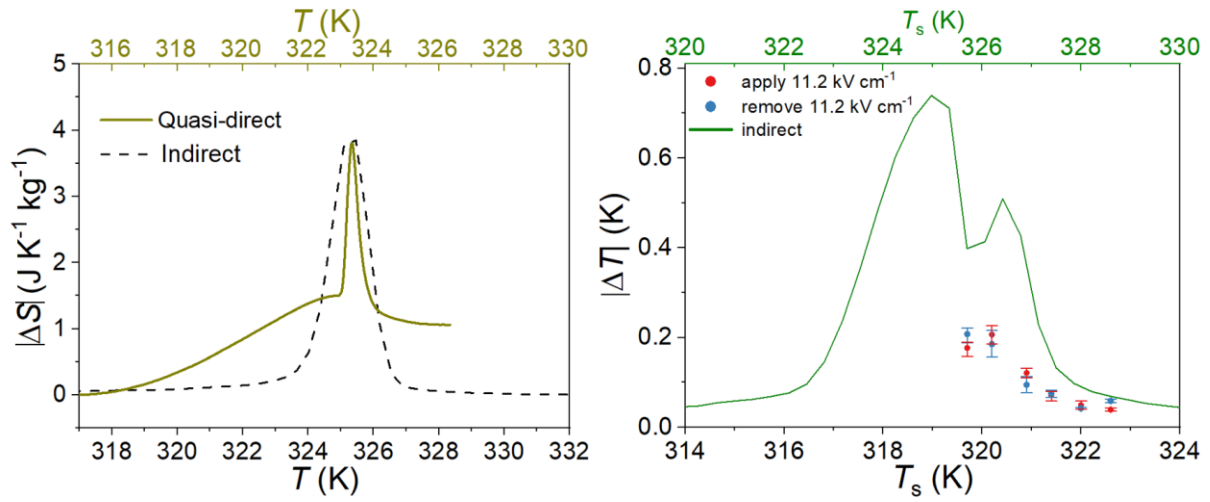


Figure 4-45. Left: Comparison between indirect method (black dotted line) and quasi-direct method (dark green) for $|\Delta S|$ in Pellet 1 under $|\Delta E| = 5.6 \text{ kV cm}^{-1}$. Right: Comparison between indirect method (green line) and direct method (red and blue dots) for $|\Delta T|$ in Pellet 2 under $|\Delta E| = 11.2 \text{ kV cm}^{-1}$. The dots are the average values. The upper and lower bounds of the error bar represent the highest and lowest observed values, respectively.

4.3.3. Landau modelling

Model construction

Similar to BF₄, LD modelling is also performed in AH. With the Curie-Weiss constant ~ 1445 K and $T_0 = 317$ K derived from the dielectric constant data shown in Fig. 4-33, we obtain $a = 8.19 \times 10^7 \text{ C}^{-2} \text{ m}^{-2} \text{ N K}^{-1}$ and $T_0 = 317$ K.

Then four equations were chosen for fitting the Landau coefficient b , c and two other values T_C and P_s . Results of $T_C = 322.5$ K and $P_s = 3.26$ match well the experimental data.

- $\Delta F = 0$ at T_C
- $\partial F / \partial P = 0$ at T_C
- $\partial F / \partial P = 0$ at $T = 324.3$ K and $P_s = 2.52 \mu\text{C cm}^{-2}$
- $\Delta S_0 = \frac{1}{2} a P_s$ at $P_s = 2.45 \mu\text{C cm}^{-2}$, $\Delta S_0 = 17.8 \text{ J K}^{-1} \text{ kg}^{-1}$

The model parameters are obtained as below,

Table 4-4. Landau coefficients derived for AH.

<i>a</i>	$8.19 \times 10^7 \text{ C}^{-2} \text{ m}^{-2} \text{ N K}^{-1}$
<i>b</i>	$-1.70 \times 10^{12} \text{ C}^{-4} \text{ m}^6 \text{ N}$
<i>c</i>	$1.19 \times 10^{15} \text{ C}^{-6} \text{ m}^{10} \text{ N}$
T_0	317 K

Model results

Overall, we find that there is good agreement between our model and experiments. The discrepancies between the observed and calculated ΔS are due to the fact that the phase transition is not instant.

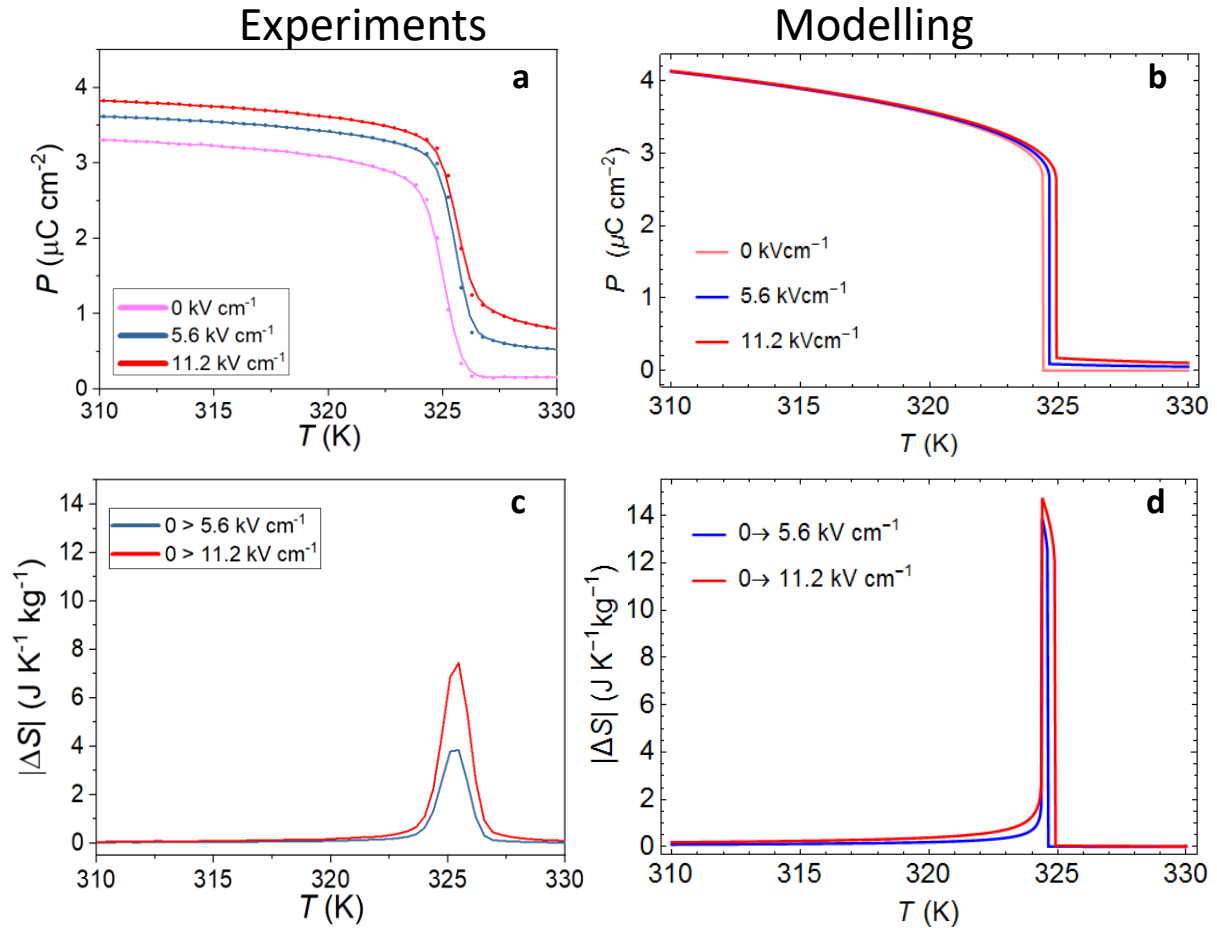


Figure 4-46. Comparison of results from experiments (left) and Landau modelling (right). (a)(b): $P(T)$ under electric fields. (c)(d): $\Delta S(T)$ driven by electric fields.

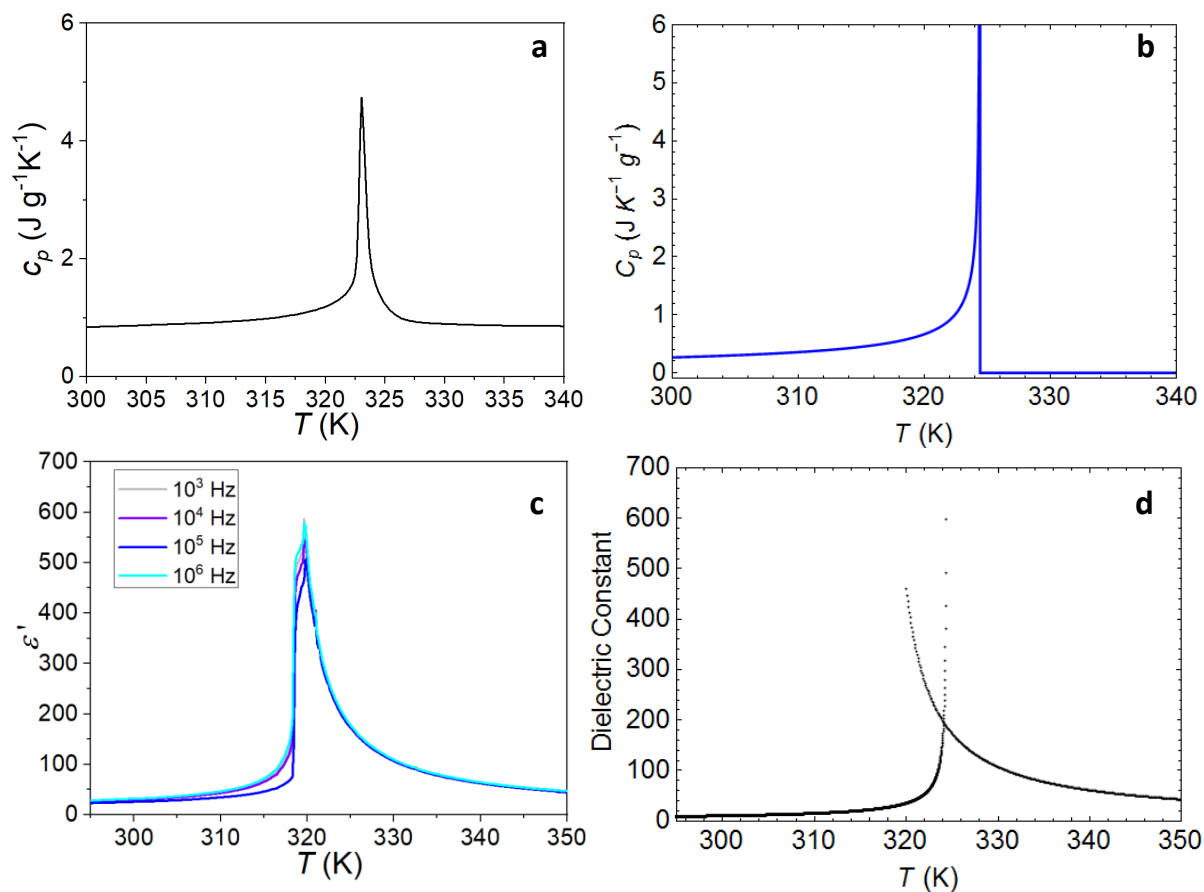


Figure 4-47. Comparison of results from experiments (left) and Landau modelling (right). **(a)(b):** heat capacity $c_p(T)$ under zero fields. **(c)(d):** Dielectric constant as function of T .

High-field EC effects predicted by the model are large over a wide range of temperatures and gives a wide range of starting temperatures when the first-order ferroelectric phase transition is driven supercritically.

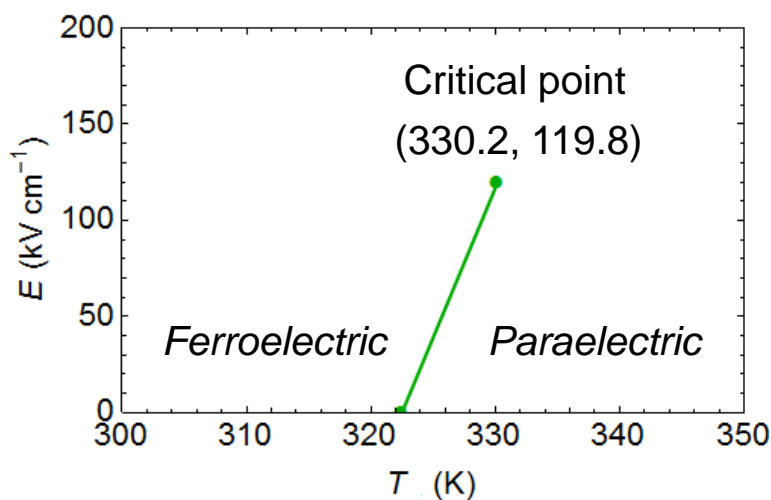


Figure 4-48. Calculated E - T phase diagram for BF4.

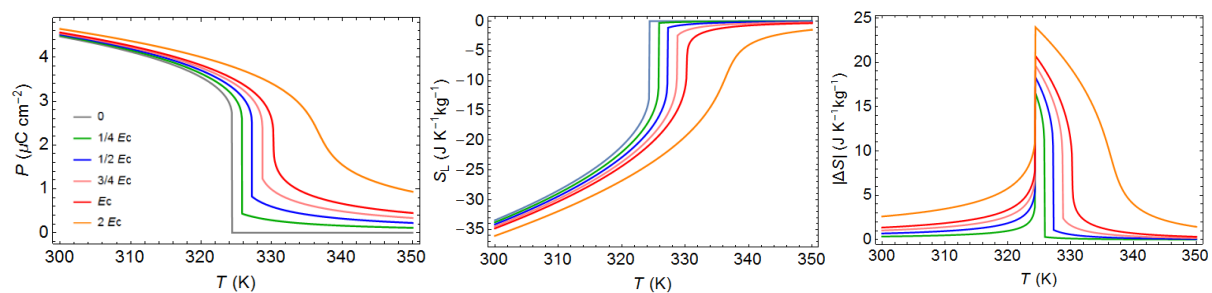


Figure 4-49. The model results of $P(T, E)$, $S_L(T, E)$ and $|\Delta S(T, E)|$ at high electric fields up to $2E_C$, where $E_C = 119.8 \text{ kVcm}^{-1}$.

4.4 Conclusions

Summary

In this chapter, I presented both experimental measurements and Landau modelling for evaluating the EC effects in [Hdabco][BF₄] and [AH][ReO₄], which are molecular ferroelectric materials with similar structures.

In [Hdabco][BF₄], indirect measurements based on the Maxwell relation have been used to evaluate the isothermal entropy change ΔS induced by electric field. The ‘standard’ indirect measurements give $\Delta S \sim -11.5 \text{ J K}^{-1} \text{ kg}^{-1}$ while ‘modified’ indirect measurements give $\Delta S \sim -15.5 \text{ J K}^{-1} \text{ kg}^{-1}$ in response to $|\Delta E| = 12 \text{ kV cm}^{-1}$ near the transition at 376 K.

However, due to the electrical and mechanical breakdown of samples, no sufficiently high electric field was applied to shift the T_C . Landau model predicts that $|\Delta E| = 663.6 \text{ kV cm}^{-1}$ can drive BF₄ to the critical points and access a wider range of operating temperatures.

In [AH][ReO₄], indirect, quasi-direct and direct measures were performed to evaluate ΔS and ΔT . The indirect measurements give $|\Delta S| \sim 3.9 \text{ J K}^{-1} \text{ kg}^{-1}$ at $|\Delta E| = 5.6 \text{ kV cm}^{-1}$ which is in a good agreement with the quasi-direct value $|\Delta S| \sim 3.8 \text{ J K}^{-1} \text{ kg}^{-1}$. The direct measurements give $|\Delta T| \sim 0.2 \text{ K}$ for $|\Delta E| = 11.2 \text{ kV cm}^{-1}$, which is lower than the corresponding value $|\Delta T| \sim 0.7 \text{ K}$ from the indirect method. Landau model predicts that $|\Delta E| = 119.8 \text{ kV cm}^{-1}$ give drive [AH][ReO₄] to the critical points, which is achievable by fabricating thin films. This will lead to $|\Delta S| \sim 20 \text{ J K}^{-1} \text{ kg}^{-1}$ within $\sim 20 \text{ K}$ of operating temperature range without loss from thermal hysteresis.

Conclusions

Overall, molecular ferroelectric materials BF₄ and AH show the highest EC strength among the reported EC materials. Moreover, this material family shows great tunability in the ferroelectric and mechanical properties via chemical alteration. This work can open the possibility for a new class of ferroelectric materials for EC cooling.

While working on those projects, the author started to realise the difficulty of achieving sufficient entropy change using an electric field without unwanted Joule heating or electric breakdown. In the next chapter, pressure is used to drive the entropy change in Dabco-based ferroelectric materials.

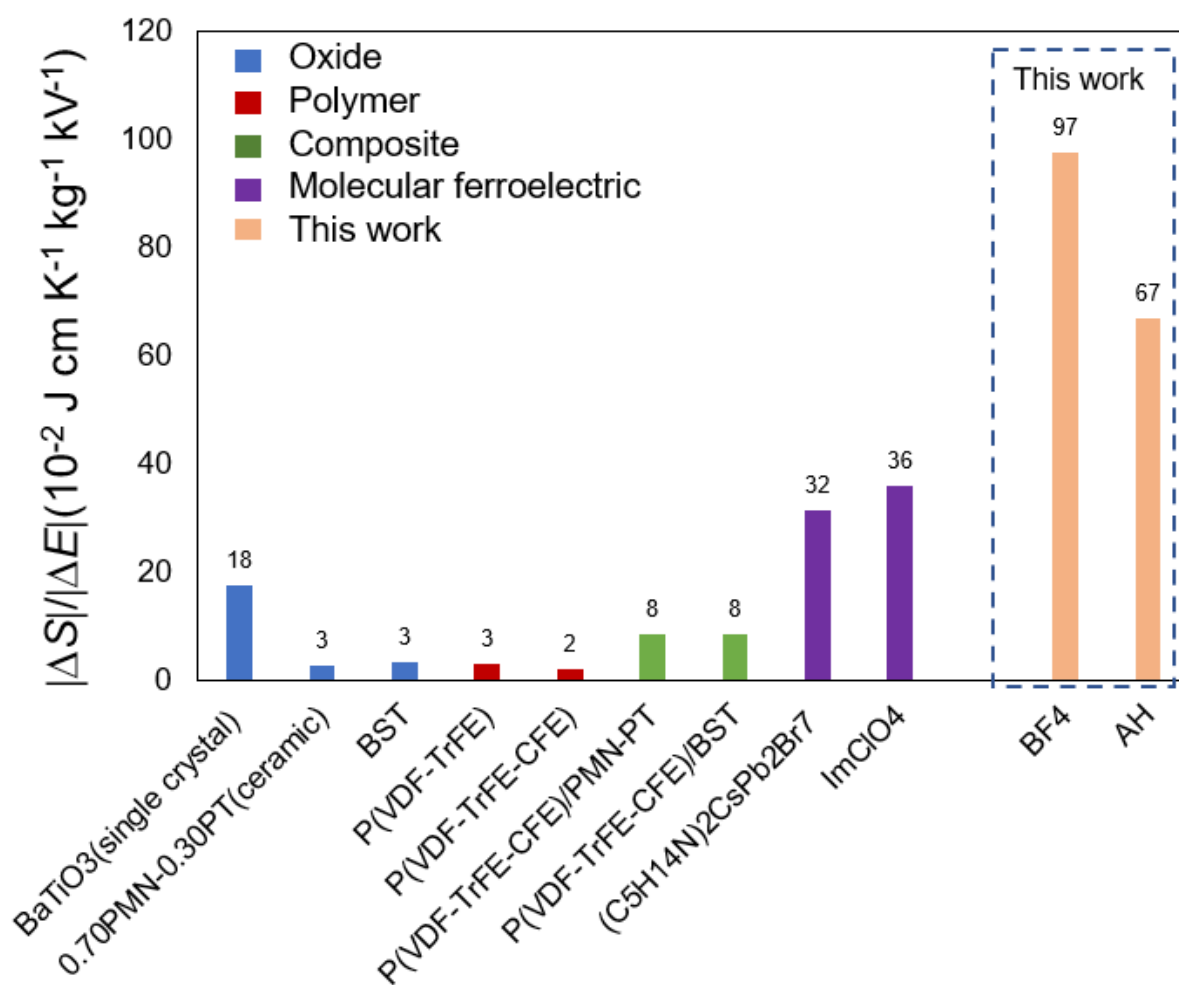


Figure 4-50. comparison of EC strength of BF4 and AH against other reported EC materials.

5. Barocaloric effects in Dabco-based ferroelectric materials

5.1 Overview

Motivation

The aforementioned BF₄ and two materials with similar composition, namely [Hdabco][ClO₄] and [Hdabco][ReO₄], are very promising for EC effects because of their large changes in entropy. However, they suffer from electrical leakage and therefore Joule heating, which ultimately lead to breakdown. Eventually, insulating crystals were only obtained in BF₄ composition for investigating EC effects. Crystals in the other two compositions were found too leaky for EC measurements. For convenience, [Hdabco][ClO₄] and [Hdabco][ReO₄] are referred as ClO₄ and ReO₄.

Using hydrostatic pressure to drive caloric effects in these materials overcome the mentioned limitations. In ferroelectric materials, the ferroelectric-paraelectric phase transition is associated with changes in crystal structures and volume. Therefore, pressure can be an alternative field to drive the caloric effects in ferroelectric materials. Moreover, applied pressure does not generate Joule heating so the thermal response driven by pressure is not compromised. This suggests promising BC effects in BF₄, ClO₄ and ReO₄ due to their large $|\Delta S_0|$.

In the following, this chapter describes the experimental results and how the results were used to evaluate BC effects in BF₄, ClO₄ and ReO₄.

5.2 Experiments

5.2.1 Material synthesis

The synthesis of BF_4 is described in Chapter 4. The synthesis of ClO_4 and ReO_4 is similar, both via the slow-evaporation method. The precursor materials 1,4-diazabicyclo[2.2.2]octane (Dabco), perchloric acid solution (HClO_4 , 70 wt. % in H_2O) and perrhenic acid solution (HReO_4 , 77 wt. % in H_2O) were purchased from Sigma-Aldrich. Water was obtained from a Millipore Simpapak 2 water purification system. All materials were used as received.

The HClO_4 (2 ml, 23.2 mmol) and Dabco (2.60 g, 23.2 mmol) were mixed in water (20 ml) at a 1:1 mole ratio. The HReO_4 (1 ml, 6.6 mmol) and Dabco (0.74 g, 6.6 mmol) were mixed in water (5 ml) at a 1:1 mole ratio. The mixed aqueous solution is placed in a glass jar covered by a piece of Parafilm with slits, which let the water evaporate at room temperature.

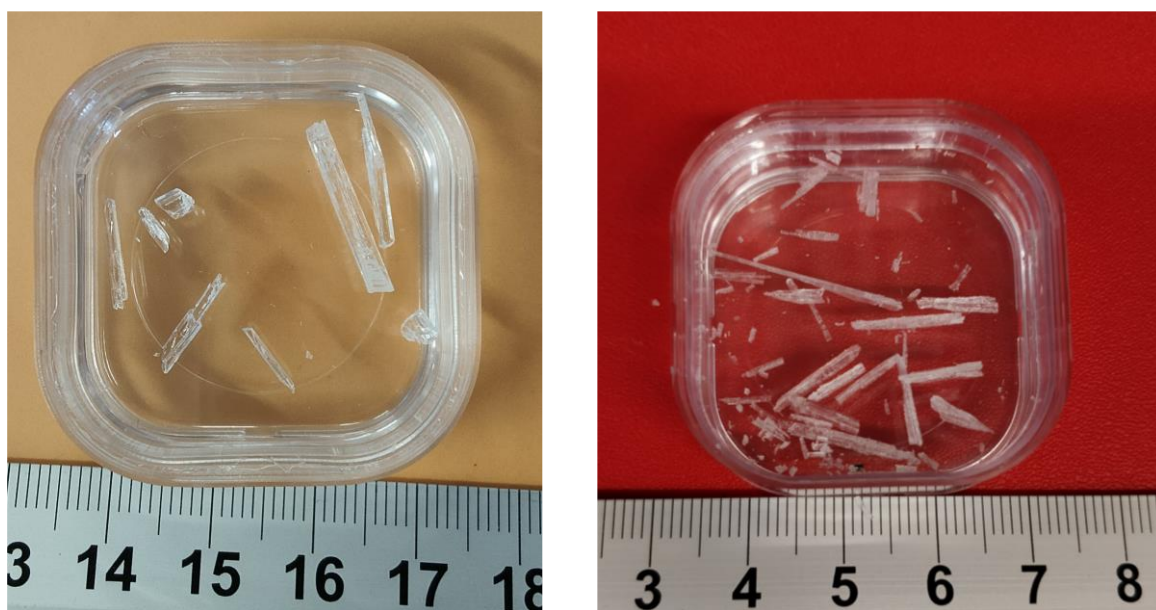


Figure 5-1. The transparent crystals of ClO_4 (left) and ReO_4 (Right). The unity of the scale is in centimetre(cm).

5.2.2 X-ray diffraction

Measurements of X-ray diffraction at room temperature (292 K) on the ClO₄ and ReO₄ powder samples are shown in Fig. 5-2. The crystal structure from our diffraction pattern matches with database^{161,162}, indicating the correct chemical composition and no secondary crystalline phases.

Temperature-dependant X-ray diffraction data are used from literature^{95, 96} to identify the crystal structure at different temperatures, as shown in Table 5-1. Also, the lattice parameter as a function of temperature yields the specific volume as a function of temperature $V_{sp}(T)$, which is used for deriving the volume change at T_C , ΔV_0 and the entropy change associated with thermal expansion.

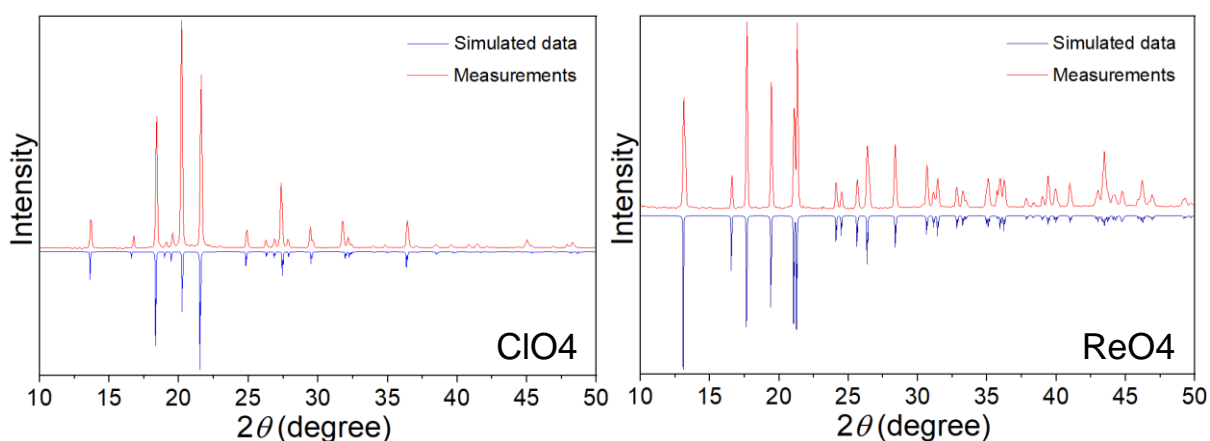


Figure 5-2. Comparison of the simulated XRD pattern from databased and the experimentally measured one in ClO₄ and ReO₄ powder samples at room temperature.

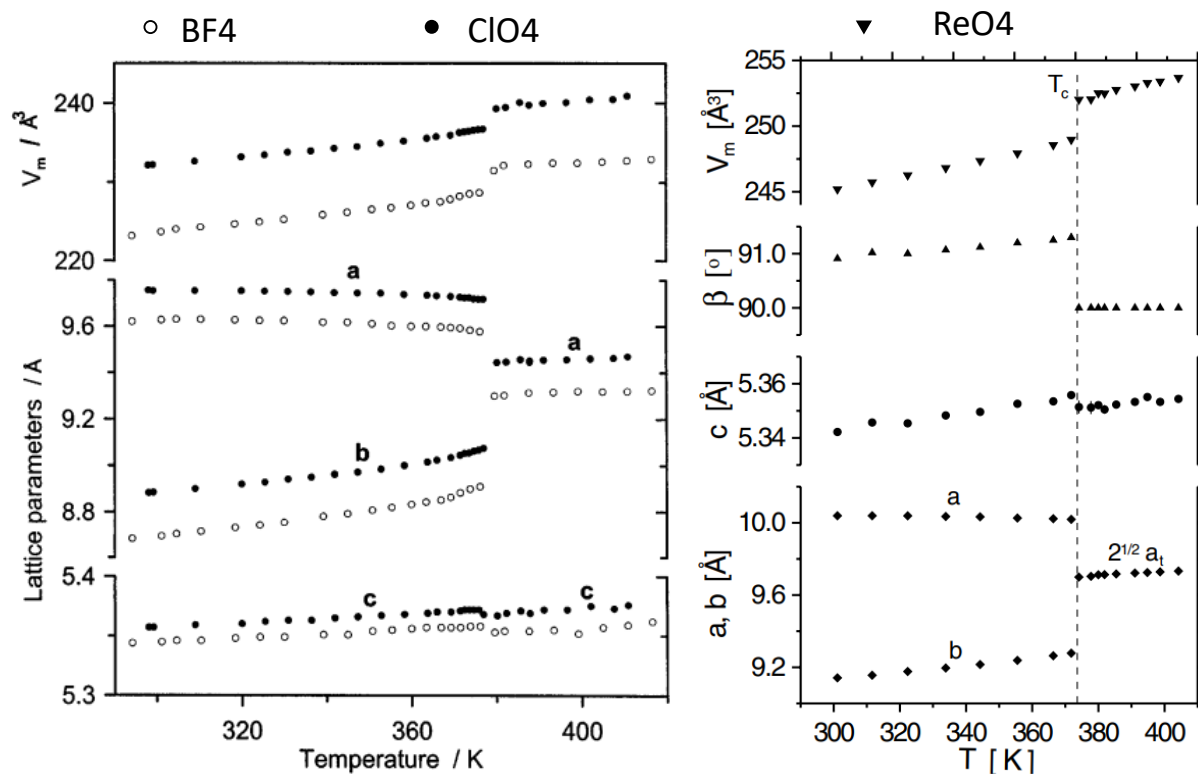


Figure 5-3. Left: Temperature dependence of the unit-cell dimensions and molecular volume of BF₄⁹⁵ and ClO₄⁹⁵. Right: The temperature dependence of the unit-cell dimensions in ReO₄⁹⁶.

Table 5-1. The crystal structures of BF₄, ClO₄ and ReO₄. The information was taken from ref^{95,96}.

	Below T_c	Above T_c
BF₄	Orthorhombic	Tetragonal
ClO₄	Orthorhombic	Tetragonal
ReO₄	Monoclinic	Tetragonal

The specific volume as a function of temperature $V_{sp}(T)$ is evaluated from the molecular volume V_m from above. V_{sp} is V_m divided by the weight of a single molecular, which is molecular weight divided by Avogadro constant, $N_A = 6.022 \times 10^{23} \text{ mol}^{-1}$. After conversion, the $V_{sp}(T)$ for BF_4 , ClO_4 and ReO_4 is displayed in Fig. 5-4. The volume change at the transition $|\Delta V_0| = 8.52 \times 10^{-6} \text{ m}^3 \text{ kg}^{-1}$ (1.2%), $10.50 \times 10^{-6} \text{ m}^3 \text{ kg}^{-1}$ (1.6%) and $5.71 \times 10^{-6} \text{ m}^3 \text{ kg}^{-1}$ (1.4%) for BF_4 , ClO_4 and ReO_4 , respectively. Notable, the magnitude of $|\Delta V_0|$ is calculated as the difference between two neighbouring points at the jump. However, the temperature interval is $\sim 4 \text{ K}$ for BF_4 , $\sim 4 \text{ K}$ ClO_4 and $\sim 8 \text{ K}$ for ReO_4 , which might be larger than the region of phase transition. Therefore, the $|\Delta V_0|$ could be overestimated.

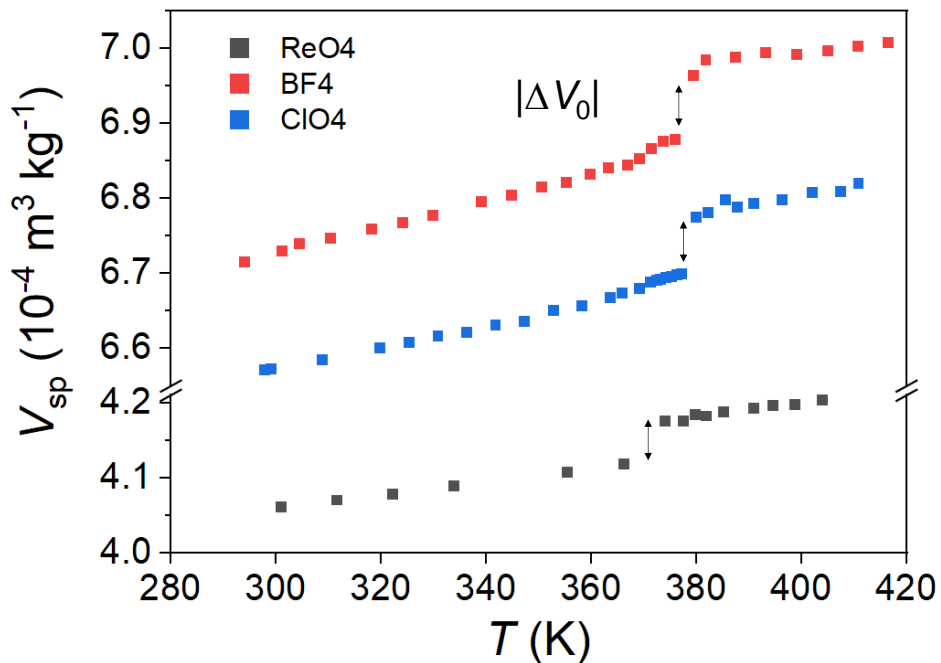


Figure 5-4. Specific volume $V_{sp}(T)$ derived with molecular volume data from ref^{95,96}. The data was taken using the digitizer(apps.automeris.io), which might be subjected to errors during data reading.

5.2.3 Calorimetry under zero pressure

The results of heat flow measurements of BF4 are presented in Chapter 4. Heat flow measurements at a heating rate of 5 K min⁻¹ were performed on the ClO4 and ReO4 crystals of mass ~ 8.949 mg and ~ 9.360 mg, respectively.

ClO4 undergoes a reversible phase transition at 374 K on cooling and 380 K on heating, with a hysteresis of ~ 4 K, as shown in Fig. 5-5. The latent heat $|Q_0| \sim 26 \text{ J g}^{-1}$. The entropy change under zero pressure is $|\Delta S_0| \sim 61.1 \text{ J K}^{-1} \text{ kg}^{-1}$ (Fig. 5-4).

ReO4 has phase transition at 372 K on cooling and 378 K on heating, with ~ 6 K hysteresis. The latent heat is $|Q_0| \sim 12 \text{ J g}^{-1}$, and the zero-field entropy change is $|\Delta S_0| \sim 31.6 \text{ J K}^{-1} \text{ kg}^{-1}$. This indicates smaller BC effects than ClO4 and BF4.

Table 5-2. Calorimetry results of BF4, ClO4 and ReO4.

	<i>T_c</i> on heating (K)	<i>T_c</i> on cooling (K)	ΔS (J K⁻¹ kg⁻¹)	Q_0 (kJ K⁻¹ kg⁻¹)
BF4	375	380	58.0	21
ClO4	374	380	61.1	26
ReO4	372	378	31.6	12

Those observations of $|\Delta S_0|$ are in good agreement with the data of Katrusiak, A. and Szafranski, M^{95,96}, with less than a 3% of difference except ClO4. Katrusiak, A.'s corresponding $|\Delta S_0|$ in ClO4 is ~ 70.1 J K⁻¹ kg⁻¹ while ours is ~ 61.1 J K⁻¹ kg⁻¹. This could be due to a difference in the integration baseline. The values of $|\Delta S_0|$ are higher than the EC effects $|\Delta S| \sim 11.5 \text{ J K}^{-1} \text{ kg}^{-1}$ in BF4 driven by a $|\Delta E| = 12 \text{ kV cm}^{-1}$. This indicates a much higher cooling power of BC than EC in Dabco-based ferroelectric materials if the full phase transition can be achieved by pressure.

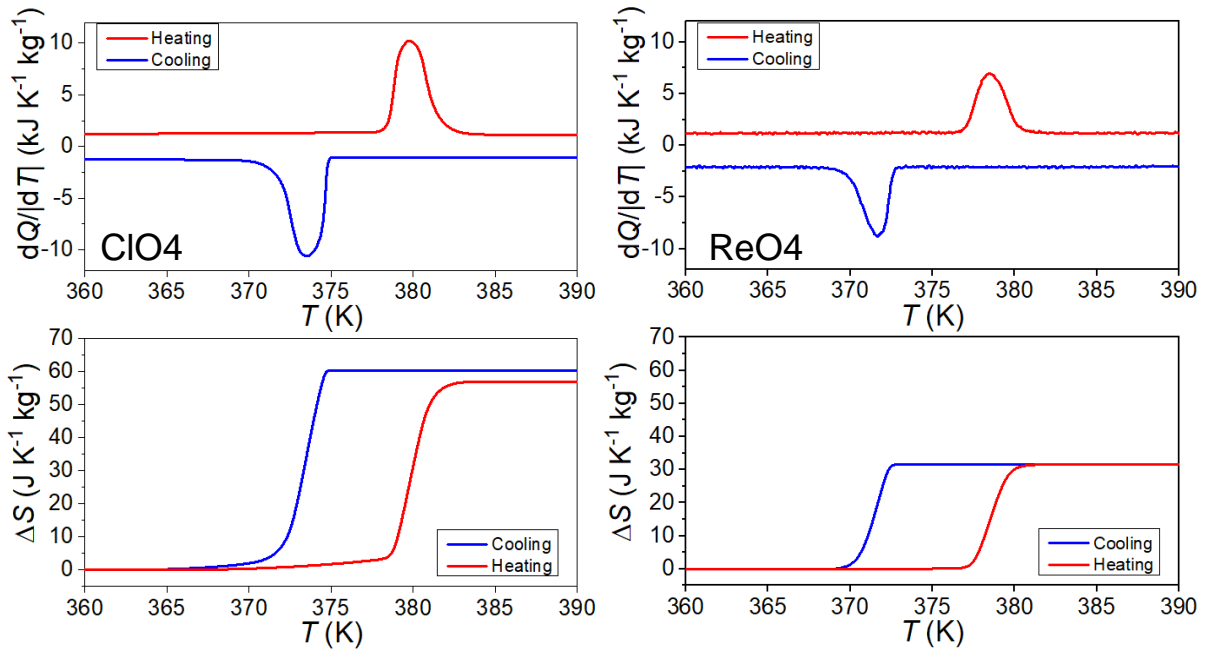


Figure 5-5. Top: Heat measurements. $dQ/dT > 0$ means endothermic. **Bottom:** The values ΔS with respect to 360 K, which is derived from the integration of $(dQ/dT)/T$ over T . The left is for ClO_4 and the right is for ReO_4 .

The $c_p(T)$ results of BF_4 , ClO_4 and ReO_4 are displayed in Fig. 5-6. The baseline (in black) is to fit the c_p of the low-temperature and high-temperature phases, away from the phase transition. The entropy associated with thermal expansion without phase transition in the materials can be obtained from the $c_p(T)$ baseline. This is used later for constructing the S - T curve to evaluate the BC effects.

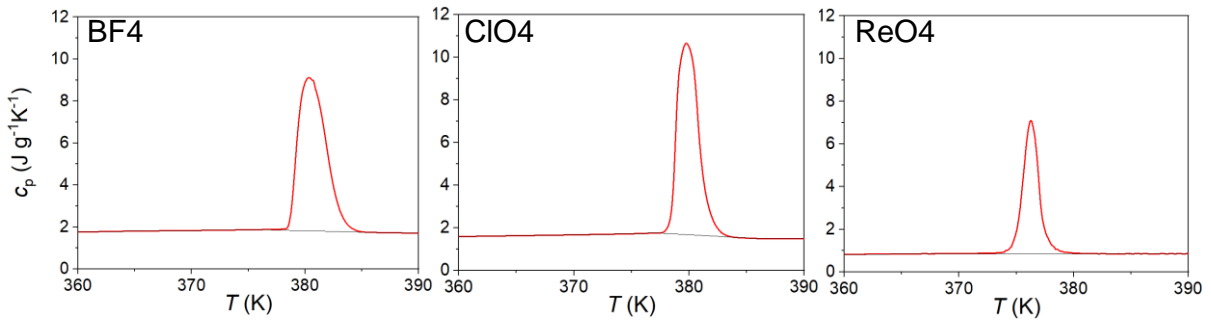


Figure 5-6. Specific heat capacity c_p measured from calorimetry on heating for BF_4 , ClO_4 and ReO_4 . The baseline (black) was identified via a cubic polynomial baseline fitting. This baseline represents the c_p at the ferroelectric and the paraelectric phases, without the contribution of latent heat.

5.2.4 Calorimetry under pressure

To study the barocaloric properties of BF₄, ClO₄ and ReO₄, calorimetry measurements at different pressures were performed using a Setaram Instrumentation μ DSC7 EVO microcalorimeter equipped with a 260D Isco pressure pump with nitrogen gas as a pressure-transmitting media. BF₄(46.3 mg), ClO₄(53.3 mg) and ReO₄(17.5 mg) crystal powders were measured at different isobaric pressures and at ± 1.2 K min⁻¹ heating or cooling rate. As the operating temperature is limited up to 393 K, above which phase transitions are not recorded.

As shown in Fig. 5-6, the pressure increase shifts the phase transition towards higher temperature. Those peaks also indicate that the first-order phase transition of width ~ 10 K. The values of T_C show a linear relation to the applied pressure. The barocaloric coefficients of dT_C/dp are shown as the linear slopes in Fig.5-7. are ~ 13.9 , 12.4 and 16.9 K kbar⁻¹ for BF₄, ClO₄ and ReO₄, respectively. Those values are comparable with those observed in other BC materials summarized in Table 5-6 at the end of this chapter. Based on the volume change $|\Delta V_0|$ at T_C from the $V_{sp}(T)$ in Fig. 5-4, and the $|\Delta S_0|$ from Fig. 5-5, Clausius–Clapeyron equation $\frac{dT_C}{dp} = \frac{\Delta V_0}{\Delta S_0}$, yields barocaloric coefficients of 14.7 , 12.1 and 18.4 K kbar⁻¹ for BF₄, ClO₄ and ReO₄, respectively. Those values are in good agreement.

Table 5-3. Comparison of dT_C/dp values from the calorimetry and the calculation based on Clausius–Clapeyron equation.

	dT_C/dp from calorimetry in Fig.5-7 (K kbar ⁻¹)	dT_C/dp from Clausius–Clapeyron equation (K kbar ⁻¹)
BF4	13.9	14.7
ClO4	12.4	12.1
ReO4	16.9	18.4

The direction of the shift in phase transition is because the low-temperature phase has lower volumes than the high-temperature phase. Therefore, the pressure enhanced the stability of lower volume low-temperature phase, shifting the T_C towards higher temperatures. This is consistent with the unite cell dimensions results shown in Fig.5-4.

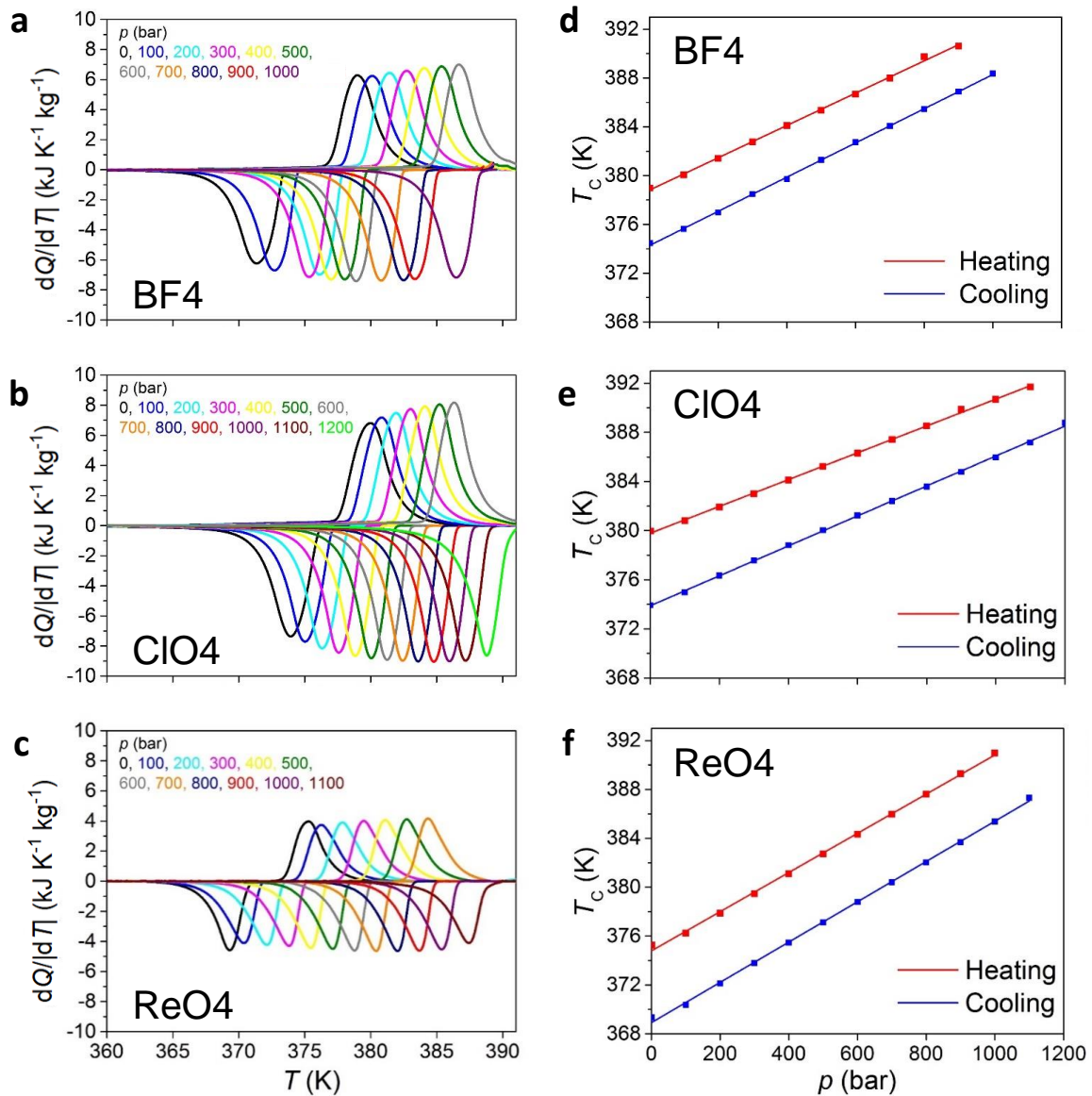


Figure 5-7. (a-c): Pressure-dependent calorimetry measurements under constant pressures, from 0 bar to 1200 bar for BF₄, ClO₄ and ReO₄, respectively. The upward peaks are endothermic during heating and the downward peaks are exothermic during cooling. **(d-f):** Temperature-pressure phase diagram, with the paraelectric phase above and the ferroelectric phase below the phase boundary. The boundary on heating is different from on cooling due to the thermal hysteresis. The values of ferroelectric-paraelectric phase transition temperature T_c are derived from the peak positions in the left panel.

5.3 Evaluation of barocaloric effects

5.3.1 Construction of S - T curves

In order to evaluate the barocaloric effects, the entropy-temperature curve S - T is constructed as it is commonly used for designing the thermal pumps and the thermodynamic cycles. Key parameters such as isothermal entropy change ΔS and the adiabatic temperature change ΔT are deduced from the S - T curve. The quasi-direct method is the most common way of constructing the S - T curve and the key is to obtain the total entropy under different pressures^{113,121}. Then, isothermal entropy change is $\Delta S(p,T) = S'(p,T) - S'(0,T)$ and similarly the adiabatic temperature change is $\Delta T(p,T) = T'(p,S) - T'(0,S)$.

The construction of the entropy-temperature S' - T curve includes three contributions, as shown in Fig. 5-8:

- (1) the entropy change of transition ΔS_0 from latent heat
- (2) the entropy change due to heat capacity outside the transition S_C
- (3) the pressure-induced additional entropy change ΔS_+

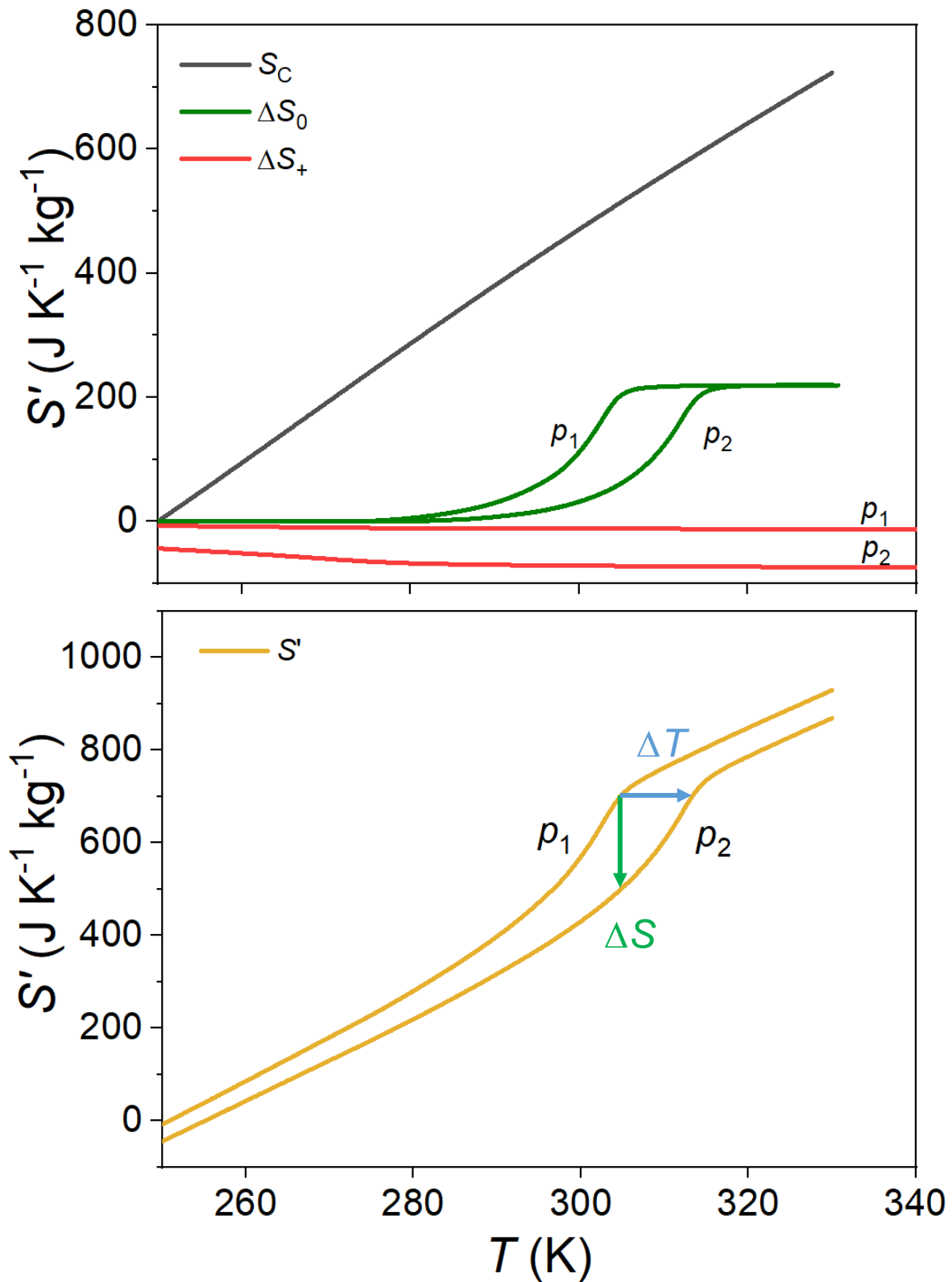


Figure 5-8. The construction process of S' curves and deduction of $|\Delta S|$ and $|\Delta T|$. **Top panel:** Three contributions ΔS_0 , ΔS_+ and S_C . **Bottom panel:** The sum-up of the entropy of the system as a function of temperature at different pressures. The vertical trajectory corresponds to $|\Delta S|$ and the horizontal trajectory corresponds to $|\Delta T|$ induced by pressure change $|\Delta p|$.

Firstly, the entropy change of transition ΔS_0 arises from the latent heat Q_0 . This can be calculated using $S' = \int_{T_1}^{T_2} (dQ/dT)/T dT$, where T_C is the transition temperature. Experimentally, the isobaric heat flow $dQ/|dT|$ over temperature under applied pressure was measured (Fig. 5-6). Fig. 5-9 shows the integration of $(dQ/|dT|)/T$ over temperature yields the entropy changes ΔS_0 for each pressure.

$|\Delta S_0|$ at a pressure ranging from 0 to 1200 bar is around $54.0 \text{ J K}^{-1} \text{ kg}^{-1}$, $64.8 \text{ J K}^{-1} \text{ kg}^{-1}$ and $28.7 \text{ J K}^{-1} \text{ kg}^{-1}$ for BF_4 , ClO_4 and ReO_4 , respectively. Those are all in good agreement with the value of $58.0 \text{ J K}^{-1} \text{ kg}^{-1}$, $61.1 \text{ J K}^{-1} \text{ kg}^{-1}$ and $31.6 \text{ J K}^{-1} \text{ kg}^{-1}$ obtained from the zero-pressure calorimetry, shown in Table. 5-2.

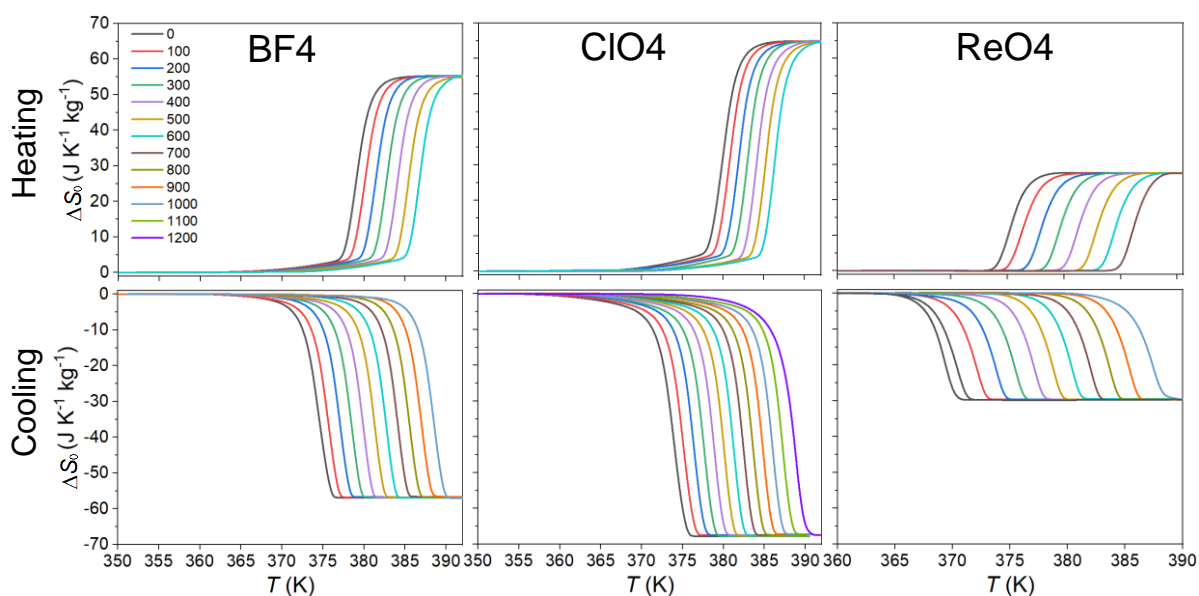


Figure 5-9. Isobaric temperature-dependent entropy curves at different pressures obtained on heating (**Top**) and on cooling (**Bottom**). The values of S' were from the integration of calorimetry peaks using $S_{350 \text{ K}} + \Delta S = S_{350 \text{ K}} + \int_{350 \text{ K}}^T (dQ/dT)/T dT$. Here, S' is with respect to $S(T = 350 \text{ K}, p = 0)$.

Secondly, the entropy change due to heat capacity outside the transition S_C is displayed in Fig.5-10. The results are deduced from the $c_p(T)$ at zero pressure data shown in Fig. 5-6 by using $S_C(T) = \int_{T_1}^{T_2} \left(\frac{C_p(T)}{T}\right)_p dT$. One thing to note is that c_p should exclude the contribution from latent heat to avoid double counting the $|\Delta S_0|$ from the previous step. The subtraction is shown in the black baseline fitting in Fig. 5-6. In the following construction of entropy-temperature curve at different pressure, c_p is assumed unchanged after applying pressures.

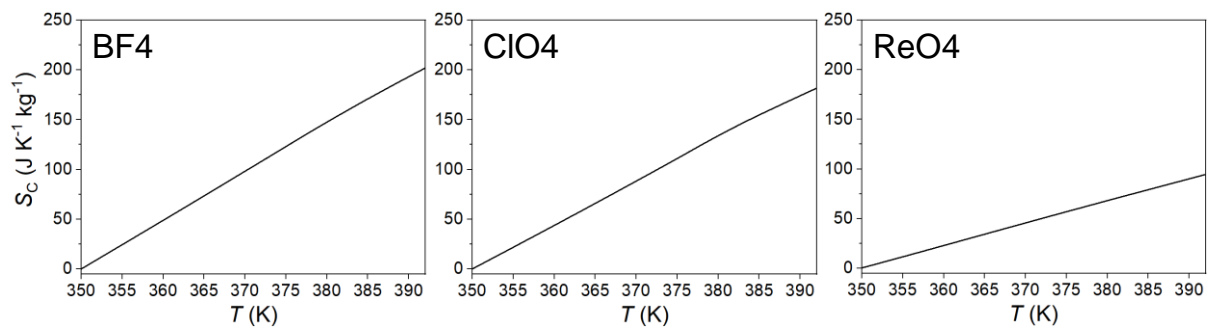


Figure 5-10. S_C the entropy change due to heat capacity. The values are deduced from the $c_p(T)$ data after excluding $|\Delta S_0|$ from the latent heat, as shown in the black baseline in Fig. 5-6. $S_C(T) = \int_{T_1}^{T_2} \left(\frac{C_p(T)}{T}\right)_p dT$.

Thirdly, the pressure-induced additional entropy change ΔS_+ can be calculated using Maxwell relation as $\Delta S_+(p) = -\int_{p_1}^{p_2} \left(\frac{\partial V}{\partial T}\right)_p dp$, where $\left(\frac{\partial V}{\partial T}\right)_p$ is assumed to be independent of pressure i.e. $\left(\frac{\partial V}{\partial T}\right)_p \approx \left(\frac{\partial V}{\partial T}\right)_{p=0}$. Maxwell relation is also applied for the indirect method²³ to evaluate the caloric effects. In the case of barocaloric effects, the specific volume V_{sp} as the order parameter, is typically measured as a function of field at different temperatures. Alternatively, one can equally measure the order parameter as a function of temperature at different fields. Here, this method is applied. Experimentally, $\left(\frac{\partial V}{\partial T}\right)_{p=0}$ was deduced from the slope of $V_{sp}(T)$. As the datasets are in a few discrete points with variation, linear fitting was performed in Fig. 5-11 to identify $\left(\frac{\partial V}{\partial T}\right)_{p=0}$. In this linear fitting, $\left(\frac{\partial V}{\partial T}\right)_p$ is assumed constant over T near phase transition. The values of $\left(\frac{\partial V}{\partial T}\right)_{p=0}$ are displayed in Table 5-4. To minimize the error.

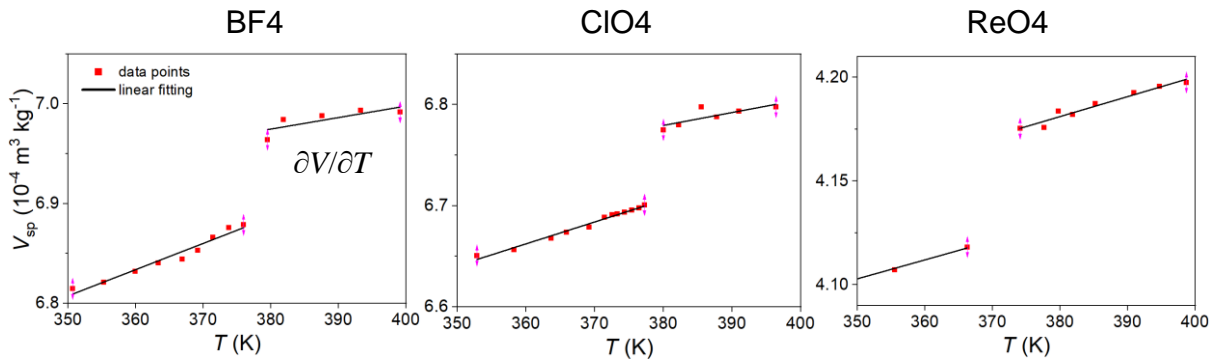


Figure 5-11. The $V_{sp}(T)$ at zero pressure in the region of interest(350-400 K). $(\partial V/\partial T)$ are derived from the linear fitting. The $V_{sp}(T)$ data was from ref^{95,96}.

Table 5-4. $(\partial V/\partial T)$ at zero pressure for BF4, ClO4 and ReO4.

	BF4	ClO4	ReO4
$\partial V/\partial T$ below T_C ($\text{m}^3 \text{kg}^{-1} \text{K}^{-1}$)	2.63×10^{-7}	2.17×10^{-7}	0.91×10^{-7}
$\partial V/\partial T$ above T_C ($\text{m}^3 \text{kg}^{-1} \text{K}^{-1}$)	1.15×10^{-7}	1.28×10^{-7}	0.96×10^{-7}

To make a conservative estimation of ΔS_+ , the $\left(\frac{\partial V}{\partial T}\right)_p$ of the high-temperature phase is used. If the low-temperature phase $\left(\frac{\partial V}{\partial T}\right)_p$ is adopted, the resulting difference in ΔS_+ is $\sim +15 \text{ J K}^{-1} \text{kg}^{-1}$ for BF4 under 1000 kbar. In addition, we assume $\left(\frac{\partial V}{\partial T}\right)_p$ is constant for pressure up to 1200 bar.

The $|\Delta S_+|$ results are displayed in Fig.5-12. Notably, $(\frac{\partial V}{\partial T})_p$ tends to decrease at very higher pressure as shown in literature¹⁶³, instead of staying constant. Therefore, this approximation could lead to an overestimation of $|\Delta S_+|$ and thus the total $|\Delta S|$.

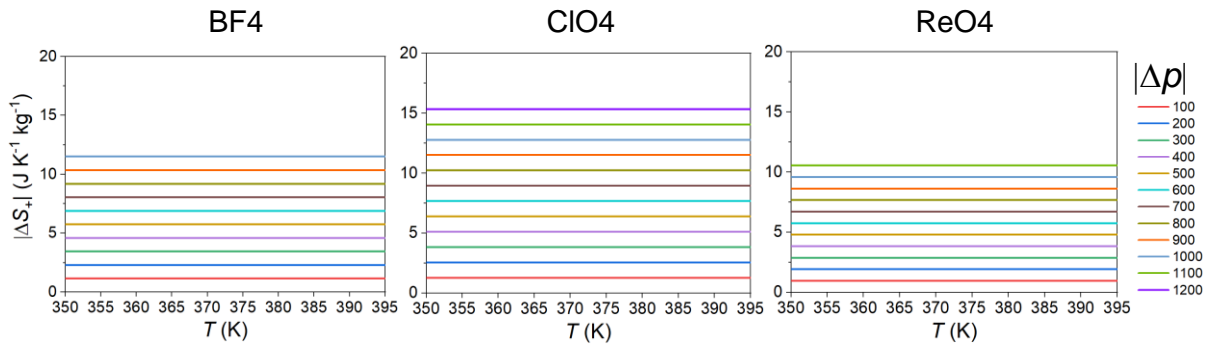


Figure 5-12. The pressure-induced additional entropy change ΔS_+ . The pressure change $|\Delta p|$ is in the unit of bar. The results are used to construct the entropy-temperature $S'-T$ curve.

After combining $|\Delta S_0|$, S_C and ΔS_+ as illustrated above, the derived entropy-temperature curve $S'(T,p)$ with respect to the absolute entropy at 350 K and $p \sim 0$ is shown in Fig. 5-13. By following isothermal trajectories in the plots of $S'(T,p)$ obtained on cooling, we were able to evaluate $\Delta S(T, \Delta p)$ on increasing pressure. Similarly, by following isothermal trajectories in the plots of $S'(T,p)$ obtained on heating, we were able to evaluate $\Delta S(T, \Delta p)$ on decreasing pressure.

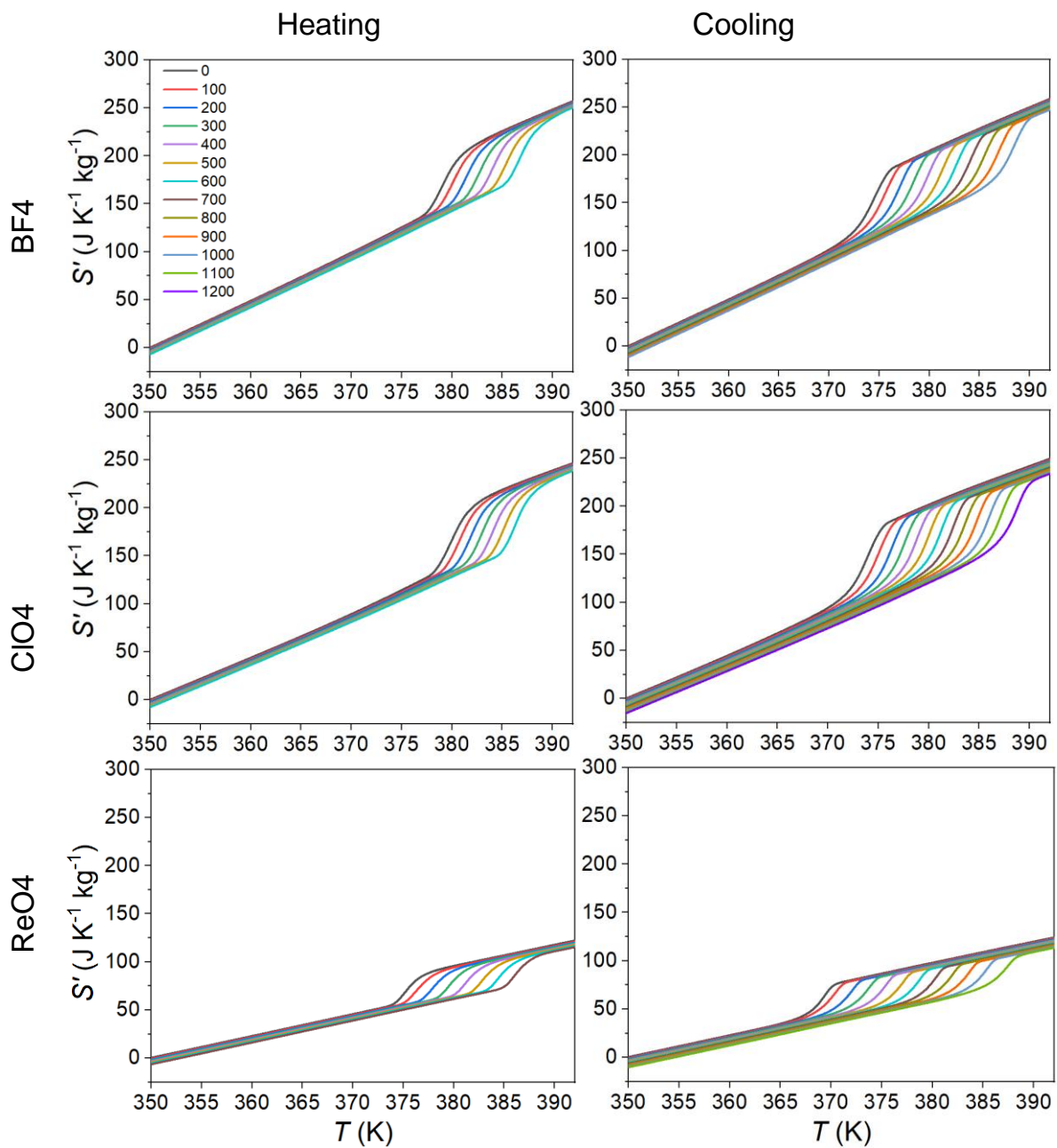


Figure 5-13. Entropy $S'(T,p)$ with respect to the absolute entropy at 350 K and $p \sim 0$ on heating(**left**) and cooling(**right**). The legend represents the values of applied pressure in bar.

5.3.2 Isothermal entropy changes

Fig.5-14 shows the $\Delta S(T, \Delta p)$ derived from the $S-T$ curves in Fig. 5-13. This shows the values of entropy change when the material is subjected to a pressure change ($p \rightarrow 0$ or $0 \rightarrow p$) in an isothermal condition, i.e. the application or removal of the pressure is sufficiently slow such that the temperature is unchanged. The application of pressure leads to a negative ΔS because the pressure makes the material more ordered while the removal of pressure leads to a positive ΔS because the material becomes less ordered. Among these three materials, ClO4 has the highest $|\Delta S|$ because of its highest $|\Delta S_0|$ from the latent heat.

The value of ΔS firstly increases to a max value ΔS_{\max} close to ΔS_0 near T_C and then stays constant. This means the full entropy from the phase transition is achieved by pressure. At high pressures, the value of ΔS_{\max} is larger than ΔS_0 . This is because of the contribution from ΔS_+ due to the pressure, which exists both within and outside the phase transition. Our largest isothermal entropy change $|\Delta S_{\text{peak}}|$ as a function of $|p|$ is shown in Fig. 5-15(Top).

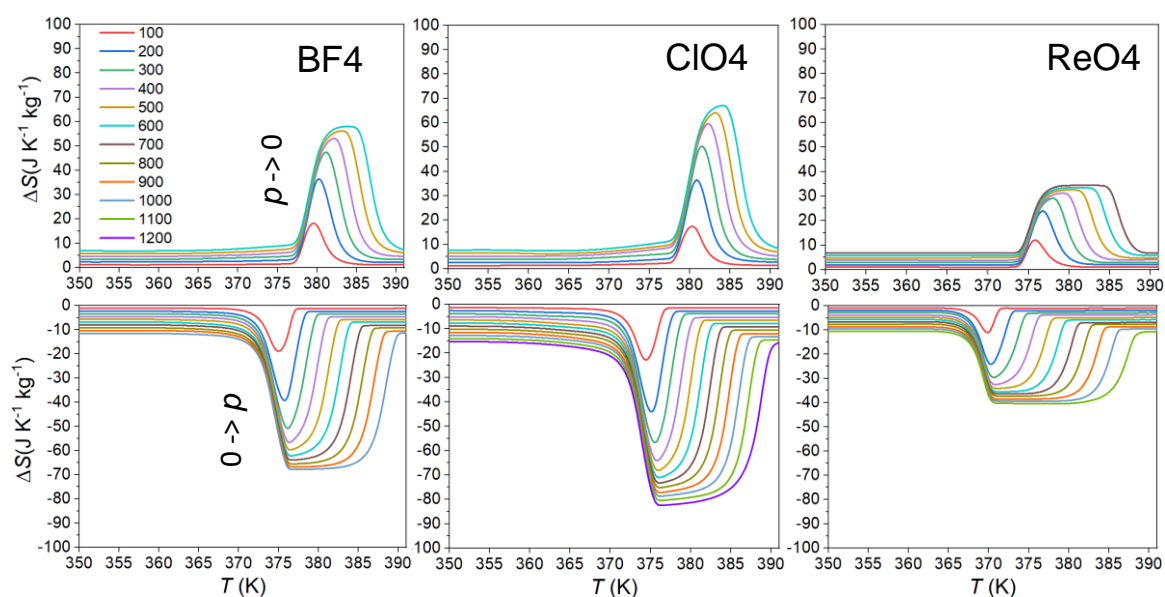


Figure 5-14. Isothermal entropy change ΔS on applying ($0 \rightarrow p$, shown in left) and removing ($p \rightarrow 0$, shown in right) pressures, deduced from Fig. 5-13.

Based on the data of ΔS , the parameter refrigerant capacity (RC) can be defined as $RC = |\Delta S_{\text{peak}}| \times [\text{FWHM of } \Delta S(T)]$. RC is the product of ΔS_{peak} and the temperature range at which the value of the entropy change becomes half of the maximum, also known as the full width at half maximum (FWHM). The purpose of RC is to measure the capability of transferring energy because it has the same unit (J kg^{-1}) with work and heat. The maximum RC is around 1000 J kg^{-1} , 1300 J kg^{-1} and 700 J kg^{-1} for BF_4 , ClO_4 and ReO_4 , respectively.

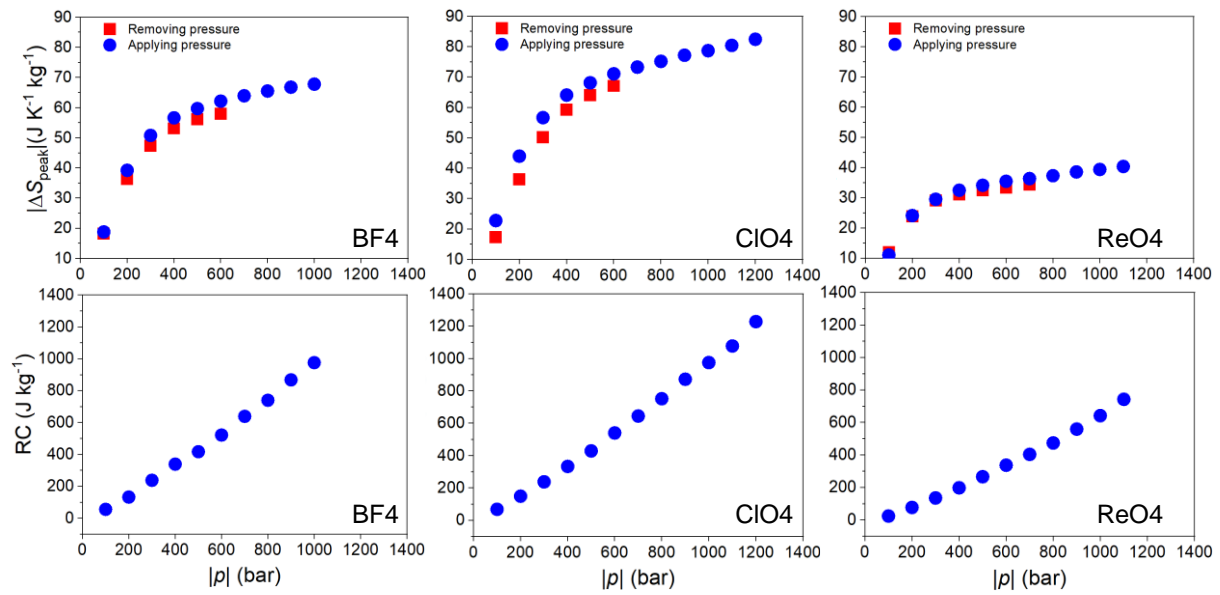


Figure 5-15. Top: the peak isothermal entropy change $|\Delta S_{\text{peak}}|$ for pressure changes of magnitude $|p|$, on applying pressure (blue) and removing pressure (red). The values are deduced from the peak maximum in Fig.5-14. **Bottom:** refrigerant capacity (RC) as a function of pressures. $RC = |\Delta S_{\text{peak}}| \times [\text{FWHM of } \Delta S(T)]$.

5.3.3 Adiabatic temperature changes

By following adiabatic trajectories in $S'(T, p)$ (Fig. 5-13), we established both the adiabatic temperature change $\Delta T(T_s, \Delta p)$ on increasing and decreasing pressure at starting temperature T_s . This shows the values of ΔT when the material is subjected to a pressure change ($p \rightarrow 0$ or $0 \rightarrow p$) in an adiabatic condition i.e. the application or removal of the pressure is sufficiently fast such that the heat exchange with the environment can be ignored. The results of $\Delta T(T_s, \Delta p)$ are displayed in Fig. 5-16. Among these three materials, ReO4 shows the highest ΔT because ReO4 has the smallest ΔS_0 so the transition temperature is shifted most. This is explained in following paragraph.

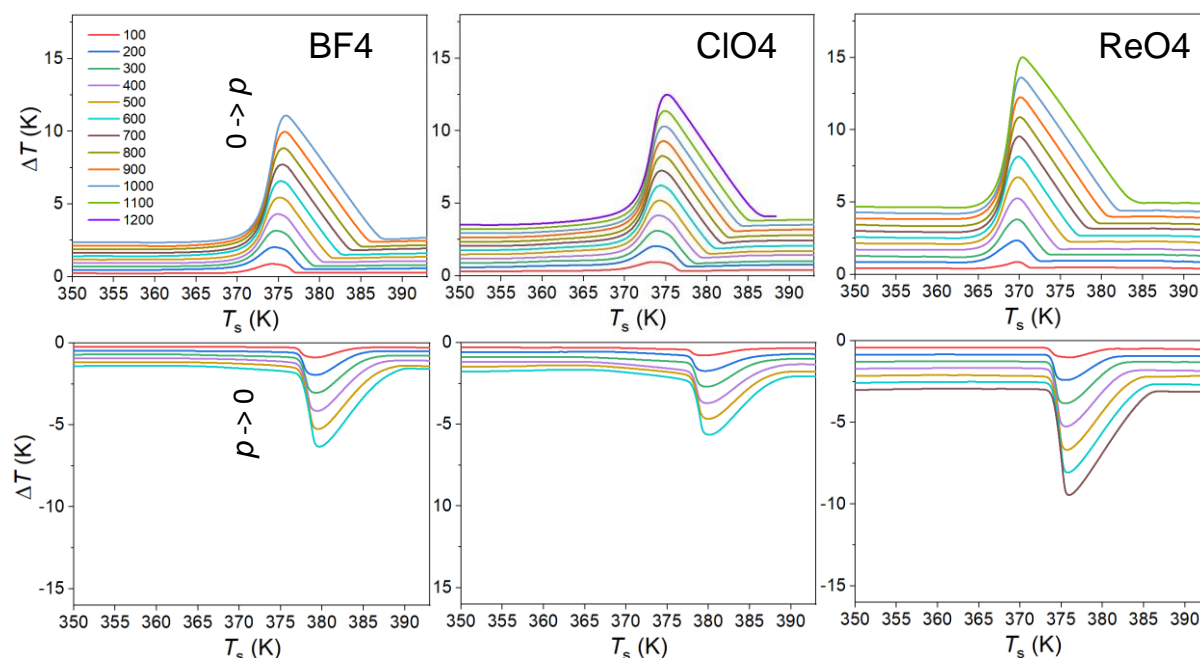


Figure 5-16. Adiabatic temperature change ΔT as a function of starting temperature (T_s) on applying ($0 \rightarrow p$) (Top) and removing ($p \rightarrow 0$) pressures (Bottom). The results are deduced from Fig. 5-13.

The largest adiabatic change $|\Delta T_{\text{peak}}|$ increases linearly with $|p|$, as shown in Fig. 5-17(Top). The value $|\Delta T_{\text{peak}}|/|p|$ is close to but smaller than the dT_C/dp from Clausius–Clapeyron equation. As shown in the adiabatic trajectories in $S'(T, p)$ (Fig. 5-13), the $|\Delta T_{\text{peak}}|$ is nearly the magnitude of T_C shifted by the p . Without considering S_C and ΔS_+ , $|\Delta T_{\text{peak}}|/|p|$ should be the same with dT_C/dp from Clausius–Clapeyron equation.

Table 5-5. Comparison of $|\Delta T_{\text{peak}}|/|p|$ and dT_C/dp from Clausius–Clapeyron equation.

	$ \Delta T_{\text{peak}} / p $ in Fig.5-17 (K kbar ⁻¹)	dT_C/dp from Clausius–Clapeyron equation (K kbar ⁻¹)
BF4	11.1	14.7
ClO4	10.4	12.1
ReO4	13.6	18.4

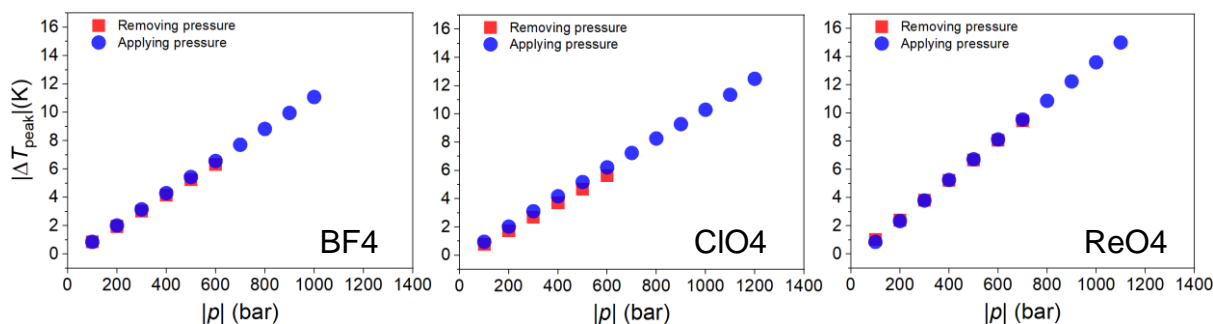


Figure 5-17. The peak adiabatic temperature change $|\Delta T_{\text{peak}}|$ for pressure changes of magnitude $|p|$, on applying pressure (blue) and removing pressure (red). The values are deduced from the peak maximum in Fig. 5-16.

5.3.4 Reversibility

Due to the thermal hysteresis, the ΔS and ΔT shown above are not fully reversible. When the material is in paraelectric phase, the application of pressure can lead to the transition from paraelectric phase to the ferroelectric phase, if the pressure crosses the phase boundary (the blue line). This is because the ferroelectric phase has lower volume and is thus stabilised by the pressure. However, the subsequent removal may not cause a reverse of the phase transition because the transition from the ferroelectric phase to the paraelectric phase follows another phase boundary (the red line). Therefore, only the EC effects above $T_C(p=0, \text{heating})$ are reversible, partially or totally.

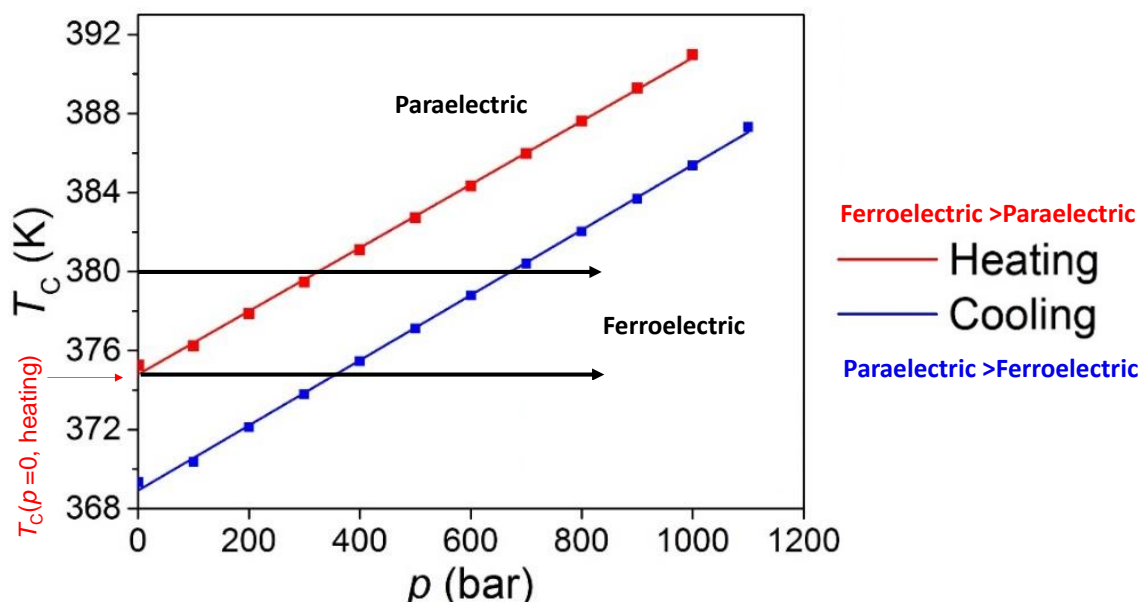


Figure 5-18. Schematic $T-p$ phase diagram showing that BC effects are only reversible above $T_C(p=0, \text{heating})$ because of the thermal hysteresis.

The reversible BC effects can be derived by following isothermal trajectories between $S'(T,p)$ on cooling and $S'(T,p=0)$ on heating. This yields the reversible part of ΔS on increasing and then decreasing pressure. Similarly, the reversible ΔS can be obtained by following adiabatic trajectories between $S'(T,p)$ on cooling and $S'(T,p=0)$ on heating. The results of reversible ΔS and ΔT are shown in Fig. 5-19. The peak values of reversible BC effects are shown in Fig. 5-20. Specifically, the reversible $|\Delta S|$ is $63.9 \text{ J K}^{-1} \text{ kg}^{-1}$, $73.2 \text{ J K}^{-1} \text{ kg}^{-1}$ and $38.2 \text{ J K}^{-1} \text{ kg}^{-1}$ in BF_4 ,

ClO4 and ReO4 respectively. The reversible $|\Delta T|$ is 7.4 K, 7.4 K and 9.9 K in BF4, ClO4 and ReO4 respectively.

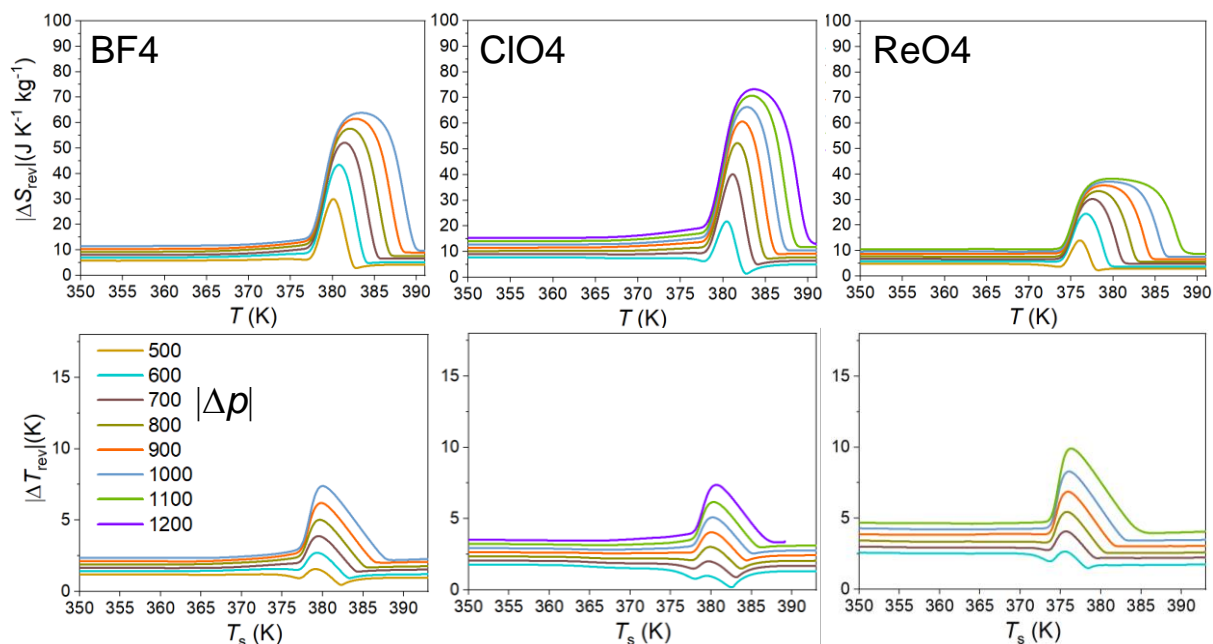


Figure 5-19. (a): Reversible isothermal entropy change ΔS_{rev} as a function of starting temperature (**Top**) and Adiabatic temperature change ΔT_{rev} as a function of starting temperature (T_s) (**Bottom**) on applying ($0 \rightarrow p$) and (**b**) removing ($p \rightarrow 0$) pressures, deduced from Fig. 5-13.

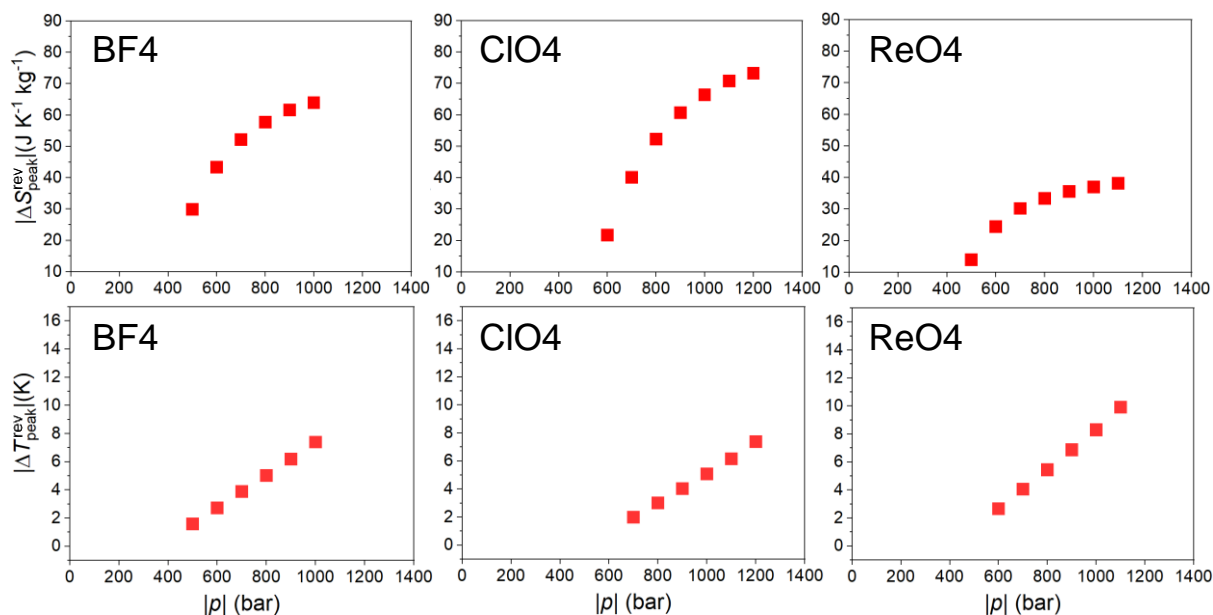


Figure 5-20. The peak reversible isothermal entropy change (**Top**) and reversible adiabatic temperature change (**Bottom**) for pressure changes of magnitude $|p|$. The values are deduced from the peak maximum in Fig. 5-19.

5.4 Conclusions

Summary

In this chapter, three ferroelectric materials, namely BF₄, ClO₄ and ReO₄, which are usually focused on EC effects, were studied for their BC effects via the quasi-direct method. The pressure-dependent calorimetry, specific heat capacity under zero pressure and temperature-dependent X-ray diffraction data from literature^{95,96} were combined for evaluating the ΔS and ΔT at the ferroelectric-paraelectric phase transition at ~ 380 K.

Conclusions

As shown in Table.5-6, the maximum reversible ΔS driven by pressure in BF₄ is five times higher than their irreversible EC counterparts. The reversible ΔT one order of magnitude higher than the corresponding irreversible EC counterparts. This suggests that a new research area of ferroelectric materials with high $|\Delta S_0|$. They are not only promising for the EC effects but also BC effects due to the coupling between the ferroelectric polarization and the crystal structure. In addition, BC effects can avoid mechanical and electrical breakdown. The studied materials can be used in the form of powders or fragments without compromising their BC effects, in order to improve heat exchange.

Regarding the BC effects, ClO₄ shows the largest reversible $|\Delta S| \sim 73.2 \text{ J K}^{-1} \text{ kg}^{-1}$ for $|\Delta p| = 1200$ bar due to its highest ΔS_0 . BF₄ shows reversible $|\Delta S| = 63.9 \text{ J K}^{-1} \text{ kg}^{-1}$ for $|\Delta p| = 1000$ bar, and ReO₄ shows reversible $|\Delta S| = 38.2 \text{ J K}^{-1} \text{ kg}^{-1}$ for $|\Delta p| = 1100$ bar. The maximum reversible $|\Delta T|$ observed is 7.4 K for BF₄ and ClO₄, and 9.9 K for ReO₄. The value of reversible ΔS of BF₄, ClO₄ and ReO₄ is higher or comparable to most of the reported BC materials and only falls behind NPG. The high reversible value of ΔS is because of the high ΔS_0 and relatively small hysteresis.

Overall, the organic ferroelectric materials that I studied have shown large BC effects and therefore could be an environmentally friendly alternative for the solid-state refrigerant in barocaloric heat pumps.

Table 5-6. Performance of caloric properties of BF₄, ClO₄ and ReO₄ to materials with reported giant barocaloric effects. T_c , transition temperature; $|\Delta S|$, isothermal entropy change; $|\Delta T|$, adiabatic temperature change; $|Q|$, isothermal heat; $|\Delta p|$, hydrostatic pressure required to drive the phase transition; RC, refrigerant capacity at $|\Delta p|$ pressure. $|\Delta S|$, $|\Delta T|$ and $|Q|$ arise at T_c , due to application of $|\Delta p|$.

Materials	T_c (K)	ΔS (J K ⁻¹ kg ⁻¹)	Q (J g ⁻¹)	ΔT (K)	Hysteresis (K)	RC (J kg ⁻¹)	dT/dp (K kbar ⁻¹)	$ \Delta p $ (bar)	Reversible	Reference
BF ₄ (EC effects)	375	11.5	4.3	0.48	5	17.3	-	$\frac{\Delta E}{12 \text{ kVcm}^{-1}}$	No	Chapter 4
BF ₄	375	63.9	24.0	7.4	5	639	13.9	1000	yes	This work
ClO ₄	374	73.2	27.4	7.4	5	681	12.4	1200	yes	This work
ReO ₄	372	38.2	14.3	9.9	5	471	16.9	1100	yes	This work
NPG	320	500	160.0	30	18	26000	10.3	5200	yes	¹²¹
Ni _{49.26} Mn _{36.08} In _{14.66}	293	24	7.0	4.5	10	120	1.8	2600	partially	⁸¹
LaFe _{11.35} Co _{0.47} Si _{1.2}	237	9	2.0	2.2	-	81	9.4	2000	partially	⁸⁶
Gd ₅ Si ₂ Ge ₂	270	11	3.0	1.1	5	180	3.8	2000	partially	⁸⁴
Fe ₄₉ Rh ₅₁	308	13	3.8	8.1	10	105	6.4	2500	partially	⁸⁵
Mn ₃ GaN	285	22	6.2	4.5	-	125	6.5	1400	partially	¹¹⁵
(MnNiSi) _{0.62} (FeCoGe) _{0.38}	330	70	23.1	16.0	15	1000	9.3	2700	yes	¹¹⁶
BaTiO ₃	400	2	0.6	1.5	4	10	5.6	1000	yes	¹¹¹
(NH ₄) ₂ SO ₄	219	60	13.1	8.0	6	276	5.7	1000	yes	¹¹³
(NH ₄) ₂ SnF ₆	110	61	6.7	11.0	0.5	450	15.7	1000	yes	¹⁶⁴
[TPrA]Mn[dca] ₃	330	31	10.1	4.1	1	500	23.1	68.9	yes	¹⁶⁵
[TPrA]Cd[dca] ₃	385	12	6.2	1.4	3	150	38.2	68.9	yes	¹⁶⁶
AgI	390	60	23.4	18	25	2500	14	2500	yes	¹¹⁴

6. Barocaloric effects in ureasil materials

6.1 Overview

Motivation

As discussed in previous chapters, a critical selection criteria for caloric materials is large isothermal entropy changes ΔS . Although Dabco-based ferroelectric materials have been found relatively large ΔS driven by pressure, they still fall behind commercial refrigerants. One underlying reason is that the ΔS between different crystal structures in solid states is limited. Therefore people are still seeking caloric materials with $|\Delta S|$ comparable to the commercial refrigerant, e.g. R134a.

Polymer materials tend to exhibit dramatically higher $|\Delta S_0|$ and $|Q_0|$ than the reported solid-solid phase transition because they have giant configurational change associated with crystallization^{81,167}, especially in the fusion process, which is the phase transition between the solid crystalline phase to the viscous amorphous phase. The BC effect for the liquid-solid-transition(fusion) in C_nH_{2n+2} ($n = 16$ and 18)¹⁶⁸ was reported with maximum $|\Delta S| \sim 700 \text{ J kg}^{-1} \text{ K}^{-1}$. Other common polymer materials, such as polyethylene glycol (PEG)¹⁶⁹ and polycaprolactone (PCL) show the values of $|\Delta S_0| \sim 500 \text{ J K}^{-1} \text{ kg}^{-1}$ during the fusion process. In contrast, the majority of solid-state barocaloric materials^{23,121} have shown entropy changes $|\Delta S_0|$ up to $80 \text{ J K}^{-1} \text{ kg}^{-1}$.

However, susceptibility to leaks makes the liquid state unfavourable, especially in the scenario of electronic applications. Herein, we demonstrate a new approach to transform the solid-liquid transition of polymers into a gel-to-solid phase transition as shown in Fig. 6-1. Ureasil and ureathanesil¹⁷⁰⁻¹⁷² are two classes of materials consisted of polymeric networks, which fulfill the above-mentioned requirements of gel-to-solid phase transitions while keeping their large $|\Delta S_0|$ associated with the latent heat. The solid-state transitions can avoid leaking issues and provide more possibilities for device designs.

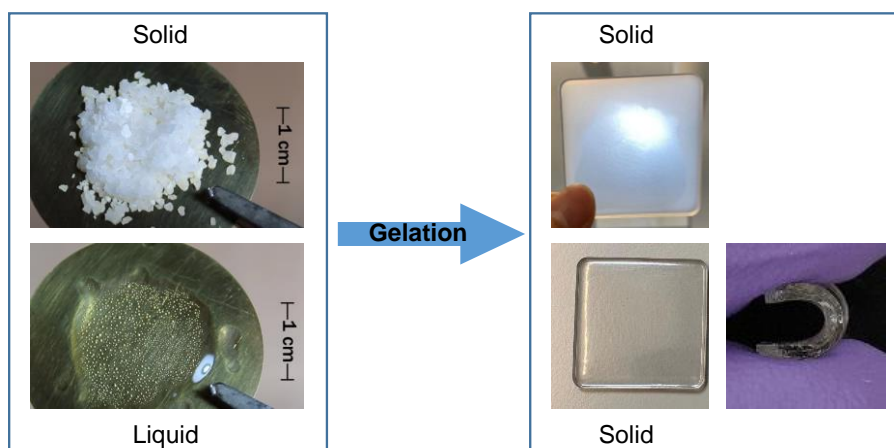


Figure 6-1. Left panel: before gelation, ED-2000 polymer has a solid-liquid phase transition, with the solid low-temperature phase and liquid high-temperature phase. Right panel: after gelation, ED-2000 turns into ED-2000 ureasil, which has a solid-solid phase transition, with the cloudy low-temperature phase as well as the transparent and flexible high-temperature phase.

The structures of ureasil and ureathanesil materials consist of poly(oxyalkylene) chains cross-linked to silica domains via urea linkages ($-\text{NH}(\text{C}=\text{O})\text{NH}-$)¹⁷³ or urethane linkages ($-\text{O}(\text{CO})\text{O}-$) respectively. The cross-linked siliceous network connects the polymer chains and confines the chain mobility in the amorphous phase, thus yielding the polymer in a gel state. In contrast, the amorphous phase is viscous liquid before gelation due to the sliding motion of molecular chains. In this work, ureasil and ureathanesil materials referred as ureasil for convenience because both serve for the gelation purpose and the difference caused by the urea/urethane linkages are assumed negligible due to the small weight percent (~ 6% in ED-2000).

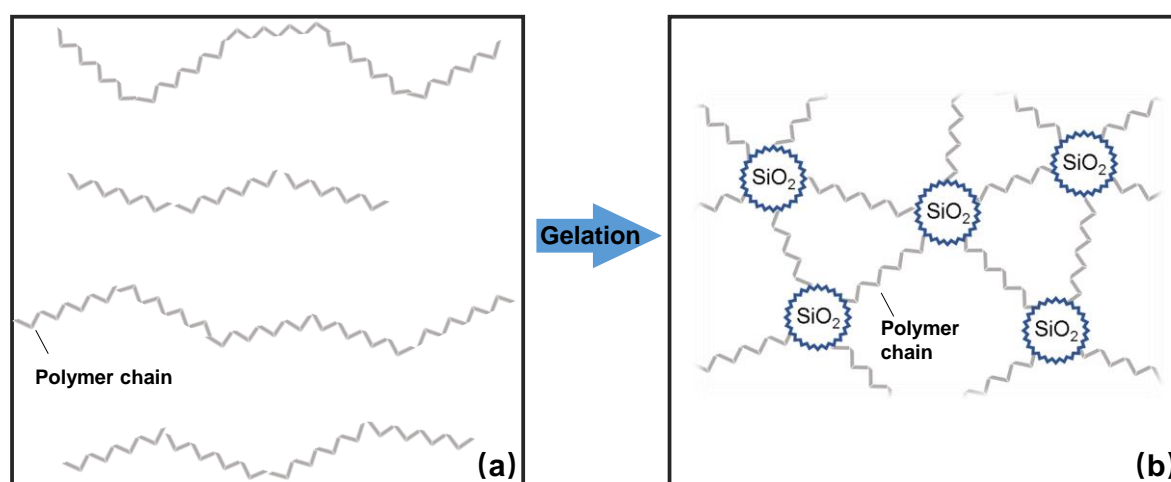


Figure 6-2. Schematic illustration of the formation of siliceous junction points. (a) the free-rotating polymer chains in the amorphous phase before gelation. (b) after gelation, the polymer chains are cross-linked by the siliceous network.

Ureasil materials are promising for BC solid-state cooling applications because the gelled amorphous phase still shows molecular mobility and thus has giant configurational change at crystallization. This yields solid-solid phase transitions with high ΔS , which fit the BC cooling applications. In addition, by tuning the chain length and molecular shapes in the poly(oxyalkylene) chains, one can modify the physical and mechanical properties of the ureasil materials. The great tunability could lead to a new class of BC materials. Also, most precursor polymers are inexpensive and commonly used in industry. These advantages make ureasil materials even more interesting for large-scale applications of refrigeration devices.

To date, ureasil type of materials have been extensively studied as lightguiding substrate materials due to their excellent optical properties^{174–177} and mechanical flexibility¹⁷⁷. However, this is chapter, I will be focusing on their BC effect.

6.2 Precursor selection for designing ureasil materials

Polymer materials consisting of poly(oxyalkylene) chains are commonly used for fabricating ureasils^{174–177}. Selection of proper precursor materials is essential in designing ureasils with desired BC properties. Two main targets are close-to-room-temperature T_C and large isothermal entropy change at the phase transition $|\Delta S_0|$. Both T_C and $|\Delta S_0|$ are closely related to the chain length and the molecular shape¹⁷⁸ of a series of poly(oxyalkylene) in ureasils.

First, we started from PEG as the precursor due to its large entropy change ΔS_0 , which is comparable to the commercial refrigerant¹²¹, as shown in Fig.6-3. Also, PEG is a well-understood polymer such that many of the material properties are available in literature¹⁶⁹. Then the optimal precursors for BC effects were searched by changing the chain length and the molecular shape of the polymer chains.

6.2.1 Chain-length selection

The chain length of polymers is commonly expressed in terms of molecular weight¹⁷⁹. For example, PEG-2000 represents PEG with an average molecular weight of 2000 g mol⁻¹ for a single polymer chain. The DSC results of PEG polymers in Fig.6-3 show the increasing trend of both T_C and $|\Delta S_0|$ as a function of molecular weight. The data of PEG 300, 600 and 2000 are from my own calorimetry measurements while others are taken from literature¹⁶⁹. The same trend is also reported in literature¹⁸⁰.

This trend is explained by the classic Flory–Vrij theory^{181,182}. In principle, the polymer crystal are regarded as many rigid segments of packed polymer chains which are freely jointed at both ends. The rigid segments require more energy than the free ends when the crystalline region transforms to amorphous. A polymer with a smaller molecular weight will have more chain ends per unit volume, so it requires less energy to transform to the amorphous phase¹⁸². Hence T_C of smaller molecular weight polymers will be lower than T_C of larger molecular weight ones.

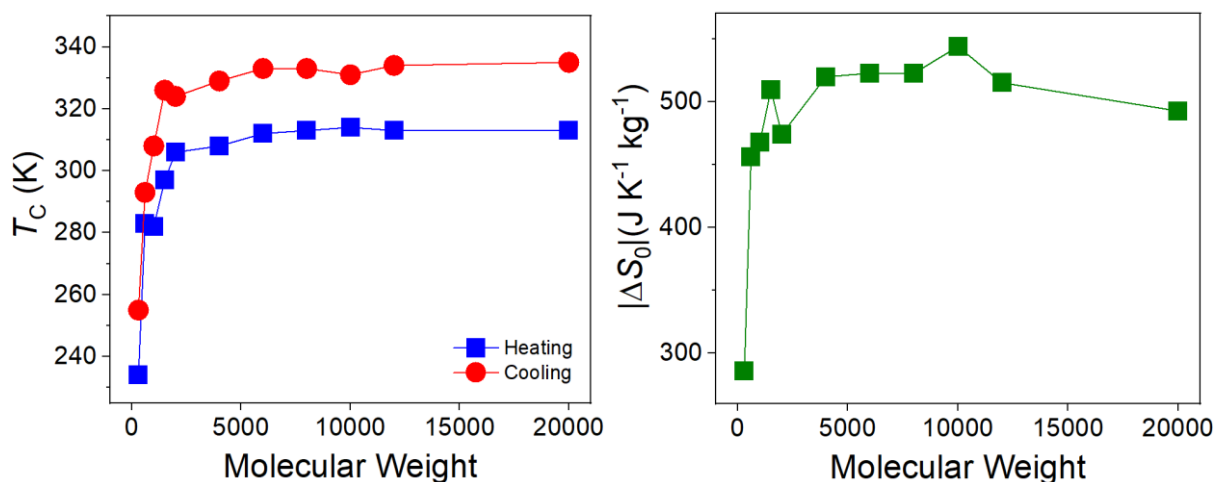


Figure 6-3. T_C and $|\Delta S_0|$ as a function of molecular weight for PEG polymer, with the molecular weight = 300, 600, 1000, 1500, 2000, 4000, 6000, 8000, 10000, 12000 and 20000. The data of PEG 300, 600 and 2000 are from my own calorimetry measurements while others are from literature¹⁶⁹.

Heat flow measurements were performed for PEG-300, PEG-600 and PEG-2000 to select proper chain length for fabricating ureasil materials. As shown in Fig. 6-4, PEG-600 and PEG-2000 exhibit reversible phase transition with large entropy change. However, in PEG-300 the phenomenon of ‘cold crystallization’ is observed, which is an exothermic crystallization process taking place upon heating rather than cooling¹⁸³. There was no distinct exothermic peak upon cooling for PEG-300. Instead, the exothermic peak happens upon heat at ~ 210 K, as marked by the blue arrow in Fig.6-4. This is commonly seen in other polymers such as Poly(ethylene terephthalate) (PET)^{184,185} and poly(butylene terephthalate) (PBT)¹⁸⁶. The reason is that the low chain mobility has limited the crystallization rate upon cooling, leading to the metastable supercooled amorphous phase. The crystallization then happens in the subsequent heating when the chain mobility is higher¹⁸³. The low mobility in polymer chains of PEG-300 may cause reversibility problems for BC effects which require cyclic phase transition driven by pressure. Therefore, PEG-300 is not moved forward for ureasil fabrication. Only PEG-600 and PEG-2000 were selected for their close-to-room-temperature T_C and large isothermal entropy change $|\Delta S_0|$.

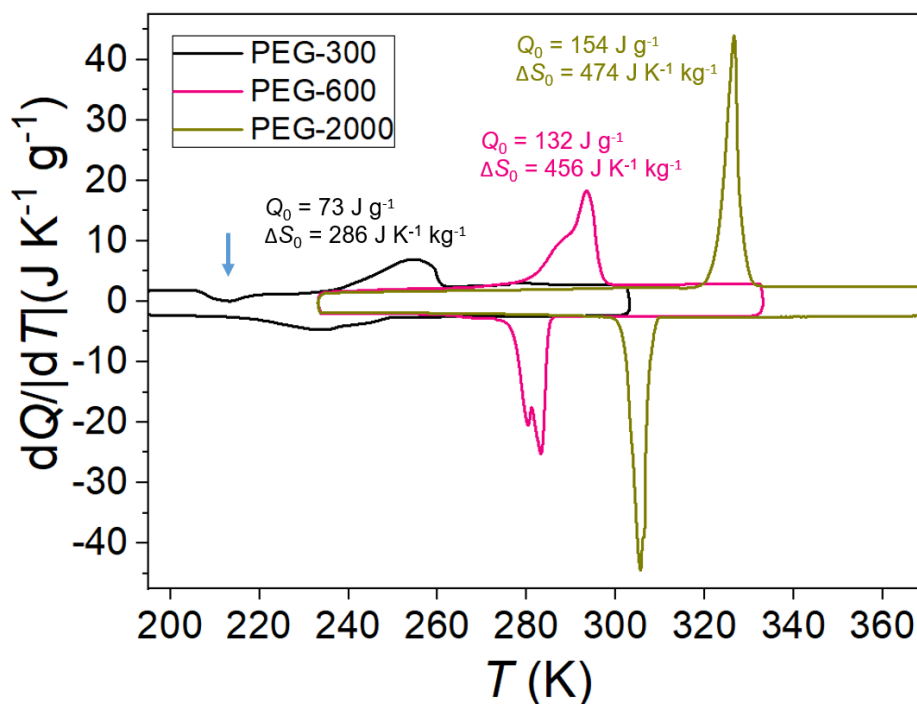


Figure 6-4. DSC measurements to compare precursors PEG-300, PEG-600 and PEG-2000 before gelation. $dQ/dT > 0$ means endothermic. The values of Q_0 and ΔS_0 can be derived from the dQ/dT data on heating. The blue arrow marks the ‘cold crystallization’.

Crystallization temperatures after gelation

To characterize the materials before and after gelation, the calorimetry measurements under zero pressure were performed with a heating and cooling rate of 5 K min⁻¹ as shown in Fig.6-5a. The heat flow dQ/dT measurements show that the PEG-2000 ureasil undergoes a reversible phase transition at 307 K on heating and 285 K on cooling, with a hysteresis of ~ 22 K. After gelation, T_C decreases by ~ 20 K without affecting much the hysteresis.

Interestingly, ‘cold crystallization’ was also observed PEG-600 ureasil after gelation, as shown in Fig.6-5b. No exothermic peak happens on cooling but upon heat at ~ 260 K after the glass transition at ~ 220 K. This suggests that gelation may limit the mobility of polymer chains because they are confined in a crosslinked network.

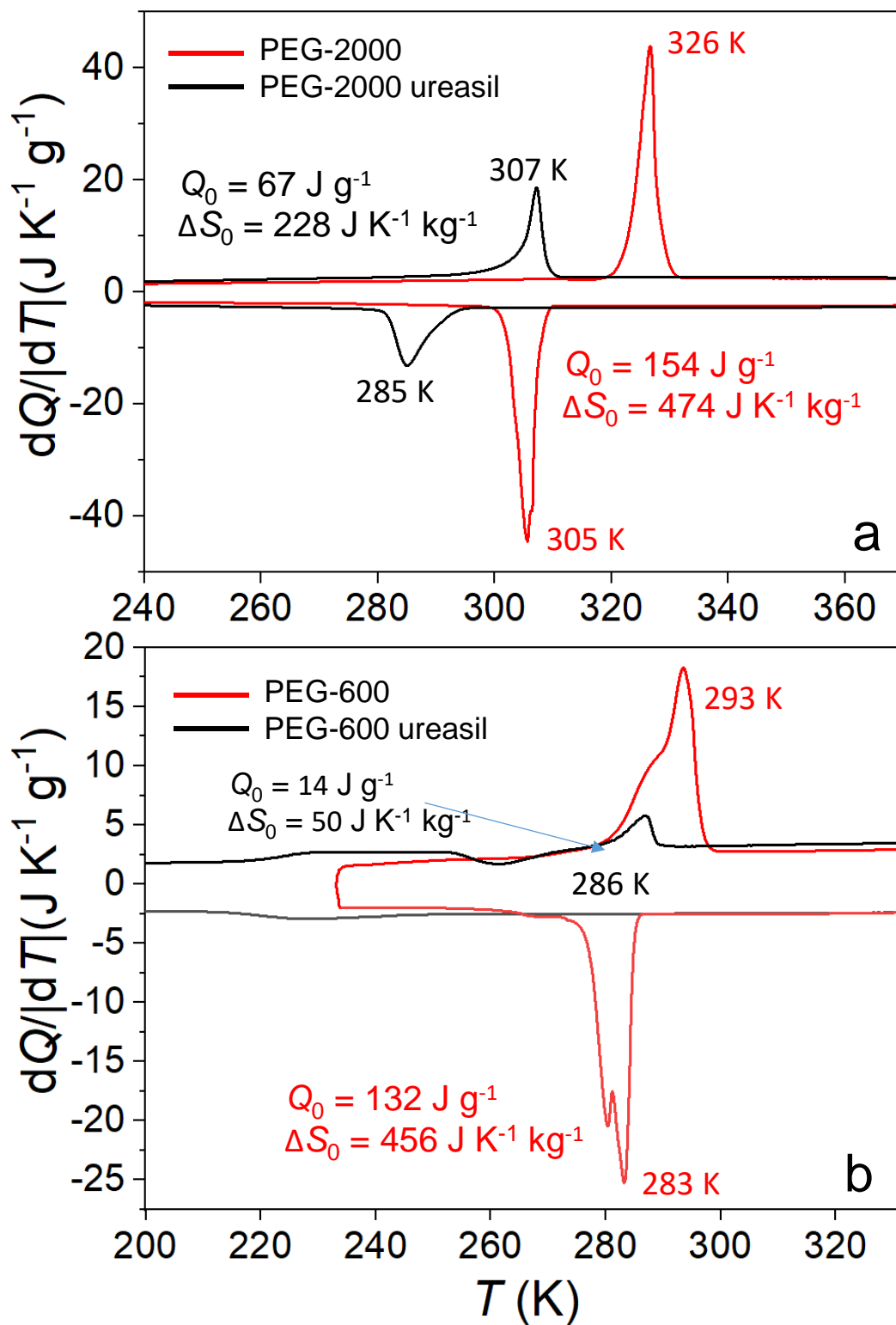


Figure 6-5. DSC measurements to compare polymers before (in red) and after gelation (in black). **(a)** PEG-2000 and PEG-2000 ureasil. **(b)** PEG-600 and PEG-600 ureasil. $dQ/dT > 0$ means endothermic. The values of Q_0 and ΔS_0 can be derived from the dQ/dT data on heating.

Entropy change of the crystallization after gelation

PEG-2000 exhibits $|\Delta S_0| \sim 474 \text{ J K}^{-1} \text{ kg}^{-1}$ before gelation and $228 \text{ J K}^{-1} \text{ kg}^{-1}$ after gelation (Fig.6-5). The corresponding latent heat $Q_0 \sim 154 \text{ J g}^{-1}$ before gelation and 67 J g^{-1} after gelation. The value of $|\Delta S_0|$ in PEG-2000 ureasil is substantially higher than traditional inorganic barocaloric materials, e.g. BaTiO_3 ¹¹¹ with $|\Delta S_0| \sim 2 \text{ J K}^{-1} \text{ kg}^{-1}$ and $(\text{NH}_4)_2\text{SO}_4$ ¹¹³ with $|\Delta S_0| \sim 60 \text{ J K}^{-1} \text{ kg}^{-1}$ indicating much larger BC effects.

PEG-600 exhibits $|\Delta S_0| \sim 456 \text{ J K}^{-1} \text{ kg}^{-1}$ before gelation but only $50 \text{ J K}^{-1} \text{ kg}^{-1}$ after gelation. The reason could be that the crystallization process has been undermined by the low chain mobility so the crystallinity PEG-600 ureasil has been substantially reduced. This suggests that PEG-600 ureasil requires further modification to promote the crystallization rate for better BC effects. Yoshihara, N et al.¹⁸⁵ have identified effective strategies of adding heterogeneous nucleating agents, co-polymerizing and alloying with miscible polymers to address this issue in PET, which could be possibly applied to PEG-600 in the future. Here, PEG-600 is not proceeded with further characterizations and BC performance evaluations.

In summary, PEG polymers with a molecular weight of 2000 and 600 were fabricated into ureasil materials. Only PEG-2000 ureasil with large $|\Delta S_0| \sim 228 \text{ J K}^{-1}$ is subjected to further study of the molecular shape of polymer chains.

6.2.2 Molecular-shape tuning

The crystallization of polymers is related to the molecular shapes because they determine the steric hindrance between the polymer chains¹⁸⁷. Branch chains on the polymer backbone would generate steric effects and thus do not easily adopt crystalline structures. Starting from PEG, the polymer branched chains are tuned to design the polymers for BC ureasil materials. To tailor the materials for BC application and select the appropriate precursor polymers, calorimetry measurements were conducted on three kinds of polymers with different molecular shapes. The purpose was to investigate the impact of the gelation on T_C and $|\Delta S_0|$. The ideal polymer materials should possess a big $|\Delta S_0|$ at a T_C near room temperature.

Jeffamine ED and Jeffamine D polymer series were studied as they have similar structures with PEG and are commonly used for ureasils. The structure of PEG is commonly expressed as $H-(O-CH_2-CH_2)_n-OH$, where n is the number of the repeating units in one single chain. The structure of Jeffamine D is polypropylene glycol (PPG) with $-NH_2$ as the end-cap. Jeffamine D is expressed as $NH_2-(O-CH(CH_3)-CH_2)_n-NH_2$, shown in Fig.6-6 top. In terms of steric hindrance, Jeffamine D polymers are composed of one more branched methyl group ($-CH_3$) which generates steric effects and thus hinders the chain packing during crystallization. Jeffamine ED a block co-polymer of PPG and PEG (PEG-co-PPG) with $-NH_2$ as the end-cap. Here, we assume the difference in the end groups ($-NH_2$ in Jeffamine ED and D; $-OH$ and $-H$ in PEG) has no impact on the polymer properties and we only focus on the changes in the polymer backbone. In addition, Jeffamine ED-2003 are assumed as Jeffamine ED-2000 (molecular weight of 2000 g mol^{-1}) due to the material availability. PEG-2000, ED-2000, and D-2000 were selected for ureasil fabrication.

Crystallization temperatures after gelation

Before gelation, the T_C is $\sim 326 \text{ K}$ and 307 K for PEG-2000 and ED-2000, respectively. D-2000 exhibit no distinct crystallization peak during the heat flow measurements, as shown in Fig.6-6 top. Therefore, T_C decreases when adding the branched chains to the polymer backbones as branched chains generate steric hindrance for crystallization. After gelation, the same trend was observed in the ureasil materials after gelation, in Fig.6-6 bottom. The T_C is $\sim 307 \text{ K}$ and 283 K for PEG-2000 ureasil and ED-2000 ureasil, respectively. The gelation decreases the T_C for both PEG-2000 and ED-2000.

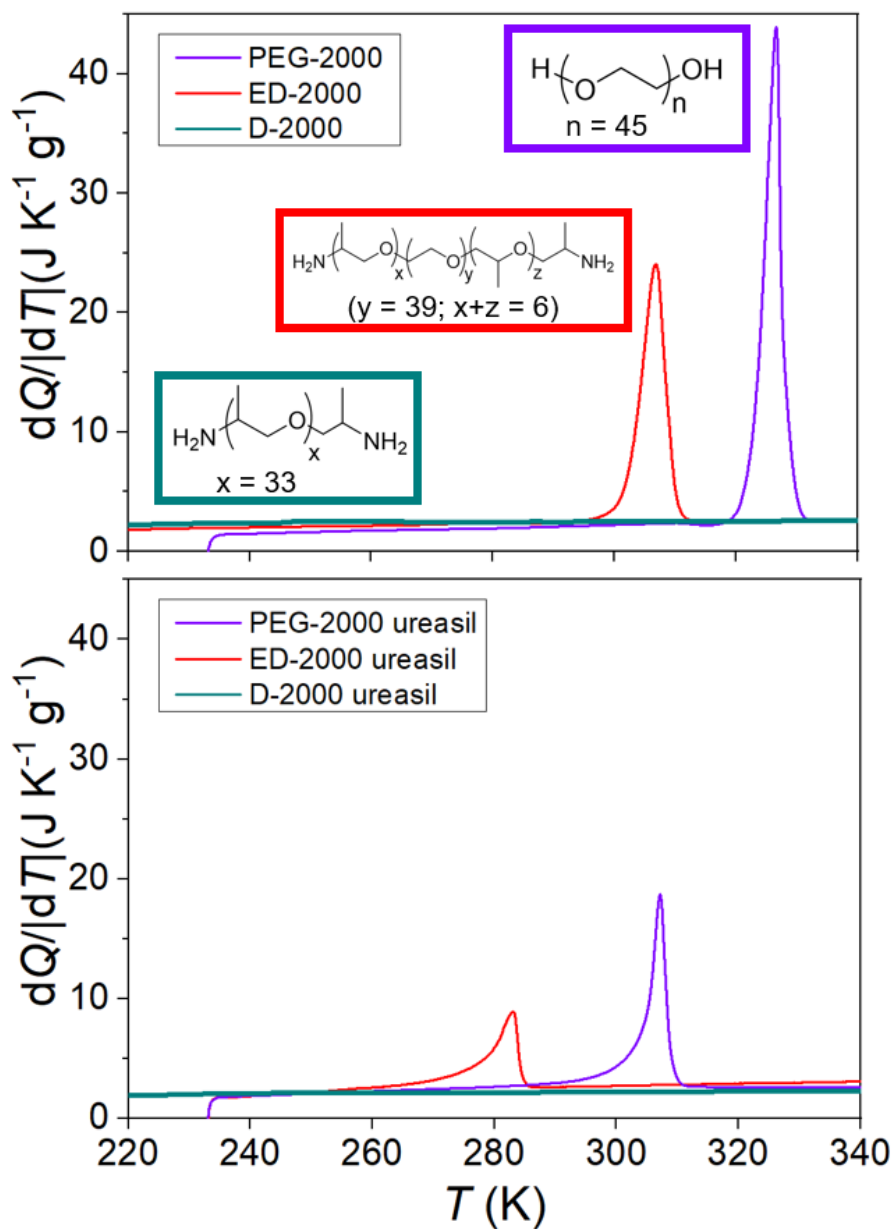


Figure 6-6. The heat flow measures before(top) and after(bottom) gelation. **Top:** Comparison of the temperature-dependent heat flow dQ/dT data for PEG-2000(purple), Jeffamine ED-2003(red) and Jeffamine D-2000(black). The inset boxes are the chemical structure of each material. **Bottom:** the heat flow measurements for the corresponding ureasil materials after gelation.

Entropy change of the crystallization after gelation

Before gelation, PEG-2000 exhibits $|\Delta S_0| \sim 474 \text{ J K}^{-1} \text{ kg}^{-1}$ and ED-2000 exhibits lower $|\Delta S_0| \sim 474 \text{ J K}^{-1} \text{ kg}^{-1}$. D-2000 exhibit no distinct crystallization peak so no $|\Delta S_0|$ can be calculated. After gelation, the same trend was observed in the ureasil materials after gelation, in Fig.6-6 bottom. The $|\Delta S_0| \sim 228 \text{ J K}^{-1} \text{ kg}^{-1}$ for PEG-2000 ureasil and $|\Delta S_0| \sim 178 \text{ J K}^{-1} \text{ kg}^{-1}$ for ED-2000 ureasil. Therefore, $|\Delta S_0|$ decreases when adding the branched chains on the polymer backbones as branched chains generate steric hindrance for crystallization.

In order to see how $|\Delta S_0|$ and T_C change with different precursor polymers, i.e. different molecular weights and molecular shapes, Fig. 6-7 summarises the results for the selected precursor polymers before gelation. The patterns are summarized as follows. Firstly, the increase of molecular weights promotes the crystallization of polymer chains, i.e. higher T_C and larger $|\Delta S_0|$. Secondly, the increase of branch chains(the number of branch chains: Jeffamine D > Jeffamine ED > PEG) hinders the crystallization of polymer chains, i.e. lower T_C and smaller $|\Delta S_0|$. The reasons were explained previously. Based on these observed patterns, the desired precursor polymers should have large molecular weights and structures with less bran chains. Therefore, PEG-2000 ureasil and ED-2000 ureasil are selected for evaluating BC effects and further characterizations. They tend to show large $|\Delta S_0|$ and close-to-room-temperature T_C with reversible phase transitions.

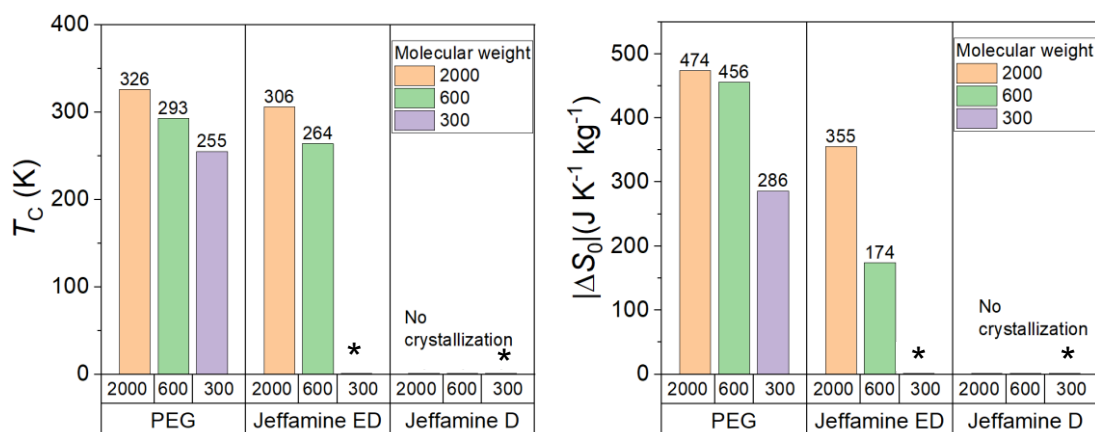
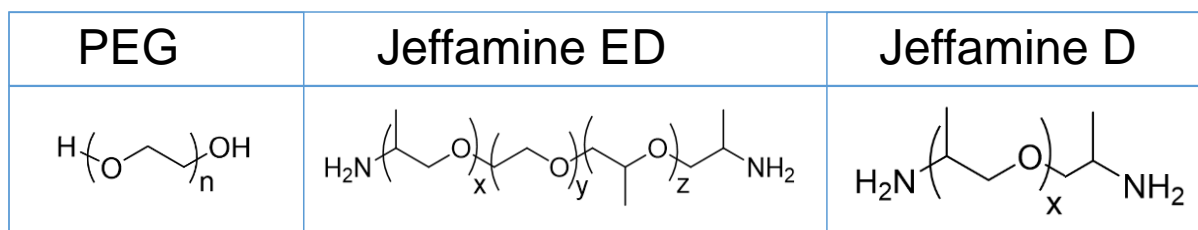


Figure 6-7. The pattern of changes in T_C and $|\Delta S_0|$ when using different polymer precursors. The purpose is to identify the optimal choice of materials for following barocaloric measurements. **Top panel:** the backbone structure of PEG, Jeffamine ED and Jeffamine D polymers. The notation ‘ n ’ represents the repeating number of the polymer units. In the case of Jeffamine ED, $n = x + y + z$. **Bottom panel:** The magnitudes of T_C , $|\Delta S_0|$ and hysteresis for each polymer composition. All the results shown are from my own calorimetry measurements. The values of T_C are measured on heating. Notation ‘*’ marks materials that were not tested.

6.3 Experiments on selected ureasil materials

6.3.1 Ureasil synthesis

The chemical synthesis was performed by Dr Bolong Zhang from Photoactive Materials Group, Department of Materials Science and Metallurgy, University of Cambridge. Polyethylene glycol 2000 (PEG-2000, $M_w = 2000 \text{ g mol}^{-1}$), O,O'-Bis(2-aminopropyl) polypropylene glycol-block-polyethylene glycol-block-polypropylene glycol (commercial Jeffamine® ED-2003, $M_w = 2000 \text{ g mol}^{-1}$) and the silica precursor, 3-(triethoxysilyl)propylisocyanate (ICPTES, 95.0%) were purchased from Sigma-Aldrich. Tetrahydrofuran (THF (CH_2)₄O, $\geq 99.9\%$), ethanol (EtOH, 95.0%), and hydrochloric acid (12 mol L^{-1}) were purchased from Fisher Scientific. Water was obtained from a Millipore Simpак 2 water purification system. All materials were used as received. For convenience, PEG-2000 and ED-2003, after gelation, are referred as PEG-2000 ureasil and ED-2000 ureasil.

Ureasil materials were prepared via a sol-gel¹⁸⁸ process, as shown below in Fig.6-8. PEG-2000 (20g, 10 mmol), ICPTES (5 g, 20 mmol) and THF (25 g) were added in a round bottom flask and stirred for 24 h at 70°C under N₂. The resulting UPTES(PEG-2000) stock solution was kept in sealed glass vials for later usage without further purification. A blend of HCl solution (0.5 mol L^{-1} , 100 μL), ethanol (100 μL) and UPTES(PEG-2000) stock solution (per 3 g) was mixed homogeneously by stirring for 30s, and quickly poured into a polypropylene container in the desired shape, sealed with Parafilm M®, ageing in the dark for 3 days. The container was then exposed in air for 5 days to ensure the solvent residue evaporated. The remaining product is a gelled PEG-2000 ureasil block. The preparation of ED-2000 ureasil is the same as shown in Fig.6-9.

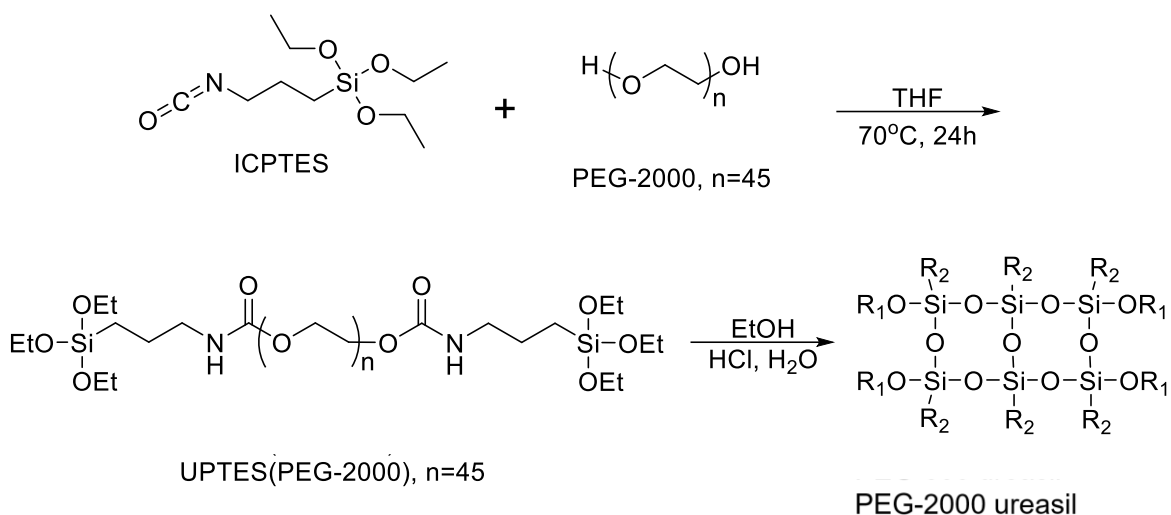


Figure 6-8. Synthetic route for the preparation of PEG-2000 ureasil.

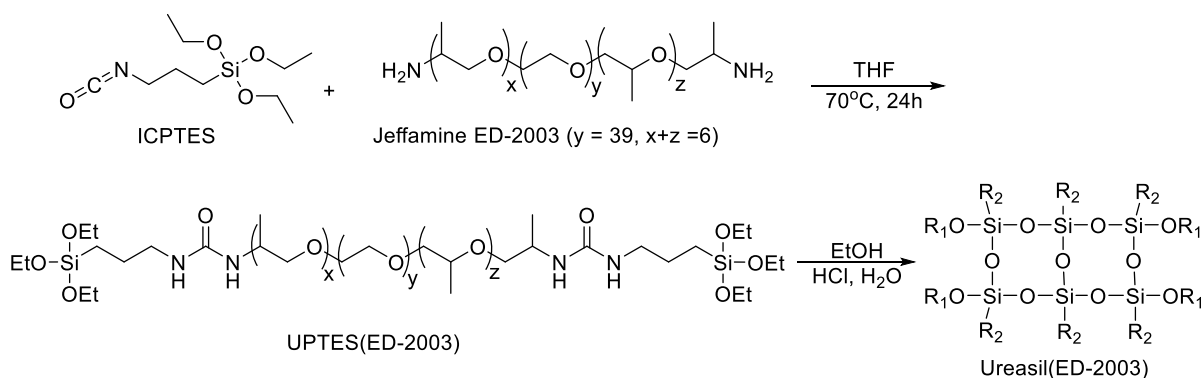


Figure 6-9. Synthetic route for the preparation of ED-2000 ureasil.

The PEG-2000 ureasil and ED-2000 ureasil are shown in Fig.6-10 and Fig.6-11. Both ureasil materials stay solid at room temperature. When heated up from the crystalline phase to the amorphous phase, the ureasil materials become softer and transparent. This shows that our gelation process has successfully transformed the molten amorphous phase into the flexible gel state, which avoids leaking issues and provides more possibilities for device designs.

Heating

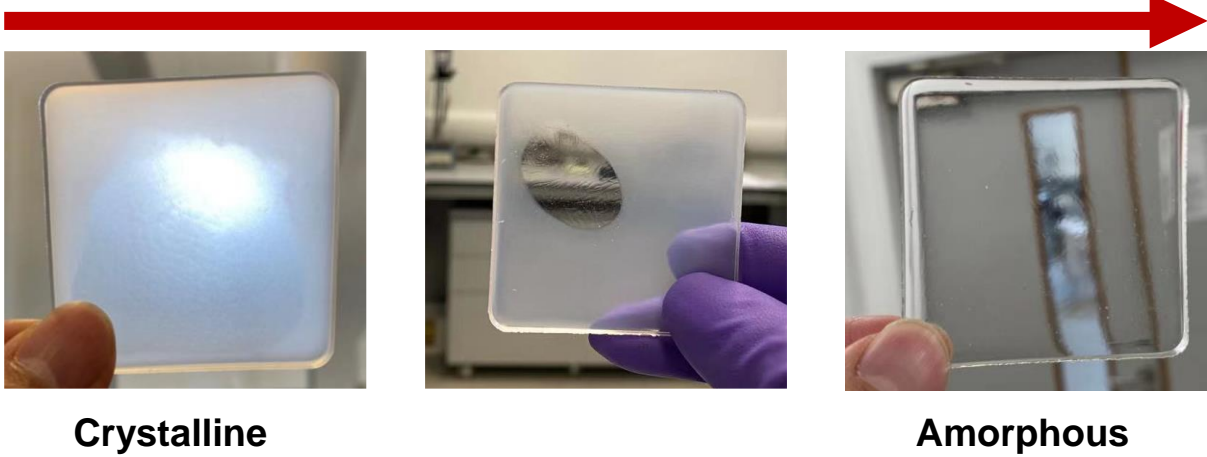


Figure 6-10. The ED-2000 ureasil obtained. The material is stiff and looks cloudy at room temperature. As heated up the material becomes soft and transparent.

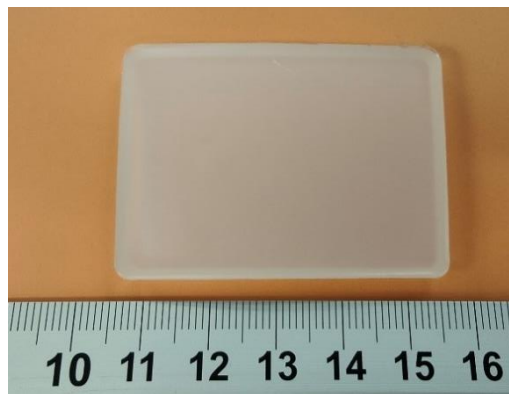


Figure 6-11. The PEG-2000 ureasil sample at room temperature. It is stiffer than ED-2000 ureasil.

6.3.2 Polarized optical microscopy

A Swift 350T polarized optical microscopy (POM), equipped with a Canon 400D camera and a microscopic hot stage was used for characterizing the crystalline microstructure of PEG-2000 ureasil. The material was cut into a thin piece to prepare the sample for optical observation.

The polarized optical microscopy visually displayed the microstructure change before and after the phase transition, which is the polymer crystallization¹⁸⁹. As shown Fig.6-12, the sample was continuously heated from 20°C (a) to 50°C (f). In Fig.6-12 (a), the sample exhibits birefringent ring-banded spherulites, evidencing the crystalline phase. As the temperature increases, the birefringent gradually vanishes, showing the transformation to the amorphous phase.

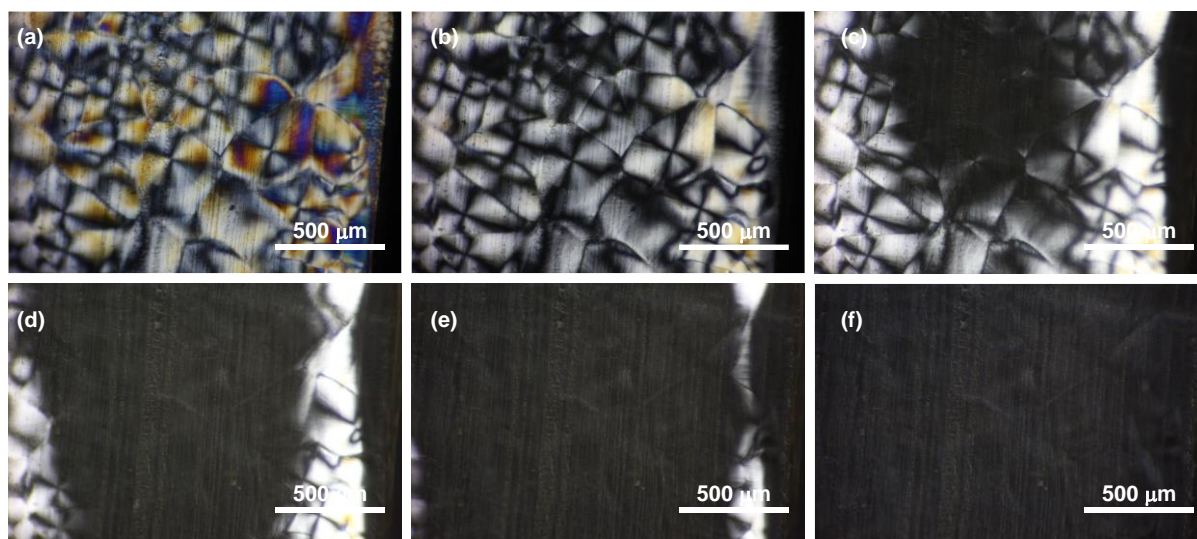


Figure 6-12. Polarized optical micrographs of U-2000 urethanesils during heating. From (a) to (f), the sample was continuously heated from 20°C to 50°C. The vanish of the birefringence patterns shows the transition from the crystalline phase to amorphous phase.

6.3.3 Specific heat capacity measurements

Characterisation of the specific heat capacity $c_p(T)$ of PEG-2000 ureasil and ED-2000 ureasil is displayed in Fig.6-13. The inset is the total c_p including the contribution from the latent heat at the phase transition. The baseline (in red) is to fit the c_p of the low-temperature and high-temperature phases, away from the phase transition. This is used to calculate the extra entropy ΔS_+ later in the evaluation of BC effects.

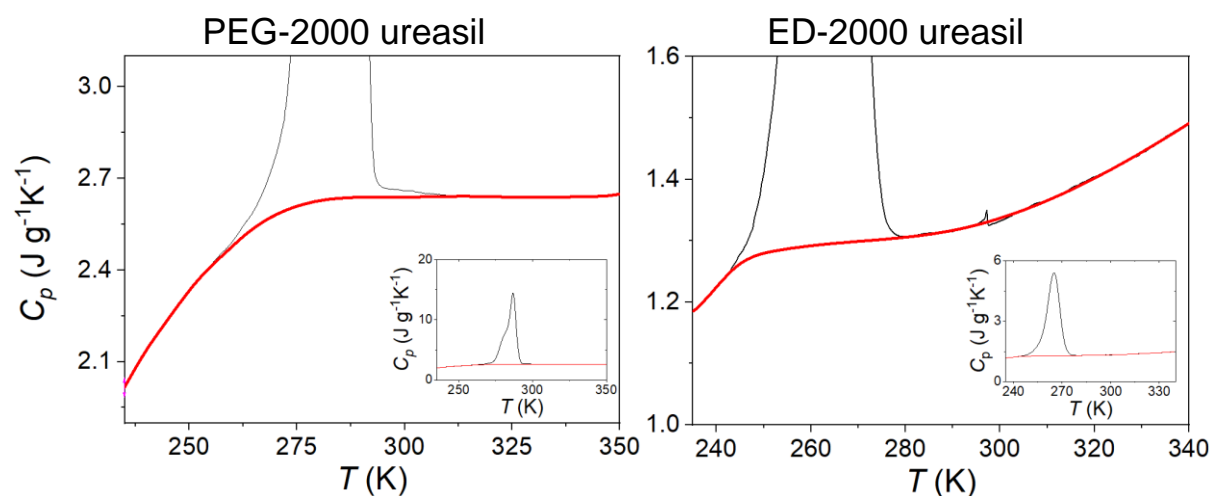


Figure 6-13. Specific heat capacity c_p measured from calorimetry on cooling. The baseline (red) was identified via a cubic polynomial baseline fitting. This baseline represents the c_p at the low-temperature and high-temperature phases, without the contribution of latent heat. The inset is the c_p before subtraction of latent heat.

6.3.4 Dilatometry

The specific volume as a function of temperature $V_{sp}(T)$ can be obtained from dilatometry in combination with the density of the sample. The density is the mass of the sample divided by its volume. Here, I measured a monolith sample with a mass of 6.237 g and a volume of 5.6 cm³ at 19.1 °C. This yields the density of 1.11 g cm⁻³ for the PEG-2000 ureasil. In comparison, the U-2000 polymer before gelation, which is PEG-2000 has a density of 1.21 g cm⁻³ at 20 °C, according to the data on Sigma Aldrich. Correspondingly, the specific volume V_{sp} of PEG-2000 ureasil at 19.1 °C is 0.898 cm³ g⁻¹.

The density of ED-2000 ureasil ~ 1.06 g cm⁻³ at 17.3 °C is slightly lower than PEG-2000 ureasil. This is because the branched group – CH₃ generates steric effects hindering the crystalline structures. ED-2000 ureasil is therefore softer. The specific volume V_{sp} of ED-2000 ureasil at 17.3 °C is 0.942 cm³ g⁻¹.

The specific volume as a function of temperature $V_{sp}(T)$ is evaluated from the dilatometry data. In principle, the dilatometer records the length changes that occur during the heat treatment of a sample. Length changes can be used to determine the volume change. The volume change ΔV is assumed as $\frac{(L_i + \Delta L)^3}{L_i^3} - 1$, where L_i is the initial length and ΔL is the change in length. In this measurement, a cube of PEG-2000 ureasil and ED-2000 ureasil samples with an edge of 3.5 mm were measured during heating at the rate of 5 K min⁻¹ as shown in Fig.6-14.

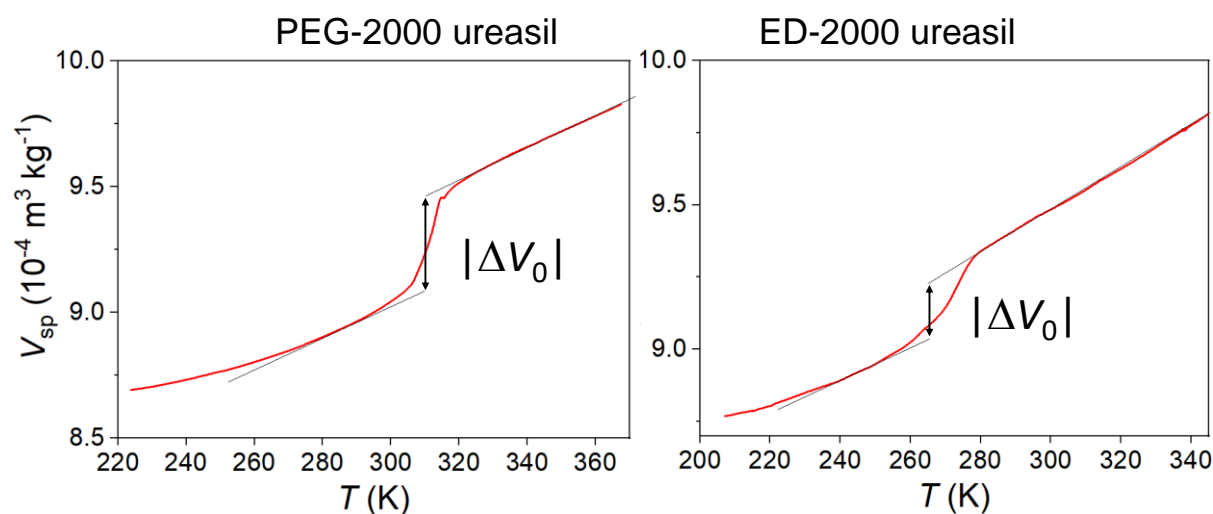


Figure 6-14. Specific volume $V_{sp}(T)$ on heating, revealing a large volume change $|\Delta V_0| \sim 4.2\%$ for PEG-2000 ureasil and $|\Delta V_0| \sim 2.1\%$ for ED-2000 ureasil.

For PEG-2000 ureasil, V_{sp} undergoes a large $\sim 4.2\%$ increase of $\Delta V_0 = 0.38 \times 10^{-4} \text{ m}^3 \text{ kg}^{-1}$ across the phase transition. The thermal expansion coefficient at constant pressure $\alpha = \left(\frac{\partial V}{\partial T}\right)_p$ was calculated based on the dilatometry measurement data by taking the gradient of linear fits on the plot of specific volume V_{sp} as a function of T . From those data, $\frac{\partial V}{\partial T}$ at atmospheric pressure is $5.6 \times 10^{-7} \text{ m}^3 \text{ kg}^{-1} \text{ K}^{-1}$ and $6.3 \times 10^{-7} \text{ m}^3 \text{ kg}^{-1} \text{ K}^{-1}$ for the low-temperature and high-temperature phase, respectively.

ED-2000 ureasil undergoes a large $\sim 2.1\%$ increase of $\Delta V_0 = 0.19 \times 10^{-4} \text{ m}^3 \text{ kg}^{-1}$ across the phase transition. The linear fits of the thermal expansion coefficient at atmospheric pressure $\alpha = \left(\frac{\partial V}{\partial T}\right)_{p=0}$ are $5.6 \times 10^{-7} \text{ m}^3 \text{ kg}^{-1} \text{ K}^{-1}$ at the low-temperature phase and $7.3 \times 10^{-7} \text{ m}^3 \text{ kg}^{-1} \text{ K}^{-1}$ at the high-temperature phase.

The value of $|\Delta V_0|$ can also be deduced from the Clausius–Clapeyron equation²³ $\frac{dT_C}{dp} = \frac{\Delta V_0}{\Delta S_0}$ with the data of T_C shift under pressure and the isothermal entropy change at zero pressure. Using ΔS_0 and $\frac{dT_C}{dp}$ from the pressure-dependent calorimetry in Fig.6-15, $|\Delta V_0| = 2.36\%$ is obtained, which is lower than the dilatometry result of 4.2%. In ED-2000 ureasil, $|\Delta V_0| = 2.1\%$ is also lower than the corresponding Clausius–Clapeyron value of 1.49%. This could be from experimental inaccuracy in dilatometry measurements as ΔV was deduced by cubed ΔL and the error can be amplified.

Notably, the thermal expansion coefficients $\left(\frac{\partial V}{\partial T}\right)_{p=0}$ of PEG-2000 ureasil and ED-2000 ureasil are also big even outside the phase transition region, indicating that the BC effects can possibly operate in a wide temperature range. This is beneficial for making practice cooling applications.

6.3.5 Calorimetry under pressure

To study the thermal response of ureasil materials under pressure, calorimetry measurements at $\pm 1.2 \text{ K min}^{-1}$ under different pressures were performed using a Setaram Instrumentation $\mu\text{DSC7 EVO}$ microcalorimeter equipped with a 260D Isco pressure pump with nitrogen gas as a pressure-transmitting media.

Small pieces of PEG-2000 ureasil (43.1 mg) and ED-2000 ureasil (51.3 mg) were measured at different isobaric pressures. As shown in Fig.6-15, the pressure increase shifts the phase transition in both PEG-2000 ureasil and ED-2000 ureasil towards higher temperatures. The values of T_C show a linear relation to the applied pressure, with a barocaloric coefficient of $dT_C/dp \sim 8.3 \text{ K kbar}^{-1}$ in PEG-2000 and $dT_C/dp \sim 7.9 \text{ K kbar}^{-1}$ in ED-2000 ureasil. These dT_C/dp values are comparable with those observed in other BC materials summarized in Table 6-1 at the end of this chapter. The shift of phase transition is consistent with enhanced stability of the more ordered and lower volume crystalline phase at the expense of the more disordered amorphous phase due to pressure.

Notably, the low-amplitude peaks between 290 K ~ 310 K in Fig.6-15b are not from the sample but the instrument. They correspond to a phase transition in the polytetrafluoroethylene (PTFE) rings present in the high-pressure sample holder. In the following data processing steps(Fig.6-16), those peaks are subtracted.

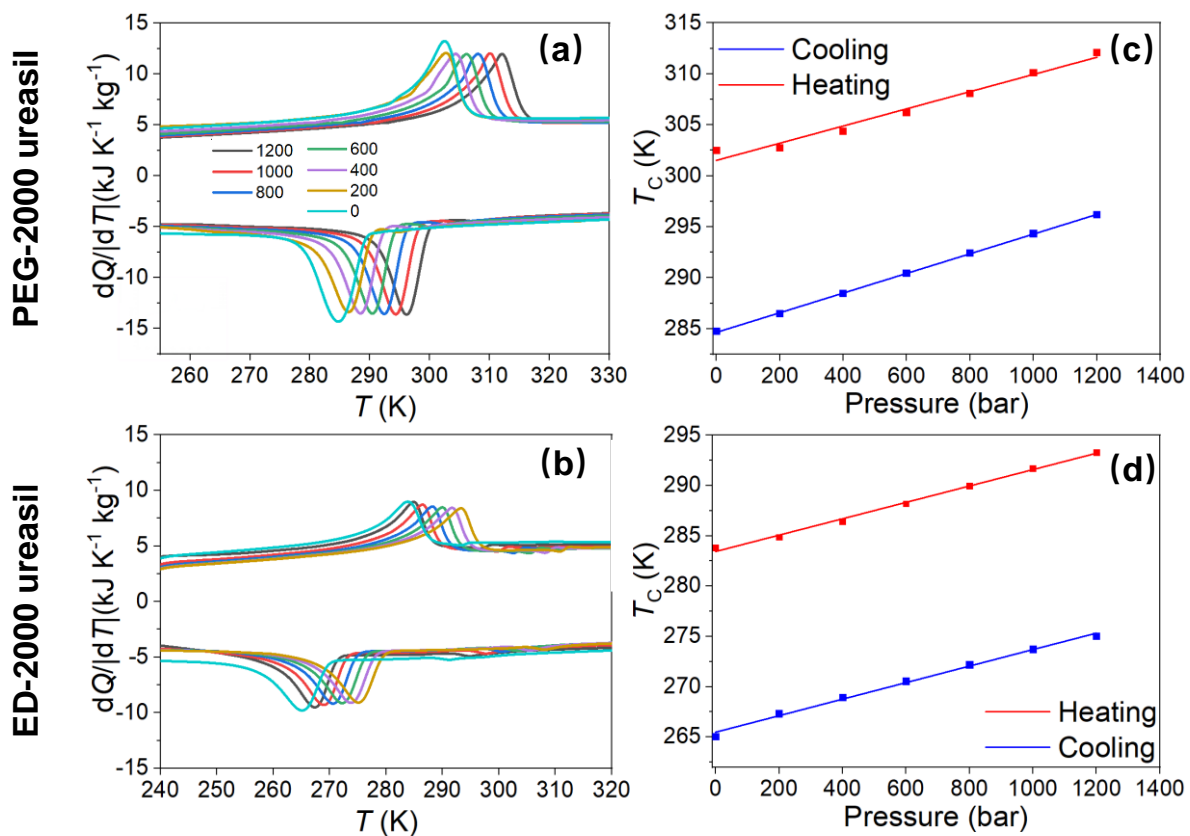


Figure 6-15. (a)(b): Pressure-driven phase transition in PEG-2000 and ED-2000 ureasil. Measurements of temperature-dependent heat flow dQ/dT under constant pressures, from 0 bar to 1200 bar. The upward peaks are endothermic during heating and downward peaks are exothermic during cooling. (c)(d): Phase diagrams, with the amorphous phase above and the crystalline phase below the phase boundary. The boundary on heat is different from that on cooling due to the thermal hysteresis. The values of crystallization temperature T_C are derived from the peak positions in (a)(b). The blue and red dots are from experimental observations. The straight lines connecting the dots are just a guide to eyes for visualizing the phase boundaries.

6.4 Evaluation of barocaloric effects

6.4.1 Construction of S - T curves

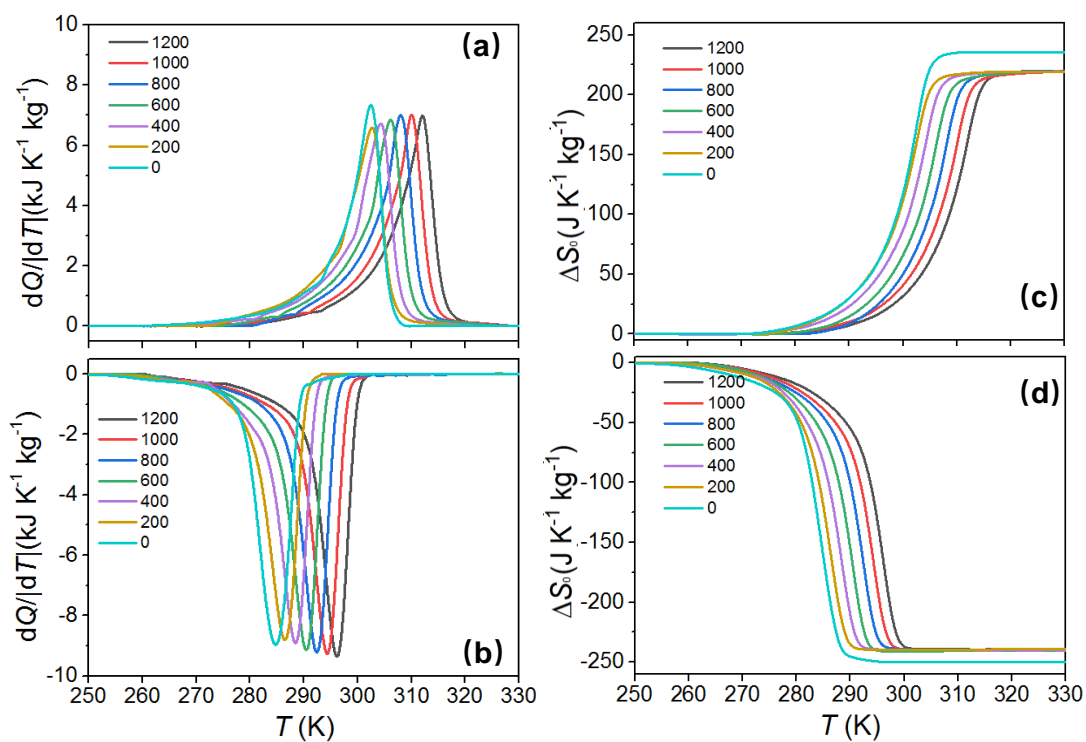
The quasi-direct method is used for constructing the S - T curve as described in Methodology and implemented in Chapter 4. The key parameters isothermal entropy change and adiabatic temperature change are derived via $\Delta S(p,T) = S'(p,T) - S'(0,T)$ and $\Delta T(p,T) = T'(p,S) - T'(0,S)$.

The construction of entropy-temperature S - T curve includes three contributions (1) the entropy change of transition $|\Delta S_0|$ from latent heat, (2) the entropy change due to heat capacity outside the transition S_C and (3) the pressure-induced additional entropy change ΔS_+ .

Firstly, the entropy change of transition $|\Delta S_0|$ arises from the transition itself, from the crystalline phase to the amorphous phase. Experimentally, the isobaric heat flow dQ/dT over temperature under applied pressure was measured (Fig.6-15) and then subjected to the subtraction of baseline away from the phase transition to yield $|\Delta S_0|$ purely from the phase transition, as shown in Fig.6-16(a)(b);(e)(f). The values of $|\Delta S_0|$ is the difference in S' before and after phase transition.

For PEG-2000 ureasil, $|\Delta S_0|$ at a pressure ranging from 0 to 1200 bar is around $228 \text{ J K}^{-1} \text{ kg}^{-1}$ on heating and $240 \text{ J K}^{-1} \text{ kg}^{-1}$ on cooling. For ED-2000 ureasil, $|\Delta S_0|$ at a pressure ranging from 0 to 1200 bar is around $150 \text{ J K}^{-1} \text{ kg}^{-1}$ on both heating and cooling.

PEG-2000 ureasil



ED-2000 ureasil

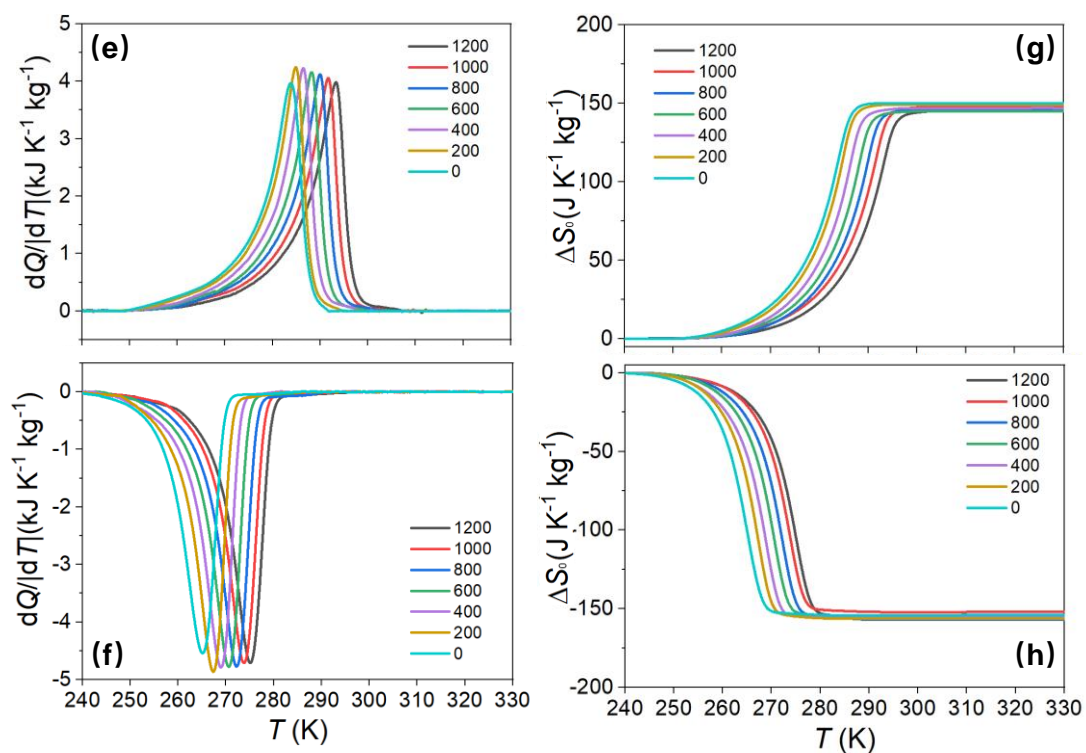


Figure 6-16. Left panel: Measurements of dQ/dT on heating and cooling across the phase transition for different pressure after baseline subtraction. (a)(b) are for PEG-2000 ureasil and (e)(f) are for ED-2000 ureasil. Right panel: The ΔS_0 associated with the phase transition derived from the left.

Secondly, the entropy change due to heat capacity outside the transition S_C is deduced from the $c_p(T)$ data shown in Fig.6-13 by using $S_C(T) = \int_{T_1}^{T_2} \left(\frac{C_p(T)}{T}\right)_P dT$. One thing to note is that c_p should exclude the contribution from latent heat to avoid double counting the $|\Delta S_0|$ from the previous step. The subtraction is shown in the red line fitting in Fig.6-13. In the following construction of the entropy-temperature curve at different pressures, c_p is assumed unchanged after applying pressures.

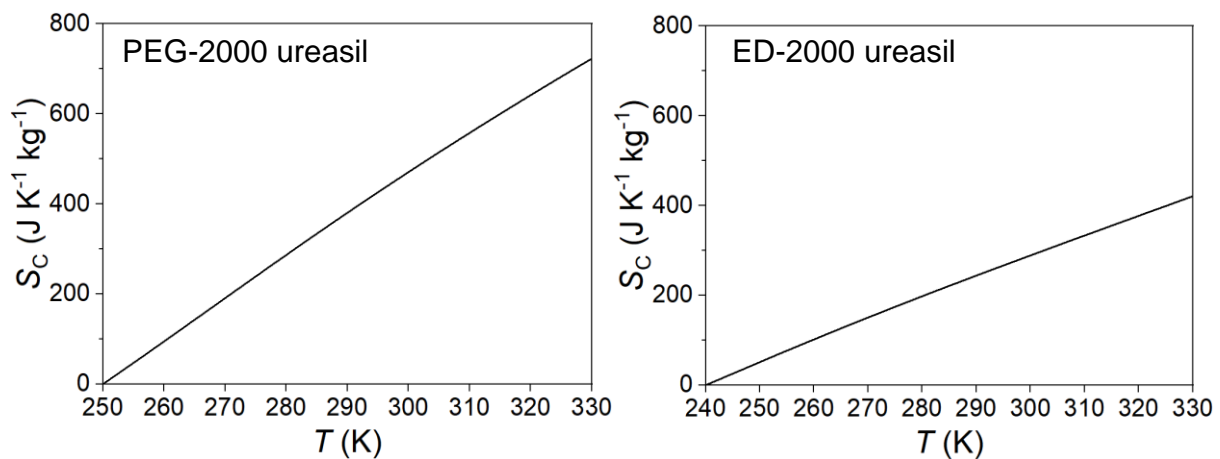


Figure 6-17. S_C , the entropy change due to heat capacity. The values are deduced from the $c_p(T)$ data after excluding $|\Delta S_0|$ from the latent heat via $S_C(T) = \int_{T_1}^{T_2} \left(\frac{C_p(T)}{T}\right)_P dT$. The baselines are shown in the black baseline in Fig. 6-13.

Thirdly, the pressure-induced additional entropy change ΔS_+ can be calculated using Maxwell's relation as $\Delta S_+(p) = -\int_{p_1}^{p_2} \left(\frac{\partial V}{\partial T}\right)_p dp$, where $\left(\frac{\partial V}{\partial T}\right)_p$ is assumed to be independent of pressure, i.e. $\left(\frac{\partial V}{\partial T}\right)_p \approx \left(\frac{\partial V}{\partial T}\right)_{p=0}$. Experimentally, $\left(\frac{\partial V}{\partial T}\right)_{p=0}$ was derived from the dilatometry data at atmospheric pressure in Fig.6-14, which displays the volume change of the material as a function of temperature. The approximation of $\left(\frac{\partial V}{\partial T}\right)_p$ being constant for higher fixed pressures up to 1200 bar is assumed because of the instrumentation difficulties in changing pressure. This can be a reasonable assumption because a similar polymer polycaprolactone (PCL)'s gradient of $\left(\frac{\partial V}{\partial T}\right)_p$ only decreases 29% from 1 bar to 1200 bar¹⁶³. The resulting change in the entropy change is only around 10 ~ 25 J K⁻¹ kg⁻¹, equivalent to 5-10% of the maximum of $|\Delta S|$.

Maxwell relation is also applied for the indirect method²³ to evaluate the caloric effects, in which the order parameter, the specific volume V_{sp} in the case of barocaloric effects, is typically measured as a function of field at different temperatures. Alternatively, one can equally measure the order parameter as a function of temperature at different fields. This yields the isothermal entropy change $\Delta S(p_1 \rightarrow p_2) = -\int_{p_1}^{p_2} \left(\frac{\partial V}{\partial T}\right)_p dp$ in responding to a pressure change from p_1 to p_2 . For clarity, the ΔS from this alternative indirect method is noted as ΔS_1 . Fig.6-18(b) displays ΔS_1 in PEG-2000 ureasil and ED-2000 ureasil. The values are in good agreement with isothermal entropy change $|\Delta S_0|$ deduced from the pressure-dependent calorimetry, shown in Fig.6-16. The magnitude of ΔS_1 shows an increasing trend with temperature and pressure. This can be related to the rearrangements of amorphous polymer chains resulting in conformational entropy changes with temperature and applied pressures¹²⁵.

Although a good agreement is achieved in this work with the maximum applied pressure of 1200 bar, $\left(\frac{\partial V}{\partial T}\right)_p$ tends to decrease with higher pressure, as shown in literature¹⁶³ instead of staying constant. Therefore, this approximation could lead to an overestimation of ΔS_+ and thus the total ΔS .

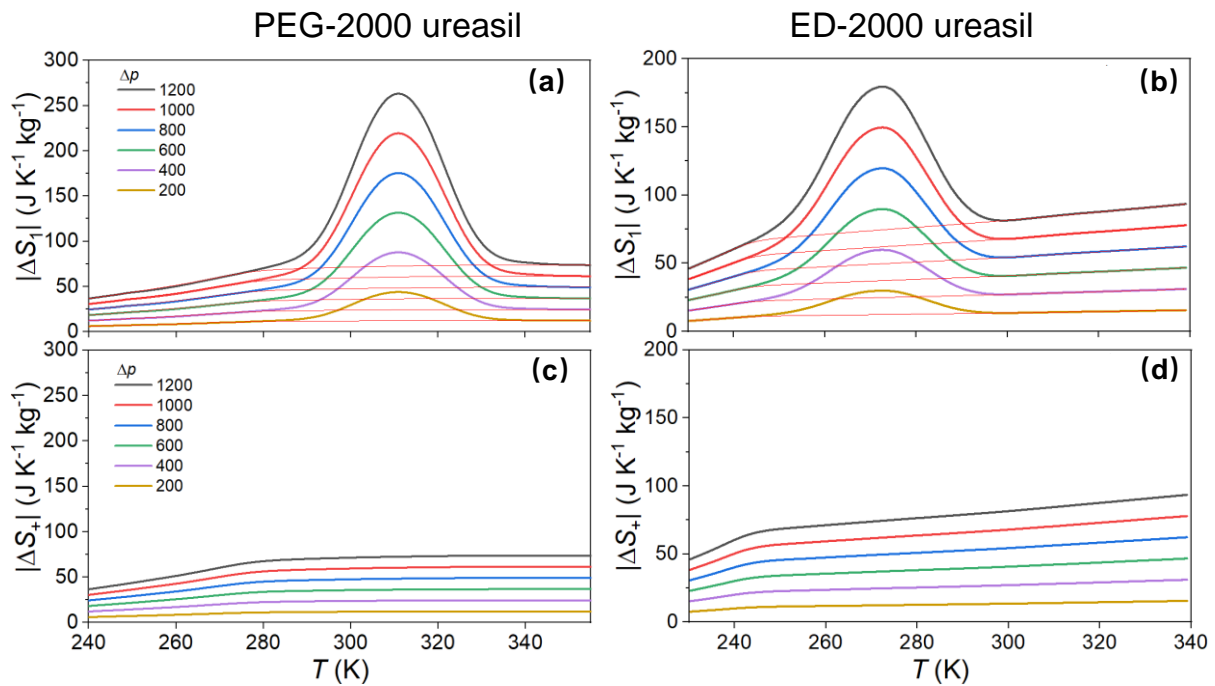


Figure 6-18. (a) (b) the total entropy change ΔS_1 deduced from the Maxwell relation. (c) (d) the entropy change after the subtraction of the contribution from latent heat. The subtraction is shown as the red baselines in (a) (b). This is the pressure-induced additional entropy change ΔS_+ that is used to construct the entropy-temperature S - T curve.

After combining those above, the derived entropy-temperature curve $S'(T,p)$ for PEG-2000 ureasil and ED-2000 ureasil are displayed in Fig.6-19.

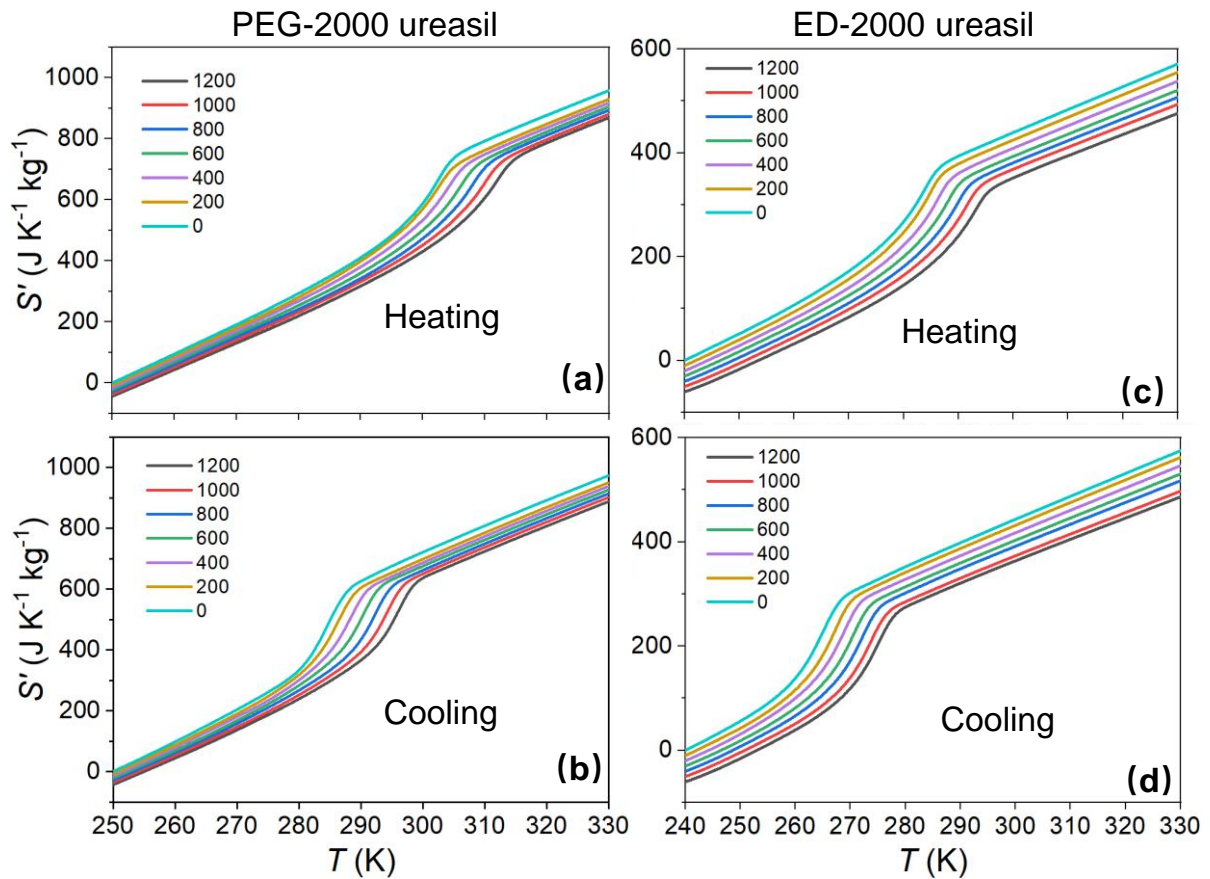


Figure 6-19. (a) (b): Entropy $S'(T,p)$ of PEG-2000 ureasil with respect to the absolute entropy at 250 K and $p \sim 0$ on heating(a) and cooling(b). (c) (d) Entropy $S'(T,p)$ of PEG-2000 ureasil with respect to the absolute entropy at 240 K and $p \sim 0$ on heating(c) and cooling(d).The legend represents the values of applied pressure in bar.

6.4.2 Isothermal entropy changes

By following isothermal trajectories in the plots of $S'(T,p)$ in Fig.6-19 obtained on cooling, we were able to evaluate $\Delta S(T, \Delta p)$ on increasing pressure ($0 \rightarrow p$), as cooling and high pressure both tend to favour the crystalline phase. Similarly, by following isothermal trajectories in the plots of $S'(T,p)$ obtained on heating, we were able to evaluate $\Delta S(T, \Delta p)$ on decreasing pressure ($p \rightarrow 0$), as heating and low pressure both tend to favour the amorphous phase.

In PEG-2000 ureasil, our largest isothermal entropy change $|\Delta S_{\text{peak}}| \sim 263.1 \text{ J K}^{-1} \text{ kg}^{-1}$ arises at $\sim 290 \text{ K}$ for applying $|p| = 1200 \text{ bar}$, as shown in Fig.6-20. Removing $|p| = 1200 \text{ bar}$ at $\sim 305 \text{ K}$ yields $|\Delta S_{\text{peak}}| \sim 236 \text{ J K}^{-1} \text{ kg}^{-1}$.

In ED-2000 ureasil, the largest isothermal entropy change $|\Delta S_{\text{peak}}| \sim 187.5 \text{ J K}^{-1} \text{ kg}^{-1}$ arises at $\sim 269 \text{ K}$ for applying $|p| = 1200 \text{ bar}$, as shown in Fig.6-20. Removing $|p| = 1200 \text{ bar}$ at $\sim 268 \text{ K}$ yields $|\Delta S_{\text{peak}}| \sim 187 \text{ J K}^{-1} \text{ kg}^{-1}$.

Interestingly, both PEG-2000 ureasil and ED-2000 ureasil exhibits high entropy change even outside the phase transition, with the $|\Delta S| \sim 50 \text{ J K}^{-1} \text{ kg}^{-1}$ at the low-temperature phase and $|\Delta S| \sim 80 \text{ J K}^{-1} \text{ kg}^{-1}$ at the higher temperature phase responding to $|p| = 1200 \text{ bar}$. This indicates that PEG-2000 ureasil and ED-2000 ureasil have a wide temperature range $> 100 \text{ K}$ for BC effects. The lower bound of $|\Delta S| \sim 50 \text{ J K}^{-1}$ is already comparable with the peak value of classic BC materials e.g. AgI^{114} ($|\Delta S_{\text{peak}}| \sim 60 \text{ J K}^{-1} \text{ kg}^{-1}$) and $\text{Mn}_3\text{GaN}^{115}$ ($|\Delta S_{\text{peak}}| \sim 22 \text{ J K}^{-1} \text{ kg}^{-1}$). This credits to the large thermal expansion coefficient of polymer materials even outside the phase transition, as measured in Fig.6-14.

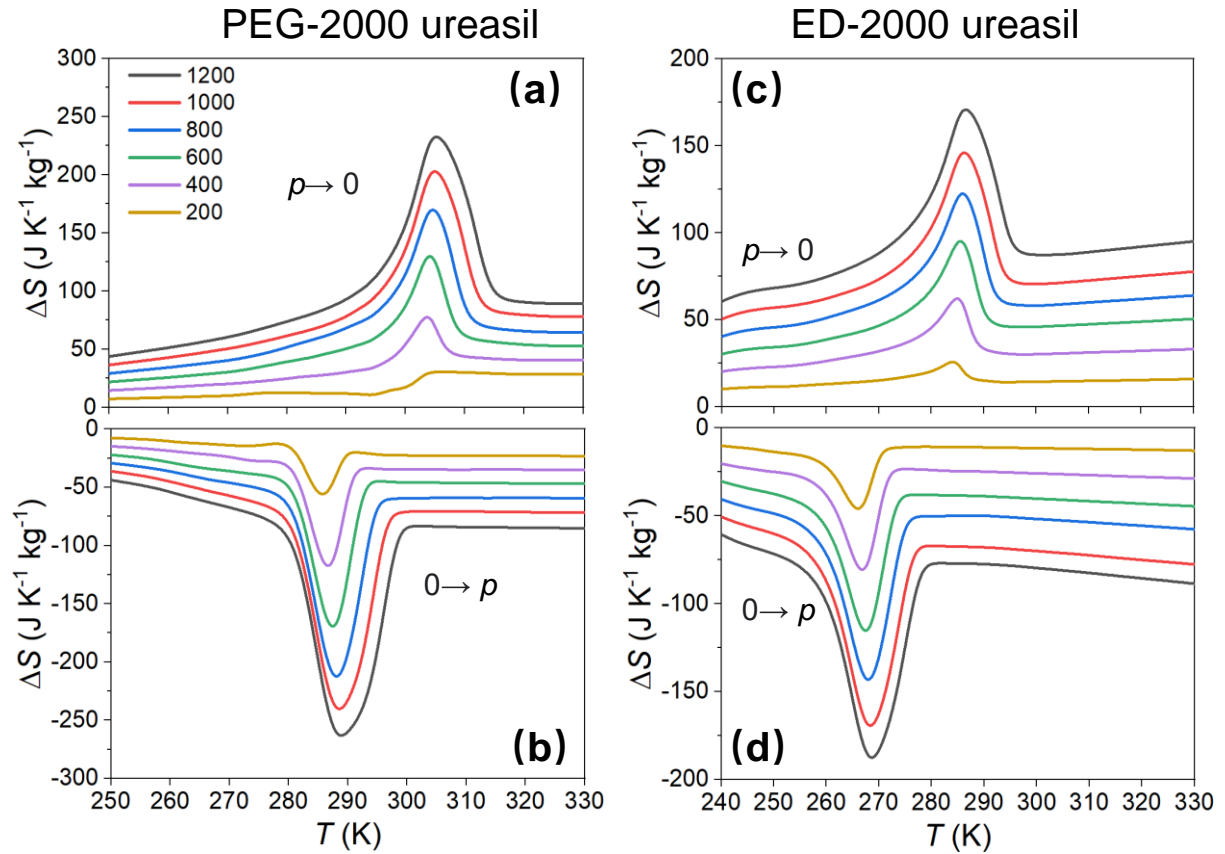


Figure 6-20. (a) (c): Isothermal entropy change ΔS on applying ($0 \rightarrow p$) and (b) (d) removing ($p \rightarrow 0$) pressures, deduced from Fig.6-19.

Based on the data of ΔS , the parameter refrigerant capacity (RC) can be defined as $\text{RC} = |\Delta S_{\text{peak}}| \times [\text{FWHM of } \Delta S(T)]$. RC is the product of ΔS_{peak} and the temperature range at which the value of the entropy change becomes half of the maximum, also known as the full width at half maximum (FWHM). The purpose of RC is to measure the capability of transferring energy because it has the same unit (J kg^{-1}) with work and heat. PEG-2000 ureasil has the maximum RC at $|p| = 1200$ bar at $\sim 4000 \text{ J kg}^{-1}$. ED-2000 ureasil has RC at $|p| = 1200$ bar $\sim 3000 \text{ J kg}^{-1}$ on applying pressure and $\sim 5000 \text{ J kg}^{-1}$ on removing pressure. The values of ΔS and RC of ED-2003 surpass many other BC materials, as shown in Table. 6-1.

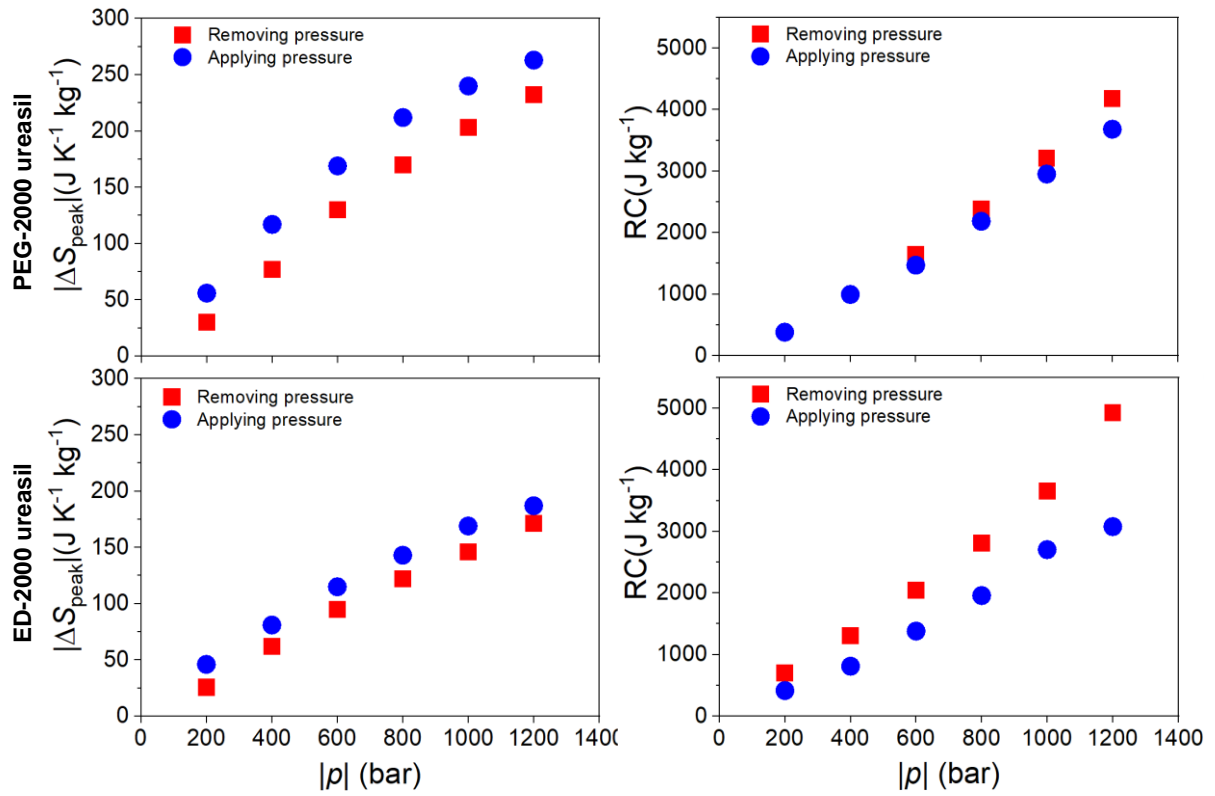


Figure 6-21. Left panel: the peak isothermal entropy change $|\Delta S_{\text{peak}}|$ for pressure changes of magnitude $|p|$, on applying pressure (blue) and removing pressure (red). The values are deduced from the peak maximum in Fig.6-20. **Right panel:** refrigerant capacity (RC) as a function of pressures. $\text{RC} = |\Delta S_{\text{peak}}| \times [\text{FWHM of } \Delta S(T)]$.

6.4.3 Adiabatic temperature changes

By following adiabatic trajectories in $S'(T, p)$ (Fig.6-19), we established both the adiabatic temperature change $\Delta T(T_s, \Delta p)$ on increasing ($0 \rightarrow p$) and decreasing ($p \rightarrow 0$) pressure at starting temperature T_s .

In PEG-2000 ureasil, the largest adiabatic temperature change is $|\Delta T_{\text{peak}}| \sim 10$ K when applying $|p| = 1200$ bar. Removing $|p| = 1200$ bar yields $|\Delta T_{\text{peak}}| \sim 11$ K.

In ED-2000 ureasil, the largest adiabatic temperature ΔT is larger than PEG-2000. Notably, the curves do not peak at the phase transition region. This is because the thermal expansion $\partial V/\partial T$ of ED-2000 ureasil at the amorphous phase is very large such that large ΔT can be obtained by compressing/expanding the ureasil without phase transition. This is also evidenced by the large ΔS_+ associated with the thermal expansion.

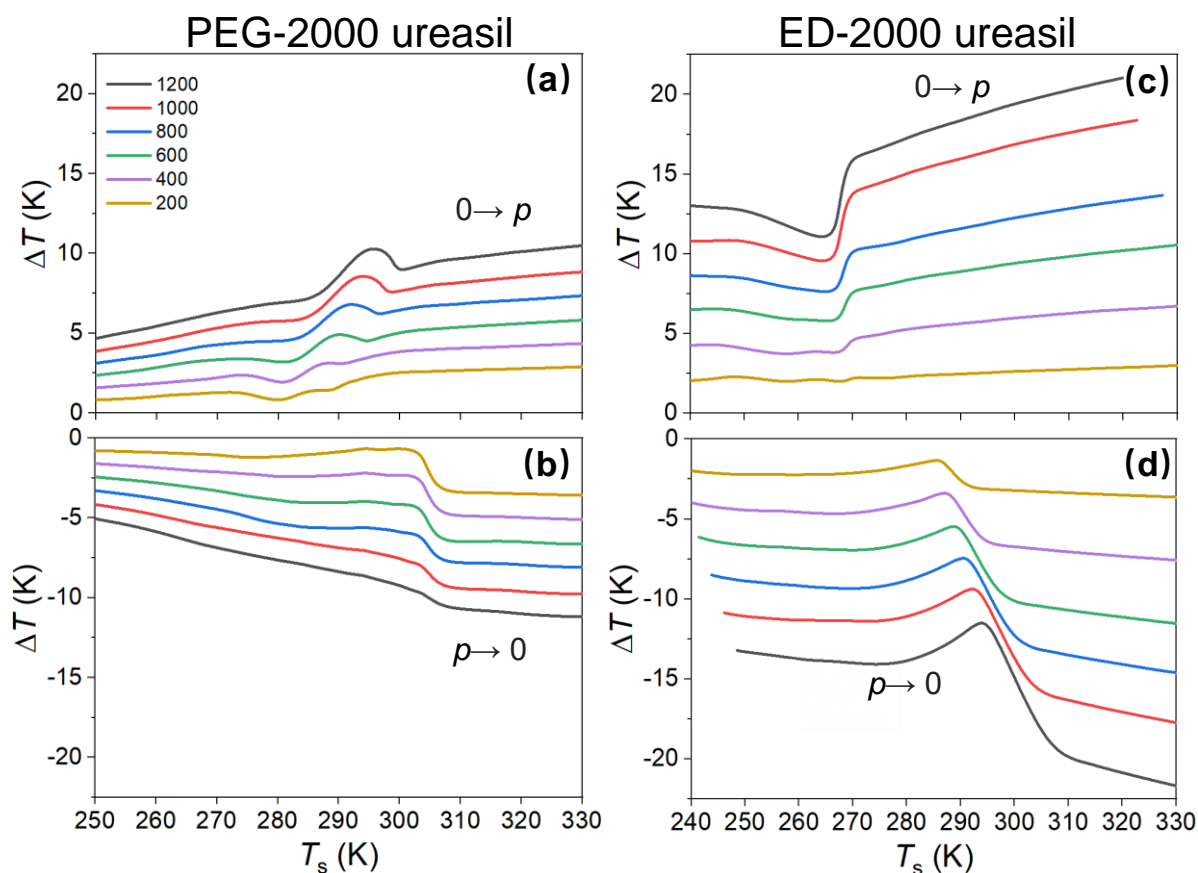


Figure 6-22. (a) (c): Adiabatic temperature change ΔT as a function of starting temperature (T_s) on applying ($0 \rightarrow p$) and (b) (d) removing ($p \rightarrow 0$) pressures, deduced from Fig.6-19.

6.4.4 Reversibility

Due to the thermal hysteresis, the ΔS and ΔT shown above are not reversible. The smallest pressure for achieving reversible BC effects is estimated based on the linear extrapolation in Fig.6-23. For PEG-2000 ureasil, a pressure $|\Delta p| \sim 1880$ bar at 302 K is required. This means that the pressure removal after applying $|\Delta p| \sim 1880$ bar at 302 K would generate BC effects. To make fully reversible BC effects, higher $|\Delta p|$ will be required. For ED-2000 ureasil, $|\Delta p| \sim 2220$ bar at 283 K would be required for reversible BC effects.

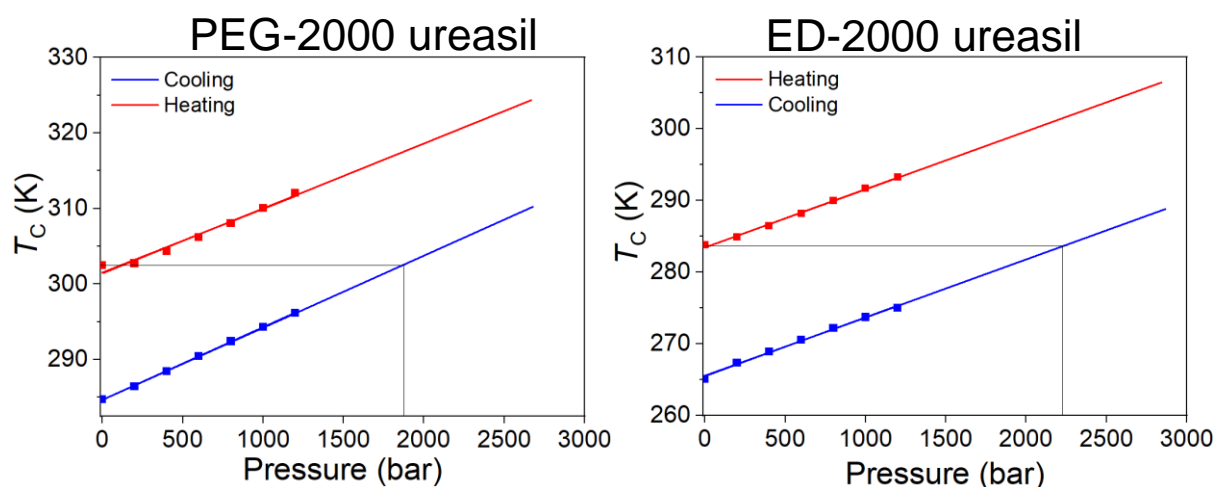


Figure 6-23. The $T - p$ phase diagrams of PEG-2000 ureasil and ED-2000 ureasil. The dots are data from experimental observations. The straight lines were from linear fitting for the purpose of extrapolation of the phase boundary at higher applied pressures, which are not achievable in the lab. The black lines are just a guide to the eyes to estimate the smallest $|\Delta p|$ for reversible BC effects.

6.4.5 Comparison with reported BC materials

The isothermal entropy change $|\Delta S|$ of $263 \text{ J K}^{-1} \text{ kg}^{-1}$ for PEG-2000 ureasil and $187 \text{ J K}^{-1} \text{ kg}^{-1}$ for ED-2000 ureasil in response to $|\Delta p| \sim 1200 \text{ bar}$ are much larger than other reported BC polymers (marked in red in Fig.6-24). Among all other BC materials with solid-solid transition (marked in blue in Fig.6-24), the ureasil materials only fall behind the NPG. The values of $|\Delta S|$ are an order of magnitude bigger than many reported BC materials, e.g., AgI^{114} ($|\Delta S| \sim 60 \text{ J K}^{-1} \text{ kg}^{-1}$), BaTiO_3^{111} ($|\Delta S| \sim 2 \text{ J K}^{-1} \text{ kg}^{-1}$) etc. In comparison with the commercial refrigerant fluid R134a¹²¹ (marked in green in Fig.6-24), ureasil materials have $|\Delta S|$ in the same order of magnitude. Other cooling properties are compared against the main BC materials, as shown in Table 6-1.

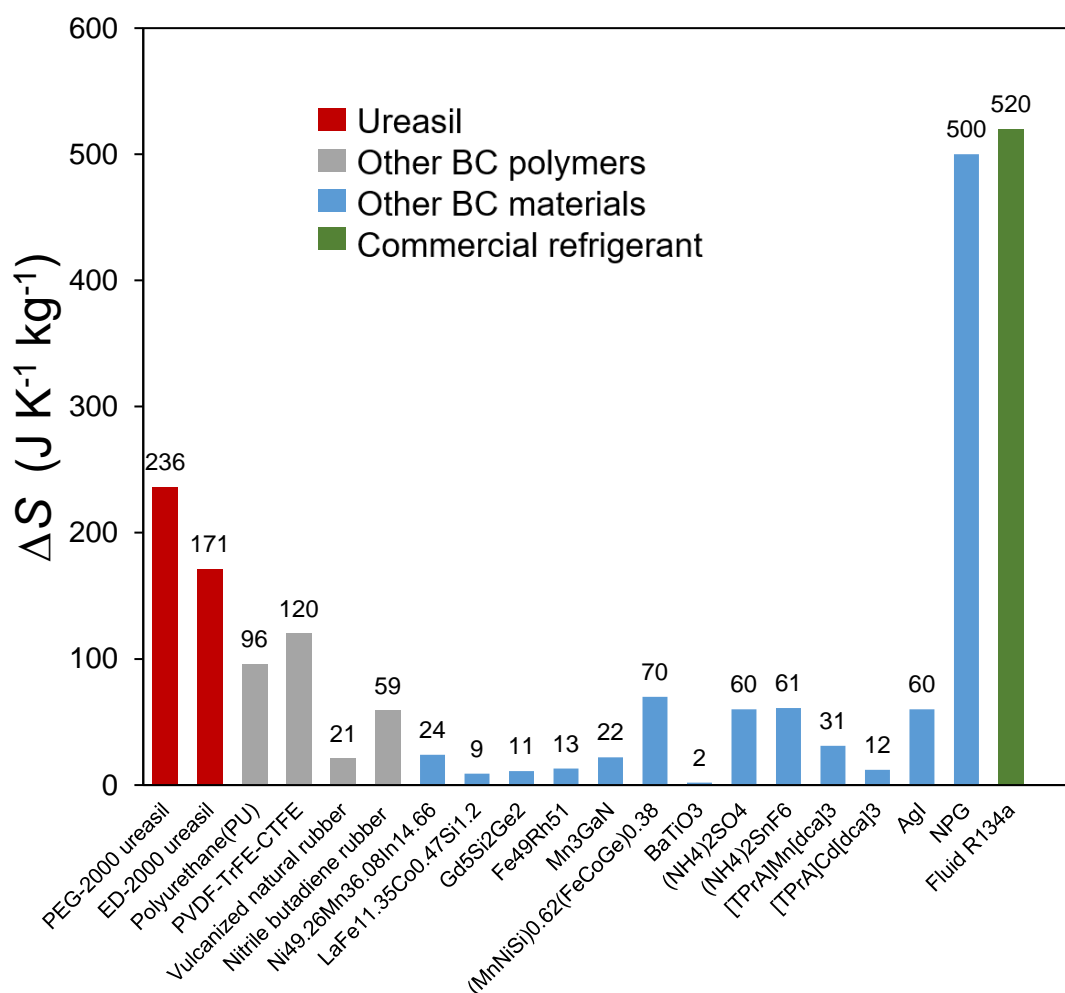


Figure 6-24. Comparison the isothermal entropy change $|\Delta S|$ against other reported BC materials.

Table 6-1. Performance comparison of caloric properties of PEG-2000 ureasil and ED-2000 ureasil to materials with reported giant barocaloric effects. As before, T_C , transition temperature; $|\Delta S|$, isothermal entropy change; $|\Delta T|$, adiabatic temperature change; $|Q|$, isothermal heat; $|\Delta p|$, hydrostatic pressure required to drive the phase transition; RC, refrigerant capacity at $|\Delta p|$ pressure. $|\Delta S|$, $|\Delta T|$ and $|Q|$ arise at T_C , due to application of $|\Delta p|$.

Materials	T_C (K)	ΔS (J/ (K kg))	Q (J/g)	ΔT (K)	Hysteresis (K)	RC (J/ kg)	dT_C/dp (K/ kbar)	$ \Delta p $ (bar)	Reversible	Reference
PEG-2000 ureasil	305	236	72.0	11	20	3682	8.3	1200	no	This work
ED-2000 ureasil	286	171	48.9	12	23	3078	8.3	1200	no	This work
Other BC polymers										
Polyurethane	333	95.6	31.8	13	-	-	-	2180	-	122
PVDF-TrFE-CTFE	368	120	44.2	18.6	-	1440	28.9	2000	yes	123
Vulcanized natural rubber	293	21	6.2	10	-	-	-	434	partially	124
Nitrile butadiene rubber	323	59	19.1	16.4	-	2700	-	3900	yes	116
Other BC materials										
NPG	320	500	160.0	30	18	26000	10.3	5200	yes	121
$Ni_{49.26}Mn_{36.08}In_{14.66}$	293	24	7.0	4.5	10	120	1.8	2600	partially	81
$LaFe_{11.35}Co_{0.47}Si_{1.2}$	237	9	2.0	2.2	-	81	9.4	2000	partially	86
$Gd_5Si_2Ge_2$	270	11	3.0	1.1	5	180	3.8	2000	partially	84
$Fe_{49}Rh_{51}$	308	13	3.8	8.1	10	105	6.4	2500	partially	85
Mn_3GaN	285	22	6.2	4.5	-	125	6.5	1400	partially	115
$(MnNiSi)_{0.62}(FeCoGe)_{0.38}$	330	70	23.1	16.0	15	1000	9.3	2700	yes	116
$BaTiO_3$	400	2	0.6	1.5	4	10	5.6	1000	yes	111
$(NH_4)_2SO_4$	219	60	13.1	8.0	6	276	5.7	1000	yes	113
$(NH_4)_2SnF_6$	110	61	6.7	11.0	0.5	450	15.7	1000	yes	164
$[TPrA]Mn[dca]_3$	330	31	10.1	4.1	1	500	23.1	68.9	yes	165
$[TPrA]Cd[dca]_3$	385	12	6.2	1.4	3	150	38.2	68.9	yes	166
AgI	390	60	23.4	18	25	2500	14	2500	yes	114
Commercial refrigerant										
Fluid R134a	310	520	161.2	-	-	-	-	10	yes	121

6.5 Conclusions

This chapter presents polymer materials with ΔS comparable to the commercial refrigerant. Here, we deployed a gelation method in ureasil polymer materials to exploit the large entropy change associated with polymer fusion while maintaining the solid-state. After systematically varying the molecular weight and molecular shape. PEG-2000 and Jeffamine ED-2000 were selected to fabricate bulk ureasil materials for BC cooling effects.

We demonstrate that gelation is an effective approach to convert the solid-liquid phase transition into gel-to-solid transition in PEG-2000 ureasil and ED-2000 ureasil. PEG-2000 ureasil exhibits $|\Delta S| \sim 263.1 \text{ J K}^{-1} \text{ kg}^{-1}$, which is one order of magnitude higher than most reported BC materials and is comparable to commercial vapour-compression refrigerant fluid R134a ($|\Delta S| \sim 520 \text{ J K}^{-1} \text{ kg}^{-1}$)¹²¹. ED-2000 ureasil shows a comparable entropy change of $|\Delta S| \sim 187.5 \text{ J K}^{-1} \text{ kg}^{-1}$. Moreover, these materials are stretchable, non-toxic and inexpensive. As the gelation method can be adaptable to other polymers, the ureasil materials present in this chapter could open a door for developing novel BC materials, thus paving the way for large-scale applications of BC refrigeration devices.

The major issue is that the reversibility of PEG-2000 ureasil and ED-2000 ureasil needs to be improved due to the big thermal hysteresis $\sim 20 \text{ K}$. This could be narrowed down by further exploring different polymer structures. Also, the thermal conductivity may be improved for building the thermal pumps. One practical approach would be blending carbon powders into the polymer.

7. Conclusions and outlook

This thesis investigated EC effects and BC in organic materials.

In the first part of the PhD project, novel molecular ferroelectric materials BF4 and AH were investigated for their EC properties. By combining experiments and modelling, it was shown that BF4 displays EC effects that are one order-of-magnitude larger than those observed in traditional EC oxides ; BF4 displays isothermal changes in entropy of $|\Delta S| = 15.5 \text{ J K}^{-1} \text{ kg}^{-1}$ for $|\Delta E| = 12 \text{ kV cm}^{-1}$, whereas BaTiO₃ displays isothermal changes in entropy of $|\Delta S| = 2.1 \text{ J K}^{-1} \text{ kg}^{-1}$ for $|\Delta E| = 4 \text{ kV cm}^{-1}$). AH shows smaller EC effects than BF4, but still larger than those observed in traditional EC oxides ($|\Delta S| \sim 7.5 \text{ J K}^{-1} \text{ kg}^{-1}$ for $|\Delta E| = 11.2 \text{ kV cm}^{-1}$). Notably, both BF4 and AH show large values of $|\Delta S|$ for small values of $|\Delta E|$, leading to very large values of EC strength $|\Delta S|/|\Delta E|$. The EC strength of BF4 is five times higher than the EC strength of the prototypical EC oxide BaTiO₃, and forty-five times higher than the EC strength of the prototypical EC polymer P(VDF-TrFE-CFE). AH shows lower values of EC strength but it is mechanically more robust and operates closer to room temperature, which is important for applications.

In the second part of the PhD project, BF4 and two materials with similar composition, namely ClO4 and ReO4, were investigated for their BC properties. These materials are very promising for EC effects because of their large changes in entropy but they suffer from electrical leakage and therefore Joule heating, which ultimately lead to breakdown. Using hydrostatic pressure to drive caloric effects in these materials overcome these limitations, and yields outstanding BC effects. Amongst the three compounds studied, ClO4 shows the largest reversible $|\Delta S|$, with values of $\sim 73.2 \text{ J K}^{-1} \text{ kg}^{-1}$ for $|\Delta p| = 1200 \text{ bar}$. BF4 shows reversible $|\Delta S| = 63.9 \text{ J K}^{-1} \text{ kg}^{-1}$ for $|\Delta p| = 1000 \text{ bar}$, and ReO4 shows reversible $|\Delta S| = 38.2 \text{ J K}^{-1} \text{ kg}^{-1}$ for $|\Delta p| = 1100 \text{ bar}$. Notably, the maximum reversible BC effects observed in BF4 are much higher than their irreversible EC counterparts. The maximum reversible $|\Delta T|$ observed is 7.4 K for BF4 and ClO4, and 9.9 K for ReO4. These results demonstrate that pressure can be an alternative driving field for caloric materials that are organic ferroelectrics, in order to avoid Joule heating and electrical breakdown. The studied materials can be used in the form of powders or fragments without compromising their BC effects, in order to improve heat exchange.

In the third and final part of the PhD project, ureasil polymeric materials were investigated for their BC properties. These compounds show very large changes in entropy when transforming from liquid to solid. By exploiting a gelation method, the liquid to solid phase transition in these compounds is transformed to a gel-to-solid phase transition, which is desirable for some caloric applications. By driving these transitions using pressure, very large BC effects of $|\Delta S| = 263 \text{ J K}^{-1} \text{ kg}^{-1}$ for $|\Delta p| = 1200 \text{ bar}$ are found, which are similar to those observed in commercial vapour-compression refrigerants, e.g. R134a.

This study began by investigating PEG, which shows high entropy changes at its liquid to solid phase transition. Then the molecular weight and molecular shape were systematically varied. PEG-2000 ureasil and ED-2000 ureasil were identified as promising BC materials and fabricated to evaluate their BC properties. PEG-2000 ureasil shows $|\Delta S| = 263.1 \text{ J K}^{-1} \text{ kg}^{-1}$ for $|\Delta p| = 1200 \text{ bar}$, which is larger than the entropy changes reported for most BC materials and comparable to the entropy changes seen in commercial vapour-compression refrigerants¹²¹. ED-2000 ureasil shows similar maximum entropy changes of $|\Delta S| \sim 187.5 \text{ J K}^{-1} \text{ kg}^{-1}$ for $|\Delta p| = 1200 \text{ bar}$. Moreover, these materials are stretchable, non-toxic and inexpensive. The highlighted novelty of ureasil materials is the broad selection of building blocks, including different polymer monomers, molecular weights, gelation matrix agents¹⁹⁰, incorporation of functional polymer chains¹⁹¹, and doping functional particles¹⁹².

For BF4, the next step will be exploring high-quality fabrication techniques (e.g. thin-film fabrication methods) to obtain larger crystals that are non-leaky. For AH, the leakage observed during direct measurements needs to be further investigated and ideally eliminated. The observed leakage could be due to low-energy dislocations, as proposed by Harada *et al.*¹⁹³. Despite their large leakage current, molecular ferroelectric materials remain promising for future EC cooling devices. This is because they show very large EC effects and strengths. If non-leaky films of these organic ferroelectric materials can be developed, their EC performance would dramatically surpass any existing EC material.

The gelation method demonstrated here for ureasil can be adaptable to many polymer materials, and this can lead to many new BC materials. In the future, a range of ureasil materials can be fabricated and tailored for practical BC cooling applications. For example, by changing T_C to meet the specifications of certain applications, by increasing thermal conductivity using metallic particles to improve heat exchange, or by reducing hysteresis using chemical alterations to reduce the magnitude of driving pressures.

Based on our results, it seems viable to build a BC prototype based on PEG-2000 ureasil because its BC performance is comparable to commercial fluid refrigerants. Potential issues such as reversibility and thermal conductivity could be addressed by the methods outlined above. Given that the raw materials for preparing PEG ureasil are inexpensive and commonly used in industry, their use in prototypes could prove useful for the commercialisation of BC technologies, cf. MC prototypes typically require relatively expensive rare-earth metals and large and expensive permanent magnets.

References

1. Radermacher, R. & Kim, K. Domestic refrigerators : recent developments. *International journal of refrigeration* **19**, (1996).
2. Pearson, A. Carbon dioxide - New uses for an old refrigerant. *International Journal of Refrigeration* **28**, 1140–1148 (2005).
3. Perkins, J. Apparatus for producing ice and cooling fluids. *British Patent* (1834).
4. Calm, J. M. & Didion, D. A. Trade-offs in refrigerant selections: Past, present, and future. *International Journal of Refrigeration* **21**, 308–321 (1998).
5. Midgley Jr, T. & Henne, A. L. *Organic Fluorides as Refrigerants. Industrial & Engineering Chemistry* vol. 22 (1930).
6. Wiley, G. R. & Miller, S. I. Thermodynamic parameters for hydrogen bonding of chloroform with Lewis bases in cyclohexane. Proton magnetic resonance study. *J Am Chem Soc* **94**, 3287–3293 (1972).
7. Latimer, W. M. & Rodebush, W. H. Polarity and ionization from the standpoint of the Lewis theory of valence. *J Am Chem Soc* **42**, 1419–1433 (1920).
8. Goymer, P. 100 years of the hydrogen bond. *Nature Chemistry* **4.11** (2012)
9. McElroy, M. B. & Salawitch, R. J. Changing composition of the global stratosphere. *Science (1979)* **243**, 763–770 (1989).
10. Montzka, S. A. *et al.* Present and future trends in the atmospheric burden of ozone-depleting halogens. *Nature* **398**, 690–694 (1999).
11. Montzka, S. A. *et al.* An unexpected and persistent increase in global emissions of ozone-depleting CFC-11. (2018)
12. Rigby, M. *et al.* Increase in CFC-11 emissions from eastern China based on atmospheric observations. *Nature* **569**, 546–550 (2019).
13. Forster, P. *et al.* Changes in atmospheric constituents and in radiative forcing. Chapter 2. in *Climate Change 2007. The Physical Science Basis* (2007).
14. Karl, T. R. & Trenberth, K. E. Modern Global Climate Change Thomas. **302**, 1719–1723 (2003).
15. Root, T., Price, J., Hall, K. & Schneider, S. Fingerprints of global warming on wild animals and plants. *Nature* **421**, 57–60 (2003).
16. Schmidhuber, J. & Tubiello, F. N. Global food security under climate change. *Proc Natl Acad Sci U S A* **104**, 19703–8 (2007).
17. Gerten, D. *et al.* Asynchronous exposure to global warming: Freshwater resources and terrestrial ecosystems. *Environmental Research Letters* **8**, (2013).
18. A Cool World Defining the Energy Conundrum of Cooling for All Contributors.
19. Crossley, S., Mathur, N. D. & Moya, X. New developments in caloric materials for cooling applications. *AIP Advances* **5**, (2015).

20. Riffat, S. B. & Ma, X. Thermoelectrics: A review of present and potential applications. *Applied Thermal Engineering* **23**, 913–935 (2003).
21. Sriksirin, P., Aphornratana, S. & Chungpaibulpatana, S. A review of absorption refrigeration technologies. *Renewable and Sustainable Energy Reviews* **5**, 343–372 (2000).
22. Tu, Y., Wang, R., Zhang, Y. & Wang, J. Progress and Expectation of Atmospheric Water Harvesting. *Joule* **2**, 1452–1475 (2018).
23. Moya, X., Kar-Narayan, S. & Mathur, N. D. Caloric materials near ferroic phase transitions. *Nature Materials* **13**, 439–450 (2014).
24. Stern-Taulats, E. *et al.* Multicaloric materials and effects. *MRS Bulletin* **43**, 295–299 (2018).
25. Giaque, W. F. & MacDougall, D. P. Attainment of Temperatures Below 1° Absolute by Demagnetization of Gd₂(SO₄)₃ · 8H₂O. *Physical Review* **43**, 768 (1933).
26. Heer, C. v., Barnes, C. B. & Daunt, J. G. The design and operation of a magnetic refrigerator for maintaining temperatures below 1K. *Review of Scientific Instruments* **25**, 1088–1098 (1954).
27. Darby, J., Hatton, J., Rollin, B. v., Seymour, E. F. W. & Silsbee, H. B. Experiments on the production of very low temperatures by two-stage demagnetization. *Proceedings of the Physical Society. Section A* **64**, 861–867 (1951).
28. Brown, G. v. Magnetic heat pumping near room temperature. *Journal of Applied Physics* **47**, 3673–3680 (1976).
29. Timbie, P. T., Bernstein, G. M. & Richards, P. L. Development of an adiabatic demagnetization refrigerator for SIRTf. *Cryogenics (Guildf)* **30**, 271–275 (1990).
30. Serlemitsos, A. T., SanSebastian, M. & Kunes, E. Design of a spaceworthy adiabatic demagnetization refrigerator. *Cryogenics (Guildf)* **32**, 117–121 (1992).
31. Steyert, W. A. Stirling-cycle rotating magnetic refrigerators and heat engines for use near room temperature. *Journal of Applied Physics* **49**, 1216–1226 (1978).
32. Yu, B., Liu, M., Egolf, P. W. & Kitanovski, A. A review of magnetic refrigerator and heat pump prototypes built before the year 2010. *International Journal of Refrigeration* **33**, 1029–1060 (2010).
33. Pecharsky, V. K. & Gschneidner, Jr., K. A. Giant Magnetocaloric Effect in Gd₅Si₂Ge₂. *Physical Review Letters* **78**, 4494–4497 (1997).
34. Trung, N. T., Zhang, L., Caron, L., Buschow, K. H. J. & Brück, E. Giant magnetocaloric effects by tailoring the phase transitions. *Applied Physics Letters* **96**, 2008–2011 (2010).
35. Joule, J. P. On some thermo-dynamic properties of solids. *Philosophical Transactions of the Royal Society of London* **149**, 91–131 (1859).
36. Rodriguez, C. & Brown, L. C. The thermal effect due to stress-induced martensite formation in B-CuAlNi single crystals. *Metallurgical and Materials Transactions A* **11**, 147–150 (1980).
37. Bonnot, E., Romero, R., Mañosa, L., Vives, E. & Planes, A. Elastocaloric effect associated with the martensitic transition in shape-memory alloys. *Physical Review Letters* **100**, 1–4 (2008).
38. Brown, L. C. The Thermal Effect in Pseudoelastic Single Crystals of β-CuZnSn. *Metallurgical and Materials Transactions A* **12**, 1491–1494 (1981).

39. Xiao, F., Fukuda, T. & Kakeshita, T. Significant elastocaloric effect in a Fe-31.2Pd (at%) single crystal. *Applied Physics Letters* **102**, 1–5 (2013).
40. Annaorazov, M. P., Nikitin, S. A., Tyurin, A. L., Asatryan, K. A. & Dovletov, A. K. Anomalously high entropy change in FeRh alloy. *Journal of Applied Physics* **79**, 1689–1695 (1996).
41. Shaw, J. A. & Kyriakides, S. Thermomechanical aspects of NiTi. *Journal of the Mechanics and Physics of Solids* **43**, 1243–1281 (1995).
42. Pieczyska, E. A., Gadaj, S. P., Nowacki, W. K. & Tobushi, H. Phase-Transformation Fronts Evolution for Stress- and Strain-Controlled Tension Tests in TiNi Shape Memory Alloy. *Experimental Mechanics* **46**, 531–542 (2006).
43. Cui, J. *et al.* Demonstration of high efficiency elastocaloric cooling with large ΔT using NiTi wires. *Applied Physics Letters* **101**, 4–8 (2012).
44. Guyomar, D. *et al.* Elastocaloric modeling of natural rubber. *Applied Thermal Engineering* **57**, 33–38 (2013).
45. Xie, Z., Sebald, G. & Guyomar, D. Comparison of direct and indirect measurement of the elastocaloric effect in natural rubber. *Applied Physics Letters* **108**, (2016).
46. Xie, Z., Sebald, G. & Guyomar, D. Temperature dependence of the elastocaloric effect in natural rubber. *Physics Letters, Section A: General, Atomic and Solid State Physics* **381**, 2112–2116 (2017).
47. Xie, Z., Sebald, G. & Guyomar, D. Comparison of elastocaloric effect of natural rubber with other caloric effects on different-scale cooling application cases. *Applied Thermal Engineering* **111**, 914–926 (2017).
48. Kobeko, P. & Kurtschatov, J. Dielektrische Eigenschaften der Seignettesalzkristalle. *Zeitschrift für Physik* **66**, 192–205 (1930).
49. Dzyaloshinskii, I. Soviet Physics Uspekhi. *Phys. Usp* **4**, (1961).
50. Holloway, D. Entering the Nuclear Arms Race: The Soviet Decision to Build the Atomic Bomb, 1939-45. *Social Studies of Science* **11**, 159–197 (1981).
51. Baumgartner, Hans. Elektrische Sättigungserscheinungen und elektrokaloischer Effekt von Kaliumphosphat KH_2PO_4 . *Doctoral dissertation* (1950).
52. Strukov BA. Electrocaloric effect in monocrystalline triglycine sulfate. *Kristallografi* **11**, 892–5 (1966).
53. Grindlay, J. & ter Haar, D. On the ferroelectric behaviour of potassium dihydrogen phosphate. *Proceedings of the Royal Society of London. Series A. Mathematical and Physical Sciences* **250**, 266–285 (1959).
54. Kittel, Charles, Paul McEuen, P. M. *Physics of ferroelectrics: a modern perspective*. vol. 8 (Springer Science & Business Media, 1996).
55. Li, W. & Ji, L. J. Perovskite ferroelectrics go metal free. *Science* **361**, 132 (2018).
56. WUL & B. Barium Titanate: a New Ferro-Electric. *Nature* 808–808 (1946).
57. Karchevskii, A. I. I. & Karachevskii, A. I. Electrocaloric effect in polycrystalline barium titanate. *Sov. Phys. Solid State (Eng. Translation)* **3**, 2249–2254 (1962).

58. Moya, X. *et al.* Giant electrocaloric strength in single-crystal BaTiO₃. *Advanced Materials* **25**, 1360–1365 (2013).
59. Kikuchi, A. & Sawaguchi, E. Electrocaloric effect in SrTiO₃. *Journal of the Physical Society of Japan* **19**, 1497–1498 (1964).
60. Thacher, P. Electrocaloric Effects in Some Ferroelectric and Antiferroelectric Pb(Zr,Ti)O₃ Compounds. *Journal of Applied Physics* **1996**, (1968).
61. Tuttle, B. A. & Payne, D. A. The Effects Of Microstructure On The Electrocaloric Properties Of Pb(Zr,Sn,Ti)O₃ Ceramics. *Ferroelectrics* **37**, 603–606 (1981).
62. Shebanovs, L., Sternberg, A., Lawless, W. N. & Borman, K. Isomorphous ion substitutions and order-disorder phenomena in highly electrocaloric lead-scandium tantalate solid solutions. *Ferroelectrics* **184**, 239–242 (1996).
63. Shebanov, L. & Borman, K. On lead-scandium tantalate solid solutions with high electrocaloric effect. *Ferroelectrics* **127**, 143–148 (1992).
64. Shebanov, L. A., Birks, E. & Borman, K. J. X-ray studies of electrocaloric lead-scandium tantalate ordered solid solutions. *Ferroelectrics* **90**, 165–172 (1989).
65. Shebanovs, L., Borman, K., Lawless, W. N. & Kalvane, A. Electrocaloric effect in some perovskite ferroelectric ceramics and multilayer capacitors. *Ferroelectrics* **273**, 137–142 (2002).
66. Sebald, G. *et al.* Electrocaloric and pyroelectric properties of 0.75Pb(Mg_{1/3}Nb_{2/3})O₃-0.25PbTiO₃ single crystals. *Journal of Applied Physics* **100**, (2006).
67. Hagberg, J., Uusimäki, A. & Jantunen, H. Electrocaloric characteristics in reactive sintered 0.87 Pb (Mg_{1/3}Nb_{2/3}) O₃ -0.13 PbTiO₃. *Applied Physics Letters* **92**, (2008).
68. Rožič, B. *et al.* Influence of the critical point on the electrocaloric response of relaxor ferroelectrics. *Journal of Applied Physics* **110**, 0–5 (2011).
69. Bai, Y. *et al.* Thickness dependence of electrocaloric effect in high-temperature sintered Ba_{0.8}Sr_{0.2}TiO₃ ceramics. *Journal of Alloys and Compounds* **736**, 57–61 (2018).
70. Bai, Y., Han, X., Ding, K. & Qiao, L.-J. Combined effects of diffuse phase transition and microstructure on the electrocaloric effect in Ba_{1-x}Sr_x TiO₃ ceramics Enhanced electrocaloric effect in lead-free BaTi_{1-x}Sn_xO₃ ceramics near room temperature Combined effects of diffuse phase trans. *Appl. Phys. Lett.* **1031**, 162902–162904 (2013).
71. Bai, Y., Han, X., Qiao, L. & Table, V. Optimized electrocaloric refrigeration capacity in lead-free (1-x)BaZr_{0.2}Ti_{0.8}O_{3-x}Ba_{0.7}Ca_{0.3}TiO₃ ceramics. *Appl. Phys. Lett.* **252904**, 1–5 (2015).
72. Singh, G. *et al.* Electro-caloric effect in 0.45BaZr_{0.2}Ti_{0.8}O₃-0.55Ba_{0.7}Ca_{0.3}TiO₃ single crystal. *Applied Physics Letters* **102**, 082902 (2013).
73. Liu, X. Q., Chen, T. T., Wu, Y. J. & Chen, X. M. Enhanced electrocaloric effects in spark plasma-sintered Ba_{0.65}Sr_{0.35}TiO₃-based ceramics at room temperature. *Journal of the American Ceramic Society* **96**, 1021–1023 (2013).
74. Saranya, D., Chaudhuri, R., Parui, J. & Krupanidhi, S. B. Electrocaloric effect of PMN-PT thin films near morphotropic phase boundary. *Bull. Mater. Sci* **32**, 259–262 (2009).

75. Lawless, W. N. & Clark, C. F. Dielectric and electrothermal measurements on $(\text{Cd}_{0.83}\text{Pb}_{0.17})_2\text{Nb}_2\text{O}_7$ at liquid-nitrogen temperatures. *Physical Review B* **36**, 459–465 (1987).
76. Kar-Narayan, S. & Mathur, N. D. Predicted cooling powers for multilayer capacitors based on various electrocaloric and electrode materials. *Applied Physics Letters* **95**, 4–7 (2009).
77. Kar-Narayan, S. & Mathur, N. D. Direct and indirect electrocaloric measurements using multilayer capacitors. *Journal of Physics D: Applied Physics* **43**, 032002 (2010).
78. Kar-Narayan, S. *et al.* Direct electrocaloric measurements of a multilayer capacitor using scanning thermal microscopy and infra-red imaging. *Applied Physics Letters* **102**, 1–5 (2013).
79. Bai, Y., Zheng, G. P. & Shi, S. Q. Kinetic electrocaloric effect and giant net cooling of lead-free ferroelectric refrigerants. *Journal of Applied Physics* **108**, 1–13 (2010).
80. Mischenko, A. S., Zhang, Q., Scott, J. F., Whatmore, R. W. & Mathur, N. D. Giant electrocaloric effect in thin-film $\text{PbZr}_{0.95}\text{Ti}_{0.05}\text{O}_3$. *Science* **311**, 1270–1271 (2006).
81. Neese, B. *et al.* Large Electrocaloric Effect in Ferroelectric Polymers Near Room Temperature. *Science* **321**, 821–823 (2008).
82. Lovinger, A. J. Ferroelectric polymers. *Science* **220**, 1115–1121 (1983).
83. Zhang, Q. M., Bharti, V. & Zhao, X. Giant Electrostriction and Relaxor Ferroelectric Behavior in Electron-Irradiated Poly(vinylidene fluoride-trifluoroethylene) Copolymer. *Science* **280**, 2101–2104 (1998).
84. Lu, S. G., Rožič, B., Zhang, Q. M., Kutnjak, Z. & Neese, B. Enhanced electrocaloric effect in ferroelectric poly(vinylidene-fluoride/trifluoroethylene) 55/45 mol % copolymer at ferroelectric-paraelectric transition. *Applied Physics Letters* **98**, 2009–2012 (2011).
85. Li, X. *et al.* Giant electrocaloric effect in ferroelectric poly(vinylidene fluoride- trifluoroethylene) copolymers near a first-order ferroelectric transition. *Applied Physics Letters* **101**, (2012).
86. Lu, S. G. *et al.* Comparison of directly and indirectly measured electrocaloric effect in relaxor ferroelectric polymers. *Applied Physics Letters* **97**, 202901 (2010).
87. Scott, J. F. *Electrocaloric Materials. Annual Review of Materials Research* vol. 41 (2011).
88. Li, Q. *et al.* Relaxor Ferroelectric-Based Electrocaloric Polymer Nanocomposites with a Broad Operating Temperature Range and High Cooling Energy. *Advanced Materials* **27**, 2236–2241 (2015).
89. Zhang, G. *et al.* Ferroelectric Polymer Nanocomposites for Room-Temperature Electrocaloric Refrigeration. *Advanced Materials* **27**, 1450–1454 (2015).
90. Zhang, G. *et al.* Colossal Room-Temperature Electrocaloric Effect in Ferroelectric Polymer Nanocomposites Using Nanostructured Barium Strontium Titanates. *ACS Nano* **9**, 7164–7174 (2015).
91. Qian, J. *et al.* Interfacial Coupling Boosts Giant Electrocaloric Effects in Relaxor Polymer Nanocomposites: In Situ Characterization and Phase-Field Simulation. *Advanced Materials* **31**, 1–9 (2019).
92. Zhang, G. *et al.* Nanoconfinement-Induced Giant Electrocaloric Effect in Ferroelectric Polymer Nanowire Array Integrated with Aluminum Oxide Membrane to Exhibit Record Cooling Power Density. *Advanced Materials* **31**, 8 (2019).

93. Jian, X.-D. *et al.* Direct Measurement of Large Electrocaloric Effect in Ba(Zr_xTi_{1-x})O₃ Ceramics. *ACS Applied Materials & Interfaces* **10**, 4801–4807 (2018).
94. Liu, H. Y., Zhang, H. Y., Chen, X. G. & Xiong, R. G. Molecular Design Principles for Ferroelectrics: Ferroelectrochemistry. *J Am Chem Soc* **142**, 15205–15218 (2020).
95. Katrusiak, A. & Szafranski, M. Ferroelectricity in NH···N Hydrogen Bonded Crystals. *Physical Review Letters* **82**, 576 (1999).
96. Szafranski, M., Katrusiak, A. & McIntyre, G. J. Ferroelectric Order of Parallel Bistable Hydrogen Bonds. *Physical Review Letters* **89**, 215507 (2002).
97. Harada, J. *et al.* Plastic/Ferroelectric Crystals with Easily Switchable Polarization: Low-Voltage Operation, Unprecedentedly High Pyroelectric Performance, and Large Piezoelectric Effect in Polycrystalline Forms. *J Am Chem Soc* **141**, 9349–9357 (2019).
98. Harada, J. *et al.* Directionally tunable and mechanically deformable ferroelectric crystals from rotating polar globular ionic molecules. *Nature Chemistry* **8**, 946–952 (2016).
99. Xiong, R. *et al.* Metal-free three-dimensional perovskite ferroelectrics. *Science (1979)* **361**, 151–155 (2018).
100. Wang, J.-J. *et al.* Extraordinarily Large Electrocaloric Strength of Metal-Free Perovskites. *Advanced Materials* **32**, 1906224 (2020).
101. Li, M. *et al.* Soft Perovskite-Type Antiferroelectric with Giant Electrocaloric Strength near Room Temperature. *J Am Chem Soc* **142**, 20744–20751 (2020).
102. Li, W. *et al.* The strong electrocaloric effect in molecular ferroelectric ImClO₄ with ultrahigh electrocaloric strength. *Journal of Materials Chemistry A* **8**, 16189–16194 (2020).
103. McLinden, M. O. *Thermophysical Properties of Refrigerants, ASHRAE Handbook--Fundamentals (2005 revision)*. (2005).
104. Ma, D. C. *et al.* Electrocaloric properties of ferroelectric-paraelectric superlattices controlled by the thickness of paraelectric layer in a wide temperature range. *AIP Advances* **4**, (2014).
105. Alex Müller, K. *et al.* Cooling by adiabatic pressure application in Pr_{1-x}La_xNiO₃. *Applied Physics Letters* **73**, 1056–1058 (1998).
106. Mañosa, L. *et al.* Giant solid-state barocaloric effect in the Ni-Mn-In magnetic shape-memory alloy. *Nature Materials* **9**, 478–481 (2010).
107. Mañosa, L. *et al.* Inverse barocaloric effect in the giant magnetocaloric La-Fe-Si-Co compound. *Nature Communications* **2**, 1–5 (2011).
108. Wu, R. R. *et al.* Giant barocaloric effect in hexagonal Ni₂ In-type Mn-Co-Ge-In compounds around room temperature. *Scientific Reports* **5**, 1–11 (2015).
109. Stern-Taulats, E. *et al.* Barocaloric and magnetocaloric effects in Fe₄₉Rh₅₁. *Physical Review B - Condensed Matter and Materials Physics* **89**, 1–8 (2014).
110. Liu, Y. *et al.* Giant room-temperature barocaloric effect and pressure-mediated electrocaloric effect in BaTiO₃ single crystal. *Applied Physics Letters* **104**, (2014).

111. Stern-Taulats, E. *et al.* Inverse barocaloric effects in ferroelectric BaTiO₃ ceramics. *APL Materials* **4**, (2016).
112. Mikhaleva, E. A. *et al.* Caloric characteristics of PbTiO₃ in the temperature range of the ferroelectric phase transition. *Physics of the Solid State* **54**, 1832–1840 (2012).
113. Lloveras, P. *et al.* Giant barocaloric effects at low pressure in ferroelectric ammonium sulphate. *Nature Communications* **6**, (2015).
114. Aznar, A. *et al.* Giant barocaloric effects over a wide temperature range in superionic conductor AgI. *Nature Communications* **8**, (2017).
115. Matsunami, D., Fujita, A., Takenaka, K. & Kano, M. Giant barocaloric effect enhanced by the frustration of the antiferromagnetic phase in Mn₃GaN. *Nature Materials* **14**, 73–78 (2014).
116. Lloveras, P. *et al.* Giant reversible barocaloric response of (MnNiSi)_{1-x}(FeCoGe)_x ($x = 0.39, 0.40, 0.41$). *APL Materials* **7**, 061106 (2019).
117. Hull, S. Superionics: crystal structures and conduction processes. *Reports on Progress in Physics* **67**, 1233 (2004).
118. Cazorla, C. & Errandonea, D. Giant Mechanocaloric Effects in Fluorite-Structured Superionic Materials. *Nano Letters* **16**, 3124–3129 (2016).
119. Sagotra, A. K., Chu, D. & Cazorla, C. Room-temperature mechanocaloric effects in lithium-based superionic materials. *Nature Communications* **9**, 1–7 (2018).
120. Sagotra, A. K., Errandonea, D. & Cazorla, C. Mechanocaloric effects in superionic thin films from atomistic simulations. *Nature Communications* **8**, 1–7 (2017).
121. Lloveras, P. *et al.* Colossal barocaloric effects near room temperature in plastic crystals of neopentylglycol. *Nature communications* **10.1** (2019): 1-7.
122. Bocca, J. R. *et al.* Giant barocaloric effect in commercial polyurethane. *Polymer Testing* **100**, 107251 (2021).
123. Patel, S., Chauhan, A., Vaish, R. & Thomas, P. Elastocaloric and barocaloric effects in polyvinylidene difluoride-based polymers. *Applied Physics Letters* **108**, 072903 (2016).
124. Usuda, E. O., Bom, N. M. & Carvalho, A. M. G. Large barocaloric effects at low pressures in natural rubber. *European Polymer Journal* **92**, 287–293 (2017).
125. Usuda, E. O., Imamura, W., Bom, N. M., Paixão, L. S. & Carvalho, A. M. G. Giant Reversible Barocaloric Effects in Nitrile Butadiene Rubber around Room Temperature. *ACS Applied Polymer Materials* **1**, 1991–1997 (2019).
126. Sinyavsky, Y. v & Brodyansky, V. M. Experimental testing of electrocaloric cooling with transparent ferroelectric ceramic as a working body. *Ferroelectrics* **131**, 321–325 (1992).
127. Epstein, R. I. & Malloy, K. J. Electrocaloric devices based on thin-film heat switches. *Journal of Applied Physics Applied Physics Letters* **106**, (2009).
128. Ju, Y. S. Solid-State Refrigeration Based on the Electrocaloric Effect for Electronics Cooling. *Journal of Electronic Packaging* **132**, 041004 (2010).

129. Wang, Y. D. *et al.* A heat-switch-based electrocaloric cooler. *Applied Physics Letters* **107**, 242901–162904 (2015).
130. Zhang, T., Qian, X. S., Gu, H., Hou, Y. & Zhang, Q. M. An electrocaloric refrigerator with direct solid to solid regeneration. *Applied Physics Letters* **110**, 243503–224102 (2017).
131. Plaznik, U. *et al.* Bulk relaxor ferroelectric ceramics as a working body for an electrocaloric cooling device. *Applied Physics Letters* **106**, (2015).
132. Ma, R. *et al.* Highly efficient electrocaloric cooling with electrostatic actuation. *Science* **357**, 1130–1134 (2017).
133. Bradeško, A. *et al.* Coupling of the electrocaloric and electromechanical effects for solid-state refrigeration. *Applied Physics Letters* **109**, 143508 (2016).
134. West, A. R., Sinclair, D. C. & Hirose, N. *Characterization of Electrical Materials, Especially Ferroelectrics, by Impedance Spectroscopy. Journal of Electroceramics* vol. 1 (1997).
135. Schenk, T., Yurchuk, E. & Mueller, S. About the deformation of ferroelectric hystereses. *Appl. Phys. Rev* **1**, 41103 (2014).
136. Mañosa, L., Bou, M., Calles, C. & Cirera, A. Low-cost differential scanning calorimeter. *American Journal of Physics* **64**, 283–287 (1996).
137. Faye, R. *et al.* Heat flow in electrocaloric multilayer capacitors. *Journal of Alloys and Compounds* **834**, 155042 (2020).
138. Liu, Y., Strozyk, H., Dkhil, B. & Defay, E. Insight into electrocaloric cooling power in multilayer capacitors using infra-red camera. *Applied Physics Letters* **109**, 212902 (2016).
139. Nair, B. *et al.* Large electrocaloric effects in oxide multilayer capacitors over a wide temperature range. *Nature* **575**, 468–472 (2019).
140. Crossley, S. Electrocaloric materials and devices. (Doctoral thesis). (2013).
141. Krenke, T. *et al.* Hysteresis effects in the magnetic-field-induced reverse martensitic transition in magnetic shape-memory alloys. *Journal of Applied Physics* **108**, 043914 (2010).
142. Landau, L. D. *Collected papers of LD Landau.* (Pergamon, 1965).
143. Ginzburg, V. L. Phase transitions in ferroelectrics: some historical remarks. *Uspekhi Fizicheskikh Nauk* **171**, 1091 (2001).
144. Pertsev, N. A., Zembilgotov, A. G. & Tagantsev, A. K. Effect of Mechanical Boundary Conditions on Phase Diagrams of Epitaxial Ferroelectric Thin Films. *Physical Review Letters* **80**, 1988–1991 (1998).
145. Zhang, X. *et al.* Sizable electrocaloric effect in a wide temperature range tuned by tensile misfit strain in BaTiO₃ thin films. *Journal of Applied Physics* **109**, (2011).
146. Lin, S., Lü, T., Jin, C. & Wang, X. Size effect on the dielectric properties of BaTiO₃ nanoceramics in a modified Ginsburg-Landau-Devonshire thermodynamic theory. *Physical Review B - Condensed Matter and Materials Physics* **74**, (2006).
147. Cross, L. E. A phenomenological gibbs function for BaTiO₃, giving correct e field dependence of all ferroelectric phase changes. *Ferroelectrics* **59**, 197–203 (1984).

148. Lee, S., Rossetti, G. A., Liu, Z. K. & Randall, C. A. Intrinsic ferroelectric properties of the nonstoichiometric perovskite oxide $\text{Ba}_{1-x}\text{Ti}_{1-y}\text{O}_{3x-2y}$. *Journal of Applied Physics* **105**, (2009).
149. Mischenko, A. S., Zhang, Q., Scott, J. F., Whatmore, R. W. & Mathur, N. D. Giant electrocaloric effect in thin-film $\text{PbZr}_{0.95}\text{Ti}_{0.05}\text{O}_3$. *Science* **311**, 1270–1 (2006).
150. Liu, Y. *et al.* Fast Growth of Thin MAPbI₃ Crystal Wafers on Aqueous Solution Surface for Efficient Lateral-Structure Perovskite Solar Cells. *Advanced Functional Materials* **1807707**, 1–6 (2019).
151. Saidaminov, M. I. *et al.* High-quality bulk hybrid perovskite single crystals within minutes by inverse temperature crystallization. *Nature Communications* **6**, 1–6 (2015).
152. Chen, Y. X. *et al.* General Space-Confined On-Substrate Fabrication of Thickness-Adjustable Hybrid Perovskite Single-Crystalline Thin Films. *J Am Chem Soc* **138**, 16196–16199 (2016).
153. Liu, Y. *et al.* Two-Inch-Sized Perovskite $\text{CH}_3\text{NH}_3\text{PbX}_3$ (X = Cl, Br, I) Crystals: Growth and Characterization. *Advanced Materials* **27**, 5176–5183 (2015).
154. Szafranski, M. & Katrusiak, A. Short-range ferroelectric order induced by proton transfer-mediated ionicity. *Journal of Physical Chemistry B* **108**, 15709–15713 (2004).
155. Yu, S. S., Liu, S. X. & Duan, H. B. Dielectric response and anhydrous proton conductivity in a chiral framework containing a non-polar molecular rotor. *Dalton Transactions* **44**, 20822–20825 (2015).
156. Kolodiazny, T. *et al.* Giant magnetocapacitance in cerium sesquioxide. *Physical Review B* **98**, 054423 (2018).
157. Nataf, G. F., Aktas, O., Granzow, T. & Salje, E. K. H. Influence of defects and domain walls on dielectric and mechanical resonances in LiNbO_3 . *Journal of Physics: Condensed Matter* **28**, 015901 (2015).
158. Katrusiak, A. & Szafranski, M. Ferroelectricity in $\text{NH}\cdots\text{N}$ Hydrogen Bonded Crystals. *Physical Review Letters* **82**, 576 (1999).
159. Szafranski, M. & Katrusiak, A. Short-range ferroelectric order induced by proton transfer-mediated ionicity. *Journal of Physical Chemistry B* **108**, 15709–15713 (2004).
160. Szafranski, M. & Katrusiak, A. Thermodynamic behaviour of bistable $\text{NH}^+\cdots\text{N}$ hydrogen bonds in monosalts of 1,4-diazabicyclo[2.2.2]octane. *Chemical Physics Letters* **318**, 427–432 (2000).
161. Olejniczak, A., Anioła, M., Szafranski, M., Budzianowski, A. & Katrusiak, A. New polar phases of 1,4-diazabicyclo[2.2.2]octane perchlorate, an $\text{NH}^+\cdots\text{N}$ hydrogen-bonded ferroelectric. *Crystal Growth and Design* **13**, 2872–2879 (2013).
162. Budzianowski, A., Katrusiak, A. & Szafranski, M. Anomalous protonic-glass evolution from ordered phase in $\text{NH}^+\cdots\text{N}$ hydrogen-bonded dabcoHBF ferroelectric. *Journal of Physical Chemistry B* **112**, 16619–16625 (2008).
163. Pionteck, J. Determination of Pressure Dependence of Polymer Phase Transitions by pVT Analysis. *Polymers* **2018**, Vol. 10, Page 578 **10**, 578 (2018).
164. Flerov, I. N. *et al.* Thermal, structural, optical, dielectric and barocaloric properties at ferroelastic phase transition in trigonal $(\text{NH}_4)_2\text{SnF}_6$: A new look at the old compound. *Journal of Fluorine Chemistry* **183**, 1–9 (2016).
165. Bermúdez-García, J. M. *et al.* Giant barocaloric effect in the ferroic organic-inorganic hybrid [TPrA][Mn(dca)3] perovskite under easily accessible pressures. *Nature Communications* **8**, 1–8 (2017).

166. Bermúdez-García, J. M. *et al.* Giant barocaloric tunability in [(CH₃CH₂CH₂)₄N]Cd[N(CN)₂]₃ hybrid perovskite. *Journal of Materials Chemistry C* **6**, 9867–9874 (2018).
167. Qian, X. *et al.* High-entropy polymer produces a giant electrocaloric effect at low fields. *Nature* **600**, 664–669 (2021).
168. Lin, J. *et al.* Colossal and reversible barocaloric effect in liquid-solid-transition materials *n*-alkanes. *Nature Communications* **13**, 1–7 (2022).
169. Kou, Y. *et al.* Thermal analysis and heat capacity study of polyethylene glycol (PEG) phase change materials for thermal energy storage applications. (2019).
170. Kim, M. R., Park, H. J., Cheon, K. H., Yeom, C. K. & Lee, K. Y. Novel behavior in a polymer solution: the disappearance of the melting temperature (T_m) and enthalpy change (ΔH_m) of the solvent. *Scientific Reports* **10**, 1–11 (2020).
171. Meazzini, I. *et al.* Targeted design leads to tunable photoluminescence from perylene dicarboxydiimide–poly(oxyalkylene)/siloxane hybrids for luminescent solar concentrators. *Journal of Materials Chemistry C* **4**, 4049–4059 (2016).
172. Wang, Z., Nie, J., Qin, W., Hu, Q. & Tang, B. Z. Gelation process visualized by aggregation-induced emission fluorogens. *Nature Communications* **7**, 1–8 (2016).
173. Lyu, G. *et al.* Aggregation-induced emission from silole-based lumophores embedded in organic–inorganic hybrid hosts. *Journal of Materials Chemistry C* **9**, 13914–13925 (2021).
174. Willis-Fox, N., Kraft, M., Arlt, J., Scherf, U. & Evans, R. C. Tunable White-Light Emission from Conjugated Polymer-Di-Ureasil Materials. *Advanced Functional Materials* **26**, 532–542 (2016).
175. Kaniyoor, A., McKenna, B., Comby, S. & Evans, R. C. Design and Response of High-Efficiency, Planar, Doped Luminescent Solar Concentrators Using Organic–Inorganic Di-Ureasil Waveguides. *Advanced Optical Materials* **4**, 444–456 (2016).
176. Meazzini, I. *et al.* Ureasil organic–inorganic hybrids as photoactive waveguides for conjugated polyelectrolyte luminescent solar concentrators. *Materials Chemistry Frontiers* **1**, 2271–2282 (2017).
177. Collins, R. A. *et al.* Photoactive organic-inorganic hybrid polymer waveguides for optical device technologies. *Photosensitive Materials and their Applications* **11367**, 94–101 (2020).
178. Bunn, C. W. The melting points of chain polymers. *Journal of Polymer Science* **16**, 323–343 (1955).
179. Fetters, L. J., Lohse, D. J., Richter, D., Witten, T. A. & Zirkel, A. Connection between Polymer Molecular Weight, Density, Chain Dimensions, and Melt Viscoelastic Properties. *Macromolecules* **27**, 4639–4647 (2002).
180. Mandelkern, L., Allou, A. L. & Gopalan, M. Enthalpy of fusion of linear polyethylene. *Journal of Physical Chemistry* **72**, 309–318 (1968).
181. Flory, P. J. & Vrij, A. Melting Points of Linear-Chain Homologs. The Normal Paraffin Hydrocarbons. *J Am Chem Soc* **85**, 3548–3553 (1963).
182. Hu, W. The melting point of chain polymers. *The Journal of Chemical Physics* **113**, 3901 (2000).
183. Tsujimoto, Y., Sakurai, T., Ono, Y., Nagano, S. & Seki, S. Cold Crystallization of Ferrocene-Hinged π -Conjugated Molecule Induced by the Limited Conformational Freedom of Ferrocene. *Journal of Physical Chemistry B* **123**, 8325–8332 (2019).

184. Kong, Y. & Hay, J. N. The enthalpy of fusion and degree of crystallinity of polymers as measured by DSC. *European Polymer Journal* **39**, 1721–1727 (2003).
185. Yoshihara, N., Shibaya, M. & Ishihara, H. Cold crystallization behaviors of poly(ethylene terephthalate). *Journal of Polymer Engineering* **25**, 97–114 (2005).
186. Furushima, Y., Schick, C. & Toda, A. Crystallization, recrystallization, and melting of polymer crystals on heating and cooling examined with fast scanning calorimetry. *Polymer Crystallization* **1**, e10005 (2018).
187. van Krevelen, D. W. & te Nijenhuis, K. Transition Temperatures. *Properties of Polymers* 129–188 (2009)
188. Ogoshi, T. & Chujo, Y. Organic-inorganic polymer hybrids prepared by the sol-gel method. *Composite Interfaces* **11**, 539–566 (2005).
189. Bellare, J. R., Davis, H. T., Miller, W. G. & Scriven, L. E. Polarized optical microscopy of anisotropic media: Imaging theory and simulation. *Journal of Colloid and Interface Science* **136**, 305–326 (1990).
190. Catauro, M., Piccolella, S. & Leonelli, C. FT-IR Characterization of Antimicrobial Hybrid Materials through Sol-Gel Synthesis. *Applied Sciences* **10**, 1180 (2020).
191. Lyu, G. *et al.* Aggregation-induced emission from silole-based lumophores embedded in organic–inorganic hybrid hosts. *Journal of Materials Chemistry C* **9**, 13914–13925 (2021).
192. Brennan, L. J. *et al.* Large area quantum dot luminescent solar concentrators for use with dye-sensitised solar cells. *Journal of Materials Chemistry A* **6**, 2671–2680 (2018).
193. Harada, J. *et al.* Ferroelectricity and Piezoelectricity in Free-Standing Polycrystalline Films of Plastic Crystals. *J Am Chem Soc* **140**, 346–354 (2018).

Appendices

1. Interesting failed attempts and side projects

1.1 EC effects in metal-free perovskites

When searching for EC materials, materials with large entropy change and strongly temperature-dependent polarisation $|\partial P/\partial T|$ are desired. In 2018, Ye, Heng-Yun, *et al.*⁹⁹ reported a new ferroelectric material Mdabco (N-methyl-N'-diazabicyclo[2.2.2]octonium)–ammonium triiodide, which is referred as [Mdabco]NH₄I₃. This is a promising EC material as it shows a spontaneous polarization $P_s \sim 21 \mu\text{C cm}^{-2}$ and has a sharp first-order phase transition. Therefore, the author tried to synthesize by following the approach from ref⁹⁹.

However, due to the difficulty of growing crystals with measurable sizes and high cost of raw materials. No ideal samples were made by the author for EC measurements. Luckily, the collaborator Dr Dumitru Sirbu from Newcastle University, has fabricated multiple crystals for us. The author then conducted most of the experimental work.

Firstly, the indirect method was attempted to measure the EC effects. However, this was not successful. When heating to 420 K, which is close to the reported T_C of 448 K, the $P(E)$ loops becomes fatty, indicating leakage and sample failure(Fig. A-1). After cooling back to room temperature, the sample turned yellow, as shown in Fig. A-2, suggesting irreversible changes in the chemical composition.

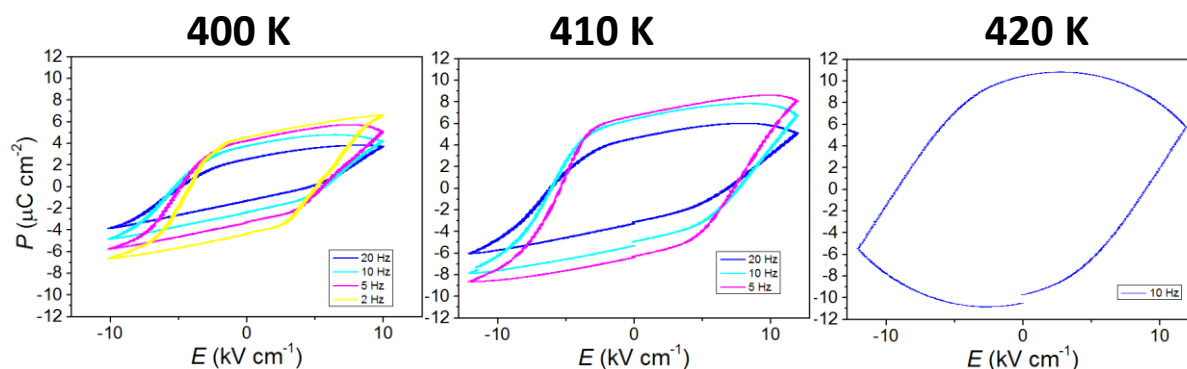


Figure A-1. $P(E)$ loops of [Mdabco]NH₄I₃ measured at different temperatures and different frequencies. At the temperature of 420 K, the $P(E)$ loop clearly shows leakage.

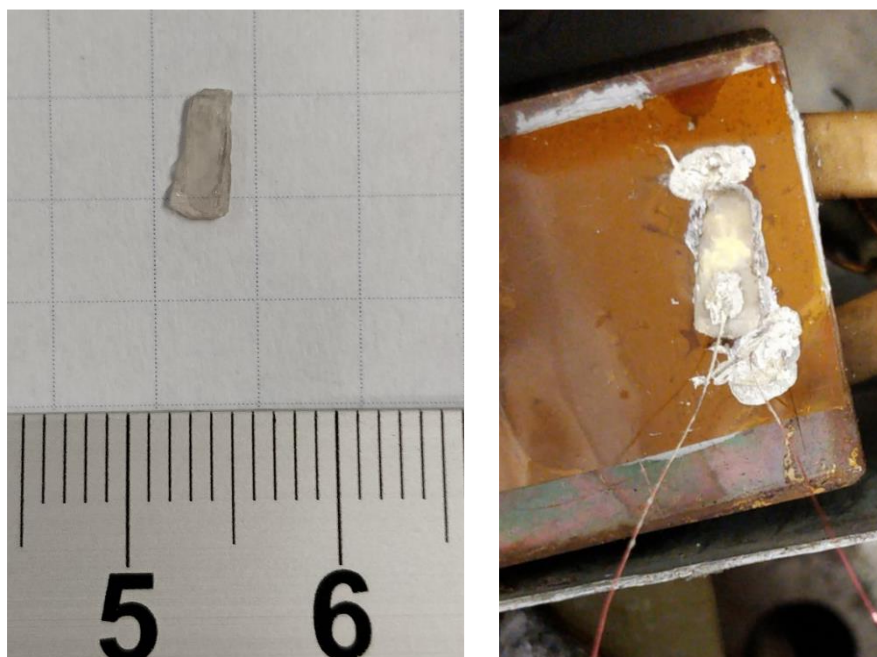


Figure A-2. **Left:** photograph of the single crystal of $[\text{Mdabco}]\text{NH}_4\text{I}_3$ before measurement. The crystal is nearly transparent and colourless. **Right:** photograph after the ferroelectric measurements upon heating to 420 K. The colour of the crystal turned yellow, suggesting changes in chemical composition.

The yellow colour could possibly be from the molecular iodine reacting with the electrode material, silver paste. Therefore, DSC measurements in Fig. A-3 were performed. The results show that the peaks associated with phase transition are at different temperatures during the first and second cycles. This indicates an irreversible phase transition happened during the first cycle. Mixing the sample with electrode materials silver or carbon does not change the position of heat flow peaks. DSC measurement under inert nitrogen flow does not change the peaks either. Therefore, the irreversible change is not caused by the chemical reaction with the electrode materials or with oxygen. This could be due to the material decomposition upon heating.

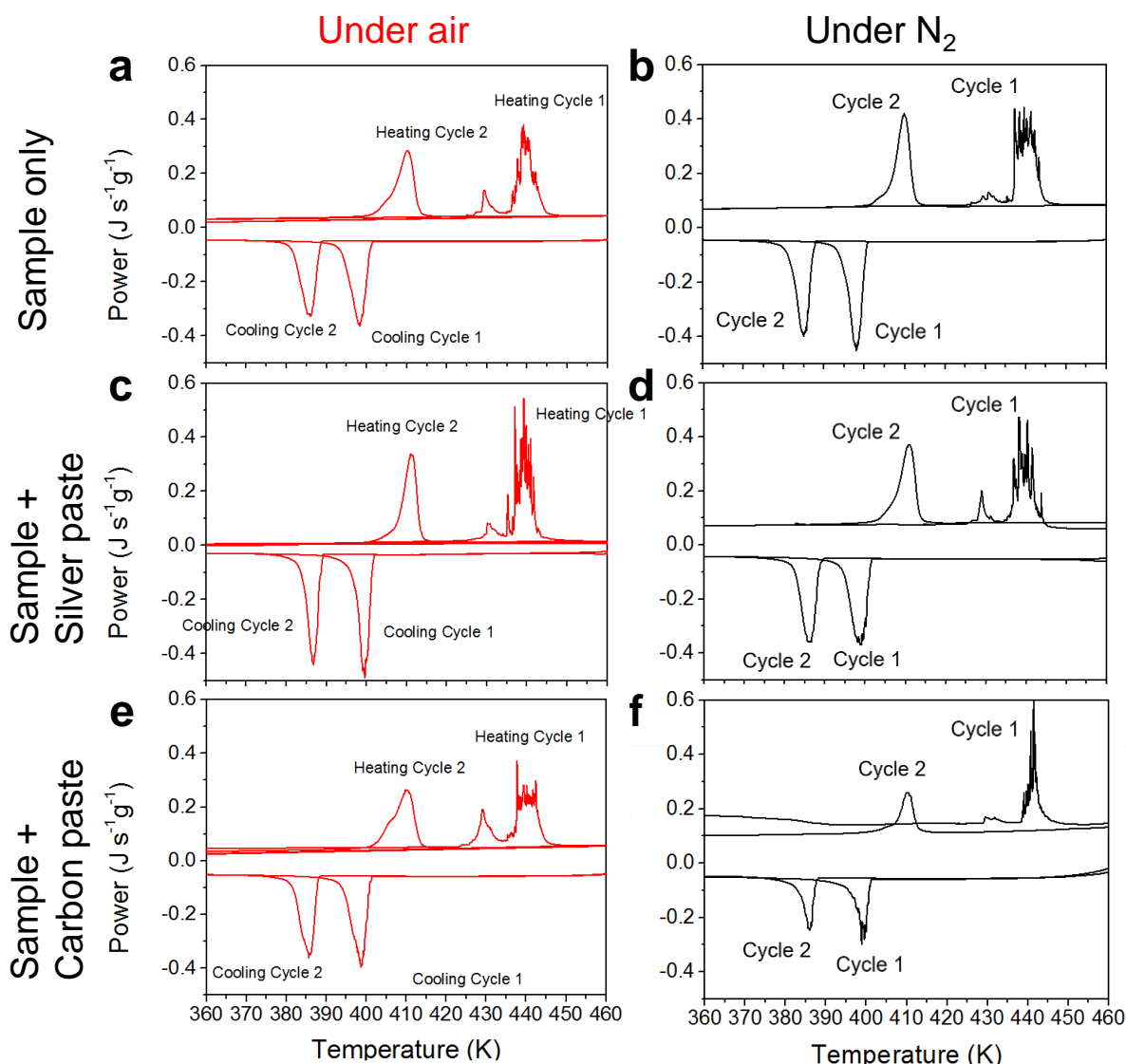


Figure A-3. DSC measurements on $[\text{Mdabco}]\text{NH}_4\text{I}_3$. (a)(c)(e) were performed under air while (b)(d)(f) were performed under nitrogen flow. (a)(b) were the sample only. (c)(d) were the sample mixed with silver paste. (e)(f) were the sample mixed with carbon paste. The results show that peaks of heat flow do not vary the nitrogen atmosphere or addition of silver/carbon.

Therefore, thermogravimetric analysis(TGA) and DSC were performed simultaneously, as shown in Fig. A-4. This experiment was performed by Dr Dumitru Sirbu at Newcastle University. Clearly, the decrease of sample weight starting from $\sim 165^\circ\text{C}$ (438 K) proved the decomposition of $[\text{Mdabco}]\text{NH}_4\text{I}_3$. The chemical reaction in the $[\text{Mdabco}]\text{NH}_4\text{I}_3$ needs to be further investigated. A reversible phase transition is required for the EC effects.

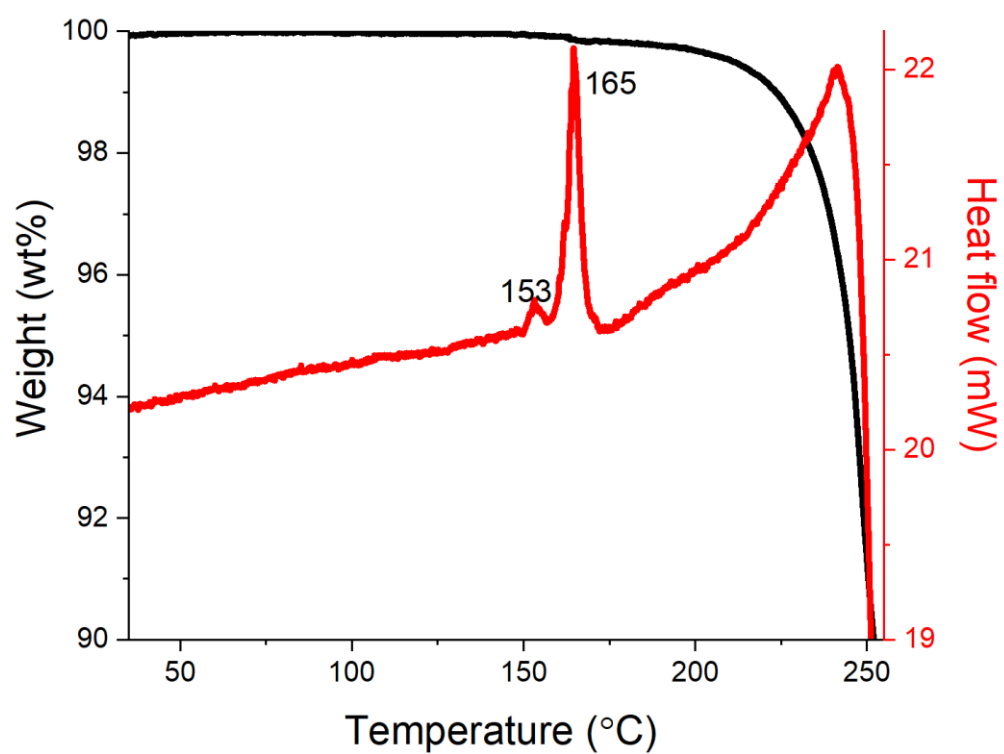


Figure A-4. TGA/DSC measurements. The TGA(black) shows the weight loss of the sample during heating. The DSC(red) shows the heat flow associated with the weight loss. This experiment was performed by Dr Dumitru Sirbu.

1.2 BC effects in metal-free perovskites

Among the reported materials, another material $[\text{Dabco}]\text{NH}_4\text{Br}_3$ was also successfully synthesised in the form of crystal. Measurements of EC effects were attempted, but the crystals were leaky. The preliminary results of BC effects in $[\text{Dabco}]\text{NH}_4\text{Br}_3$ are shown in this section.

Fig. A-5(a)(b) shows the results of pressure-dependent calorimetry. Upon heating, $[\text{Dabco}]\text{NH}_4\text{Br}_3$ shows sharp peaks, while upon cooling, peak splitting was observed. The entropy derived from heating $|\Delta S_0| \sim 28 \text{ J K}^{-1} \text{ kg}^{-1}$ matches that from cooling. This splitting could be due to the existence of multiple low-temperature phases that are energetically very similar. However, further investigation is required for conclusions.

The BC effects are estimated as shown in Fig. A-5. Notably, only the entropy associated with the latent heat is considered. $[\text{Dabco}]\text{NH}_4\text{Br}_3$ shows $|\Delta S| \sim 20 \text{ J K}^{-1} \text{ kg}^{-1}$ in response to $|\Delta p| \sim 1200 \text{ bar}$, which is lower than the full entropy change $|\Delta S_0| \sim 28 \text{ J K}^{-1} \text{ kg}^{-1}$. This value of $|\Delta S|$ is smaller than the materials reported in Chapter 5 and Chapter 6. In addition, the thermal hysteresis is $\sim 20 \text{ K}$. This suggests that driving the full entropy reversibly will need much higher pressure, which is beyond the limit of our instrument. Therefore, $[\text{Dabco}]\text{NH}_4\text{Br}_3$ was not proceeded for further study.

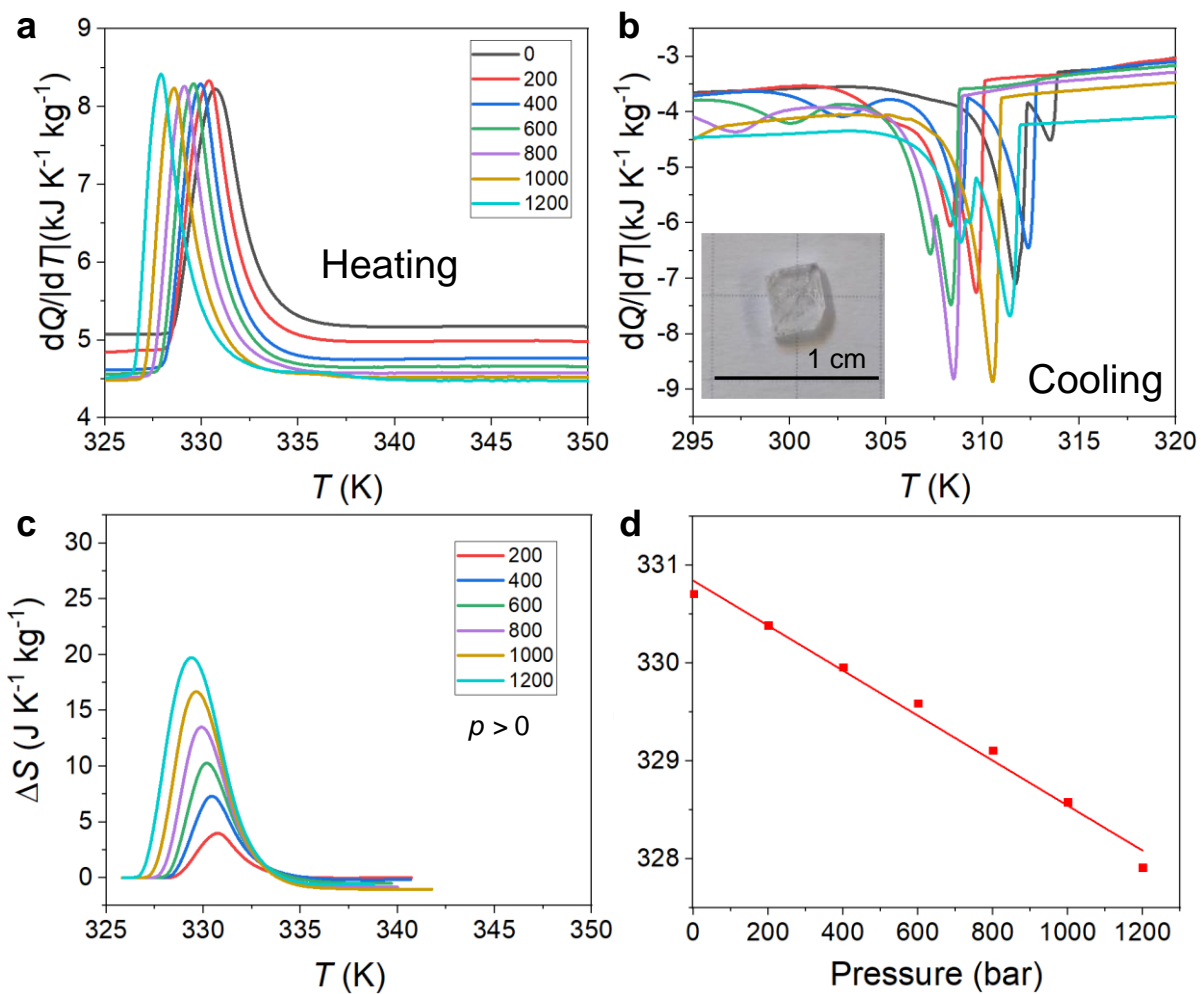


Figure A-5. (a)(b) the pressure-dependant calorimetry measurement on heating(a) and cooling(b). The inset in (b) is the photograph of $[\text{Dabco}]\text{NH}_4\text{Br}_3$ crystal used for the measurements. (c) the entropy change ΔS driven by pressure deduced from (a). (d) the phase transition temperature T_C as a function of pressure. The value of T_C is identified by the maximum of peaks in (a)

2. Data processing script in Python 3.0

The scripts below are designed for processing experimental data. A big difference made here is that my scripts yield very dense datasets. When it comes to fitting, it gives more representative results than selecting a few data points. More scripts related to this dissertation can be accessed from (<https://github.com/liuzipenguk/data-processing>.)

2.1 Arrhenius fitting for impedance datasets

```
import re
import os
from glob import glob
import pandas as pd
import numpy as np
import matplotlib as mpl
import matplotlib.pyplot as plt
from sklearn.linear_model import LinearRegression
from scipy import integrate
from scipy.signal import find_peaks
from scipy.fftpack import fft
from scipy import signal, misc
from scipy.ndimage import gaussian_filter1d

df = pd.read_csv(r'C:\PhD-Zipeng\Research projects\DABCO\BF4\New impedance low
to 40Hz\5th Run another sample\Heating individual
files\375.08.tab',delimiter='\t',encoding= 'unicode_escape')
df.head(10)

E_ima = df['Resistance']
E_ima_smooth = gaussian_filter1d(E_ima.iloc[:,6.5])

plt.plot(df['4294A_Frequency'],E_ima,'g--')
plt.plot(df['4294A_Frequency'],E_ima_smooth,'r')
plt.xscale('log')
plt.xlabel('rows')
plt.ylabel('E imaginary')
plt.xlim((1000,5000))
plt.show()

# find peak
indices = find_peaks(E_ima_smooth, prominence=0)[0]
print(indices)
```

```

#find temperature with regular expression
path = r'C:\PhD-Zipeng\Research projects\DABCO\BF4\New impedance low to
40Hz\4th Run back to 103-106 Hz_E2shape is back\Individual
files_heating_1Kmin'
files = os.listdir(path)
temperature = list()
for file in files:
    if file.endswith(".tab"):
        num = re.findall(r"\d+\.\d+", file)
        temperature.append(float(num[0]))
print(temperature)

#loop for all files
path = r'C:\PhD-Zipeng\Research projects\DABCO\BF4\New impedance low to
40Hz\4th Run back to 103-106 Hz_E2shape is back\Individual
files_heating_1Kmin'

files = glob(path + "/*.tab")

lst_T=list()
lst_f_relax=list()
i = 0

for file in files:
    df = pd.read_csv(file,delimiter='\t',encoding= 'unicode_escape')
    E_ima = df['4294A_D']
    E_ima_smooth = gaussian_filter1d(E_ima.iloc[:, 10.2)
    indices = find_peaks(E_ima_smooth, prominence=0)[0]

    lst_T.append(temperature[i])
#    print(temperature[i]) # for debug

    f_relaxation = df.loc[int(indices[0]),'4294A_Frequency']
    lst_f_relax.append(f_relaxation)
    i = i+1

dic={"T":lst_T,
     "f_relaxation":lst_f_relax}
dt=pd.DataFrame(dic)
dt.head(10)

dt.to_csv(r'C:\PhD-Zipeng\Research projects\DABCO\BF4\New impedance low to
40Hz\4th Run back to 103-106 Hz_E2shape is back\Arrhenius fitting\f0 vs T
Cooling.csv')

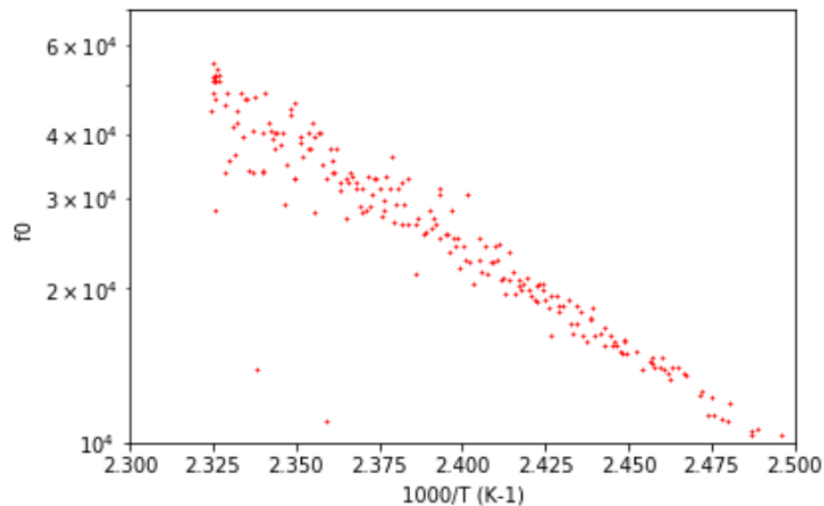
```

```

T = dt['T']
one_over_T = 1000/T

plt.plot(one_over_T,dt['f_relaxation'],'r+',linewidth=1, markersize=2)
plt.yscale("log")
plt.xlabel('1000/T (K-1)')
plt.ylabel('f0 ')
plt.xlim((2.3,2.7))
plt.ylim((9000,30000))
plt.show()

```



2.2 Construction of 3D plots of dielectric constant

```

import re
import os
from glob import glob
import pandas as pd
import numpy as np
import matplotlib as mpl
import matplotlib.pyplot as plt
from sklearn.linear_model import LinearRegression
from scipy import integrate
from scipy.signal import find_peaks

```

```

from scipy.fftpack import fft
from scipy import signal, misc
from scipy.ndimage import gaussian_filter1d

path = r'C:\PhD-Zipeng\Research projects\DABCO\BF4\Impedance\Arrhenius
fitting\Heating'
files = os.listdir(path)
temperature = list()
for file in files:
    if file.endswith(".tab"):
        num = re.findall(r"\d+\.\d+", file)
        temperature.append(float(num[0]))
print(temperature)

path = r'C:\PhD-Zipeng\Research projects\DABCO\BF4\Impedance\Arrhenius
fitting\Heating'

files = glob(path + "/*.tab")

dt=pd.DataFrame()

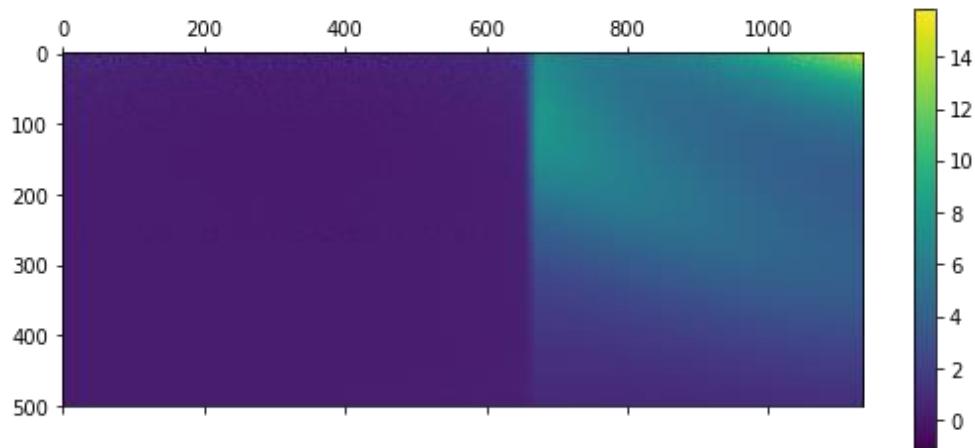
# lst_T=list()
# lst_E2=list()
i = 0

for file in files:
    df = pd.read_csv(file,delimiter='\t',encoding= 'unicode_escape')
    E_ima = df['E imaginary']
    E_ima_smooth = gaussian_filter1d(E_ima.iloc[:, 10.2])
    dt.insert(i, str(temperature[i]),E_ima )
    i = i+1

dt.head(10)

mpl.pyplot.matshow(dt,cmap='viridis')
# plt.axis([58,70,0,10])
plt.colorbar()
# ax.set_xscale('log')
plt.show()

```



2.3 Traditional indirect method for $P(E, T)$ datasets

```

import re
import os
from glob import glob
import pandas as pd
import numpy as np
import matplotlib as mpl
import matplotlib.pyplot as plt

from scipy import integrate
from scipy import interpolate
from scipy.signal import find_peaks
from scipy.interpolate import interp1d
from scipy.signal import savgol_filter
df = pd.read_csv(r'C:\\PhD-Zipeng\\Research projects\\PUND\\BF4 PUND PE
Heating\\PECorrected\\377.08.csv',encoding= 'unicode_escape')
print(df.head(5))
df.drop(['P_SI'],axis=1,inplace=True)
df.drop(['E_SI'],axis=1,inplace=True)

# convert P into C/m^2
# convert E into V/m
thickness = 250 # unit in micro-metre

P_SI = df['Corrected P']*0.01
E_SI = df['#Drive Voltage']/(thickness*0.000001)

df.insert(len(df.columns), "E_SI", E_SI)
df.insert(len(df.columns), "P_SI", P_SI)

```

```

print('#-----below is after interting columns of P_SI AND
E_SI0-----#')
print(df.head(5))
print('#-----#')
-----#')
plt.plot(df['E_SI'],df['P_SI'],'go--')
plt.xlabel('E_SI')
plt.ylabel('P_SI')
plt.show()

## loop for all

path = 'C:\\PhD-Zipeng\\Research projects\\PUND\\BF4 PUND PE
Heating\\PECorrected'
output_path = 'C:\\PhD-Zipeng\\Research
projects\\DABCO\\BF4\\No16_2x42mm2_250um\\PUND indirect\\Raw data_SI units'
files = glob(path + "/*.csv")
thickness = 250 # unit in micro-metre
i = 0

for file in files:
    df = pd.read_csv(file,delimiter=',')
    df.drop(['P_SI'],axis=1,inplace=True)
    df.drop(['E_SI'],axis=1,inplace=True)

    P_SI = df['Corrected P']*0.01
    E_SI = df['#Drive Voltage']/(thickness*0.000001)

    df.insert(len(df.columns), "E_SI", E_SI)
    df.insert(len(df.columns), "P_SI", P_SI)

    file_name = output_path +'\\'+ str(temperature[i])+'.csv'

    df.to_csv(file_name, index=None)
    i = i+1

#https://docs.scipy.org/doc/scipy/reference/generated/scipy.interpolate.interp
1d.html
x = P_upper['E_SI']
y = P_upper['P_SI']

## smooth data if necessary

# y = savgol_filter(P_upper['P_SI'], 21, 1)
# plt.plot(x, y)

```

```

# plt.show()

f = interp1d(x, y, fill_value="extrapolate", kind='next')
xnew = np.linspace(0, 1200000, num=200, endpoint=True)

plot1 = plt.plot(x, y,)
plot2 = plt.plot(xnew, f(xnew), 'r-')
plt.legend(['raw data', 'fitting data'], loc='best')
plt.xlabel('E_SI')
plt.ylabel('P_SI')
plt.show()

plot1 = plt.plot(x, y,)
plot2 = plt.plot(xnew, f(xnew), 'r-')
plt.legend(['raw data', 'linear'], loc='best')
plt.axis([1100000, 1200000, 0.01, 0.012])
plt.xlabel('E_SI')
plt.ylabel('P_SI')
plt.show()

P_upper_fitting = pd.DataFrame()
P_upper_fitting.insert(len(P_upper_fitting.columns), "E_SI", xnew)
P_upper_fitting.insert(len(P_upper_fitting.columns), "P_SI", f(xnew))

P_smooth = savgol_filter(P_upper_fitting["P_SI"], 11, 1)
P_upper_fitting.insert(len(P_upper_fitting.columns), "P_smooth", P_smooth)

plt.plot(P_upper_fitting["E_SI"], P_upper_fitting["P_SI"], 'r-')
plt.plot(P_upper_fitting["E_SI"], P_upper_fitting["P_smooth"], 'g')
plt.xlabel('E_SI')
plt.ylabel('P_SI')
plt.legend(['raw data', 'savgol_filter smoothed'], loc='best')
plt.show()
print('Length of data rows = ', len(P_upper_fitting))
P_upper_fitting.head(5)

path = 'C:\\PhD-Zipeng\\Research projects\\PUND\\BF4 PUND PE
Heating\\PECorrected'
files = os.listdir(path)
temperature = list()
for file in files:
    if file.endswith(".csv"):
        num = re.findall(r"\d+\.\d+", file)
        temperature.append(float(num[0]))

```

```

print(temperature)

path = 'C:\\PhD-Zipeng\\Research
projects\\DABCO\\BF4\\No16_2x42mm2_250um\\PUND indirect\\Raw data_SI units'
output_path = 'C:\\PhD-Zipeng\\Research
projects\\DABCO\\BF4\\No16_2x42mm2_250um\\PUND indirect\\PE matrix'
files = glob(path + "/*.csv")

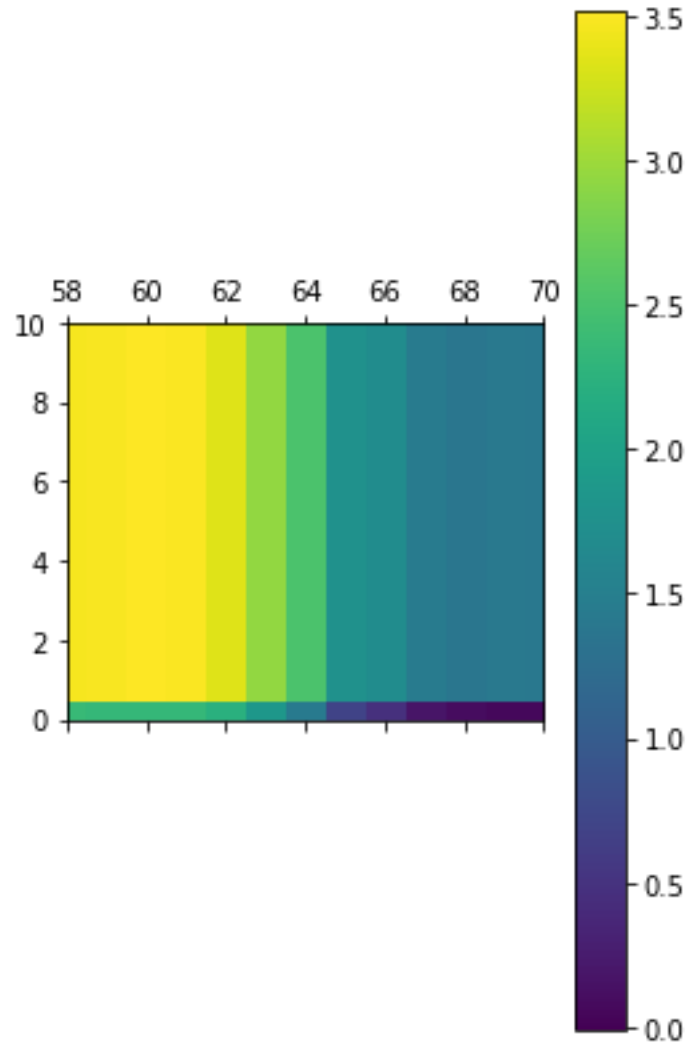
P_upper_fitting = pd.DataFrame()
E = np.linspace(0, 1200000, num=240, endpoint=True)
P_upper_fitting.insert(len(P_upper_fitting.columns), "E_SI", E)

i= 0
for file in files:
    df = pd.read_csv(file,delimiter=',', engine='python')
    index1 = df['P_SI'].idxmax()
    index2 = df['P_SI'].idxmin()
    P_upper = df.loc[index1:index2, [ 'E_SI','P_SI']]
    x = P_upper['E_SI']
    y = P_upper['P_SI']
    f = interp1d(x, y, fill_value="extrapolate",kind='next')

    column_name = str(temperature[i])
    P_upper_fitting.insert(len(P_upper_fitting.columns), column_name, f(E))
    i = i+1

print(P_upper_fitting.shape)
P_T = P_upper_fitting.transpose()
P_T_uCcm = P_T[0:1].append(P_T[1:]*100)
mpl.pyplot.matshow(P_T_uCcm[1:].transpose(),interpolation='nearest',cmap='viridis')
plt.axis([58,70,0,10])
plt.colorbar()
plt.show()

```



2.4 PUND-version of indirect method for $P(E, T)$ datasets

```

import re
import os
from glob import glob
import pandas as pd
import numpy as np
import matplotlib as mpl
import matplotlib.pyplot as plt

from scipy import integrate
from scipy import interpolate
from scipy.signal import find_peaks
from scipy.interpolate import interp1d
from scipy.signal import savgol_filter
from scipy.ndimage import gaussian_filter1d

```

```

path = 'C:\\PhD-Zipeng\\Research projects\\DABCO\\BF4\\No16_PUND_cooling'
files = os.listdir(path)
temperature = list()
for file in files:
    if file.endswith(".csv"):
        num = re.findall(r"\d+.\d+", file)
        temperature.append(float(num[0]))
print(temperature)
len(temperature)

path = 'C:\\PhD-Zipeng\\Research projects\\DABCO\\BF4\\No16_PUND_cooling'
# output_path = 'C:\\PhD-Zipeng\\Research
projects\\DABCO\\BF4\\No16_2x42mm2_250um\\PUND indirect\\PE matrix'
files = glob(path + "/*.csv")

P_upper_fitting = pd.DataFrame()
E = np.linspace(0, 1200000, num=241, endpoint=True)
P_upper_fitting.insert(len(P_upper_fitting.columns), "E_SI", E)

i = 0
for file in files:
    df = pd.read_csv(file, delimiter=',', engine='python')
    index1 = df['P_SI'].idxmax()
    index2 = df['P_SI'].idxmin()
    P_upper = df.loc[index1:index2, [ 'E_SI', 'P_SI' ]]
    x = P_upper['E_SI']
    y = P_upper['P_SI']
    f = interp1d(x, y, fill_value="extrapolate", kind='next')

#     column_name = str(temperature[i])
    column_name = temperature[i]
    P_upper_fitting.insert(len(P_upper_fitting.columns), column_name, f(E))
    i = i+1

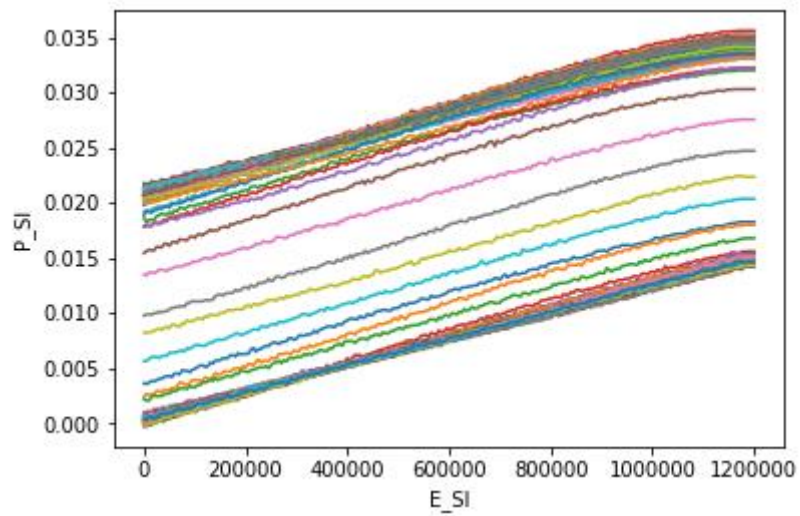
print(P_upper_fitting.shape)
print(P_upper_fitting.shape[0], 'slice of E')
print(P_upper_fitting.shape[1]-1, 'slice of T')
P_upper_fitting.head(5)

i = 0
for j in range(len(temperature)):
    plt.plot(P_upper_fitting['E_SI'], P_upper_fitting[(temperature[i])])
    i = i + 1

plt.xlabel('E_SI')
plt.ylabel('P_SI')

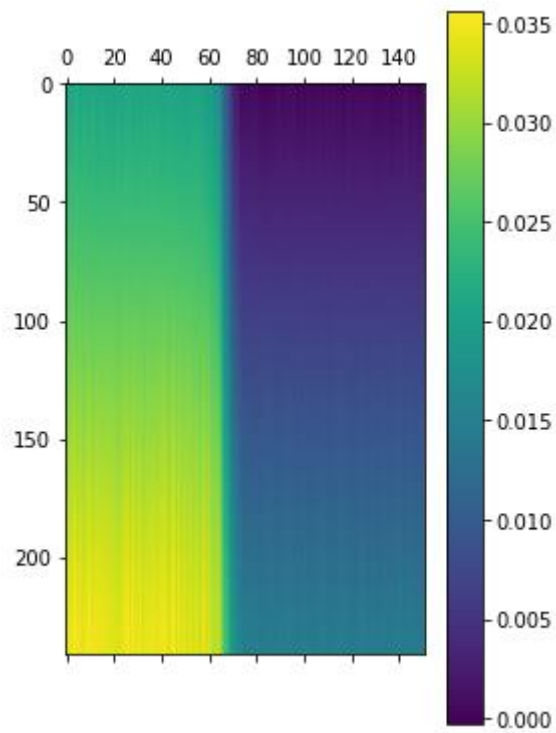
```

```
plt.show()
```



```
P_T = P_upper_fitting.transpose()  
mpl.pyplot.imshow(P_T[1:].transpose(), interpolation='nearest', cmap='viridis')  
# plt.axis([58,70,0,10])  
plt.colorbar()  
plt.show()
```

```
P_T.to_csv(r'C:\PhD-Zipeng\Research  
projects\DABCO\BF4\No16_PUND_cooling\ds\PET phase diagram'+'.csv')
```



3. Landau modelling script in Wolfram Mathematica

```

(** Model parameters are in SI units and are taken from Ye Heng-Yun et al.Science,
361(6398),151-155. **)
(** parameter a is calculated from Curie-
Weiss fitting but T0 is assumed as 392 K according to the DSC data **)
(** Tc is assumed as 444 K according the DSC data. **)

With[{T0 = 392, Tc = 444.72, a = 8032012},
  Solve[{ $\frac{1}{2} a P s^2 (Tc - T0) + \frac{1}{4} b P s^4 + \frac{1}{6} c P s^6 + \frac{1}{8} d P s^8 = 0$  /. Ps  $\rightarrow 21.74 * 10^{-2}$ ,
    b P3 + c P5 + d P7 + a P (T - T0) = 0 /. P  $\rightarrow 22.84 * 10^{-2}$  /. T  $\rightarrow 317.648$ ,
    b P s3 + c P s5 + d P s7 + a P s (Tc - T0) = 0 /. Ps  $\rightarrow 21.74 * 10^{-2}$ }, {b, c, d}]
Out[ ]= {{b  $\rightarrow 1.04788 \times 10^{11}$ , c  $\rightarrow -8.3575 \times 10^{12}$ , d  $\rightarrow 1.25909 \times 10^{14}$ }}

In[ ]:= Clear[parameters]
parameters = {T0  $\rightarrow 392$ , a  $\rightarrow 8032012$ , b  $\rightarrow 1.0478780537808589 * 10^{11}$ ,
  c  $\rightarrow -8.357496261092144 * 10^{12}$ , d  $\rightarrow 1.2590879528938481 * 10^{14}$ };
Tiin = 320; Tfin = 500; NoPin = 500;
ΔE0Range = Range[0, 20, 5]

Out[ ]= {0, 5, 10, 15, 20}

In[ ]:= (*Polarization at zero field*)
PsEqs0up[E0_, T_] :=
  Ps /. FindRoot[-e0 + b p3 + c p5 + d p7 + a p (T - T0) /. parameters /. e0  $\rightarrow E0 \times 10^5$  /.
  p  $\rightarrow Ps * 10^{-2}$ , {Ps, 20, 0.0, 30}] // Quiet;
PsEqs0down[E0_, T_] := Ps /. FindRoot[-e0 + b p3 + c p5 + d p7 + a p (T - T0) /. parameters /.
  e0  $\rightarrow E0 \times 10^5$  /. p  $\rightarrow Ps * 10^{-2}$ , {Ps, 0.1, 0.0, 30}] // Quiet;
PsTable0up[E0_, Ti_, Tf_, NoP_] := ParallelTable[{T, PsEqs0up[E0, T]},
  {T, Ti, Tf,  $\frac{Tf - Ti}{NoP}$ }};
PsTable0down[E0_, Ti_, Tf_, NoP_] := ParallelTable[
  {T, PsEqs0down[E0, T]}, {T, Ti, Tf,  $\frac{Tf - Ti}{NoP}$ }};

Tcin0 = 444.7;
Psdata0a = PsTableSup[#, Tiin, Tcin0, NoPin] & /@ {0};
Psdata0b = PsTableSdown[#, Tcin0 + 0.05, Tfin, NoPin] & /@ {0};
Psdata0 = Flatten[Join[Psdata0a, Psdata0b], 1];
Ps0[T_] := Interpolation[Psdata0, InterpolationOrder  $\rightarrow 1$ ][T]
(*5 kV/cm*)
PsEqs5up[E0_, T_] :=
  Ps /. FindRoot[-e0 + b p3 + c p5 + d p7 + a p (T - T0) /. parameters /. e0  $\rightarrow E0 \times 10^5$  /.

```

```

Ps /. FindRoot[-e0 + b p3 + c p5 + d p7 + a p (T - T0) /. parameters /. e0 → E0 × 105 /.
p → Ps * 10-2, {Ps, 20, 0.0, 30}] // Quiet;
PsEqs5down[E0_, T_] := Ps /. FindRoot[-e0 + b p3 + c p5 + d p7 + a p (T - T0) /. parameters /.
e0 → E0 × 105 /. p → Ps * 10-2, {Ps, 1, 0.0, 30}] // Quiet;
PsTable5up[E0_, Ti_, Tf_, NoP_] := ParallelTable[{T, PsEqs5up[E0, T]},
{ T, Ti, Tf,  $\frac{Tf - Ti}{NoP}$  }];
PsTable5down[E0_, Ti_, Tf_, NoP_] := ParallelTable[
{ T, PsEqs5down[E0, T]}, { T, Ti, Tf,  $\frac{Tf - Ti}{NoP}$  }];
Tcin5 = 445.293;
Psdata5a = PsTable5up[#, Tiin, Tcin5, NoPin] & /@ {5};
Psdata5b = PsTable5down[#, Tcin5 + 0.05, Tfin, NoPin] & /@ {5};

```

2 | v2-Organic perovskites EC effects.nb

```

Psdata5 = Flatten[Join[Psdata5a, Psdata5b], 1];
Ps5[T_] := Interpolation[Psdata5, InterpolationOrder → 1][T]
(*10 kV/cm*)
PsEqs10up[E0_, T_] :=
Ps /. FindRoot[-e0 + b p3 + c p5 + d p7 + a p (T - T0) /. parameters /. e0 → E0 × 105 /.
p → Ps * 10-2, {Ps, 20, 0.0, 30}] // Quiet;
PsEqs10down[E0_, T_] := Ps /. FindRoot[-e0 + b p3 + c p5 + d p7 + a p (T - T0) /. parameters /.
e0 → E0 × 105 /. p → Ps * 10-2, {Ps, 1, 0.0, 30}] // Quiet;
PsTable10up[E0_, Ti_, Tf_, NoP_] := ParallelTable[{T, PsEqs10up[E0, T]},
{ T, Ti, Tf,  $\frac{Tf - Ti}{NoP}$  }];
PsTable10down[E0_, Ti_, Tf_, NoP_] := ParallelTable[
{ T, PsEqs10down[E0, T]}, { T, Ti, Tf,  $\frac{Tf - Ti}{NoP}$  }];
- . . . . .

```

```

      {T, PsEqs10down[E0, T]}, {T, Ti, Tf,  $\frac{Tf - Ti}{NoP}$ }}];
Tcin10 = 445.866;
Psdata10a = PsTable10up[#, Tiin, Tcin10, NoPin] & /@ {10};
Psdata10b = PsTable10down[#, Tcin10 + 0.05, Tfin, NoPin] & /@ {10};
Psdata10 = Flatten[Join[Psdata10a, Psdata10b], 1];
Ps10[T_] := Interpolation[Psdata10, InterpolationOrder -> 1][T]
(*15 kV/cm*)
PsEqs15up[E0_, T_] :=
  Ps /. FindRoot[-e0 + b p^3 + c p^5 + d p^7 + a p (T - T0) /. parameters /. e0 -> E0 x 10^5 /.
    p -> Ps * 10^-2, {Ps, 20, 0.0, 30}] // Quiet;
PsEqs15down[E0_, T_] := Ps /. FindRoot[-e0 + b p^3 + c p^5 + d p^7 + a p (T - T0) /. parameters /.
  e0 -> E0 x 10^5 /. p -> Ps * 10^-2, {Ps, 1, 0.0, 30}] // Quiet;
PsTable15up[E0_, Ti_, Tf_, NoP_] := ParallelTable[{T, PsEqs15up[E0, T]},
  {T, Ti, Tf,  $\frac{Tf - Ti}{NoP}$ }}];
PsTable15down[E0_, Ti_, Tf_, NoP_] := ParallelTable[
  {T, PsEqs15down[E0, T]}, {T, Ti, Tf,  $\frac{Tf - Ti}{NoP}$ }}];
Tcin15 = 446.438;
Psdata15a = PsTable15up[#, Tiin, Tcin15, NoPin] & /@ {15};
Psdata15b = PsTable15down[#, Tcin15 + 0.05, Tfin, NoPin] & /@ {15};
Psdata15 = Flatten[Join[Psdata15a, Psdata15b], 1];
Ps15[T_] := Interpolation[Psdata15, InterpolationOrder -> 1][T]
(*20 kV/cm*)
PsEqs20up[E0_, T_] :=
  Ps /. FindRoot[-e0 + b p^3 + c p^5 + d p^7 + a p (T - T0) /. parameters /. e0 -> E0 x 10^5 /.
    p -> Ps * 10^-2, {Ps, 20, 0.0, 30}] // Quiet;
PsEqs20down[E0_, T_] := Ps /. FindRoot[-e0 + b p^3 + c p^5 + d p^7 + a p (T - T0) /. parameters /.
  e0 -> E0 x 10^5 /. p -> Ps * 10^-2, {Ps, 1, 0.0, 30}] // Quiet;
PsTable20up[E0_, Ti_, Tf_, NoP_] := ParallelTable[{T, PsEqs20up[E0, T]},
  {T, Ti, Tf,  $\frac{Tf - Ti}{NoP}$ }}];
PsTable20down[E0_, Ti_, Tf_, NoP_] := ParallelTable[
  {T, PsEqs20down[E0, T]}, {T, Ti, Tf,  $\frac{Tf - Ti}{NoP}$ }}];
Tcin20 = 447.011;
Psdata20a = PsTable15up[#, Tiin, Tcin20, NoPin] & /@ {20};
Psdata20b = PsTable15down[#, Tcin20 + 0.05, Tfin, NoPin] & /@ {20};
Psdata20 = Flatten[Join[Psdata20a, Psdata20b], 1];

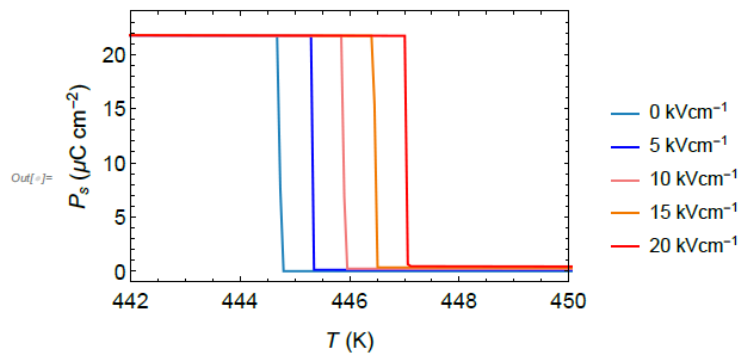
```

```
Psdata20 = Flatten[Join[Psdata20a, Psdata20b], 1];
```

```
Ps20[T_] := Interpolation[Psdata20, InterpolationOrder -> 1][T]
```

```
In[ ]:= LegendColors =  
{ColorData[16, 6], Darker[Blue, 0.01], Darker[Pink, 0.05], Darker[Orange, 0.05], Red};
```

```
Plot[{Ps0[T], Ps5[T], Ps10[T], Ps15[T], Ps20[T]},  
{T, Tiin, Tfin}, PlotStyle -> LegendColors, Frame -> True,  
FrameTicksStyle -> Directive[15], FrameStyle -> Black, FrameLabel ->  
{Style["T (K)", {15, SingleLetterItalics -> False}], Style["Ps ( $\mu\text{C cm}^{-2}$ )", 15]}, None},  
PlotLegends -> {"0 kVcm-1", "5 kVcm-1", "10 kVcm-1", "15 kVcm-1", "20 kVcm-1"},  
PlotRange -> {{442, 450}, {-1, 24}}]
```

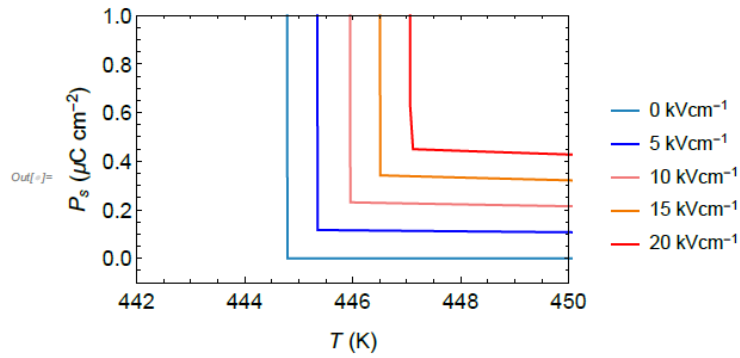


```
In[ ]:= (*Zoom-in to see Ps above superheating temperature *)  
D1+[{D-5(T), D-5(T), D-10(T), D-15(T), D-20(T)}]
```

```

In[ ]:= (*Zoom-in to see Ps above superheating temperature *)
Plot[{Ps0[T], Ps5[T], Ps10[T], Ps15[T], Ps20[T]},
  {T, Tiin, Tfin}, PlotStyle -> LegendColors, Frame -> True,
  FrameTicksStyle -> Directive[15], FrameStyle -> Black, FrameLabel ->
  {Style["T (K)", {15, SingleLetterItalics -> False}], Style["Ps ( $\mu\text{C cm}^{-2}$ )", 15], None},
  PlotLegends -> {"0 kVcm-1", "5 kVcm-1", "10 kVcm-1", "15 kVcm-1", "20 kVcm-1"},
  PlotRange -> {{442, 450}, {-0.1, 1}}]

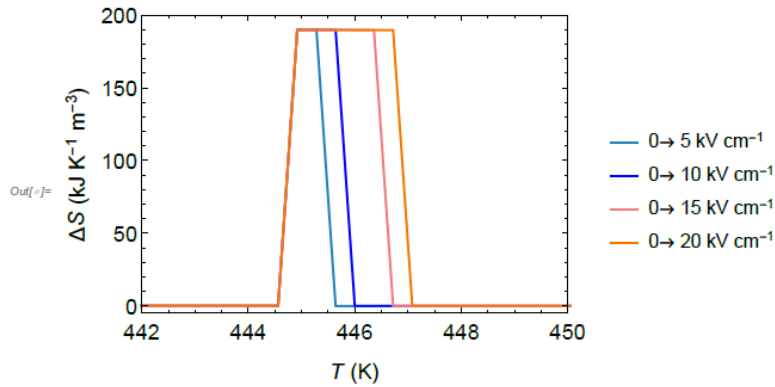
```



```

In[ ]:= ΔSdata5 = Table[{T,  $\left(\frac{a}{2} (Ps5[T]^2 - Ps0[T]^2) \times (10^{-2})^2 \times 10^{-3}\right)$ } /. parameters,
  {T, Tiin, Tfin,  $\frac{Tfin - Tiin}{NoPin}$ }}];
ΔSdata10 = Table[{T,  $\left(\frac{a}{2} (Ps10[T]^2 - Ps0[T]^2) \times (10^{-2})^2 \times 10^{-3}\right)$ } /. parameters,
  {T, Tiin, Tfin,  $\frac{Tfin - Tiin}{NoPin}$ }}];
ΔSdata15 = Table[{T,  $\left(\frac{a}{2} (Ps15[T]^2 - Ps0[T]^2) \times (10^{-2})^2 \times 10^{-3}\right)$ } /. parameters,
  {T, Tiin, Tfin,  $\frac{Tfin - Tiin}{NoPin}$ }}];
ΔSdata20 = Table[{T,  $\left(\frac{a}{2} (Ps20[T]^2 - Ps0[T]^2) \times (10^{-2})^2 \times 10^{-3}\right)$ } /. parameters,
  {T, Tiin, Tfin,  $\frac{Tfin - Tiin}{NoPin}$ }}];
ListPlot[{ΔSdata5, ΔSdata10, ΔSdata15, ΔSdata20}, Joined → True,
  Frame → True, FrameTicksStyle → Directive[15], FrameStyle → Black,
  FrameLabel → {Style["T (K)", {15, SingleLetterItalics → False}],
  Style["ΔS (kJ K-1 m-3)", {15, SingleLetterItalics → False}], None},
  PlotLegends → {"θ → 5 kV cm-1", "θ → 10 kV cm-1", "θ → 15 kV cm-1", "θ → 20 kV cm-1"},
  AspectRatio → 0.7, PlotStyle → LegendColors, PlotRange → {{442, 450}, {-5, 200}}]

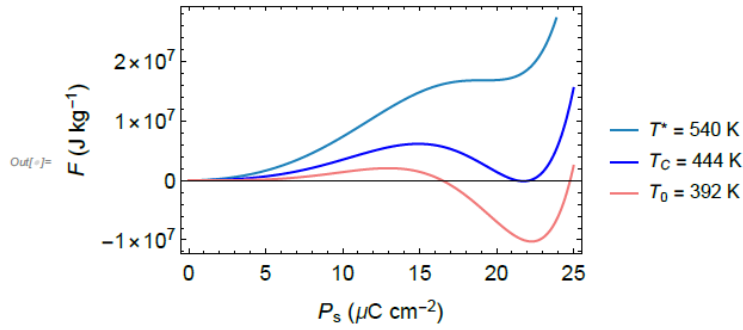
```



```

In[477]:= (* Check the Free Energy at T0, Tc and T*. *)
Plot[{{1/2 a P^2 (T - T0) + 1/4 b P^4 + 1/6 c P^6 + 1/8 d P^8 /. P -> p * 10^-2 /. parameters /. T -> 540,
1/2 a P^2 (T - T0) + 1/4 b P^4 + 1/6 c P^6 + 1/8 d P^8 /. P -> p * 10^-2 /. parameters /. T -> 444,
1/2 a P^2 (T - T0) + 1/4 b P^4 + 1/6 c P^6 + 1/8 d P^8 /. P -> p * 10^-2 /. parameters /. T -> 392},
{p, 0, 25}, Frame -> True, FrameTicksStyle -> Directive[15], FrameStyle -> Black,
FrameLabel -> {Style["P_s (μC cm^-2)", {15, SingleLetterItalics -> False}],
Style["F (J kg^-1)", 15], None},
PlotLegends -> {"T* = 540 K", "T_c = 444 K", "T_0 = 392 K"}, PlotStyle -> LegendColors]

```



```

(*Compare the original data VS Landau fitted data of P(T) at zero field. *)
(*For original data, phase transition is at Tc. *)
(*For data from my Landau model, phase transition is at T*. *)

```

```

In[ ]:= Clear[rawdata]
rawdata = Import["C:\\Users\\Dev\\Desktop\\P(T)-Science1.csv"];
rawdata[[2 ;; All, 1 ;; 2]] // TableForm;
raw = ListLinePlot[rawdata[[2 ;; All, {1, 2}]],
Frame -> True, FrameTicksStyle -> Directive[15], FrameStyle -> Black,
FrameLabel -> {Style["T (K)", {15, SingleLetterItalics -> False}],
Style["P_s (μC cm^-2)", 15], None}, PlotMarkers -> Automatic,
PlotStyle -> Orange, PlotRange -> All, PlotLegends -> {"Original data from paper"}];

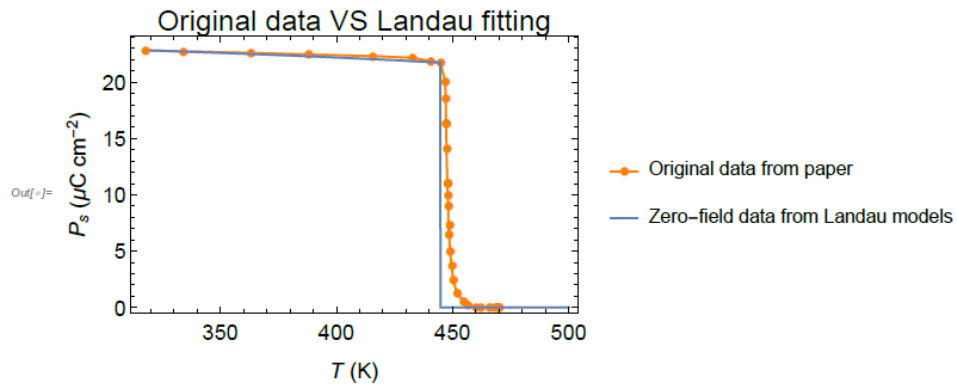
```

```

In[ ]:= simulationdata =
  Plot[{Ps0[T]}, {T, Tini, Tfin}, Frame -> True, FrameTicksStyle -> Directive[15],
  FrameStyle -> Black, FrameLabel -> {Style["T (K)", {15, SingleLetterItalics -> False}],
  Style["Ps (μC cm-2)", 15], None},
  PlotLegends -> {"Zero-field data from Landau models"},
  PlotStyle -> Automatic, PlotRange -> {{300, 450}, {0, 25}}];

Show[raw, simulationdata, PlotRange -> Automatic, Frame -> True,
  PlotLabel -> Style["Original data VS Landau fitting", 20]]

```



(*Solve equations below to calculate T_c at each electric field. *)
 parameters

```

Out[ ]:= {T0 -> 392, a -> 8032012, b -> 1.04788 × 1011, c -> -8.3575 × 1012, d -> 1.25909 × 1014}

```